THE UNIVERSITY *of* LIVERPOOL

Nonlinear Adaptive Control of Permanent Magnet Synchronous Generator Based Wind Turbine: A Perturbation Estimation Approach

Thesis submitted in accordance with the
requirements of the University of Liverpool
for the degree of Doctor of Philosophy

in

Electrical Engineering and Electronics

by

Jian Chen, B.Sc.(Eng.)

September 2014

Nonlinear Adaptive Control of Permanent Magnet Synchronous Generator
Based Wind Turbine: A Perturbation Estimation Approach

by

Jian Chen

Acknowledgements

I would like to give my heartfelt thanks to my supervisor, Dr. L. Jiang, whose encouragement, guidance and support enabled me to develop a deep understanding of my work. Without his consistent and illuminating instruction, my research work could not proceed to this stage. The research skill, writing skill and presenting skill he taught me will benefit me throughout my life, as well as his inspiring insight into life philosophy and poetry.

I would like to show my gratitude to Professor Q.H. Wu, my second supervisor, for his kind guidance with his knowledge of power systems.

I offer my regards and blessings to all of the members of Electrical Drives, Power and Control Research Group, the University of Liverpool. Special thanks also go to my friends, H. Sheng, Y. Dong, S. Lin and Y. Q. Pei, for their support and friendship. My thanks also go to the Department of Electrical Engineering and Electronics at the University of Liverpool, for providing the research facilities that made it possible for me to carry out this research.

Last but not least, I am deeply grateful to my wife Wei Jiang, for her encouragement, patience and understanding, and to our parents, for their support and love, during the period of my postgraduate life.

Abstract

This thesis deals with the modeling and control of permanent magnet synchronous generator based wind turbines (PMSG-WTs). The PMSG-WTs are widely used in wind energy conversion systems(WECSs), due to their merits such as high reliability, high efficiency, low noise, high torque to weight ratio and fast dynamic response. Usually, a PMSG-WT is connected to the power grid via an AC-DC-AC converter system. The PMSG-WT can rotate at varying speed based on variable wind power input and thus achieve high efficiency as it dose not need to synchronise its rotational speed with the grid frequency.

An overview of the modeling of the PMSG-WT is give at first, with conventional vector control (VC) strategies applied for machine-side and grid-side converter. The VC strategy is a popular method widely used in industry due to its decoupled control of active/reactive power, but it may not provide satisfactory performance for the PMSG-WT as it is required to operate at varying speed in an operation envelope with wide operating range rather than one operation point. The feedback linearisation control (FLC) strategy can improve the performance of the VC with a global optimal controller crossing a wide region and variable operation points, but it has weak robustness against parameter uncertainties and external disturbances, and requires full state measurements.

To improve performance of the VC and the FLC, nonlinear adaptive controllers (NACs) designed based on FLC and perturbation estimation and their applications in machine-side and grid-side converter control of the PMSG-WT, and speed control of a permanent magnet synchronous motor (PMSM) have been studied. In the design of the proposed NAC, by defining a lumped perturbation term to present coupling nonlinear dynamics, parameter uncertainties, and other unknown disturbance, then

a perturbation observer is designed to estimate the perturbation which is used to compensate the real perturbation and realise an adaptive linearising of the original nonlinear system, without requiring the accurate system model and parameters and full state measurements, and still considering all system nonlinearities and unknown time-varying dynamics, such as tower shadow, grid faults and intermittent wind power inputs.

In this thesis, the proposed control schemes are applied for control of PMSG-WT in Region 2, Region 3 and integration with the grid. A NAC is developed for a PMSG-WT to extract maximum wind power in Region 2. Simulation and experiment studies are carried out to verify the design and results show that the proposed NAC can provide better performance in MPPT and robustness against parameter uncertainties and time-varying wind power inputs, in comparison with a convention VC and FLC.

NACs are designed for control of the pitch angle and generator control of a PMSG-WT to limit the extracted power from time-varying wind in Region 3. Simulation results of the proposed NACs are compared to a conventional VC and FLC.

The fault ride-through capability (FRTC) of the PMSG-WT at different voltage dip's levels has been enhanced by a novel NAC applied at the grid-side converter. Simulation results have shown that the proposed NAC can provide satisfactory performances with smaller inrush current and voltage overshoots during grid fault and better robustness against uncertainties.

A coordinated nonlinear adaptive control (CNAC) of the machine-side and grid-side converter in the PMSG-WT were studied. The NACs are designed based on state and perturbation observers for control of subsystems. Simulation results show that the CNAC can coordinate each other to achieve the objectives of different operating regions and enhance the FRTC of the PMSG-WT.

Finally, the proposed control schemes are applied for control of PMSM. NAC is developed for PMSM to track mechanical rotation speed and provide high robustness against system parameter uncertainties and unknown time-varying load disturbances. Simulation results show that the proposed NAC provides better performance and robustness against system parameter uncertainties and unknown time-varying

load disturbances, in comparison with a nonlinear controller with an extended non-linear observer and a conventional VC.

Declaration

The author hereby declares that this thesis is a record of work carried out in the Department of Electrical Engineering and Electronics at the University of Liverpool during the period from October 2010 to September 2014. The thesis is original in content except where otherwise indicated.

Contents

List of Figures

Chapter 1

Introduction

1.1 Background

Renewable energy sources have attracted a lot of attention in recent years, in which wind energy is the fastest growing and most competitive renewable source so far, whose worldwide installation has reached 254 GW by the end of June 2012 [1], because it is a clean, safe and exhaustless renewable power source. In many countries, wind power is promoted via government's policy, meanwhile real commercial generation projects have been established. In Europe, many large-scale offshore wind farms are planned to be built due to abundant offshore wind resources. By 2020, renewable resources may supply 20% of power consumed in Europe, whose realisation relies heavily on large-scale offshore wind farm [2]. For example, the target of the UK in 2020 requires that 9.4% of the total installed power capacity is supplied by offshore wind farms, which is equal to 10 GW [3]. The European Wind Energy Association has set a target of satisfying 23% European electricity needs with wind energy by 2030 [4]. Other countries also have promising offshore wind power resources, such as China and the USA. It is clear that the global market for electrical power produced by wind turbine generators has been increasing steadily, which directly pushes the wind technology into a more competitive area.

The development of modern wind energy conversion technology has been going on since 1970s, and its rapid development seen from 1990s. Typically, there are

two well-known strategies for operating wind energy conversion systems (WECSs), i.e., fixed-speed strategy and variable-speed strategy. Until the mid 1990s, most of the installed wind turbines (WTs) were fixed-speed ones, based on squirrel-cage induction generator (SCIG) directly connected to the grid, and generation was always done at constant speed. Recently, the variable-speed WTs (VSWTs) based on wound rotor synchronous generator (WRSG), double fed induction generator (DFIG) and permanent magnet synchronous generator (PMSG) dominate world market share due to their advantages over fixed-speed WTs (FSWTs), such as high efficiency and power quality [5, 6]. Moreover, VSWTs can control WT speed and power output to reduce load and stresses on blades and tower. Nowadays DFIG based VSWTs have been widely used in WECSs with the merits such as large operation region, small capability of power electronic devices and full controllability of active and reactive power of the DFIG [7]. However, One of the problems associated with WECS equipped with DFIG today is the presence of the gearbox which couples the WT to the generator. The gearbox is inevitable to have some drawbacks, such as increment of maintenance expenses, heat dissipation from friction and audible noise [8, 9]. According to statistics of wind farm operation, 19.4% of WT downtime is due to the gearbox and bearing system [10]. The reliability of the VSWT system can be improved significantly by using a direct-driven PMSG, which is coupled directly to WT without the gearbox, with merits such as self-excitation, high efficiency, low noise, high torque to weight ratio and fast dynamic response [11–17]. Usually, the WECS equipped with a PMSG is connected to the power grid via a full-rated back-to-back power electronic converter. In this system, the WECS dose not need to synchronize its rotational speed with the grid frequency.

1.2   Permanent Magnet Synchronous Generator Based Wind Turbine

The PMSG based WT (PMSG-WT) is a dynamic system with strong nonlinear coupled characteristics and time-varying uncertain inputs. The aerodynamic of WT introduces strong nonlinearities and uncertainties [18]. Due to time-varying
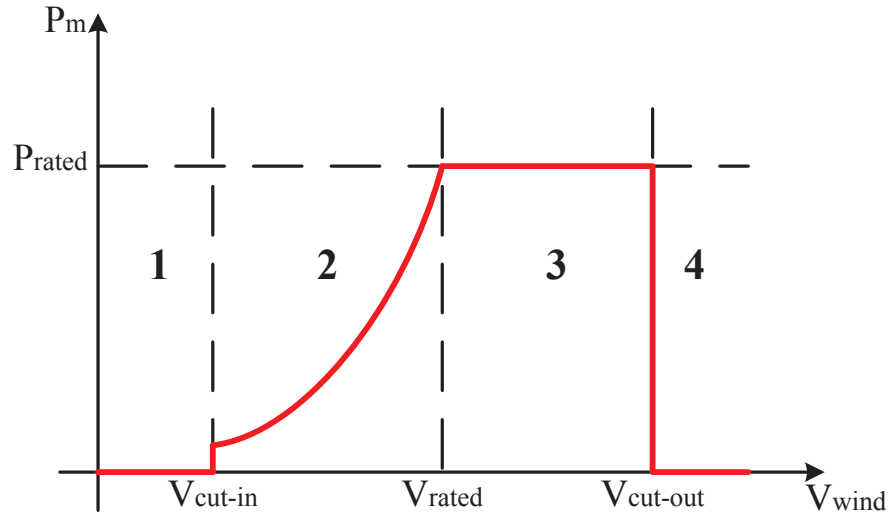
Figure 1.1: Major operating regions of the wind turbine

wind, the WTs are required to operate at wide wind speed range. Different control strategies have been applied to WECS. Normally, control objectives of the WTs are separated into four major operating regions shown in Fig. 1.1. In Region 1, the WT does not operate until wind speed reaches cut-in wind speed V_{ci}; in Region 2, wind speed is between cut-in wind speed V_{ci} and rated wind speed V_r, and the main control objective of this region is extracting the maximum power from wind by mechanical rotation speed control or mechanical torque control; in Region 3, wind speed is between rated wind speed V_r and cut-out wind speed V_{co}, and the main control objective is limiting extracted wind power by blade pitch control and generator torque control to protect the mechanical part of the WECS [19]; in Region 4, wind speed is above the cut-out wind speed V_{co}, the WT is stopped for protection. When the WT operates, the extracted wind power is converted into electrical power by the PMSG, then supplied to the power grid via a full-rated back-to-back power electronic converter.
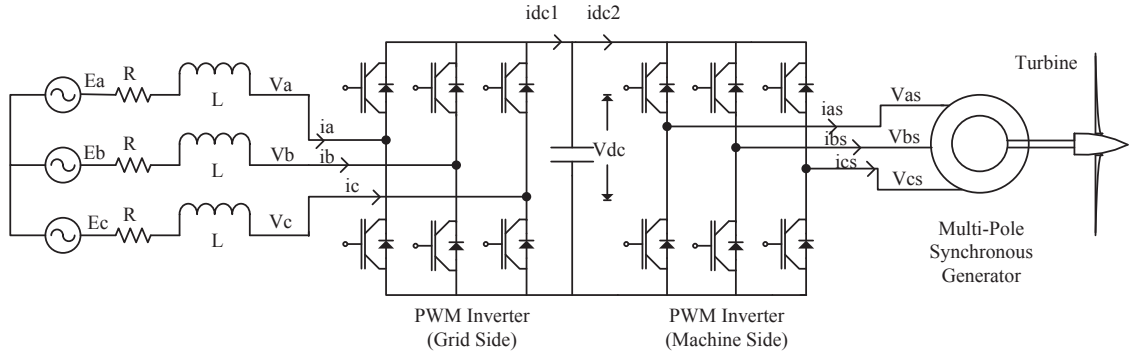
Figure 1.2: WECS equipped with a full-rated back-to-back converter

1.2.1 PMSG Topology

The PMSG-WT equipped with a full-rated back-to-back power electronic converter consists of two voltage-source converters (VSCs), i.e., machine-side converter (MSC) and grid-side converter (GSC), shown in Fig. 1.2. A DC-link is placed between the two converters. The main objective of the MSC is controlling the output power of the PMSG, which can be realised through control of the mechanical torque or the mechanical rotation speed. Meanwhile the GSC is responsible for delivering active power to the grid via the DC-link and maintaining the DC-link voltage. Two VSCs are controlled separately and the dynamic of the PMSG-WT and the power grid is decoupled via the DC-link. A transformer is often connected between the GSC and the grid.

1.2.2 Machine-Side Converter

The main objective of the MSC is to control the output power of the PMSG. In Region 1, no generating power is output. In Region 2, the maximum wind power is required to be extracted. For this purpose, the power coefficient C_p should be maximum $C_{p\max}$. It can be realised by maintaining tip speed ratio λ equal to optimal value λ_{opt} and pitch angle β at a fixed value. It in turn requires the mechanical rotation speed w_{m} to track its optimal reference w_{mopt}. In Region 3, the extracted wind power should be maintained at rated power. It requires the corresponding

pitch angle should be achieved, which in turn requires both the mechanical rotation speed w_m and the mechanical torque T_m to be kept at their rated values, respectively. The rated mechanical torque T_m is achieved through controlling the electromagnetic torque T_e to track its rated reference T_{er} when the w_m is kept at its rated reference w_{mr}.

1.2.3 Grid-Side Converter

The purposes of the GSC is to maintain the DC-link voltage V_{dc} at constant. The DC-link can generate or absorb reactive power for voltage support. The GSC is also current regulated, with the d-axis current i_{gd} used to regulate the DC-link voltage V_{dc} and the q-axis current i_{gq} component to regulate the reactive power. The q-axis grid voltage E_{gq} can be taken as zero with correct alignment of the reference frame. Then, the i_{gd} component can be used to regulate active power. Hence, the active and reactive power flowing between the grid and converter can also be controlled independently when DC-link voltage V_{dc} and grid currents (i_{gd},i_{gq}) control strategies are applied.

1.2.4 PMSG-WT Fault-Ride Through

With the fast growing penetration level of wind energy in the current power grid, the reliability of WECS has attracted much attention. To enable the reliable integration of large capacity of wind power, most of the current power grid codes require that WECS must have fault ride-through capability (FRTC) or low-voltage ride-through capability (LVRTC) [20–24]. The FRTC specifies that the WECS must be connected to the power grid during and after grid faults, or undergoing voltage dips due to load disturbances, and to provide active/reactive power control to the power grid [25]. The FRTC of WECSs can be enhanced by installing additional protection devices, such as a rectifier-boost damping resistor for protection of the DC-link voltage [26], active crowbars installed to protect the machine-side converter of the PMSG [27] and the rotor-side converter of the DFIG [28]. Using the extra device increases the cost of the whole system. Another effective alternative to enhance the

FRTC of WPGSs is to redesign or improve the control algorithms applied on the VSCs, which can avoid installation of additional equipment and allow reduction of the power rating of the protection devices [29–35]. More detailed analysis of WECS fault conditions and converter protection methods will be summarised in Chapter 4 and 5, with a proposed nonlinear adaptive control (NAC) strategy.

1.3 Control of Permanent Magnet Synchronous Generator Based Wind Turbine

The control system is an important part in a WECS. The control of PMSG-WT has attracted much attention in the last few decades, and the technology has further advanced in recent years. In this thesis, the conventional vector control (VC) with proportional-integral (PI) loops, feedback linearisation control (FLC) and proposed nonlinear adaptive control (NAC) are applied for GSC, MSC, and permanent magnet synchronous motor (PMSM) control.

In this section, three control methods are to be discussed, i.e., the VC, FLC and NAC. The comparisons of these three methods are shown in Table 1.1.

1.3.1 Vector Control

The Vector Control (VC) was first applied to the induction motor at the beginning of 1970s and latter to PMSM drive. It allows both induction and synchronous machines to achieve similar torque control performance to a separately excited direct current (DC) motor where torque and flux can be controlled separately. The VC is the current industrial stand control algorithm for the regulation of the output power of the PMSG-WT, which is widely used in industry due to its relative simple implementation and decoupling control of the active and reactive power. The VC mainly consists two steps: firstly, the system model under a three-phase natural reference frame (a-b-c) is transformed to a two-phase stationary reference frame ($\alpha - \beta$), which is then transformed to a two-phase d-q rotating reference frame in which the d-axis or q-axis is aligned with the vector of one of system variables; sec-

Table 1.1: Comparisons of VC, FLC and NAC methods

Control Methods	Advantages	Disadvantages
VC	Simplicity;	Incapable of providing global optimal performance for whole operation region.
FLC	Provide global optimal performance for whole operation region; fully decouple nonlinear system;	Weak robustness; require detailed system model.
NAC	Provide global optimal performance for whole operation region; fully decouple nonlinear system; high robustness; do not require detailed system model;	Time delay for estimation.

ondly, decouple the interaction among state variables, then the linear relationship between the controlled variables and the outputs can be achieved.

For the MSC, the output power of PMSG-WT is required to be regulated. Traditional VC scheme has been widely used in PMSG-WT [9, 17, 35–40]. In Region 2 (Fig. 1.1), the VC consists three control loops. The q-axis stator current reference i_{mqr} can be obtained from the output of the mechanical rotation speed w_{m} control loop or from a reference electromagnetic torque T_{er}. The outputs of stator currents $(i_{\mathrm{md}}, i_{\mathrm{mq}})$ control loops are the stator voltages $(V_{\mathrm{md}}, V_{\mathrm{mq}})$ generated by MSC, respectively. In Region 3, the output of the mechanical rotation speed w_{m} control loop generates the pitch angle reference β_{r}. The required stator voltages $(V_{\mathrm{md}}, V_{\mathrm{mq}})$ can be obtained from stator currents $(i_{\mathrm{md}}, i_{\mathrm{mq}})$ control. For the GSC, it aims to maintain the DC-link voltage V_{dc} at constant, then the control of the MSC and GSC can be decoupled. The d-axis grid current reference i_{gdr} is generated from the outer DC-link voltage V_{dc} control loop. The inner d-axis current i_{gd} control loop controls the GSC voltage V_{gd}, meanwhile the q-axis i_{gq} control loop is used to control V_{gq}.

Although VC is simple, there are still some disadvantages by using this approach. The major one is that VC is designed based on one operation point, which may not be capable of providing global optimal performance for varying operation points.

1.3.2 Feedback Linearisation Control

Compared with linear methods designed based on a linear model obtained from one operation point, feedback linearisation control (FLC) method can provide consistent optimal performance in an operation envelope with a wide range rather than one operation point and has already attracted lots of research efforts in design and application of FLC for nonlinear systems [35, 41–47]. The FLC is an approach for nonlinear control design. By designing a state transformation and a nonlinear feedback control law, a nonlinear system is transformed into a fully or partially decoupled linear one, then well-known and powerful linear techniques are used to complete the control design. A lot of previously intractable nonlinear problems can be converted into much more simpler problems, which can be solved by familiar linear system methods.

Although the FLC has been used to solved many practical nonlinear problems and had a number of successful applications, it still has a few of drawbacks. Firstly, it requires the accurate system model and system parameters, which may not provide capacity to handle the presence of parameter uncertainties or external disturbances; secondly, it requires full state feedback; thirdly, it always results in a complex control law so that the implementation of the FLC is not easy in practice. In fact, such a complex nonlinear controller may not always provide better performance than a simple linear controller. In order to deal with nonlinear dynamic system uncertainties and disturbances, adaptive control methods are employed to improve the performance of the FLC.

1.3.3 Nonlinear Adaptive Control

Adaptive control of nonlinear systems attracted attention in the mid 1980s and grown rapidly in the 1990s. It is because that the adaptive control can deal with unknown parameters or slowly time-varying system parameters. A complete and pedagogical presentation of nonlinear adaptive controller (NAC) has been given in [48].

Among the early estimation based results are Sastry and Isidori [49], Pomet and Praly [50], etc. Marino and Tomei had proposed one of the first output-feedback design [51,52]. The partial state feedback problem had been solved by Kanellakopoulos, Kokotović and Morse [53]. A tracking design where the regressor depends only on reference signals was given in [54]. Khalil [44] and Janković developed semi-global output feedback designs for a class which includes some systems not transformable into the output feedback form.

An important technique for the design of the output feedback control of nonlinear system has been developed by using the high gain observer in the adaptive output feedback control strategy. It can estimate robustly the states or the derivatives of the output equivalently (under local weak observability) [55]. This technique was first introduced by Elfandiari and Khali and since then it has been the impetus for many research results over the past decades [56]. It was used to achieve stabilization and semi-global stabilization of fully linearizable systems [56,57], and to design robust servomechanisms for fully linearizable systems [58]. It was also used for the output adaptive control [59], variable structure control [60] and speed control of induction motors [61]. In most of these studies, the controller is designed in two steps. Firstly, a globally bounded state feedback control is designed to meet the design objective. Secondly, a high gain observer, designed to act fast enough, recovers the performance achieved under state feedback.

In this thesis, a NAC via high gain state and perturbation observer (SPO) has been proposed for the control of GSC, MSC and PMSM. The design and analysis of the NAC using high gain state and perturbation observer has been presented in detail in [62]. In the design of the NAC, by defining a lumped perturbation term to present the coupling nonlinear dynamics, parameter uncertainties, and other un-

known disturbance, a perturbation observer is designed to estimate the perturbation which is used to compensate the real perturbation and realise an adaptive linearizing of the original nonlinear system, without requiring the accurate system model and full state measurements, and ignoring any system nonlinearities and unknown dynamics, such as tower shadow, load torque disturbance, grid faults and intermittent wind power inputs. Moreover, as such a controller adopts the estimate of states and perturbation to yield the control signal, it can be easily implemented in practice. This control strategy has been demonstrated by their applications for synchronous generator control and power electronics in power system [63–66].

1.4 Major Contributions

The thesis reports the research work undertaken based on nonlinear adaptive control of PMSG-WT based on states and perturbation estimation. The major contributions of this thesis can be summarised as follows:

The proposed nonlinear adaptive control (NAC) method is firstly applied in PMSG-WT and PMSM.

- A NAC designed based on states and perturbation observer has been applied for maximum power point tracking in Region 2. The proposed NAC can fully decoupled PMSG-WT system and provide a global optimal controller covering the whole operation region. In addition, the NAC possesses great robustness against parameter uncertainties and measurement noises. Simulation results show that the NAC has overcome the drawback of the VC designed based on one operating point and the shortcomings of the FLC relying on the full state feedback, accurate system parameters and detailed nonlinear system model.

- A nonlinear adaptive pitch control of variable-pitch PMSG-WT has been investigated. The control design has been developed based on a fully linearizable model of the PMSG-WT. Simulation studies have been undertaken on PMSG-WT and the comparison with the VC designed based on one operating point, and FLC designed based on accurate model and full state feedback.

- NAC has been investigated for the GSC to improve the FRTC of a full-rated converter based variable-speed wind turbine [63]. It does not require the detailed system model and parameters and is an output feedback controller. Thus, it has a relatively simpler controller and much better robustness than the FLC when there are model uncertainties and unknown disturbances. Comparing with other nonlinear adaptive methods, the proposed NAC can deal with time-varying uncertain dynamics. Performance enhancement has been tested by simulation studies at different voltage dip's levels, and various uncertainties, including model mismatch, measurement noises and time-varying wind power inputs. Simulation results have shown that the proposed NAC can provide satisfactory performances with smaller current and voltage overshoots during grid fault and better robustness against uncertainties, compared with the VC and the model-based FLC.

- A coordinated nonlinear adaptive controller (CNAC) has been developed for the machine-side and grid-side converter of PMSG-WT. The CNAC has a simple form and adaptive nature. Simulation results show that the CNAC can coordinate each other, realizes the control objectives of Region 2 and 3 without requiring the accurate system model and full state measurements, and provides high robustness against grid voltage dips by using pitch control.

The proposed control methods have been applied to design NAC for PMSM.

- A NAC of PMSM has been developed to track mechanical rotation speed and provide high robustness against system parameter uncertainties and unknown load torque disturbance. The idea of the NAC is based on the feedback linearizing control and states and perturbation estimation. Both simulation and experimental results have shown that the proposed NAC achieves satisfactory dynamic performances in the presence of parameter variations and unknown time-varying load torque disturbance.
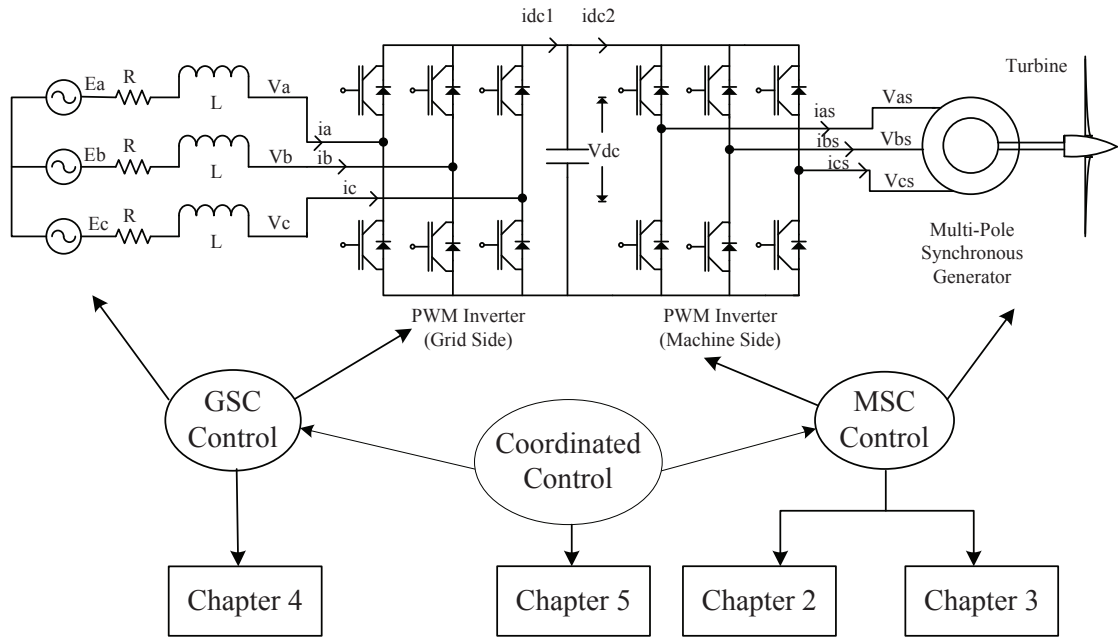
Figure 1.3: The relationships between the work in different chapters

1.5   Thesis outline

This thesis focuses on wind energy conversion system based on a PMSG. The WECS consists two voltage-source converters, i.e., MSC and GSC. The MSC is responsible to control the output power of the PMSG, whereas the objective of the GSC is to maintain the DC-link voltage and deliver active power to the grid. For the control of the MSC, it requires the PMSG-WT extracts the maximum wind power in Region 2, and limits the extracted wind power in Region 3. These two different objectives have been achieved by the proposed NAC in Chapter 2 and 3, respectively. In Chapter 4, the control objective of the GSC has been achieved by the proposed NAC. To investigate the performances of the WECS under normal and fault operation conditions, the coordinate control of the MSC and GSC has been investigated in Chapter 5. To further verification of the proposed NAC, the NAC has been applied in PMSM system in Chapter 6. Hence, the thesis is organised as follows. Fig. 1.3 shows the relationships between the work in different chapters.

The thesis is organized as follows.

Chapter 2: Maximise Power Point Tracking Controller for PMSG Based Wind Turbine

This chapter presents a nonlinear adaptive maximum power point tracking (MPP-T) control strategy for permanent magnet synchronous generator based wind turbine (PMSG-WT) when the WT works in Region 2. In the proposed controller, system nonlinearities, parameter uncertainties, time-varying wind power inputs, and external disturbance of PMSG-WT, are represented as a lumped perturbation term, which is estimated by a designed perturbation observer. The estimate is employed to compensate the real perturbation and finally achieve adaptive feedback linearizing control of original nonlinear system, without requiring the detailed system model and full state measurements. The simulation results show that the proposed control strategy provides the PMSG-WT with the maximum power efficiency and high dynamic performance even in the presence of parameter uncertainties or measurement noises.

Chapter 3: Pitch Control of Variable-Pitch PMSG-based Wind Turbine

In this chapter, a nonlinear adaptive controller (NAC) of PMSG-WT is developed to maintain the extracted wind power at rated power, without requiring accurate PMSG-WT model, parameters and full state measurements, and considering all system nonlinearities and interaction, when the WT operates in Region 3.

Chapter 4: Enhancing Fault Ride-Through Capability of a Full-Rated Converter Based Wind-Turbine

This chapter investigates a novel controller for the grid-side converter (GSC) based on nonlinear adaptive control (NAC). One lumped perturbation term is defined in the NAC to include all unknown and time-varying dynamics and external disturbances of the wind energy conversion system (WECS), and can be estimated by designing a perturbation observer. The estimate of the perturbation term is used to compensate the real perturbation and finally achieve the adaptive feedback linearizing control of the original nonlinear system, without requiring the accurate system model and full state measurements. The proposed NAC is an output feedback control, which is adaptive to parameter uncertainties and unknown nonlinearities of the WECS, and time-varying external disturbances including grid faults, voltage dips and intermittent wind power inputs. The effectiveness of the proposed NAC

is verified by simulation studies and compared with the conventional vector control (VC) and feedback linearisation control (FLC). The simulation results show that the NAC can provide better fault ride-through capability (FRTC) even though the grid voltage levels are far below their nominal values.

Chapter 5: Coordinated Nonlinear Adaptive Control of Machine-side and Grid-side Converter of PMSG-WT

This chapter proposes a new overall control strategy for the PMSG-based WECS in a wide wind speed range. This Chapter extends the author's work in Chapter 2-4. In Region 2, the (maximum power point tracking) MPPT operation is realized by mechanical rotation speed control and stator current control. The proposed MPPT control method in Chapter 2 is employed in this Chapter. In Region 3, the extracted wind power limited by pitch control and stator currents control presented in Chapter 3 is also employed in this Chapter. In Region 2 and 3, the active and reactive power injected into grid is regulated using DC-link voltage control and grid current control loop designed in Chapter 4. The proposed control strategy realizes the control objectives without requiring the accurate system model and full state measurements, and provides high robustness against wind energy conversion system (WECS) parameter uncertainties and grid voltage dips.

Chapter 6: Speed Control of a Permanent Magnet Synchronous Motor With Time-Varying Unknown Load Torque

This chapter investigates a novel controller for the surface-mounted permanent-magnet synchronous motor (SPMSM), based on NAC to optimize the speed-control performance of a SPMSM. In the proposed controller, system nonlinearities, parameter uncertainties, and external disturbance of SPMSM, are represented as a lumped perturbation term, which is estimated by a designed perturbation observer. The estimate is employed to compensate the real perturbation and finally achieve adaptive (feedback linearisation control) FLC of PMSM, without requiring the detailed system model and full state measurements. Both the simulation and experiment results show that the proposed control strategy provides the PMSM with the optimal dynamic performance even in the presence of parameter uncertainties and unknown time-varying load disturbance.

Chapter 7: Conclusions

The thesis has concluded with a summary of the results and several suggestions for future work and several suggestions for future work. The suggestions for future work will highlight the unsolved problems that remain.

1.6 Publication List Related With PhD Thesis

The publications produced from this research work are listed in this section as follows:

1. J. Chen, L. Jiang, Wei Yao, and Q. H. Wu, Perturbation estimation based nonlinear adaptive control of a full-rated converter wind-turbine for fault ride-through capability enhancement, *IEEE Trans. Power Syst.*, vol. PP, no. 99, pp. 1-11, Apr. 2014.

2. Jian Chen and L. Jiang, Nonlinear adaptive control for permanent magnet synchronous generator based wind turbine, *Sustainable Control of Offshore Wind Turbines*, A workshop at the University of Hull, 119-20 Sep. 2012.

3. Jian Chen, L. Jiang, Wei Yao, and Q. H. Wu, A feedback linearization control strategy for maximum power point tracking of a PMSG based wind turbine, in *Proc. IEEE ICRERA*, pp. 79-84, Oct. 2013.

4. W. Zhang, J. Chen, Y. X. Ren, L. Y. Li, W. Yao, and L. Jiang, Nonlinear adaptive control of induction motor with sliding mode flux observer, in *Proc. IEEE ICEMS*, 2014. (Accepted)

5. J. Chen, L. Jiang, Wei Yao, and Q. H. Wu, Nonlinear adaptive MPPT controller for PMSG based wind turbine, *IEEE Trans. Control Syst. Technol.*, 2014. (Submitted)

6. Y. X. Ren, J. Chen. L. Y. Li, L. Jiang, Wei Yao, and Q. H. Wu, Perturbation estimation based nonlinear adaptive speed control of a permanent magnet synchronous motor with time-varying unknown load torque, *IEEE Trans. Ind. Electron.*, 2014. (Submitted)

Chapter 2

Maximum Power Point Tracking Controller for PMSG Based Wind Turbine

2.1 Introduction

In the wind energy conversion system (WECS), an effective maximum power point tracking (MPPT) control strategy is essential in improving the overall efficiency and reducing cost [67, 68]. To extract maximum power from time-varying wind power, numerous studies have been carried out, in which controllers are designed based on an approximated linear model and linear techniques, such as conventional vector control (VC) with proportional-integral (PI) loops [17, 36, 37], and linear quadratic Gaussian (LQG) [69, 70], etc. Among these control strategies, the VC is the current industrial standard solution [71]. Despite the advantages of simplicity and decoupled control of active and reactive power, the VC may not provide satisfactory performance as permanent magnet synchronous generator based wind turbine (PMSG-WT) which is a highly nonlinear system, operating in a wide-range of operation points, due to time-varying wind speed [36]. Thus, the VC designed and tuned based on one operation point is not capable of providing global optimal performance for varying operation points, which stimulates lots of research efforts

on the tuning of VC with PI loops.

Feedback linearizing control (FLC) strategy has been widely applied in power electronics [35, 45], permanent magnet synchronous motor (PMSM) [46], and power systems [47]. The FLC provides nonlinear systems with better dynamic performance than the controllers designed based on an approximated linear model and linear technique [64]. To improve the performance of the VC, the FLC strategy is designed for PMSG-WT to achieve the maximum wind power generation [72]. The PMSG-WT system is transformed into an equivalent linear system via nonlinear feedback control and nonlinear coordinate transformation. Then the closed-loop mechanical rotation speed controller and current controllers are designed via linear control method. The FLC strategy can fully decouple the original nonlinear system and provide a global optimal controller crossing a wide region and variable operation points. The maximum wind power can be extracted with satisfactory dynamic performance when wind speed varies. However, the design of the FLC requires full state feedback, accurate system parameters and accurate system model to calculate full system nonlinearities, and thus always results in a complex control law and has weak robustness against parameter uncertainties and external disturbances [73]. It is because that the parameter uncertainties and external disturbances affect the calculation of the full system nonlinearities, which may degrade the performance of the FLC. In the real system operation, electrical machine parameters, such as stator resistance, inductance, field flux and other parameters of electrical machine, are strongly affected by operating temperature, saturation, skin effects and manufacturing tolerance, which deteriorates performance of the FLC [73–77]. To remedy these shortcomings of the FLC, robust control [78], sliding mode control [79], and nonlinear adaptive control (NAC) [65, 66] have been proposed to remove the dependance of the detailed model of the FLC.

In this chapter, a NAC of PMSG-WT is developed to extract maximum power from wind power and provide high robustness against system parameter uncertainties, and unknown time-varying wind power inputs. In the design of the NAC, by defining a lumped perturbation term to present coupling nonlinear dynamics, parameter uncertainties, and other unknown disturbance, then a perturbation observer

is designed to estimate the perturbation which is used to compensate the real perturbation and realize an adaptive linearizing of the original nonlinear system, without requiring the accurate system model and full state measurements, but fully taking into account of all system nonlinearities, unknown dynamics, and external disturbances caused by tower shadow and intermittent wind power inputs.

The remaining parts of this chapter is organized as follows. In Section II, the model of PMSG-WT is given. In Section III, the nonlinear adaptive control strategy based on perturbation estimation is recalled. The design of the NAC, together with the FLC, is presented in Section IV. Section V carries out simulation and experiment studies to verify the performance of the proposed NAC, compared with the VC and the FLC. Finally, conclusions of this work are presented in Section VI.

2.2 PMSG Based Variable Speed Wind Turbine

The gearless WECS equipped with a PMSG is connected to the power grid via full-rate back-to-back voltage source converters. Its configuration block diagram is shown in Fig. 2.1. Wind energy captured by the WT is transmitted to the direct-drive PMSG. The PMSG converts the mechanical power to electrical power, then supplies it to the power grid through a machine-side converter (MSC) and a grid-side converter (GSC). The MSC is responsible to extract the electric power from the wind by controlling the mechanical rotation speed and maintaining the required stator voltage, whereas the GSC has to enable independent control of the active and reactive power as the grid codes requires and transfer the active power from the generator to the grid via the DC-link. A DC voltage link decouples the operation control of the two converters [35].

2.2.1 Aerodynamic Model

The kinetic power captured from wind by a WT is expressed as following [40,68]

$$P_{\mathrm{w}} = \frac{1}{2}\rho\pi R^2 V^3 C_p(\beta, \lambda) \tag{2.2.1}$$

$$\lambda = \frac{R w_{\mathrm{m}}}{V} \tag{2.2.2}$$
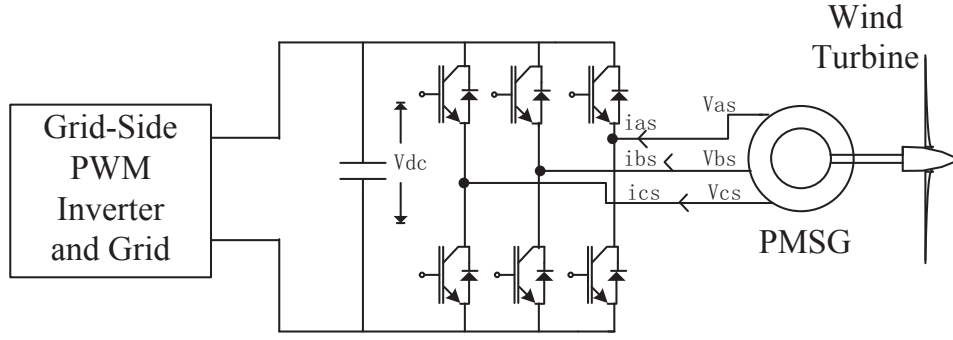
Figure 2.1: Configuration of a PMSG directly driven by a wind turbine

where ρ is the air density, R is the radius of WT, V is the wind speed, C_p is the power coefficient, β is the pitch angle, λ is the tip speed ratio, and w_m is the mechanical rotation speed. The C_p is a function of β and λ and defined by the following function [40]

$$C_p = 0.22(\frac{116}{\lambda_i} - 0.4\beta - 5)e^{\frac{-12.5}{\lambda_i}} \tag{2.2.3}$$

$$\frac{1}{\lambda_i} = \frac{1}{\lambda + 0.08\beta} - \frac{0.035}{\beta^3 + 1} \tag{2.2.4}$$

2.2.2 Permanent Magnet Synchronous Generator Model

The state-space model of the PMSG shown in Fig. 2.1 is given as:

$$\dot{x} = f(x) + g_1(x)u_1 + g_2(x)u_2 \tag{2.2.5}$$

where

$$f(x) = \begin{bmatrix} -\frac{R_\text{s}}{L_\text{md}}i_\text{md} + \frac{w_\text{e}L_\text{mq}}{L_\text{md}}i_\text{mq} \\ -\frac{R_\text{s}}{L_\text{mq}}i_\text{mq} - \frac{1}{L_\text{mq}}w_\text{e}(L_\text{md}i_\text{md} + K_e) \\ \frac{1}{J_\text{tot}}(T_\text{e} - T_\text{m} - T_\text{f} - Bw_\text{m}) \end{bmatrix},$$

$$g_1(x) = [\frac{1}{L_\text{md}} \quad 0 \quad 0]^\text{T},$$

$$g_2(x) = [0 \quad \frac{1}{L_\text{mq}} \quad 0]^\text{T},$$

$$x = [i_\text{md} \quad i_\text{mq} \quad w_\text{m}]^\text{T},$$

$$u = [u_1, u_2]^T = [V_\text{md}, V_\text{mq}]^T,$$

$$y = [y_1, y_2]^T = [h_1(x), h_2(x)]^T = [i_\text{md}, w_\text{m}]^T$$

where $x \in R^3$, $u \in R^2$ and $y \in R^2$ are state vector, input vector and output vector, respectively; $f(x)$, $g(x)$ and $h(x)$ are smooth vector fields. V_md and V_mq are the stator voltages in the d-q axis, i_md and i_mq are the stator currents in the d-q axis, R_s is the stator resistance, L_md and L_mq are d-q axis stator inductances, K_e is the permanent magnetic flux given by the magnet, p is the number of pole pairs, J_tot is the total inertia of the drive train that is equal to the summation of WT inertia constant and generator inertia constant, B is the friction coefficient of the motor, $w_\text{e}(= pw_\text{m})$ is the electrical generator rotation speed, and T_m, T_e and T_f are the WT mechanical torque, electromagnetic torque, and static friction torque, respectively.

The electromagnetic torque is expressed as:

$$T_\text{e} = p[(L_\text{md} - L_\text{mq})i_\text{md}i_\text{mq} + i_\text{mq}K_e] \tag{2.2.6}$$

2.2.3   Maximum Power Points Tracking (MPPT) Based Wind Speed Measurement

To capture the maximum wind power, the power coefficient C_p should maintain its maximum value $C_{p\text{max}}$ at any wind speed within the operating range. $C_{p\text{max}}$ is achieved by maintaining tip speed ratio λ equal to optimal value λ_opt and pitch angle β at a fixed value.

$$C_{p\text{max}} = C_p(\lambda_\text{opt}) \tag{2.2.7}$$

which in turn requires the mechanical rotation speed w_{m} to track its optimal reference w_{mr} as

$$w_{\mathrm{mopt}} = \frac{V}{R}\lambda_{\mathrm{opt}} \tag{2.2.8}$$

In this chapter, the C_p function given in [40] is used, in which the pitch angle is fixed at $\beta = 2°$, the optimal tip speed ratio is $\lambda_{\mathrm{opt}} = 7.3089$, and $C_{p\mathrm{max}} = 0.402$ [40].

2.3 Nonlinear Adaptive Control Based On Perturbation Estimation

The NAC based on a perturbation observer proposed in [62, 65] will be recalled briefly. A multi-input multi-output (MIMO) system is transformed as interacted subsystems via input/output linearisation at first. Then for each subsystem, a perturbation term is defined to include all subsystem nonlinearities, interactions between subsystems and uncertainties. A fictitious state is introduced to represent the perturbation and an extended-order high-gain observer is designed to estimate the perturbation and other system states, based upon the measurement only. The estimates of perturbations are used to compensate the real perturbations, then an adaptive linearisation and decoupled control of the original nonlinear system will be implemented. Comparing with the parameter estimation investigated in most adaptive control schemes, the technique used in the proposed control strategies can be considered as a function estimation method.

2.3.1 Input-Output Linearisation

Consider a MIMO system

$$\begin{cases} \dot{x} = f(x) + g(x)u \\ y = h(x) \end{cases} \tag{2.3.1}$$

where $x \in R^n$ is the state vector, $u \in R^m$ is the control input vector, $y \in R^m$ is the output vector, $f(x)$, $g(x)$ and $h(x)$ are smooth vector fields. The input-output

linearisation of a MIMO system is obtained via differentiating the output y_i of the system until the input u_j appears. Thus, assuming that r_i is the smallest integer such that at least one of the inputs explicitly appears in $y_i^{(r_i)}$

$$y_i^{(r_i)} = L_f^{r_i} h_i + \sum_{j=1}^{m} L_{g_j} L_f^{r_i-1} h_i u_j \tag{2.3.2}$$

where $y_i^{(r_i)}$ is the ith-order derivative of y_i, $L_{g_j} L_f^{r_i-1} h_i(x) \neq 0$ for at least one j. Performing the above procedure for each output y_i yields

$$\begin{bmatrix} y_1^{(r_1)} \\ \vdots \\ y_m^{(r_m)} \end{bmatrix} = \begin{bmatrix} L_f^{r_1} h_1 \\ \vdots \\ L_f^{r_m} h_m \end{bmatrix} + B(x) \begin{bmatrix} u_1 \\ \vdots \\ u_m \end{bmatrix} \tag{2.3.3}$$

$$B(x) = \begin{bmatrix} L_{g_1} L_f^{r_1-1} h_1 & \cdots & L_{g_m} L_f^{r_1-1} h_1 \\ \vdots & \vdots & \vdots \\ L_{g_1} L_f^{r_m-1} h_m & \cdots & L_{g_m} L_f^{r_m-1} h_m \end{bmatrix} \tag{2.3.4}$$

where $B(x)$ is a $m \times m$ control gain matrix. If $B(x)$ is invertible, the FLC of the the MIMO nonlinear system can be obtained as

$$u = B(x)^{-1} \left\{ \begin{bmatrix} -L_f^{r_1} h_1 \\ \vdots \\ -L_f^{r_m} h_m \end{bmatrix} + \begin{bmatrix} v_1 \\ \vdots \\ v_m \end{bmatrix} \right\} \tag{2.3.5}$$

where v_i are new inputs of the system. Now the input-output relations are given by

$$y_i^{(r_i)} = v_i \tag{2.3.6}$$

At this point, desired dynamics can be imposed on the system by the new system inputs.

2.3.2 Perturbation Observer

Assume all nonlinearities of system (2.3.3) are unknown, and define perturbation terms as

$$\begin{bmatrix} \Psi_1 \\ \vdots \\ \Psi_m \end{bmatrix} = \begin{bmatrix} L_f^{r_1} h_1 \\ \vdots \\ L_f^{r_m} h_m \end{bmatrix} + (B(x) - B_0) \begin{bmatrix} u_1 \\ \vdots \\ u_m \end{bmatrix} \tag{2.3.7}$$

where Ψ_i is the perturbation term, $B_0 = B(x)|_{x=x(0)}$ is the nominal control gain. Then system (2.3.3) can be rewritten as

$$
\begin{bmatrix} y_1^{(r_1)} \\ \vdots \\ y_m^{(r_m)} \end{bmatrix} = \begin{bmatrix} \Psi_1(x) \\ \vdots \\ \Psi_m(x) \end{bmatrix} + B_0 \begin{bmatrix} u_1 \\ \vdots \\ u_m \end{bmatrix} \tag{2.3.8}
$$

For the ith subsystem, defining state variables as $z_{i1} = y_i, \cdots, z_{ir_i} = y_i^{(r_i-1)}$ and a virtual state to represent the perturbation $z_{i(r_i+1)} = \Psi_i$, the i_{th} subsystem can be represented as

$$
\begin{cases} \dot{z}_{i1} & = & z_{i2} \\ & \vdots & \\ \dot{z}_{ir_i} & = & z_{i(r_i+1)} + B_{0_i}u \\ \dot{z}_{i(r_i+1)} & = & \dot{\Psi}_i \end{cases} \tag{2.3.9}
$$

where B_{0_i} is the ith row of the B_0, and $B_{0_{ij}}$ is the ith row j^{th} column element of the B_0.

For system (2.3.9), several types of perturbation observers, such as sliding mode observer, high gain observer and linear Luenberger observer, have been proposed [65]. This chapter picks up high gain observer as an example to show the design procedure, while other types observers can be designed similarly.

When all states are available, the perturbation is estimated by a second-order perturbation observer (PO) which use the last state z_{ir_i} as measurement as follows

$$
\begin{cases} \dot{\hat{z}}_{ir_i} & = & \hat{z}_{i1} + l_{i1}(z_{i1} - \hat{z}_{ir_i}) + B_{0_i}u \\ \dot{\hat{z}}_{i(r_i+1)} & = & l_{i2}(z_{ir_i} - \hat{z}_{ir_i}), \end{cases} \tag{2.3.10}
$$

where l_{i1} and l_{i2} are gains of the high gain observer. Throughout this chapter, $\hat{z}_{ir_i}$ represents the estimate of z_{ir_i}. By choosing

$$
l_{i1} = \frac{\alpha_{ij}}{\epsilon_i}, \quad l_{i2} = \frac{\alpha_{ij}}{\epsilon_i^2}, \tag{2.3.11}
$$

where $\epsilon_i, 0 < \epsilon_i < 1$ is a positive constant to be specified and the positive constants $\alpha_{ij}, j = 1, 2$, are chosen such that the roots of

$$
s^2 + \alpha_{i1}s + \alpha_{i2} = 0 \tag{2.3.12}
$$

are in the open left-half complex plan. Throughout this chapter, $\hat{z}_{ir_i}$ represents the estimate of z_{ir_i}.

When the system output $y_i = z_{i1}$ is available, a $(r_i+1)^{th}$-order states and perturbation observer (SPO) can be designed to estimate the system states and perturbation as

$$
\begin{cases}
\dot{\hat{z}}_{i1} & = & \hat{z}_{i2} + l_{i1}(z_{i1} - \hat{z}_{i1}) \\
& \cdots \\
\dot{\hat{z}}_{ir_i} & = & \hat{z}_{ir_i} + l_{ir_i}(z_{i1} - \hat{z}_{i1}) + B_{0_i}u \\
\dot{\hat{z}}_{i(r_i+1)} & = & l_{i(r_i+1)}(z_{i1} - \hat{z}_{i1}),
\end{cases}
\tag{2.3.13}
$$

where $\hat{z}_{ij}$ is the estimations of z_{ij}, $l_{ij} = \frac{\alpha_{ij}}{\epsilon_i^j}$, $j = 1, \cdots, r_i + 1$ are gains of the high gain observer, $\epsilon_i, 0 < \epsilon_i < 1$ is a small positive parameter to be specified to represent times of the time-dynamics between the observer and the real system. Parameters $\alpha_{ij}, j = 1, \cdots, r_i + 1$, are chosen such that the roots of

$$
s^{r_i+1} + \alpha_{i1}s^{r_i} + \cdots + \alpha_{ir_i}s + \alpha_{i(r_i+1)} = 0
\tag{2.3.14}
$$

are in the open left-half complex plan.

Using the estimate of perturbation $\hat{\Psi}_i = \hat{z}_{i(r_i+1)}$ to compensate the real system perturbation, the control law of the NAC can be obtained as

$$
u = B_0^{-1} \left\{
\begin{bmatrix} -\hat{\Psi}_1 \\ \vdots \\ -\hat{\Psi}_m \end{bmatrix}
+
\begin{bmatrix} v_1 \\ \vdots \\ v_m \end{bmatrix}
\right\}
\tag{2.3.15}
$$

where $v_i = -K_i\hat{z}_i$ is an output feedback when a SPO is designed. $K_i = [k_{i1}, \cdots, k_{i(r_i-1)}]^T$ are the linear feedback controller gains which can be determined via linear system method.

2.4 NAC Design

This section will present the design of NAC for the PMSG-WT.

Input/output linearisation of system (2.2.5) can be represented as

$$
\begin{bmatrix} y_1^{(1)} \\ y_2^{(2)} \end{bmatrix}
=
\begin{bmatrix} F_1(x) \\ F_2(x) \end{bmatrix}
+ B(x)
\begin{bmatrix} u_1 \\ u_2 \end{bmatrix}
\tag{2.4.1}
$$
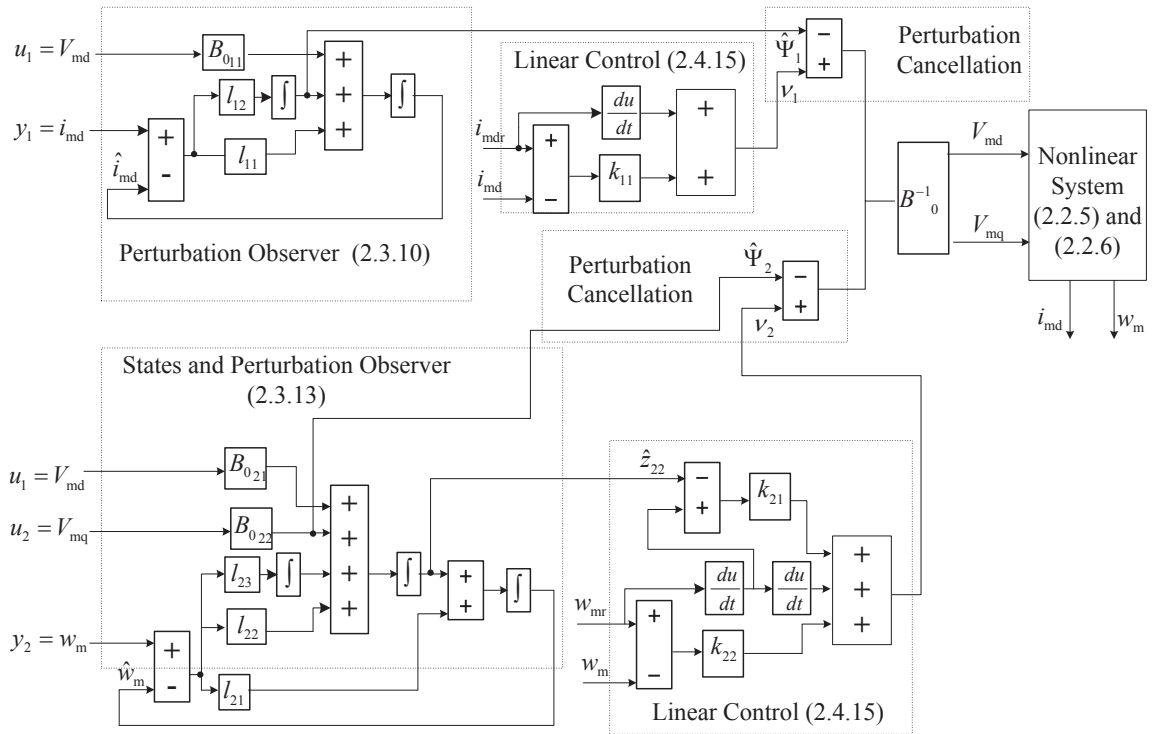
Figure 2.2: Block diagram of nonlinear adaptive controller

where

$$F_1(x) = \frac{1}{L_{\mathrm{md}}}(-i_{\mathrm{md}}R_{\mathrm{s}} + w_{\mathrm{e}}L_{\mathrm{mq}}i_{\mathrm{mq}}) \tag{2.4.2}$$

$$\begin{aligned} F_2(x) = \ & -\frac{p}{J_{\mathrm{tot}}L_{\mathrm{mq}}}[K_e + (L_{\mathrm{md}} - L_{\mathrm{mq}})i_{\mathrm{md}}]L_{\mathrm{md}}w_{\mathrm{e}}i_{\mathrm{md}} \\ & -\frac{p}{J_{\mathrm{tot}}L_{\mathrm{mq}}}[K_e + (L_{\mathrm{md}} - L_{\mathrm{mq}})i_{\mathrm{md}}](R_{\mathrm{s}}i_{\mathrm{mq}} + w_{\mathrm{e}}K_e) \\ & +\frac{pi_{\mathrm{mq}}}{J_{\mathrm{tot}}L_{\mathrm{md}}}(L_{\mathrm{md}} - L_{\mathrm{mq}})(-R_{\mathrm{s}}i_{\mathrm{md}} + L_{\mathrm{mq}}w_{\mathrm{e}}i_{\mathrm{mq}}) \\ & -\frac{1}{J_{\mathrm{tot}}}\frac{dT_{\mathrm{m}}}{dt} \end{aligned} \tag{2.4.3}$$

Note that $\frac{dT_{\mathrm{m}}}{dt}$ is not included in the FLC design, which cannot be measured directly.

$$B(x) = \begin{bmatrix} B_1(x) \\ B_2(x) \end{bmatrix} = \begin{bmatrix} \frac{1}{L_{\mathrm{md}}} & 0 \\ \frac{pi_{\mathrm{mq}}(L_{\mathrm{md}}-L_{\mathrm{mq}})}{J_{\mathrm{tot}}L_{\mathrm{md}}} & \frac{p[K_e+(L_{\mathrm{md}}-L_{\mathrm{mq}})i_{\mathrm{md}}]}{J_{\mathrm{tot}}L_{\mathrm{mq}}} \end{bmatrix} \tag{2.4.4}$$

As $det[B(x)] = \frac{p[K_e+(L_{\mathrm{md}}-L_{\mathrm{mq}})i_{\mathrm{md}}]}{J_{\mathrm{tot}}L_{\mathrm{md}}L_{\mathrm{mq}}} \neq 0$ when $K_e \neq 0$, that is, $B(x)$ is nonsingular for all nominal operation points. Thus, the FLC controller is obtained as

$$\begin{bmatrix} u_1 \\ u_2 \end{bmatrix} = B(x)^{-1}\left[\begin{bmatrix} -F_1(x) \\ -F_2(x) \end{bmatrix} + \begin{bmatrix} v_1 \\ v_2 \end{bmatrix}\right] \tag{2.4.5}$$

$$B(x)^{-1} = \begin{bmatrix} L_{\mathrm{md}} & 0 \\ -\frac{i_{\mathrm{mq}}L_{\mathrm{mq}}(L_{\mathrm{md}}-L_{\mathrm{mq}})}{K_e+(L_{\mathrm{md}}-L_{\mathrm{mq}})i_{\mathrm{md}}} & \frac{J_{\mathrm{tot}}L_{\mathrm{mq}}}{p[K_e+(L_{\mathrm{md}}-L_{\mathrm{mq}})i_{\mathrm{md}}]} \end{bmatrix} \tag{2.4.6}$$

And the original system is linearized as

$$\begin{bmatrix} y_1^{(1)} \\ y_2^{(2)} \end{bmatrix} = \begin{bmatrix} v_1 \\ v_2 \end{bmatrix} \tag{2.4.7}$$

$$v_1 = \dot{y}_{1\mathrm{r}} + k_{11}e_1 \tag{2.4.8}$$

$$v_2 = \ddot{y}_{2\mathrm{r}} + k_{21}\dot{e}_2 + k_{22}e_2 \tag{2.4.9}$$

where v_1 and v_2 are control of of linear systems, k_{11}, k_{21} and k_{22} are gains of linear controller, y_{1r} and y_{2r} the desired output references. Define $e_1 = y_{1r} - y_1$ and $e_2 = y_{2r} - y_2$ as track errors, the error dynamics are

$$\dot{e}_1 + k_{11}e_1 = 0 \tag{2.4.10}$$

$$\ddot{e}_2 + k_{21}\dot{e}_2 + k_{22}e_2 = 0 \tag{2.4.11}$$

Based on equation (2.3.7) and (2.4.1), perturbation terms $\Psi_1(x)$ and $\Psi_2(x)$ are obtained as:

$$q_1 : \begin{cases} \Psi_1(x) = F_1(x) + (B_1(x) - B_{0_1})\begin{bmatrix} u_1 \\ u_2 \end{bmatrix}, \\ B_{0_1} = \begin{bmatrix} \frac{1}{L_{d0}} & 0 \end{bmatrix} \end{cases}$$

$$\tag{2.4.12}$$

$$q_2 : \begin{cases} \Psi_2(x) = F_2(x) + (B_2(x) - B_{0_2})\begin{bmatrix} u_1 \\ u_2 \end{bmatrix} \\ B_{0_2} = \begin{bmatrix} \frac{pi_{mq}(L_{md0}-L_{mq0})}{J_{tot0}L_{d0}} & \frac{p[K_{e0}+(L_{md0}-L_{mq0})i_{md}]}{J_{tot0}L_{mq0}} \end{bmatrix} \end{cases}$$

where L_{md0}, L_{mq0}, J_{tot0}, K_{e0}, B_{0_1} and B_{0_2} are nominal values of L_{md}, L_{mq}, J_{tot}, K_e, $B_1(x)$ and $B_2(x)$, respectively .

Defining the state vectors as $z_{11} = y_1$, $z_{12} = \Psi_1$ and $z_{21} = y_2$, $z_{22} = y_2^{(1)}$, $z_{23} = \Psi_2$, and control variables as $u_1 = V_{md}$ and $u_2 = V_{mq}$. The dynamic equations of the two subsystems q_1 and q_2 become as

$$q_1 : \begin{cases} \dot{z}_{11} = \Psi_1(x) + B_{0_1}\begin{bmatrix} u_1 \\ u_2 \end{bmatrix}, \\ z_{11} = y_1 \end{cases}$$

$$\tag{2.4.13}$$

$$q_2 : \begin{cases} \dot{z}_{21} = z_{22} \\ \dot{z}_{22} = \Psi_2(x) + B_{0_2}\begin{bmatrix} u_1 \\ u_2 \end{bmatrix}, \\ z_{21} = y_2 \end{cases}$$

For sub-system q_1, a second-order PO like (2.3.10) is designed to estimate the perturbation $\hat{z}_{12} = \hat{\Psi}_1$; and for sub-system q_2, a third-order SPO like (2.3.13) is

designed to estimate the $\hat{z}_{22}$ and perturbation $\hat{z}_{23} = \hat{\Psi}_2$. By using the estimated perturbation to compensate the real perturbation, control laws for sub-systems q_1 and q_2 can be obtained as following:

$$\begin{bmatrix} u_1 \\ u_2 \end{bmatrix} = B_0^{-1} \left[\begin{bmatrix} -\hat{z}_{12} \\ -\hat{z}_{23} \end{bmatrix} + \begin{bmatrix} v_1 \\ v_2 \end{bmatrix} \right] \tag{2.4.14}$$

where $v_{1,2}$ is defined as

$$\begin{cases} v_1 &= k_{11}(z_{11\mathrm{r}} - \hat{z}_{11}) + \dot{z}_{11\mathrm{r}} \\ v_2 &= \ddot{z}_{21\mathrm{r}} + k_{22}(z_{21\mathrm{r}} - \hat{z}_{21}) \\ &\quad + k_{21}(\dot{z}_{21\mathrm{r}} - \hat{z}_{22}) \end{cases} \tag{2.4.15}$$

The final control law represented by physical variables, such as currents, inductance, total inertia, field flux and mechanical rotation speed, are given as following:

$$\begin{cases} u_1 = L_{\mathrm{md0}}[k_{11}(i_{\mathrm{mdr}} - i_{\mathrm{md}}) + \dot{i}_{\mathrm{mdr}} - \hat{\Psi}_1] \\ u_2 = -\frac{i_{\mathrm{mq}}L_{\mathrm{mq0}}(L_{\mathrm{md0}} - L_{\mathrm{mq0}})}{K_{e0} + (L_{\mathrm{md0}} - L_{\mathrm{mq0}})i_{\mathrm{md}}}[k_{11}(i_{\mathrm{mdr}} - i_{\mathrm{md}}) + \dot{i}_{\mathrm{mdr}} - \hat{\Psi}_1] \\ \quad + \frac{J_{\mathrm{tot0}}L_{\mathrm{mq0}}}{p[K_{e0} + (L_{\mathrm{md0}} - L_{\mathrm{mq0}})i_{\mathrm{md}}]}[k_{22}(w_{\mathrm{mr}} - w_{\mathrm{m}}) \\ \quad + k_{21}(\dot{w}_{\mathrm{mr}} - \hat{z}_{22}) + \ddot{w}_{\mathrm{mr}} - \hat{\Psi}_2] \end{cases} \tag{2.4.16}$$

Note that the NAC proposed only requires the nominal value of parameters of L_{md0}, L_{mq0}, K_{e0} and J_{tot0}, and measurements of two output variables i_{md} and w_{m}.

To clearly illustrate its principle, block diagram of the NAC proposed is shown in Fig. 2.2.

2.5   Simulation Results

In this thesis, Chapters 2-5 investigate the same test system shown in Fig. 1.2. They focus on different parts of the WECS. This WECS contains PMSG, WT, a full-rated back-to-back power electronic converter consists of two VSCs, i.e., MSC and GSC, DC-link, and power grid. In the WECS, the wind energy captured by the WT is converted into mechanical energy. Then the mechanical energy is transmitted to the direct-drive PMSG. The PMSG converts the mechanical power to electrical

power, then supplies it to the power grid through a MSC and a GSC. The MSC is responsible to extract the electric power from the wind by controlling the mechanical rotation speed and maintaining the required stator voltage, whereas the GSC has to enable independent control of the active and reactive power as the grid codes requires and transfer the active power from the generator to the grid via the DC-link. A DC voltage link decouples the operation control of the two converters [35].

Chapters 2 and 3 focus on WT, PMSG and MSC of the WECS shown in Fig. 1.3 of the modified manuscript. The GSC, DC-Link and power grid have been investigated in Chapter 4. In Chapter 5, the whole WECS has been investigated.

To verify the effectiveness of the proposed NAC, simulations studies are carried out and compared with the VC and FLC. The parameters of a 2-MW PMSG-WT system give in [40] is used: R=39 m, ρ=1.205 $\mathrm{kg/m^3}$, rated wind speed V_r=12 m/s, J_{tot}=10000 $\mathrm{kg \cdot m^2}$, K_e=136.25 V.s/rad, p=11, L_{md}=5.5 mH, L_{mq}=3.75 mH, and R_s=50 $\mu\Omega$.

Parameters of NACs for subsystem q_1 and q_2 are designed based on pole-placement and listed as following:

q_1 : observer: $\alpha_{11} = 3.2 \times 10^2$, $\alpha_{12} = 2.56 \times 10^4$, $\epsilon_1 = 2 \times 10^{-2}$, which locate all poles at -1.6×10^2; controller: $k_{11} = 1.6 \times 10^1$, which is obtained by placing pole at -1.6×10^1.

q_2 : observer: $\alpha_{21} = 1.5 \times 10^3$, $\alpha_{22} = 7.5 \times 10^5$, $\alpha_{23} = 1.25 \times 10^8$, $\epsilon_2 = 1 \times 10^{-3}$, which locate all poles at -5×10^2; controller: $k_{21} = 1 \times 10^2$, $k_{22} = 2.5 \times 10^3$, which are obtained by placing pole at -5×10^1.

Note that FLC uses same controller parameters as the NAC, moreover the FLC uses the full state feedback and exact parameter. In the NAC design, the value of the observer's pole is usually chosen approximately 5 to 10 times of the value of the controller's pole.

2.5.1 Time-Varying Wind

Ramp-Change Wind

The response of the PMSG to ramp-change wind is shown in Fig. 2.3-2.5. Wind speed is shown in Fig. 2.3 (a). As shown in Fig. 2.3 (b)-(c), the proposed NAC provides the best tracking performance of the mechanical rotation speed w_{m} compared with the VC and FLC when wind speed varies. The maximum relative error $(\frac{w_{\mathrm{m}}-w_{\mathrm{mr}}}{w_{\mathrm{mr}}} \times 100\%)$ is approximately 12% by the VC. It can be explained that the VC is adjusted for a specific operation point of the system and cannot ensure a satisfying dynamic behavior for varying operation points. Although the FLC can provide a satisfactory tracking performance, the tracking error of w_{m} still exists. It is because that the FLC requires the full-state measurements, but the $\frac{dT_{\mathrm{m}}}{dt}$ in (6.3.3) is not known in the FLC design.

To extract maximum wind power, the power coefficient C_p should maintain at its maximum value. As shown in Fig. 2.3 (d), the maximum power coefficient $C_{p\mathrm{max}}$ can be always achieved by the NAC even though wind varies. It means the maximum wind power can be extracted by the NAC during varying wind speed, but the power coefficient C_p cannot always be maintained at its maximum value by the VC. It needs more time to reach $C_{p\mathrm{max}}$ when wind speed varies. Fig. 2.4 (e) shows the relative tracking error $(\frac{C_p-C_{p\mathrm{max}}}{C_{p\mathrm{max}}} \times 100\%)$. Under the VC strategy, the maximum relative error reaches approximately 1.7% under varying wind speed. The FLC almost keeps the C_p at its maximum value $C_{p\mathrm{max}}$.

As shown in Fig. 2.4 (f), i_{md} can be well tracked by the VC, FLC and NAC. Fig. 2.4 (h) shows that bigger overshoot and longer recovery time of voltage V_{mq} are obtained by the VC comparing with the FLC or NAC. The response of active power and reactive power generated from the PMSG-WT are shown in Fig. 2.5 (i)-(j), respectively. Response of perturbation estimation is shown in Fig. 2.6. The perturbation can be well estimated to compensate the real perturbation.

Note that the FLC uses the full state feedback except $\frac{dT_{\mathrm{m}}}{dt}$ and extract parameters of the system, but the NAC is without requiring the details of the system information and extract parameters.
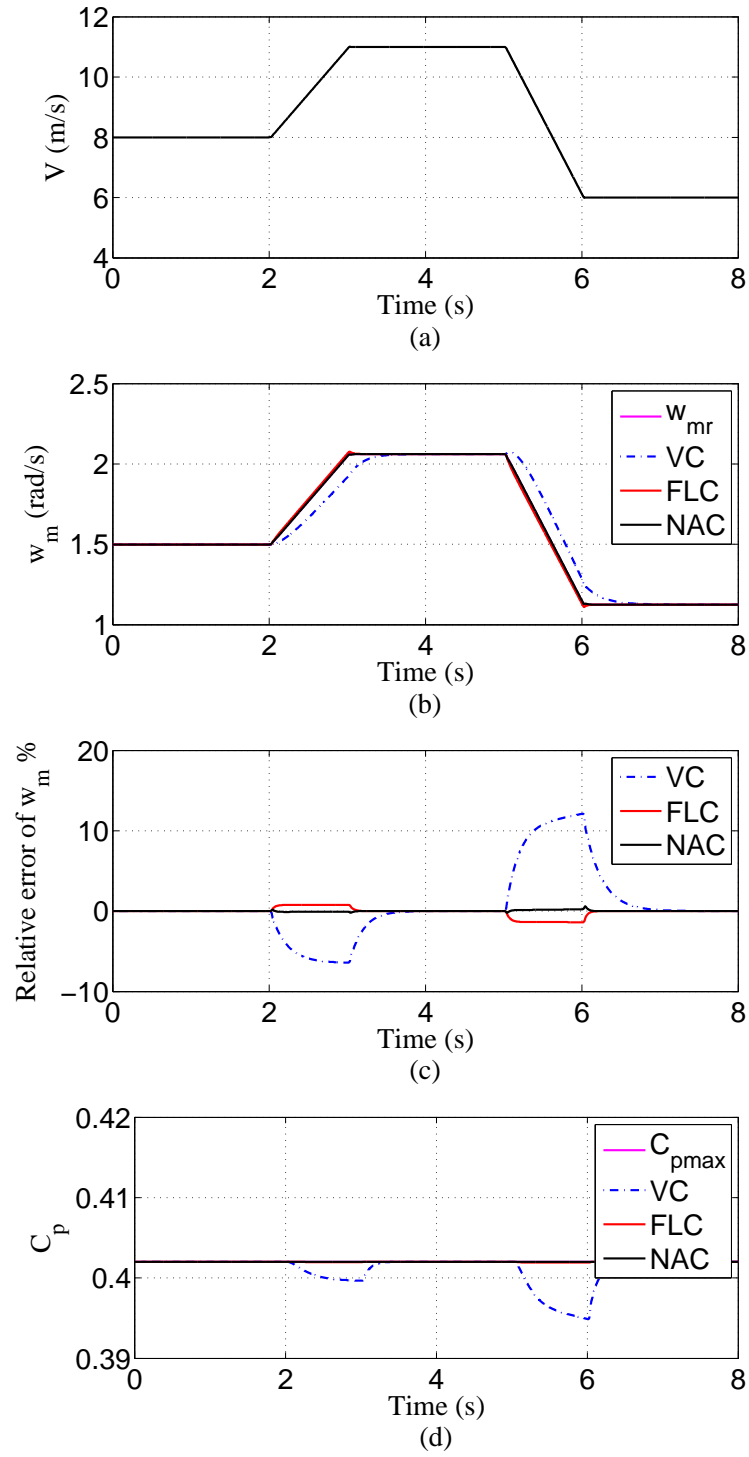
Figure 2.3: Responses of the PMSG to ramp-change wind. (a) Wind speed V. (b) Mechanical rotation speed w_{m}. (c) Relative error of mechanical rotation speed w_{m}. (d) Power coefficient C_p.
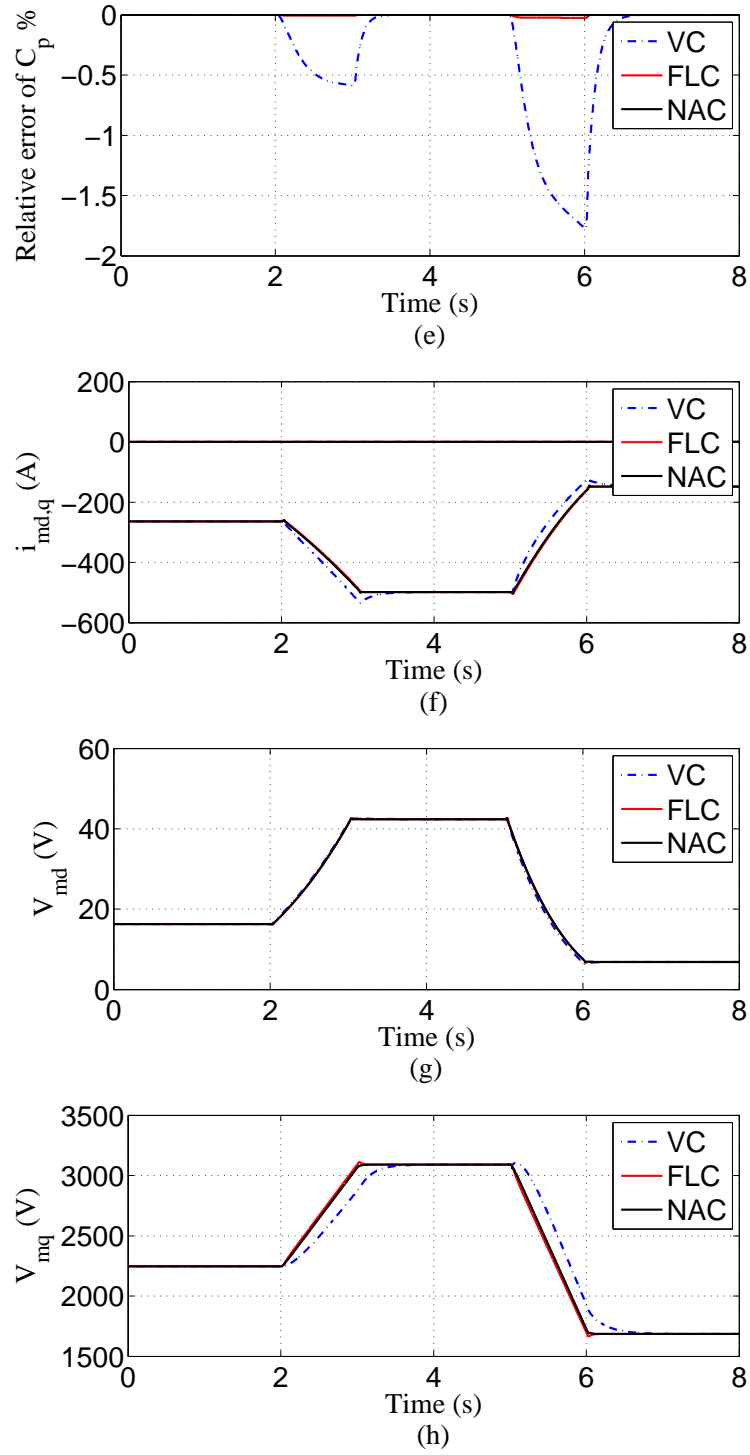
Figure 2.4: Responses of the PMSG to ramp-change wind. (e) Relative error of power coefficient C_p. (f) Stator current $i_{\mathrm{md,q}}$. (g) d-axis stator voltage V_{md}. (h) q-axis stator voltage V_{mq}.
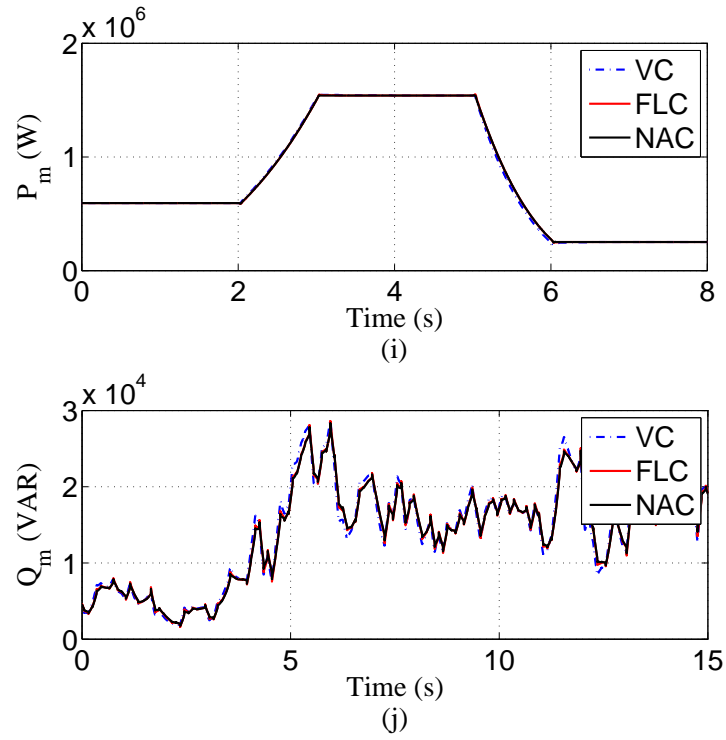
Figure 2.5: Responses of the PMSG to ramp-change wind. (i) Active generating power P_m. (j) Reactive generating power Q_m.
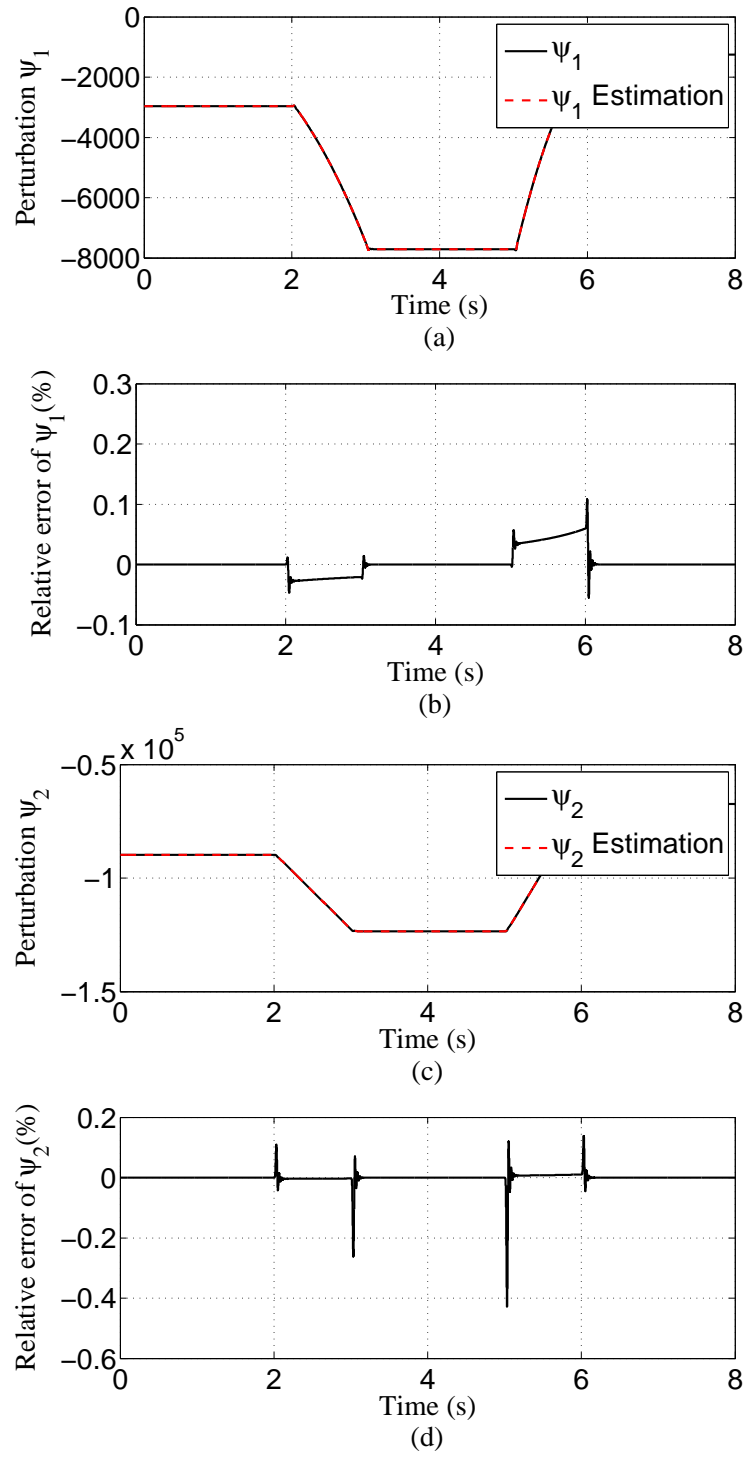
Figure 2.6: Estimate of perturbation $\psi_{1,2}(x)$
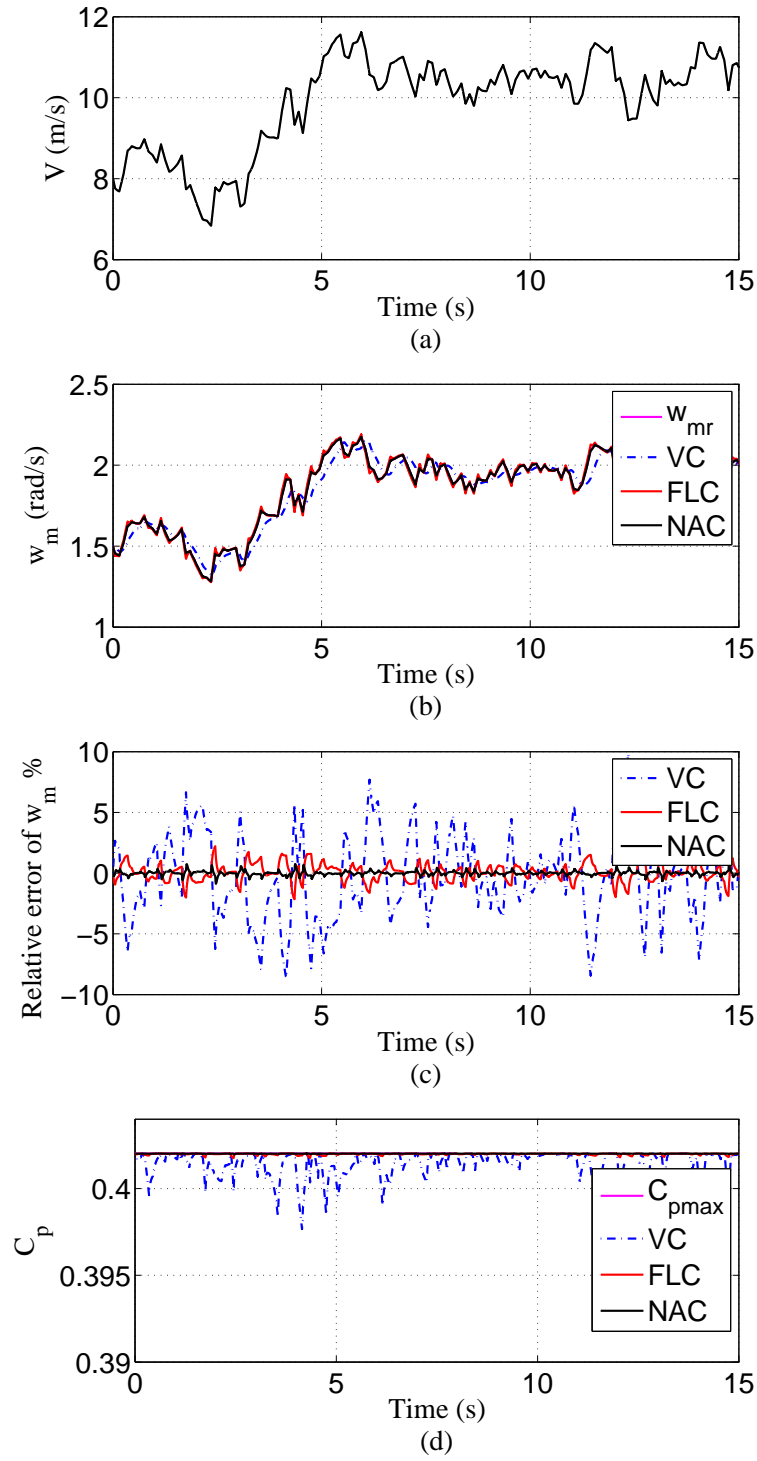
Figure 2.7: Responses of the PMSG to random wind. (a) Wind speed V. (b) Mechanical rotation speed w_m. (c) Relative error of mechanical rotation speed w_m. (d) Power coefficient C_p.
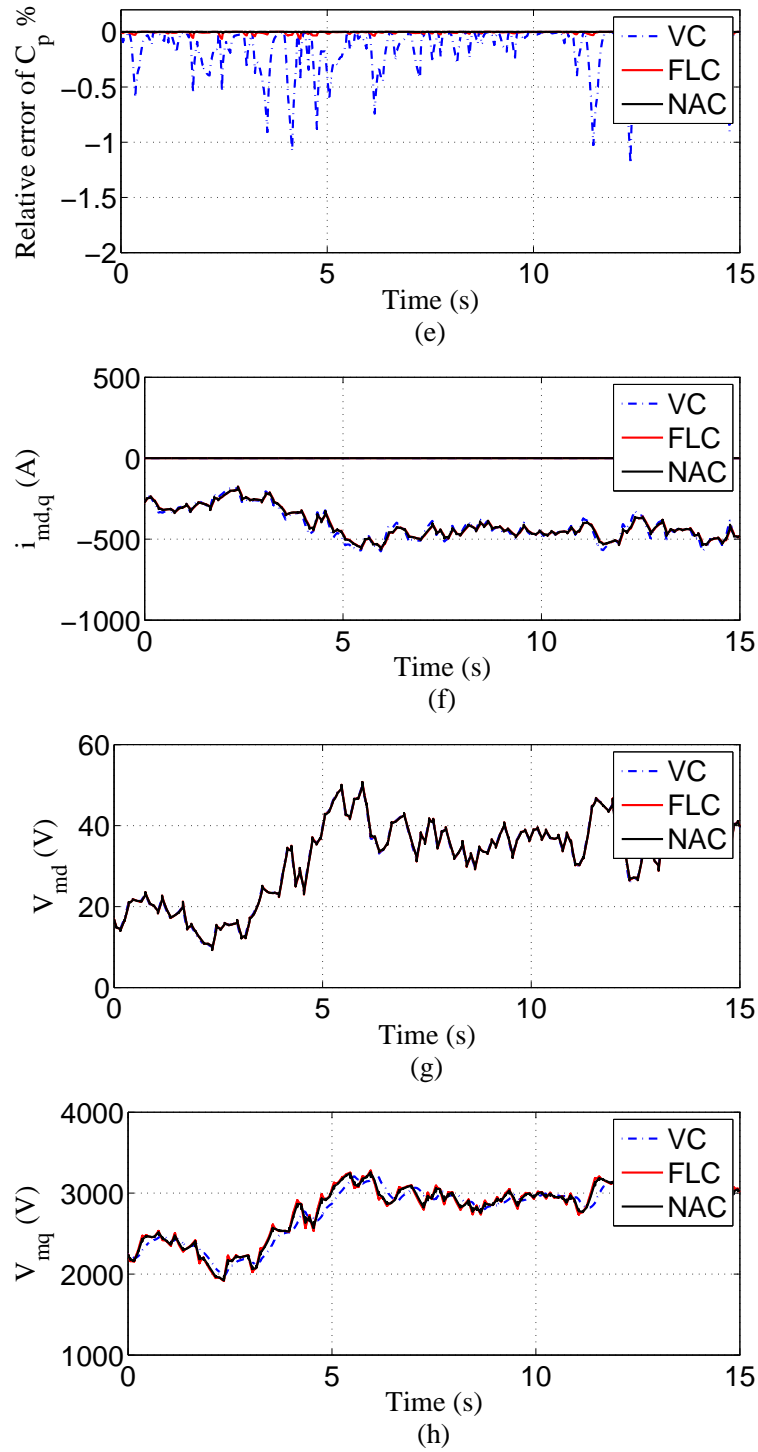
Figure 2.8: Responses of the PMSG to random wind. (e) Relative error of power coefficient C_p. (f) Stator current $i_{\mathrm{md,q}}$. (g) d-axis stator voltage V_{md}. (h) q-axis stator voltage V_{mq}.
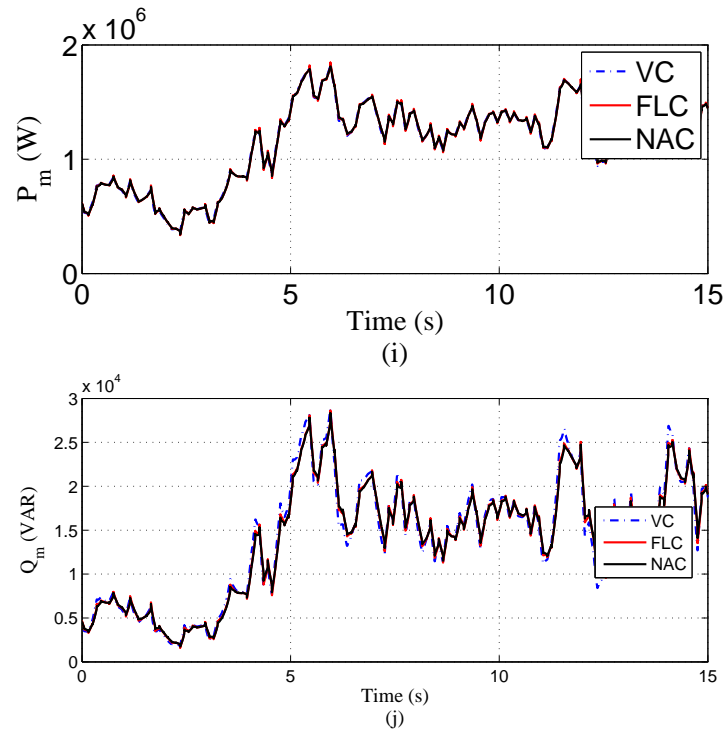
Figure 2.9: Responses of the PMSG to random wind. (i) Active generating power P_{m}. (j) Reactive generating power Q_{m}.

Random Wind

The dynamic responses of the PMSG to random wind is shown in Fig. 2.7-2.9. Random wind speed is shown in Fig. 2.7 (a). From Fig. 2.7 (b) and (c), it can be seen that when wind speed is time-varying, the VC cannot track optimal mechanical rotation speed reference w_{mr}. The maximum relative error ($\frac{w_{\mathrm{m}}-w_{\mathrm{mr}}}{w_{\mathrm{mr}}} \times 100\%$) is approximately 10% by the VC. The FLC can achieve much better tracking performance than the VC, but maximum relative error ($\frac{w_{\mathrm{m}}-w_{\mathrm{mr}}}{w_{\mathrm{mr}}} \times 100\%$) reaches about 2%. Comparing with the VC and FLC, the NAC can always provide a satisfactory tracking performance of the mechanical rotation speed w_{m} even under time-varying wind speed.

When wind speed is below the rated wind speed, the maximum wind power is achieved by maintaining C_p at its maximum value $C_{p\mathrm{max}}$. The maximum power coefficient cannot be obtained by the VC due to time-varying operation points shown in Fig. 2.7 (d) and 2.8 (e). The FLC keeps C_p very close to its maximum value $C_{p\mathrm{max}}$, but $C_{p\mathrm{max}}$ cannot be achieved. The NAC can always maintain the power coefficient C_p at its maximum value. The maximum relative error ($\frac{C_p-C_{p\mathrm{max}}}{C_{p\mathrm{max}}} \times 100\%$) is approximately 1.2% by the VC. As shown in Fig. 2.8 (f), i_{md} can be kept around zero by the VC, FLC and NAC. The dynamic responses of control inputs $V_{\mathrm{md,q}}$, the active power and reactive power are shown in Fig. 2.8 (g)-2.9 (j), respectively.

2.5.2 Robustness Against Parameter Uncertainties

In the real system, the generator parameters vary due to the operating temperature variation and saturation effect of the generator. The FLC shows a satisfactory dynamic performance as exact knowledge of system parameters are known, which cannot guarantee the robustness in the presence of parameter uncertainties or disturbances. The NAC can robust against the parameters uncertainties and external disturbances. In order to examine the robustness of the NAC and FLC, the parameter uncertainties tests have been done. In all simulation tests, wind speed V keeps at 8 m/s.

The system responses to variation of field flux K_e is shown in Fig. 2.10-2.12.

The variation of field flux K_e is shown in Fig. 2.10 (a). It can be seen from Fig. 2.10 (b) and (c) that, the mechanical rotation speed w_m cannot track its optimal reference w_mr under the FLC. The maximum relative error ($\frac{w_\mathrm{m}-w_\mathrm{mr}}{w_\mathrm{mr}} \times 100\%$) reaches approximately 70%. The maximum power coefficient is achieved by controlling w_m to track its optimal reference w_mr. When the optimal reference w_mr cannot be tracked, the power coefficient C_p cannot be maintained around maximum value $C_{p\mathrm{max}}$. As shown in Fig. 2.10 (d) and 2.11 (e), the maximum relative error ($\frac{C_p-C_{p\mathrm{max}}}{C_{p\mathrm{max}}} \times 100\%$) is approximately 40% under the FLC. The maximum wind power cannot be captured when the maximum power coefficient $C_{p\mathrm{max}}$ is not obtained. The extracted wind power has a approximately 40% decrement of maximum extracted wind power under the FLC shown in Fig. 2.11 (h). The maximum relative error of Q_m is near 80%.

It can be seen from Fig. 2.10-2.12 that, when the field flux K_e varies, the system performance under the FLC degrades greatly due to lack of extract parameters. The NAC almost always have a satisfactory performance and with a consistent response, expect that the reactive power Q_m is affected by the variation of field flux K_e.

2.5.3 Robustness Against Measurement Noises

The proposed NAC is an output feedback controller and only requires four measurements, the wind speed V, the d-q-axis stator current $i_{\mathrm{md,q}}$ and mechanical rotation speed w_m. However, the FLC needs full-state measurements. To test the robustness against the measurement noise, the mechanical rotation speed w_m has been injected white noise. The range of white noise added in the measurement w_m is $\pm 1\%$ of real w_m value. The wind speed keeps at 8 m/s as shown in Fig. 2.13 (a). It can be seen from Fig. 2.13 (b) that, the mechanical rotation speed w_m cannot track its optimal reference w_opt under the FLC, but it is well tracked under the NAC. The maximum relative error ($\frac{w_\mathrm{m}-w_\mathrm{mr}}{w_\mathrm{mr}} \times 100\%$) reaches approximately 10% under the FLC. Hence, the maximum power coefficient C_p cannot keep at its maximum value $C_{p\mathrm{max}}$ when the optimal mechanical rotation speed cannot be tracked shown in Fig. 2.13 (c). Fig. 2.13 (d) shows the response of the d-axis stator current i_d.

It can be seen from Fig. 2.13 that, the NAC is almost immune to the white noise
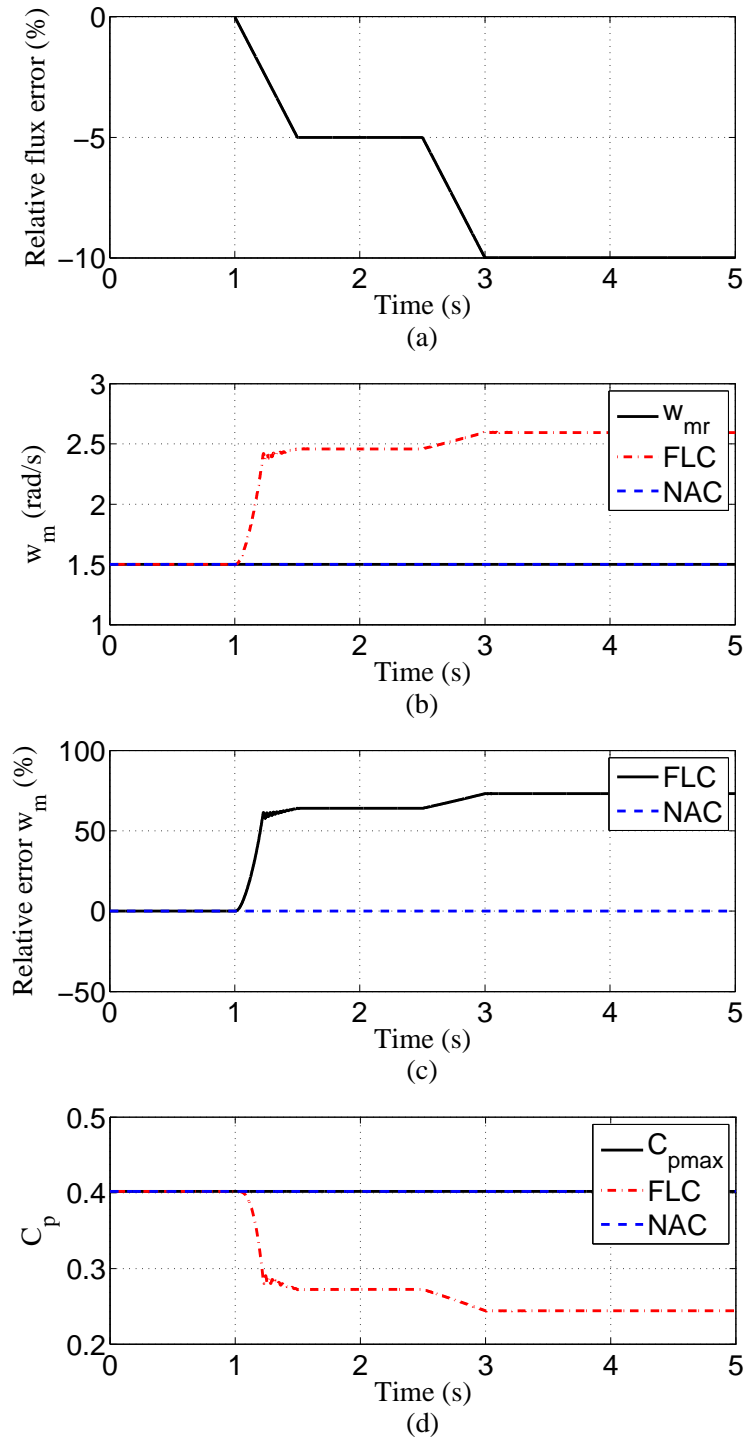
Figure 2.10: Responses of the PMSG to constant wind and field flux K_e variation. (a) Wind speed V. (b) Mechanical rotation speed w_m. (c) Relative error of mechanical rotation speed w_m. (d) Power coefficient C_p.
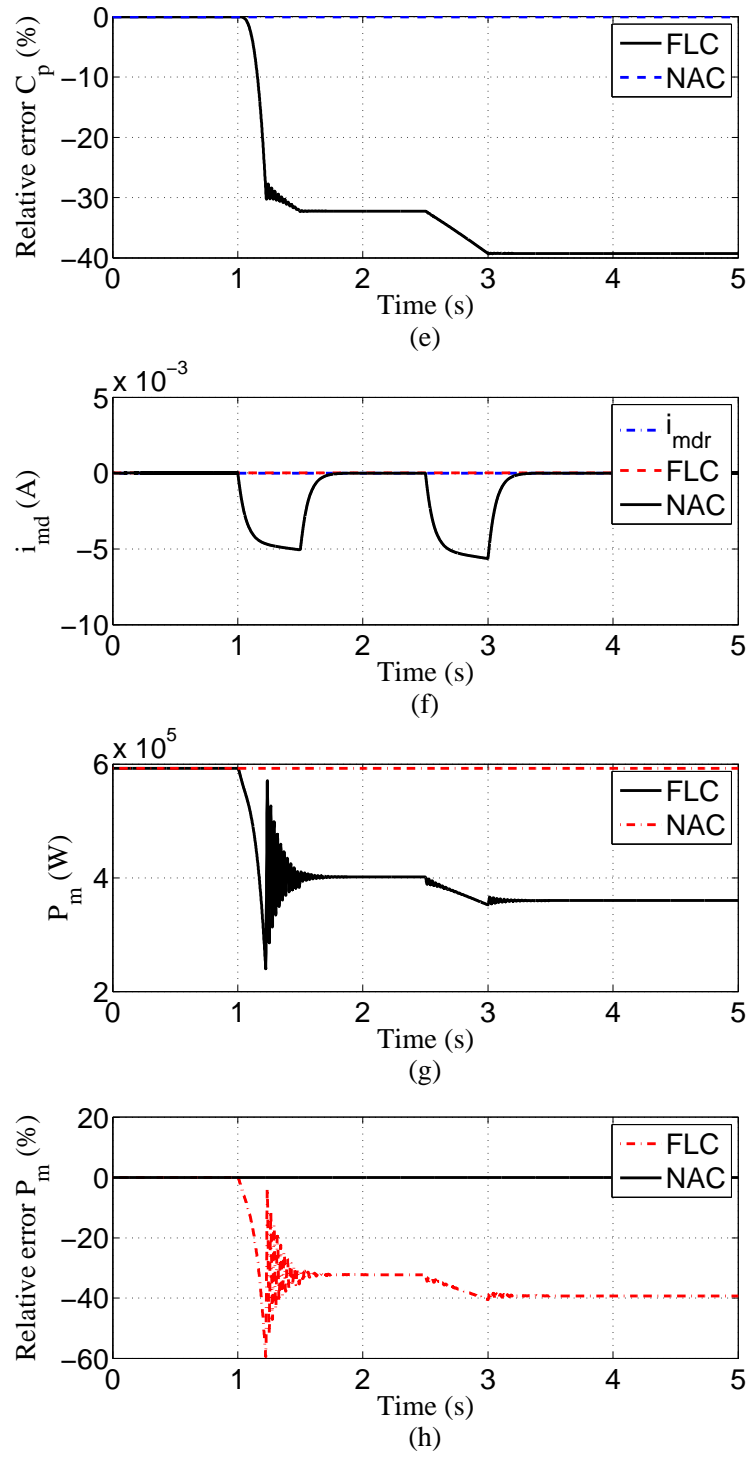
Figure 2.11: Responses of the PMSG to constant wind and field flux K_e variation. (e) Relative error of power coefficient C_p. (f) d-axis stator current i_{md}. (g) Active power P_m. (g) Relative error of active power P_m.
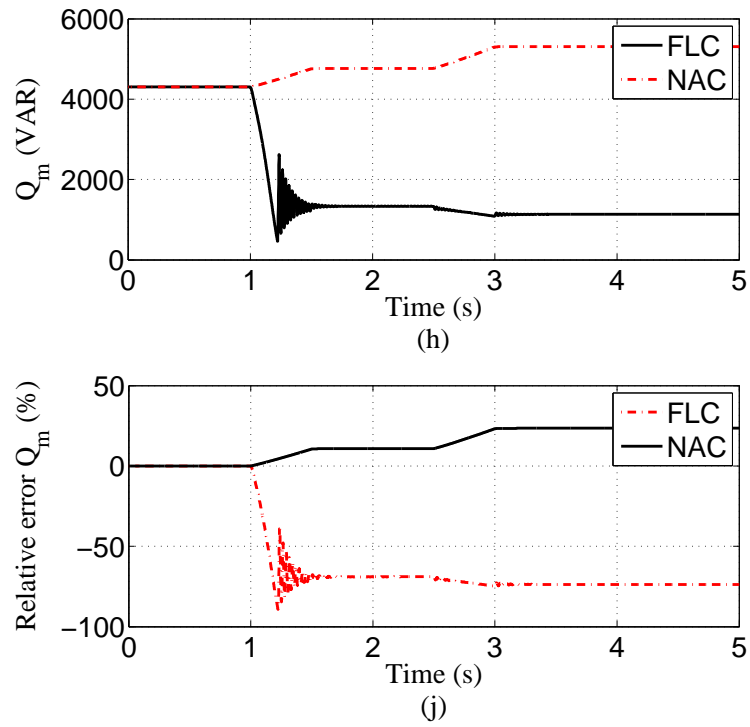
Figure 2.12: Responses of the PMSG to constant wind and field flux K_e variation. (i) Reactive power Q_{m}. (j) Relative error of reactive power Q_{m}.

in w_{m} measurement, but the injected white noise impacts the FLC performance. Note that in practice, low-pass filter (LPF) can be applied for removing all these measurement noises, without impacting on the overall dynamic performance.

2.5.4 Tower Shadow

Tower shadow is one inherent characteristic of wind turbines and produces periodic fluctuations in electrical power output of a wind turbine generator [80]. Tower shadow describes the redirection of wind due to the tower structure and produces a periodic pulse reduction in torque as each blade passes by the tower [80–82]. For a three bladed turbine, three pulsations in torque occur in one rotation known as 3p effect. This inherent characteristic of wind turbines has been considered in the following simulation case study. In this simulation test, wind speed keeps at 8 m/s measured from anemometer. This measured wind speed is use to obtain optimal mechanical rotation speed w_{mr} (2.2.8). To emulate the tower shadow, an equivalent wind speed is given in 2.14 (a), wind speed is reduced by 3% every time a blade passes in front of the tower and the duration of time a blade passes the tower is represented by an arc of $40°$ in one cycle for a three bladed turbine [80]. It can be seen from 2.14 (b) and (c) that, the mechanical rotation speed w_{m} cannot be well tracked under the FLC and with a maximum relative error ($\frac{w_{\mathrm{m}}-w_{\mathrm{mr}}}{w_{\mathrm{mr}}} \times 100\%$) reaching approximately 0.5%. This is because that the torque variation due to tower shadow is not included in the FLC, which cannot provide high robustness against external disturbance such as tower shadow. The NAC provides a satisfactory tracking performance of w_{m} and consistent response. The mechanical torque T_{m} shows in 2.14 (d).

2.6 Experimental Results

The experiment tests have been done to verify the effectiveness of the proposed NAC. In hardware implementation, the generator to be controlled is a 5 pole pairs, 250W PMSG with rated 42V input and 5.7A RMS current. It is coupled with a DC motor which is used to emulate WT (2.2.3,2.2.4). Both the PMSG and DC gen-
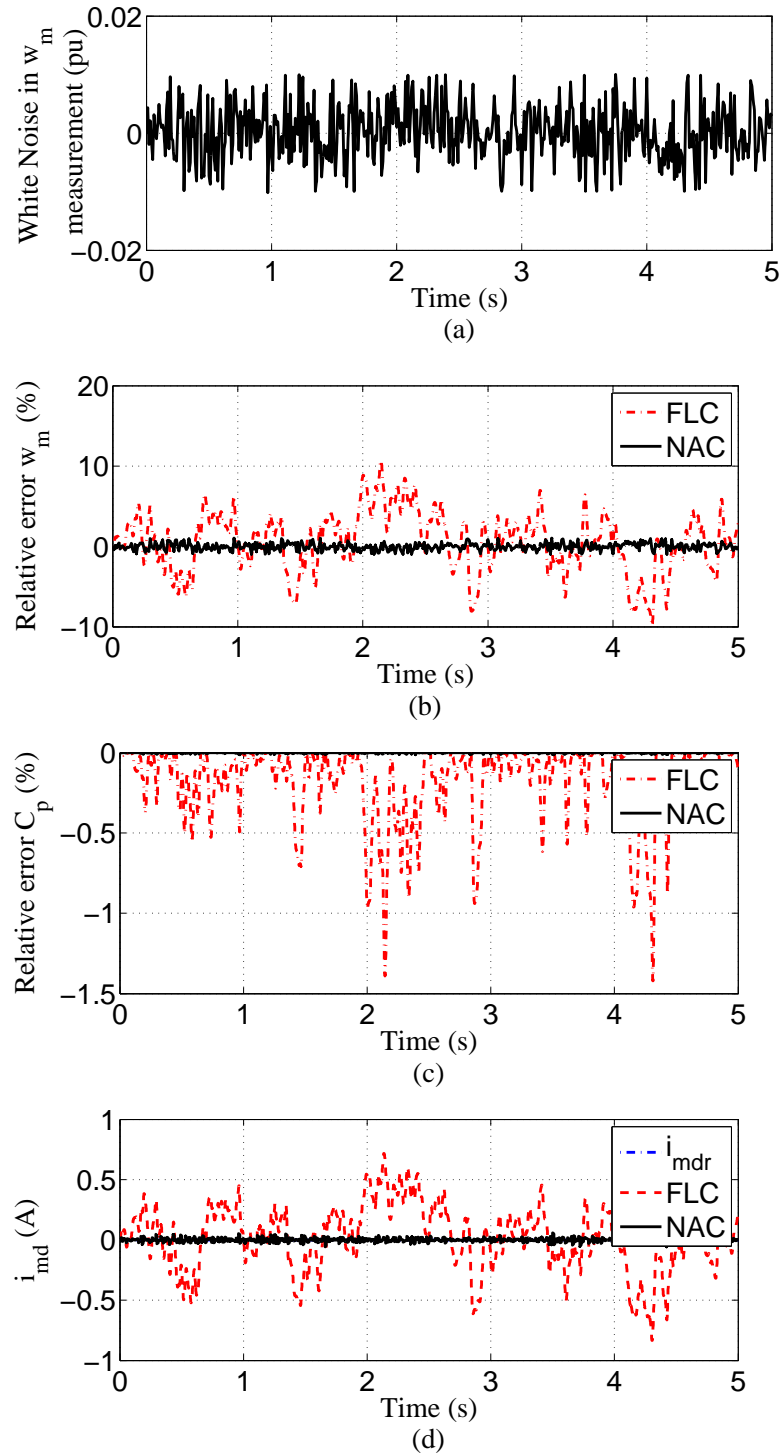
Figure 2.13: Responses of the PMSG to white noise in w_m measurement.
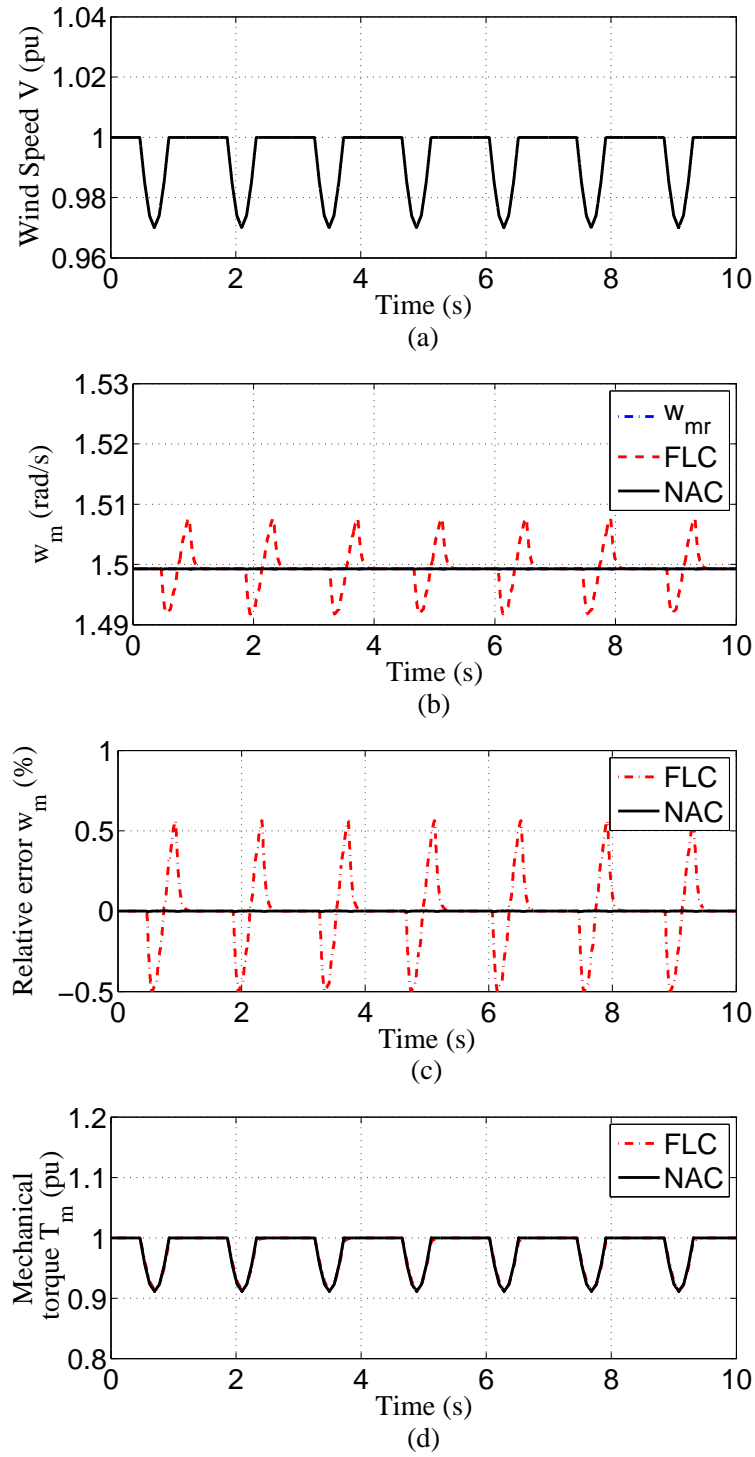
Figure 2.14: Response to constant wind speed considering tower shadow effect. (a) Equivalent wind speed V under tower shadow effect. (b) Mechanical rotation speed w_m. (c) Relative error of mechanical rotation speed w_m. (d) Tower effect on mechanical torque T_m.
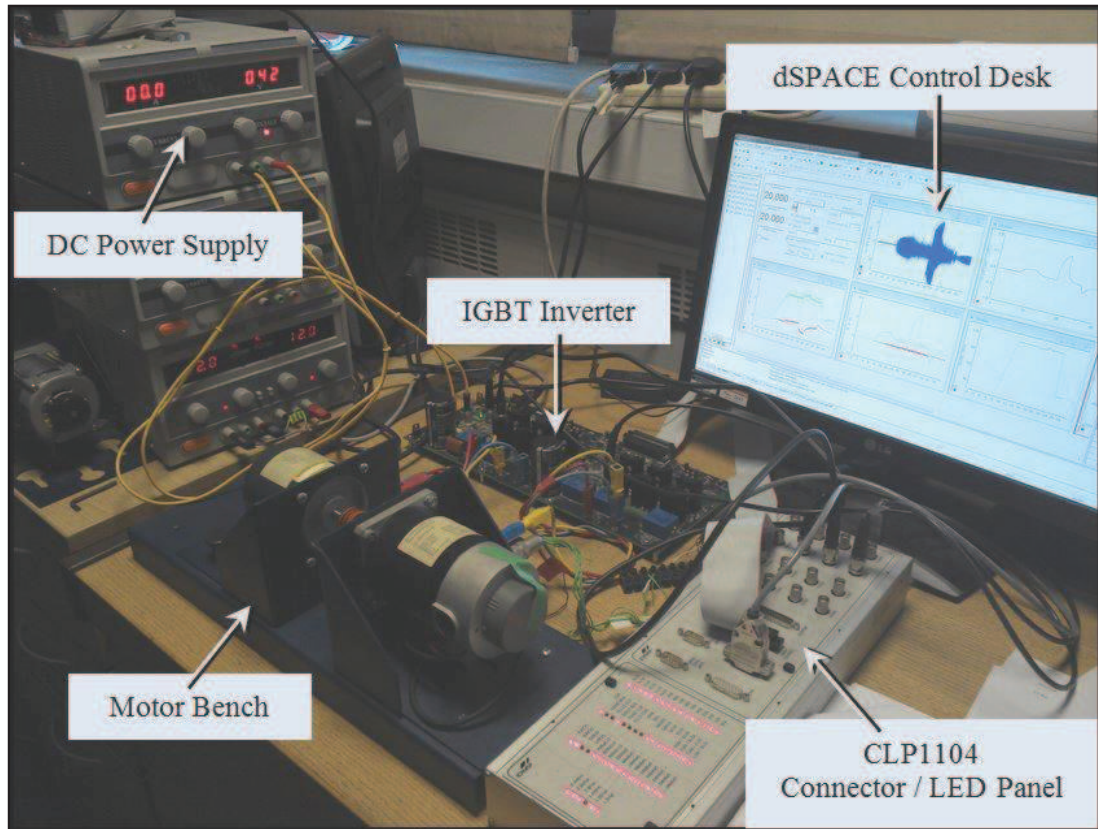
Figure 2.15: Experimental setup

erator are driving by an IGBT-based inverter, which is controlled by PWM signal produced by DS1104 dSPACE processor board. The dSPACE software can compile the Simulink control loop to C-code by using MATLAB/Simulink real-time workshop (RTW) and then downloads them to DS1104 dSPACE processor board. The dSPACE processor board is also used to receive the mechanical speed and position measured by an incremental optical 1000-line encoder, which is synchronized with the motor shaft. In addition, the measured result of motor state can be displayed on the dSPACE control desk, and both the reference control targets and controller parameters can be adjusted in real time. The experimental setup is shown in Fig. 2.15.

In the experiment tests, the parameters of the PMSG-WT system are R=0.671 m,

ρ=1.205 kg/m^3, rated wind speed V=9 m/s, J_{tot}=1.23×10^{-3}kg·m^2, K_e=0.0151V.s/rad, p=5, L_{md}=0.49 mH, L_{mq}=0.49 mH, and R_{s}=0.19 Ω, static friction torque $T_{\mathrm{f}} = 0.121$ N.m, and the C_p function is the same as (2.2.3) and (2.2.4).

Parameters of NACs for subsystem q_1 and q_2 are designed based on pole-placement and listed as following:

q_1 : observer: $\alpha_{11} = 2 \times 10^2$, $\alpha_{12} = 1 \times 10^4$, $\epsilon_1 = 5 \times 10^{-2}$, which locate all poles at -1×10^2; controller: $k_{11} = 1 \times 10^1$, which is obtained by placing pole at -1×10^1.

q_2 : observer: $\alpha_{21} = 3 \times 10^2$, $\alpha_{22} = 3 \times 10^4$, $\alpha_{23} = 1 \times 10^6$, $\epsilon_2 = 5 \times 10^{-2}$, which locate all poles at -1×10^2; controller: $k_{21} = 3.2 \times 10^1$, $k_{22} = 2.56 \times 10^2$, which are obtained by placing pole at -1.6×10^1.

Note that the FLC has not been applied in comparison with the VC and NAC. For real motors, some parameters may not same as listed on motor nameplate. However, the FLC requires the accurate system parameters to provide satisfactory performances. The inaccurate parameters may cause deterioration of performance or failure.

2.6.1 Ramp-Change Wind

Figs. 2.16-2.18 show the responses of the PMSG-WT to ramp-change wind. It can be seen from Fig. 2.16 (b) and (c), the VC cannot provide a satisfactory tracking performance of the mechanical rotation speed w_{m} as wind speed varies. The maximum tracking error of the w_{m}reaches approximately 25%. Hence, the power coefficient C_p cannot always maintain at maximum value shown in Fig. 2.16 (d). Fig. 2.17 shows the d-axis, q-axis stator voltages (V_{md}, V_{mq}), d-axis, and q-axis stator currents (i_{md}, i_{mq}). The LPF can be used to remove the noises in stator voltage and current. The mechanical power P_{w},active generating power P_{m}, and mechanical torque T_{m}) responses are shown in Fig. 2.18 (a) and (b), respectively. The P_{e} is much less than the P_{m} due to consumption power of static friction and resistance. The states and perturbations can be well estimated shown in Fig. 2.19 and 2.20.
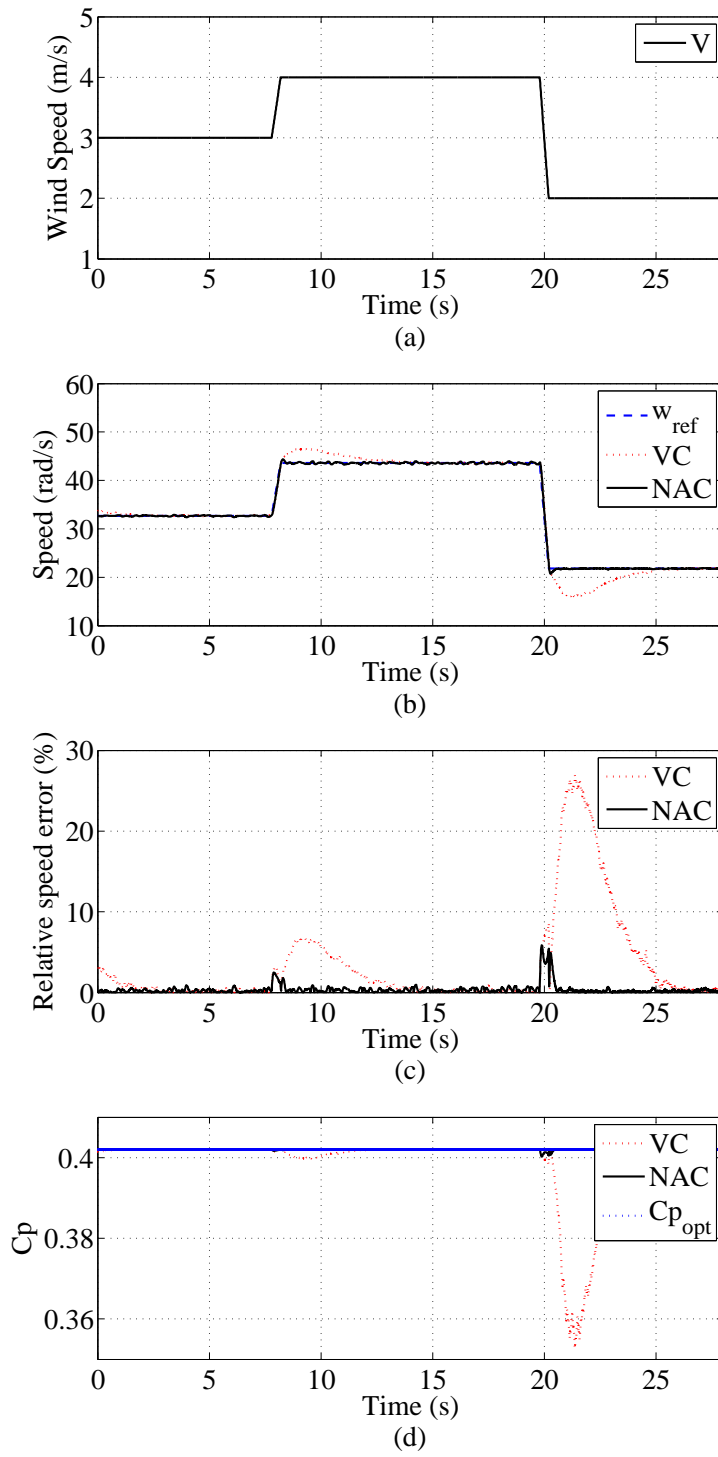
Figure 2.16: Responses of the WT to ramp-change wind. (a) Wind speed V. (b) Mechanical rotation speed w_{m}. (c) Relative error of mechanical rotation speed w_{m}. (d) Power coefficient C_p.
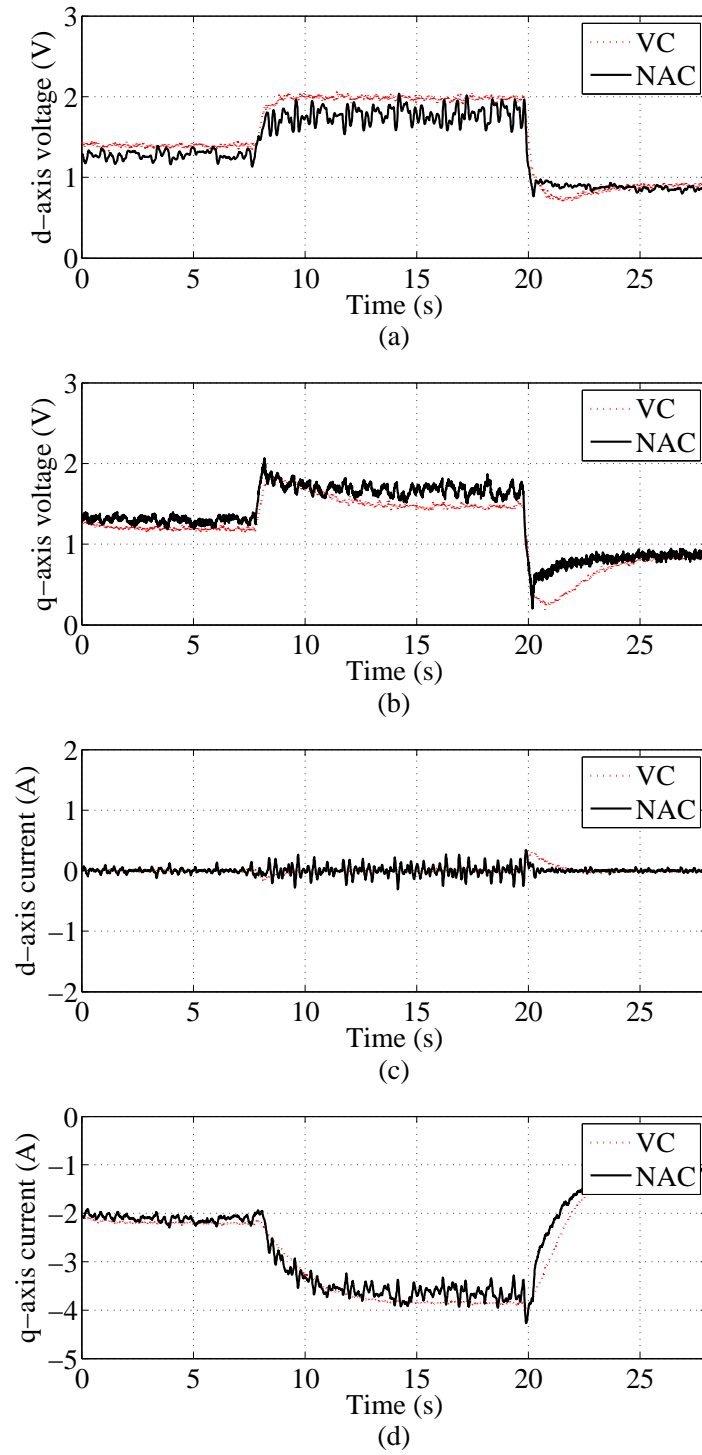
Figure 2.17: Responses of the PMSG to ramp-change wind. (a) d-axis stator voltage V_{md}. (b) q-axis stator voltage V_{mq}. (c) Stator current i_{md}. (d) Stator current i_{mq}.
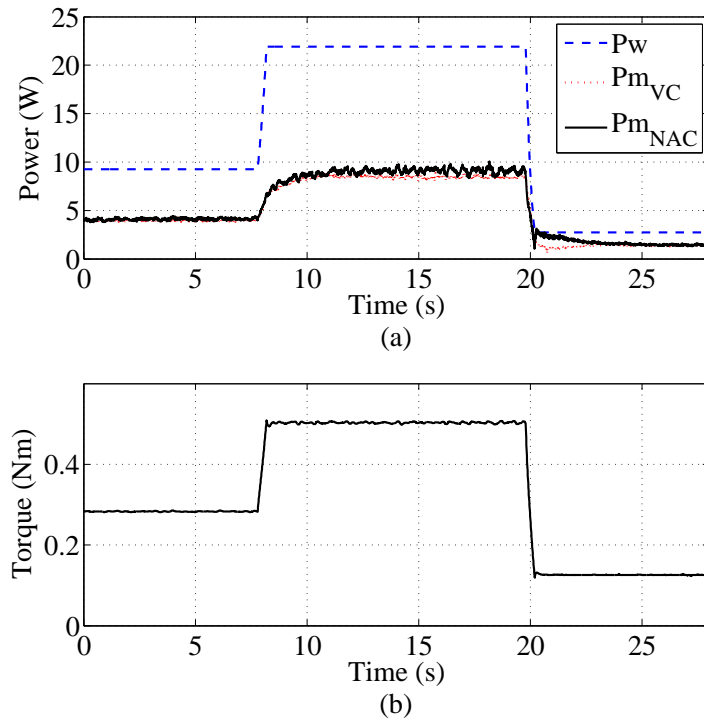
Figure 2.18: Response to ramp-change wind. (a) Mechanical power P_w and active generating power P_m. (b) Mechanical torque T_m.
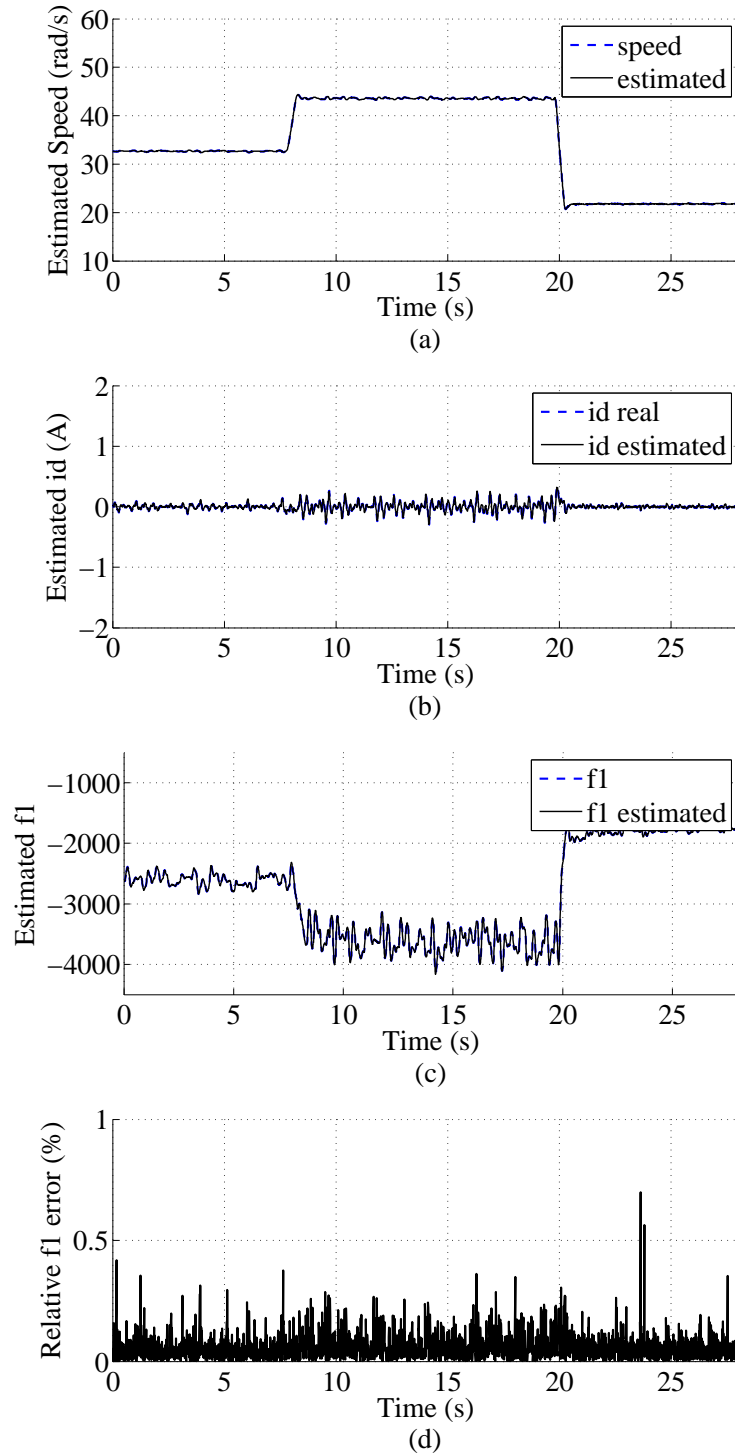
Figure 2.19: Estimates of states and perturbations
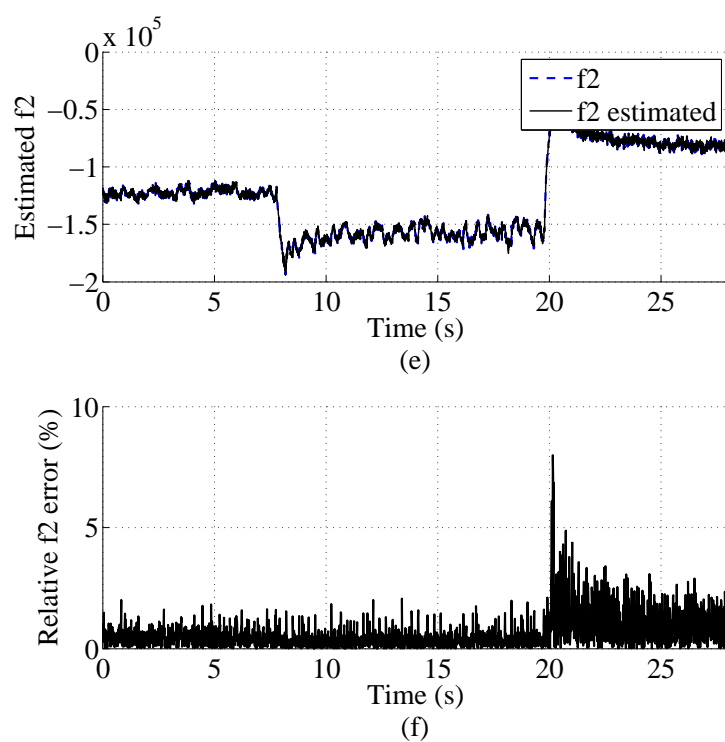
Figure 2.20: Estimates of states and perturbations
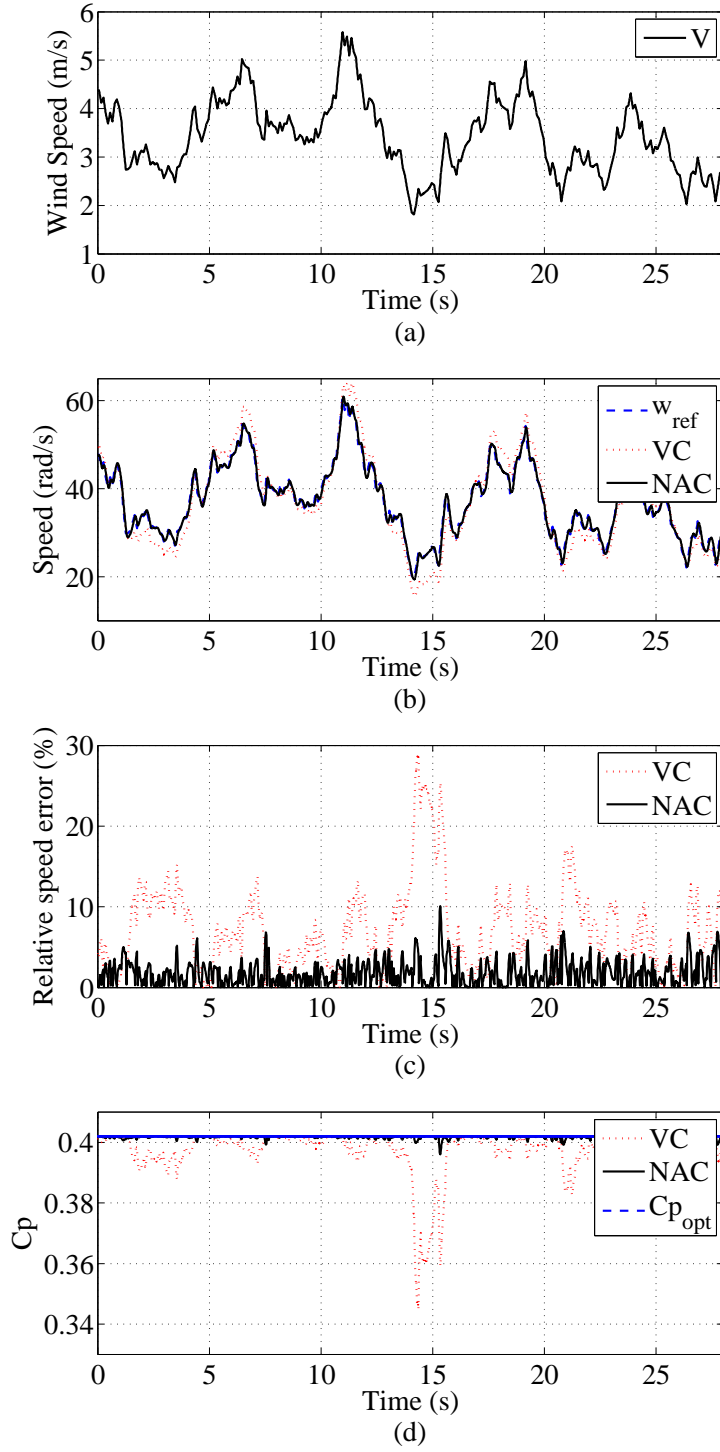
Figure 2.21: Responses of the WT to random wind. (a) Wind speed V. (b) Mechanical rotation speed w_m. (c) Relative error of mechanical rotation speed w_m. (d) Power coefficient C_p.
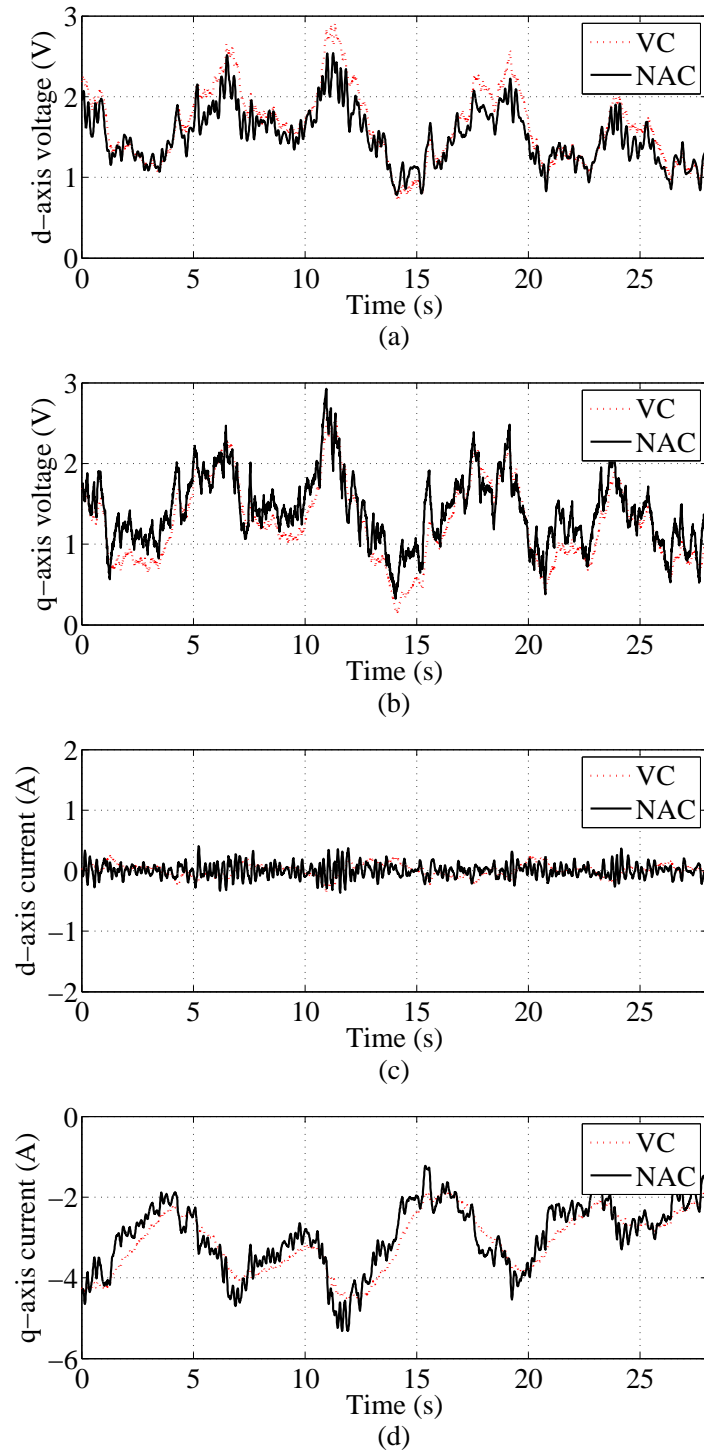
Figure 2.22: Responses of the PMSG to random wind. (a) d-axis stator voltage V_{md}. (b) q-axis stator voltage V_{mq}. (c) Stator current i_{md}. (d) Stator current i_{mq}.
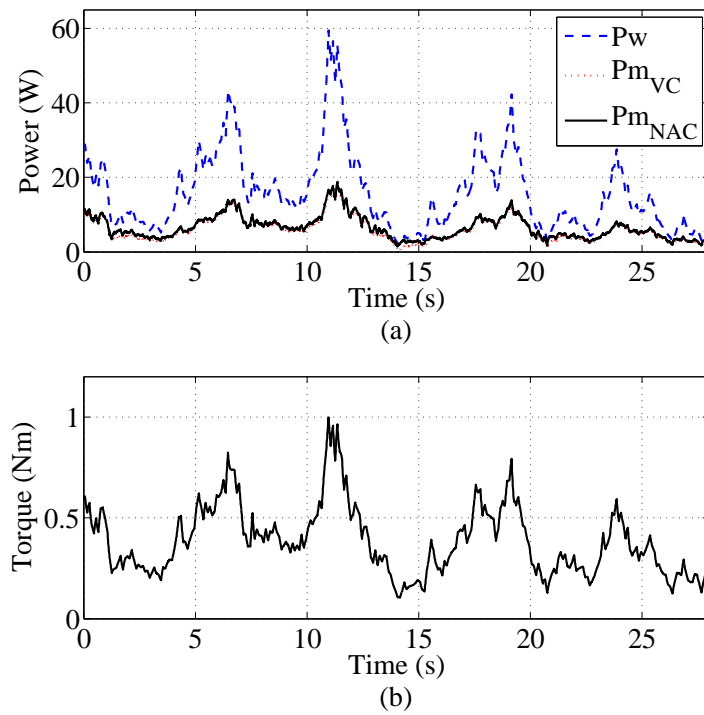
Figure 2.23: Response to random wind. (a) Mechanical power P_w and active generating power P_m. (b) Mechanical torque T_m.
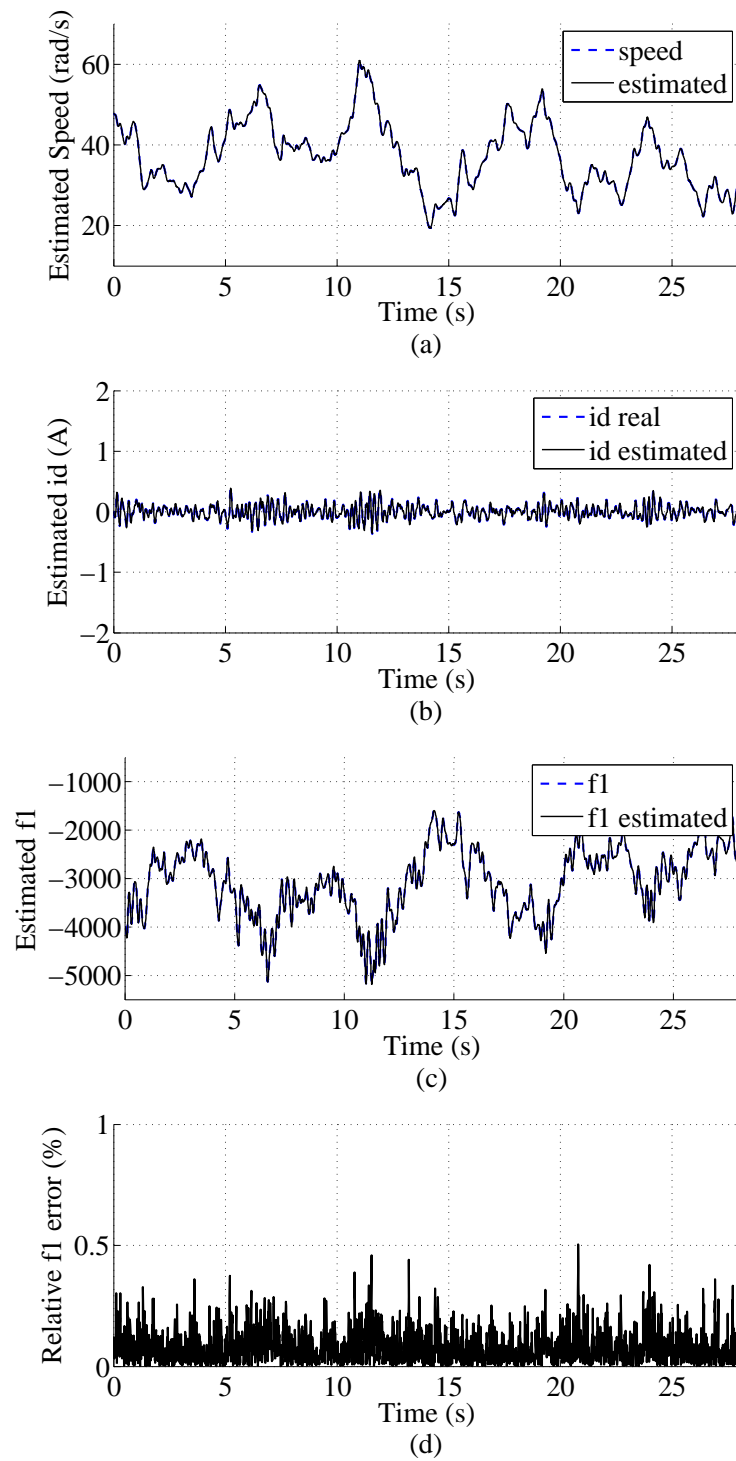
Figure 2.24: Estimates of states and perturbations
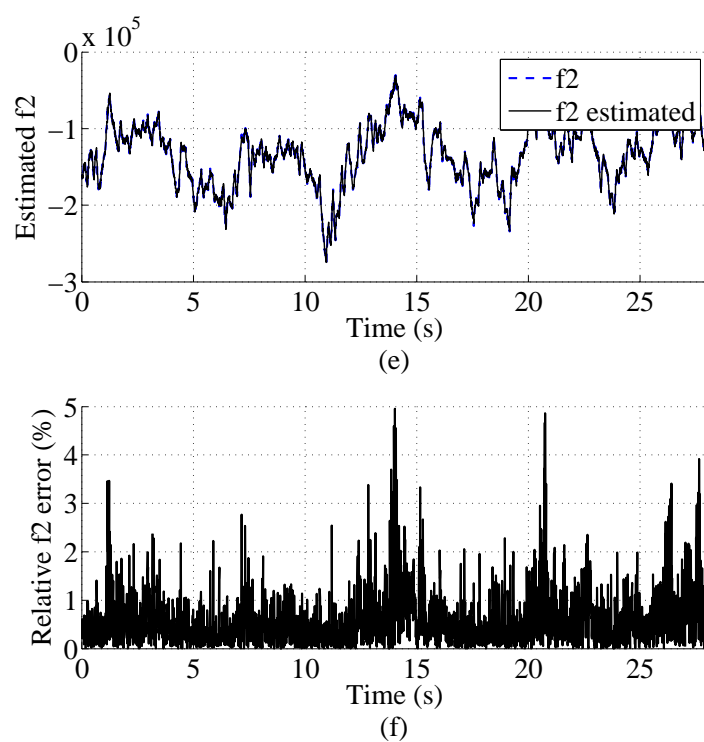
Figure 2.25: Estimates of states and perturbations

2.6.2 Random Wind

In this experiment test case, the random wind V is shown in Fig. 6.12 (a). It can be seen form Figs. 2.21-2.23 that, time-varying wind speed affects the system performances under the VC. The NAC can provide satisfactory performances under time-varying wind speed. Fig. 2.24 and 2.25 shows the states and perturbations can be well estimated.

2.7 Conclusions

This chapter has proposed a nonlinear adaptive controller for PMSG-WT to extract maximum power from time-varying wind. In the proposed NAC, the perturbation term includes all unknown and time-varying dynamics of the PMSG-WT, such as system parameter uncertainties, original nonlinearities and uncertain wind power input, which are estimated in real-time by the designed perturbation observer. The estimate is involved in the FLC loop of the NAC, which is designed based on a subsystem structure without requiring the accurate PMSG-WT model and full-state measurements, and considering all system nonlinearities and interactions. The proposed NAC has overcome the drawback of the VC designed based on one operating point and the shortcoming of the FLC relying on the full system states and detailed nonlinear system model. The simulation and experiment results have shown that the proposed NAC extracts the maximum power from wind, realizes a satisfactory dynamic performance and has a high robustness against parameter uncertainties and measurement noises.

Chapter 3

Pitch Control of Variable-Pitch PMSG-based Wind Turbine

3.1 Introduction

To keep the wind turbine (WT) within its design limits in Region 3, blade pitch and electromagnetic torque control is primarily applied in limiting the extracted wind power [83]. As the electromagnetic torque has much faster response than the mechanical torque, thus the decoupled control between wind turbine and generator can be applied. Above the rated wind speed, for the WT, the control of the mechanical rotation speed is applied to achieve the required pitch angle. The extracted wind power will change only in proportion to mechanical rotation speed when the mechanical torque is kept constant; thus, extracted wind power regulation is entirely dependent upon mechanical rotation speed regulation. For the generator, the electromagnetic torque is required to be maintained at its rated reference. When the electromagnetic torque or q-axis stator current and mechanical rotation speed are well regulated, the constant mechanical torque can be achieved.

Numerous studies designed controllers based on an approximated linear model and used the linear techniques aim to control pitch angle, such as the conventional vector control with proportional-integral (PI) loops [84, 85] and linear quadratic Gaussian (LQG) [86]. As WT contains the aerodynamic nonlinearities, the linear

controller designed based on one one operation point cannot obtain the optimal performance over a time-varying operation conditions. To improve the performance of the conventional VC and LQG, the H_∞ control method has been applied for pitch control of the WT [87, 88]. Feedback linearisation controller (FLC) has been widely and successfully applied in solving many practical nonlinear problems [35, 45, 89]. In [83], an FLC with an Extended Kalman Filter has been successfully used to control a FAST model of the WT. In the FLC design, full state information with no noise are required to be known. Although the FLC provides better performance than the linear quadratic regulator (LQR) at low wind speeds, no performance enhancements are seen at high wind speed, due to the effects of model uncertainties. It is because that the FLC requires the accurate system model [76]. Sliding mode control and nonlinear adaptive control (NAC) can be used to enhance the performance of the FLC, which remove the dependance of the detailed model of the FLC .

In this chapter, a nonlinear adaptive controller (NAC) is developed for permanent magnet synchronous generator based WT (PMSG-WT) to limit the extracted wind power and provide high performance in Region 3. In the designed NAC, it contains one mechanical rotation speed controller, two stator current controllers. One third-order states and perturbation observer (SPO), and two second-order perturbation observer (PO) are employed to estimate the perturbation including coupling nonlinear dynamics, parameter uncertainties, and other unknown disturbance of PMSG-WT, to compensate the real perturbation and realise an adaptive linearising of the PMSG-WT. The proposed NAC improves the robustness of the feedback linearisation control (FLC) and remove the dependance of the detailed model of the FLC and overcomes the shortcoming of the VC designed based one operating point.

The remaining parts of this chapter is organized as follows. In Section II, the model of the PMSG-WT is presented. The design of the NAC, based on a FLC, is presented in Section III. Section IV carries out simulation studies to verify the performance of the proposed NAC, compared with the VC and the FLC. Finally, conclusions of this work are presented in Section V.

3.2   Model and Problem Formulation

The state-space model of the PMSG-WT is given as [40]:

$$\dot{x} = f(x) + g_1(x)u_1 + g_2(x)u_2 + g_3(x)u_3 \qquad (3.2.1)$$

where

$$
\begin{aligned}
f(x) &= \begin{bmatrix} -\dfrac{\beta}{\tau_\beta} \\ -\dfrac{R_\mathrm{s}}{L_\mathrm{md}}i_\mathrm{md} + \dfrac{w_\mathrm{e}L_\mathrm{mq}}{L_\mathrm{md}}i_\mathrm{mq} \\ -\dfrac{R_\mathrm{s}}{L_\mathrm{mq}}i_\mathrm{mq} - \dfrac{1}{L_\mathrm{mq}}w_\mathrm{e}(L_\mathrm{md}i_\mathrm{md} + K_e) \\ \dfrac{1}{J_\mathrm{tot}}(T_\mathrm{e} - T_\mathrm{m} - T_\mathrm{f} - Bw_\mathrm{m}) \end{bmatrix}, \\
g_1(x) &= [-\tfrac{\beta}{\tau_\beta} \quad 0 \quad 0 \quad 0]^\mathrm{T}, \\
g_2(x) &= [0 \quad \tfrac{1}{L_\mathrm{md}} \quad 0 \quad 0]^\mathrm{T}, \\
g_3(x) &= [0 \quad 0 \quad \tfrac{1}{L_\mathrm{mq}} \quad 0]^\mathrm{T}, \\
x &= [\beta \quad i_\mathrm{md} \quad i_\mathrm{mq} \quad w_\mathrm{m}]^\mathrm{T}, \\
u &= [u_1, u_2, u_3]^T = [\beta_\mathrm{r}, V_\mathrm{md}, V_\mathrm{mq}]^T, \\
y &= [y_1, y_2, y_3]^T = [h_1(x), h_2(x), h_3(x)]^T = [w_\mathrm{m}, i_\mathrm{md}, i_\mathrm{mq}]^T
\end{aligned}
$$

where $x \in R^4$, $u \in R^3$ and $y \in R^3$ are state vector, input vector and output vector, respectively; $f(x)$, $g(x)$ and $h(x)$ are smooth vector fields. β and β_r are pitch angle and required pitch angle, τ_β is the actuator time constant, V_md and V_mq are the stator voltages in the d-q axis, i_md and i_mq are the stator currents in the d-q axis, R_s is the stator resistance, L_md and L_mq are d-q axis stator inductances, K_e is the permanent magnetic flux given by the magnet, p is the number of pole pairs, J_tot is the total inertia of the drive train that is equal to the summation of WT inertia constant and generator inertia constant, B is the friction coefficient of the motor, $w_\mathrm{e}(= pw_\mathrm{m})$ is the electrical generator rotation speed, and T_m, T_e and T_f are the WT mechanical torque, electromagnetic torque and static friction torque, respectively.

The electromagnetic torque is expressed as:

$$T_\mathrm{e} = p[(L_\mathrm{md} - L_\mathrm{mq})i_\mathrm{md}i_\mathrm{mq} + i_\mathrm{mq}K_e] \qquad (3.2.2)$$

Figure 3.1: Brief overall control structure of the PMSG-WT

3.2.1 Pitch Control

To maintain the extracted wind power at rated power in Region 3, it requires the corresponding pitch angle should be achieved, which in turn requires both the mechanical rotation speed w_m and the mechanical torque T_m should be kept at their rated values, respectively. The rated mechanical torque T_m is achieved when the electromagnetic torque T_e can track its rated reference T_{er} and the w_m is kept at it rated value. It can be seen from (3.2.2) that, the electromagnetic torque T_e can be maintained at T_{er} if the q-axis stator current i_{mq} can track its rated reference i_{mqr} and i_{md} is kept at 0.

The brief overall control scheme is shown in Fig. 3.1. As can be seen, the control scheme consists three controllers: the blade pitch controller and two stator current controllers.

3.3 NAC Design

This section will present the design of NAC for the PMSG-WT based on the feedback linearisation.

3.3.1 NAC Design of WT Pitch Control

Input/output linearization of WT speed dynamics can be represented from system (3.2.1)as

$$y_1^{(2)} = \frac{1}{J_{\text{tot}}}(\dot{T}_{\text{m}} - \dot{T}_{\text{e}}))$$ (3.3.1)

As the electromagnetic torque has much faster response than the mechanical torque, thus from the perspective of control of WT, $\dot{T}_{\text{e}} \simeq 0$. The (3.3.1) can be expressed as

$$
\begin{aligned}
y_1^{(2)} &= \frac{1}{J_{\text{tot}}}\dot{T}_{\text{m}} \\
&= F_1(x) + B1(x)u_1
\end{aligned}
$$ (3.3.2)

where

$$
\begin{aligned}
F_1(x) &= A[-\frac{C_p}{w_m} - \frac{RV}{F^2}E]\frac{dw_{\text{m}}}{dt} \\
&\quad - \frac{AE\beta}{\tau_\beta}[-0.088e^{-12.5\tau} - \frac{0.08V^2}{F} + \frac{0.105\beta^2}{(1+\beta^3)^2}]\frac{d\beta}{dt}
\end{aligned}
$$ (3.3.3)

$$B1(x) = \frac{AE\beta}{\tau_\beta}[-0.088e^{-12.5\tau} - \frac{0.08V^2}{F} + \frac{0.105\beta^2}{(1+\beta^3)^2}]$$ (3.3.4)

where

$$
\begin{aligned}
A &= \frac{\rho\pi R^2 V^3}{2w_{\text{m}}} \\
E &= (39.27 - 319\tau + 1.1\beta)e^{-12.5\tau} \\
F &= w_{\text{m}}R + 0.08\beta V \\
\tau &= \frac{1}{\lambda + 0.08\beta} - \frac{0.035}{\beta^3 + 1}
\end{aligned}
$$ (3.3.5)

Note that $\frac{dV}{dt}$ is not included in the FLC design, which cannot be measured directly.

As $det[B1(x)] = \frac{AE\beta}{\tau_\beta}[-0.088e^{-12.5\tau} - \frac{0.08V^2}{F} + \frac{0.105\beta^2}{(1+\beta^3)^2}] \neq 0$ when $V \neq 0$ and $\beta \neq 0$, that is, $B(x)$ is nonsingular for all nominal operation points. Thus, the FLC controller is obtained as

$$u_1 = B1(x)^{-1}(-F_1(x) + v_1) \tag{3.3.6}$$

And the original system is linearized as

$$y_1^{(2)} = v_1 \tag{3.3.7}$$

$$v_1 = \ddot{y}_{1r} + k_{11}\dot{e}_1 + k_{12}e_1 \tag{3.3.8}$$

where v_1 is control of of linear systems, k_{11} and k_{12} are gains of linear controller, y_{1r} is the desired output reference, and $e_1 = y_{1r} - y_1$ as track errors. The error dynamic is

$$\ddot{e}_1 + k_{11}\dot{e}_1 + k_{12}e_1 = 0 \tag{3.3.9}$$

Based on equation (2.3.7) and (3.3.2), perturbation term $\Psi_1(x)$ is obtained as:

$$q_1: \begin{cases} \Psi_1(x) = F_1(x) + (B1(x) - B1(0))u_1 \\ B1(0) = \frac{AE\beta}{\tau_\beta}[-0.088e^{-12.5\tau} - \frac{0.08V^2}{F} + \frac{0.105\beta^2}{(1+\beta^3)^2}] \end{cases} \tag{3.3.10}$$

where $B1(0)$ is nominal value of $B1(x)$.

Defining the state vectors as $z_{11} = y_1$, $z_{12} = y_1^{(1)}$, $z_{13} = \Psi_1$, and control variable as $u_1 = \beta_r$. The dynamic equation of the subsystem q_1 becomes as

$$q_1: \begin{cases} \dot{z}_{11} = z_{12} \\ \dot{z}_{12} = \Psi_1(x) + B1(0)u_1 \\ z_{11} = y_1 \end{cases}, \tag{3.3.11}$$

For sub-system q_1, a third-order SPO like (2.3.13) is designed to estimate the $\hat{z}_{12}$ and perturbation $\hat{z}_{13} = \hat{\Psi}_2$. By using the estimated perturbation to compensate the real perturbation, control laws for sub-system q_1 can be obtained as following:

Jian Chen

$$u_1 \;=\; B1(0)^{-1}(-\hat{z}_{13} + v_1) \tag{3.3.12}$$

where v_1 is defined as

$$v_1 \;=\; \ddot{z}_{11\mathrm{r}} + k_{12}(z_{11\mathrm{r}} - \hat{z}_{11}) + k_{11}(\dot{z}_{11\mathrm{r}} - \hat{z}_{12}) \tag{3.3.13}$$

3.3.2   NAC Design of PMSG

Input/output linearisation of system (3.2.1) can be represented as

$$\begin{bmatrix} y_2^{(1)} \\ y_3^{(1)} \end{bmatrix} = \begin{bmatrix} F_2(x) \\ F_3(x) \end{bmatrix} + B(x) \begin{bmatrix} u_2 \\ u_3 \end{bmatrix} \tag{3.3.14}$$

where

$$F_2(x) \;=\; \frac{1}{L_{\mathrm{md}}}(-i_{\mathrm{md}}R_{\mathrm{s}} + w_{\mathrm{e}}L_{\mathrm{mq}}i_{\mathrm{mq}}) \tag{3.3.15}$$

$$F_3(x) \;=\; -\frac{R_{\mathrm{s}}}{L_{\mathrm{mq}}}i_{\mathrm{mq}} - \frac{1}{L_{\mathrm{mq}}}w_{\mathrm{e}}(L_{\mathrm{md}}i_{\mathrm{md}} + K_e) \tag{3.3.16}$$

$$\tag{3.3.17}$$

Note that $\frac{dT_{\mathrm{m}}}{dt}$ is not included in the FLC design, which cannot be measured directly.

$$B2(x) = \begin{bmatrix} B_2(x) \\ B_3(x) \end{bmatrix} = \begin{bmatrix} \frac{1}{L_{\mathrm{md}}} & 0 \\ 0 & \frac{1}{L_{\mathrm{mq}}} \end{bmatrix} \tag{3.3.18}$$

As $det[B2(x)] = \frac{p[K_e + (L_{\mathrm{md}} - L_{\mathrm{mq}})i_{\mathrm{md}}]}{J_{\mathrm{tot}}L_{\mathrm{md}}L_{\mathrm{mq}}} \neq 0$ when $K_e \neq 0$, that is, $B(x)$ is nonsingular for all nominal operation points. Thus, the FLC controller is obtained as

$$\begin{bmatrix} u_2 \\ u_3 \end{bmatrix} = B2(x)^{-1} \left[\begin{bmatrix} -F_2(x) \\ -F_3(x) \end{bmatrix} + \begin{bmatrix} v_2 \\ v_3 \end{bmatrix} \right] \tag{3.3.19}$$

$$B2(x)^{-1} = \begin{bmatrix} L_{\mathrm{md}} & 0 \\ 0 & L_{\mathrm{mq}} \end{bmatrix} \tag{3.3.20}$$

And the original system is linearized as

$$
\begin{bmatrix} y_2^{(1)} \\ y_3^{(1)} \end{bmatrix} = \begin{bmatrix} v_2 \\ v_3 \end{bmatrix}
\tag{3.3.21}
$$

where

$$
v_2 = \dot{y}_{2r} + k_{21}e_2
\tag{3.3.22}
$$

$$
v_3 = \dot{y}_{3r} + k_{31}e_3
\tag{3.3.23}
$$

where v_2 and v_3 are control of of linear systems, k_{21} and k_{31} are gains of linear controller, y_{2r} and y_{3r} the desired output references. Define $e_2 = y_{2r} - y_2$ and $e_3 = y_{3r} - y_3$ as track errors, the error dynamics are

$$
\dot{e}_2 + k_{21}e_2 = 0
\tag{3.3.24}
$$

$$
\dot{e}_3 + k_{31}e_3 = 0
\tag{3.3.25}
$$

Based on equation (2.3.7) and (3.3.14), perturbation terms $\Psi_2(x)$ and $\Psi_3(x)$ are obtained as:

$$
q_2 : \begin{cases} \Psi_2(x) = F_2(x) + (B_2(x) - B_2(0)) \begin{bmatrix} u_2 \\ u_3 \end{bmatrix} , \\ B_2(0) = \begin{bmatrix} \frac{1}{L_{md0}} & 0 \end{bmatrix} \end{cases}
$$

$$
\tag{3.3.26}
$$

$$
q_3 : \begin{cases} \Psi_3(x) = F_3(x) + (B_3(x) - B_3(0)) \begin{bmatrix} u_2 \\ u_3 \end{bmatrix} \\ B_3(0) = \begin{bmatrix} \frac{1}{L_{mq0}} & 0 \end{bmatrix} \end{cases}
$$

where L_{md0} and L_{mq0}, $B_2(0)$ and $B_3(0)$ are nominal values of L_{md}, L_{mq}, $B_2(x)$ and $B_3(x)$, respectively .

Defining the state vectors as $z_{21} = y_2$, $z_{22} = \Psi_2$ and $z_{31} = y_3$, $z_{32} = y_2^{(3)}$, $z_{33} = \Psi_3$, and control variables as $u_2 = V_{md}$ and $u_3 = V_{mq}$. The dynamic equations of the

two subsystems q_2 and q_3 become as

$$q_2 : \begin{cases} \dot{z}_{21} &= \Psi_2(x) + B_2(0) \begin{bmatrix} u_1 \\ u_2 \end{bmatrix} \\ z_{21} &= y_2 \end{cases} ,$$

$$q_3 : \begin{cases} \dot{z}_{31} &= \Psi_3(x) + B_3(0) \begin{bmatrix} u_1 \\ u_2 \end{bmatrix} \\ z_{31} &= y_3 \end{cases} ,$$

(3.3.27)

For sub-system q_2, a second-order PO like (2.3.10) is designed to estimate the perturbation $\hat{z}_{22} = \hat{\Psi}_2$; and for sub-system q_3, a second-order PO like (2.3.10) is designed to estimate the perturbation $\hat{z}_{32} = \hat{\Psi}_3$. By using the estimated perturbation to compensate the real perturbation, control laws for sub-systems q_2 and q_3 can be obtained as following:

$$\begin{bmatrix} u_2 \\ u_3 \end{bmatrix} = B2(0)^{-1} \left[\begin{bmatrix} -\hat{z}_{22} \\ -\hat{z}_{32} \end{bmatrix} + \begin{bmatrix} v_2 \\ v_3 \end{bmatrix} \right]$$

(3.3.28)

where $v_{2,3}$ is defined as

$$\begin{cases} v_2 &= k_{21}(z_{21\mathrm{r}} - \hat{z}_{21}) + \dot{z}_{21\mathrm{r}} \\ v_3 &= k_{31}(z_{31\mathrm{r}} - \hat{z}_{31}) + \dot{z}_{31\mathrm{r}} \end{cases}$$

(3.3.29)

The final control law represented by physical variables, such as currents, inductance, total inertia, field flux and mechanical rotation speed, are given as following:

$$\begin{cases} u_2 = L_{\mathrm{md0}}[k_{21}(i_{\mathrm{mdr}} - i_{\mathrm{md}}) + \dot{i}_{\mathrm{mdr}} - \hat{\Psi}_2] \\ u_3 = L_{\mathrm{mq0}}[k_{31}(i_{\mathrm{mqr}} - i_{\mathrm{mq}}) + \dot{i}_{\mathrm{mqr}} - \hat{\Psi}_3] \end{cases}$$

(3.3.30)

Note that the NAC proposed only requires the nominal value of parameters of L_{md0}, L_{mq0}, and measurements of two output variables i_{md} and i_{mq}.

To clearly illustrate its principle, block diagram of the NAC proposed is shown in Fig. 3.2.
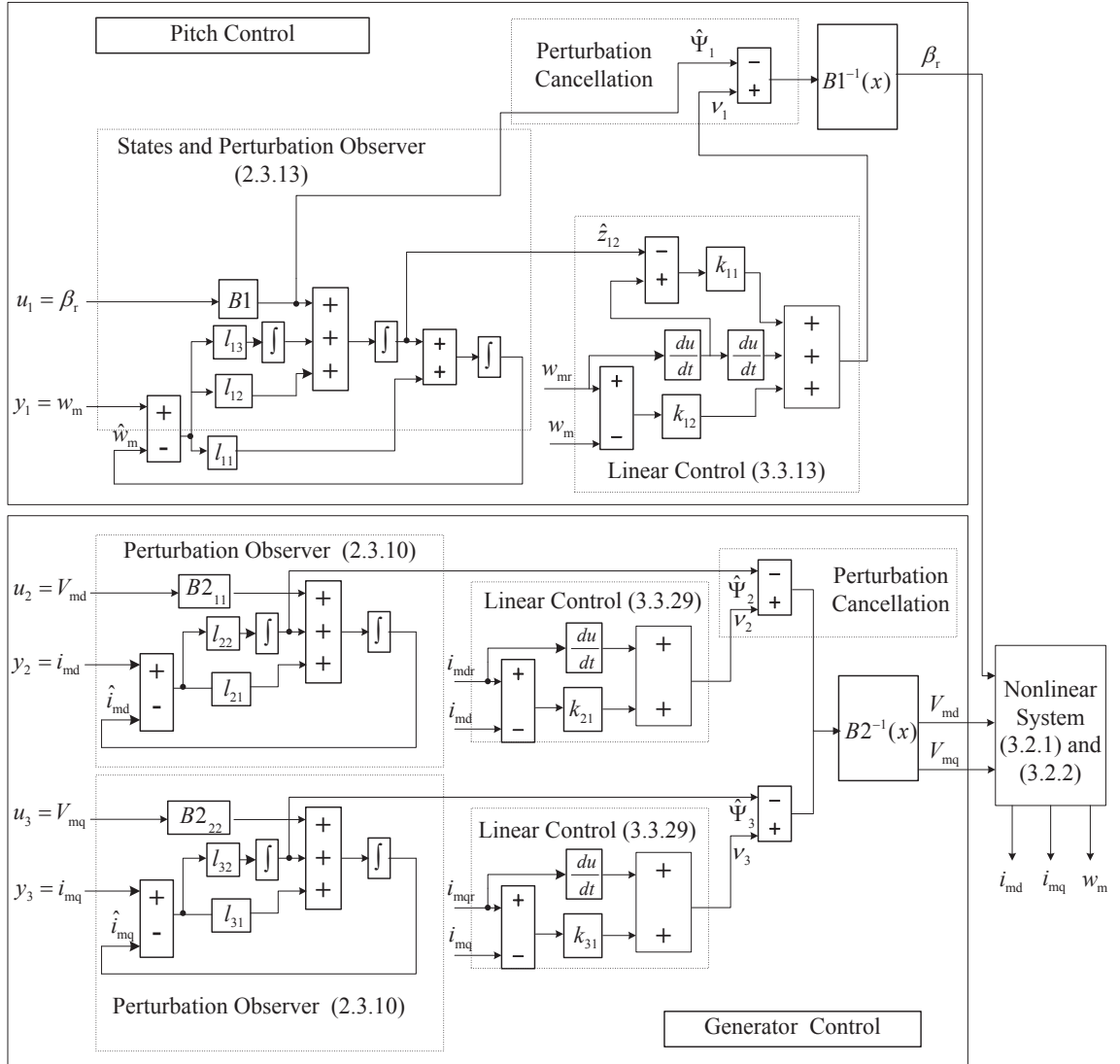
Figure 3.2: Block diagram of nonlinear adaptive controller

3.4   Simulation Results

To verify the effectiveness of the proposed NAC, simulations studies have been carried out. A 2-MW PMSG-WT given in Chapter 2 is investigated. The parameters of the PMSG-WT system are τ_β=1 s, pitch angle rate β_{rate}=$\pm$10 degree/s,R=39 m, ρ=1.205 kg/m^3, rated wind speed V_{r}=12 m/s, J_{tot}=10000 kg $\cdot$ m^2, K_e=136.25 V.s/rad, p=11, L_{md}=5.5 mH, L_{mq}=3.75 mH, and R_{s}=50 $\mu\Omega$. In this chapter, the mechanical rotation speed rated reference is $w_{\text{mr}} = 2.2489 rad/s$, The d-axis stator current reference i_{mdr} is 0 A. The rated electromagnetic torque reference is $T_{\text{er}} = 889326.7 Nm$. According to (3.2.2), the q-axis stator current reference i_{mqr} is 593.3789 A.

Parameters of NACs for subsystems q_1, q_2, and q_3 are designed based on pole-placement and listed as following:

q_1 : observer: $\alpha_{11} = 5\times10^1$, $\alpha_{12} = 1.875\times10^3$, $\alpha_{13} = 1.5625\times10^4$, $\epsilon_1 = 2\times10^{-1}$, which locate all poles at -2.5×10^1; controller: $k_{12} = 4 \times 10^2$, $k_{11} = 4 \times 10^1$, which are obtained by placing pole at -2×10^1.

q_2 : observer: $\alpha_{21} = 4 \times 10^2$, $\alpha_{22} = 4 \times 10^4$, $\epsilon_2 = 1 \times 10^{-1}$, which locate all poles at -2×10^2; controller: $k_{21} = 1.6 \times 10^2$, which is obtained by placing pole at -1.6×10^2.

q_3 : observer: $\alpha_{31} = 4 \times 10^2$, $\alpha_{32} = 4 \times 10^4$, $\epsilon_3 = 1 \times 10^{-1}$, which locate all poles at -2×10^2; controller: $k_{31} = 1.6 \times 10^2$, which is obtained by placing pole at -1.6×10^2.

Note that FLC uses same controller parameters as the NAC for all three subsystems. Moreover, the FLC uses the full state feedback and the exact parameters.

3.4.1   Ramp-Change Wind

The responses of the PMSG-WT to ramp-change wind is shown in Fig. 3.3 and 3.4. Wind speed is shown in Fig. 3.3 (a). As shown in Figs. 3.3 (b) and (c), the proposed NAC provides the best tracking performance of the mechanical rotation
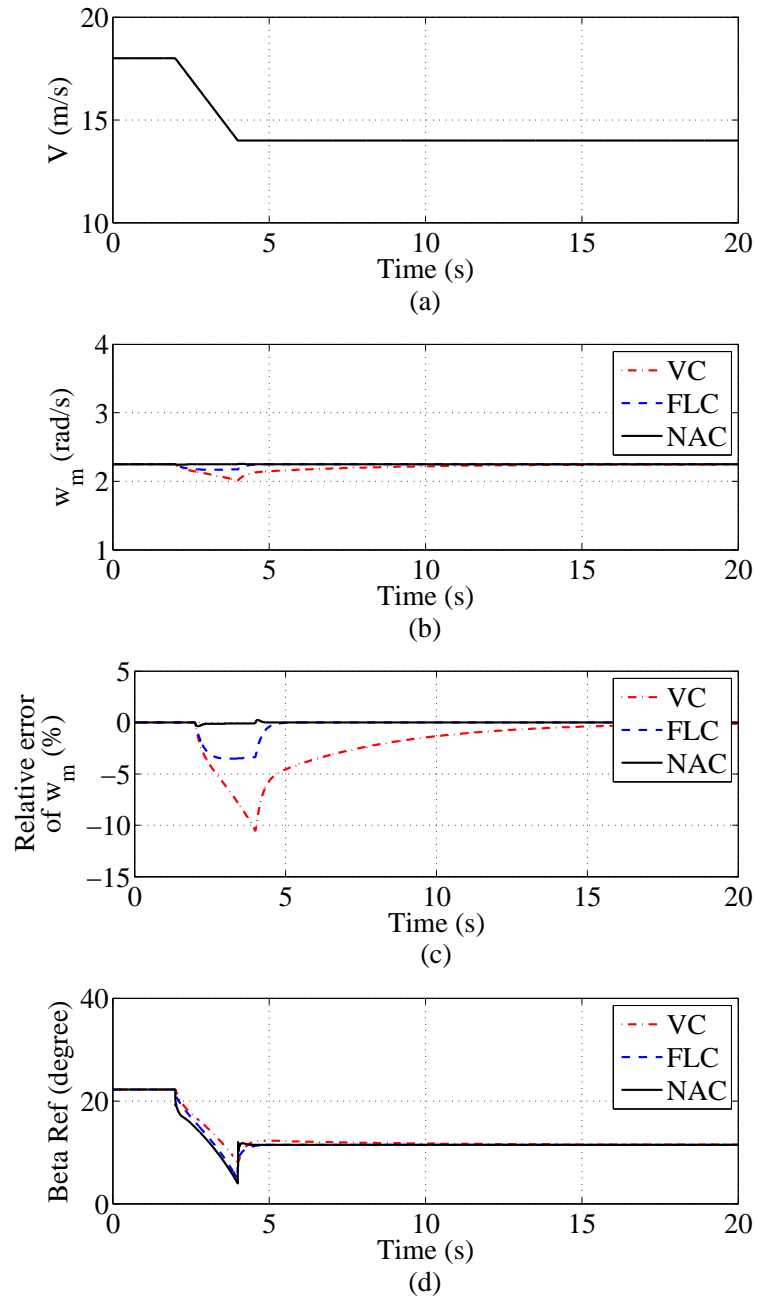
Figure 3.3: Responses of the WT to ramp-change wind. (a) Wind speed V. (b) Mechanical rotation speed w_{m}. (c) Relative error of mechanical rotation speed w_{m}. (d) Pitch angle reference.
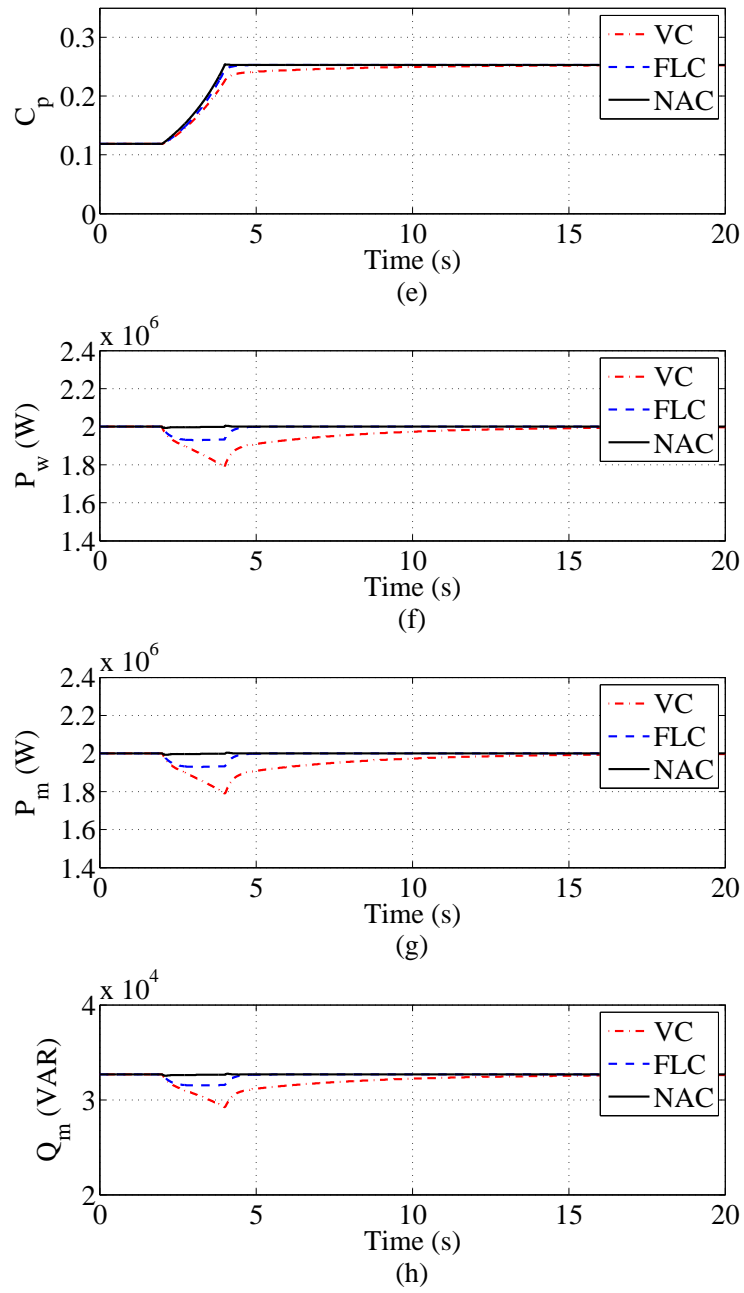
Figure 3.4: Responses of the WT to ramp-change wind. (e) Power coefficient C_{p}. (f) Mechanical power P_{w}. (g) Active generating power P_{m}. (h) Reactive generating power Q_{m}.
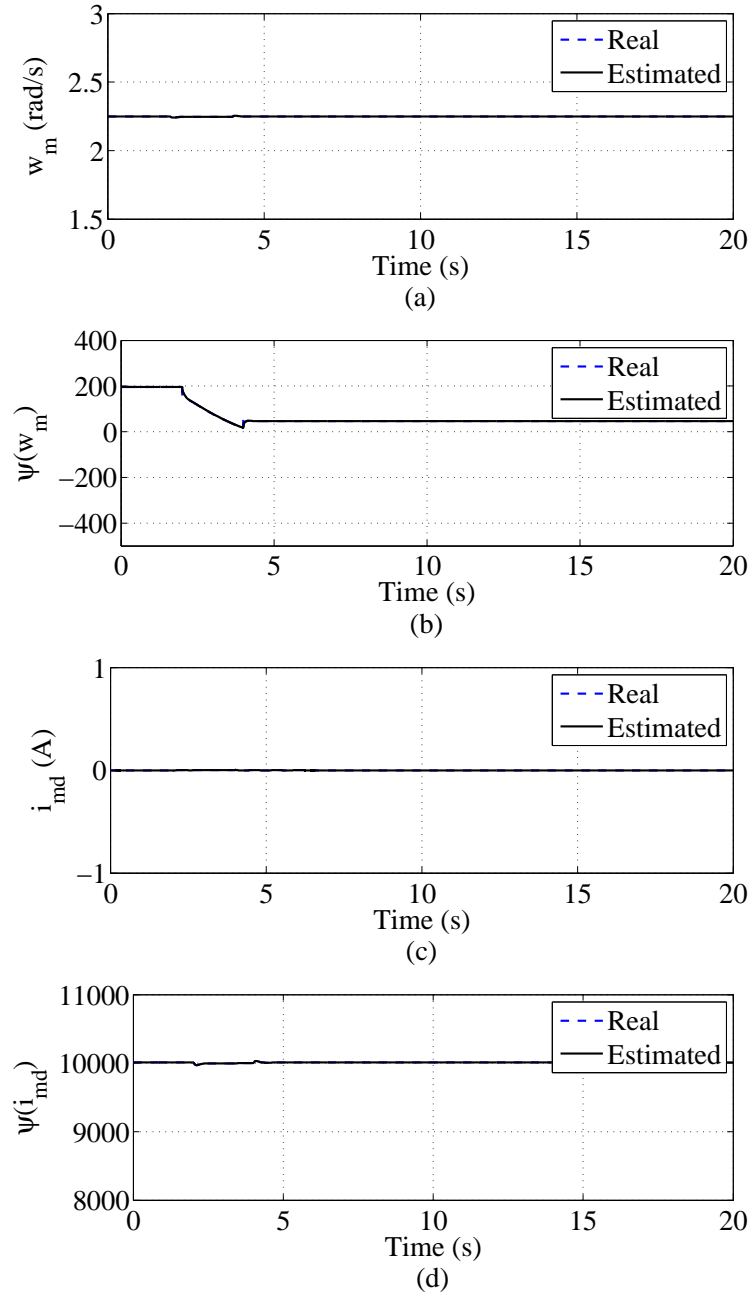
Figure 3.5: Estimates of states and perturbations
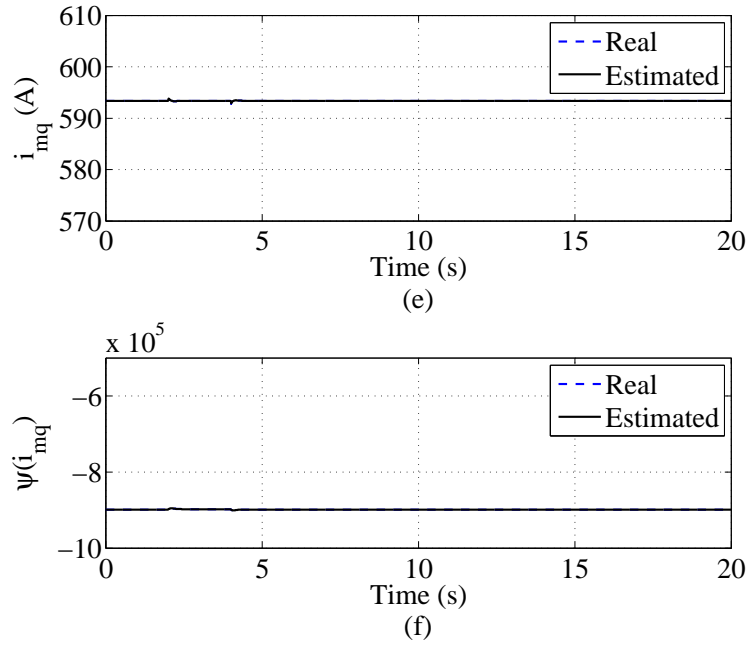
Figure 3.6: Estimates of states and perturbations

speed w_m compared with the VC and FLC when wind speed varies. The VC has the biggest tracking error and requires longest recovery time. It can be explained that the VC is adjusted for a specific operation point of the system and cannot ensure a satisfying dynamic behavior for varying operation points. Although the FLC can provide a satisfactory tracking performance, the tracking error of w_m still exists. It is because that the FLC requires the full-state measurements, but the $\frac{dV}{dt}$ in (3.3.1) is not known in the FLC design. To maintain the extracted wind power at the rated power, the pitch angle β_r will change with the varying wind speed, as shown in Fig. 3.3 (d). Fig. 3.4 (e) shows the response of the power coefficient C_p to ramp-change wind. The extracted wind power can be maintained at the rated value by the NAC even when wind speed varies, that both the VC and FLC cannot provide shown in Fig. 3.4 (f). The active generating power P_m and reactive generating power Q_m of the PMSG are shown in Fig. 3.4 (g) and (h), respectively.

During the whole operating period, the NAC can always keep consistent responses of P_m and Q_m. The performances of the VC and FLC are affected by the
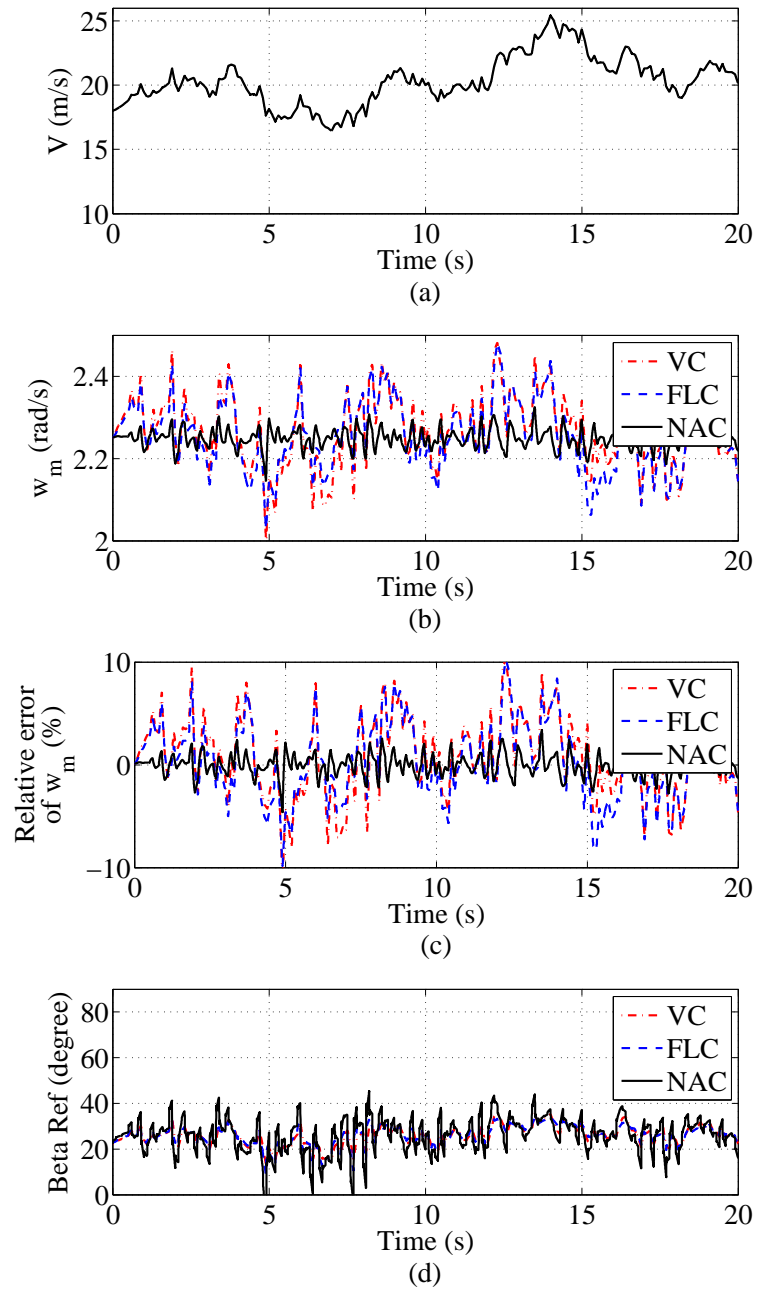
Figure 3.7: Responses of the PMSG-WT to random wind. (a) Wind speed V. (b) Mechanical rotation speed w_m. (c) Relative error of mechanical rotation speed w_m. (d) Pitch angle reference.
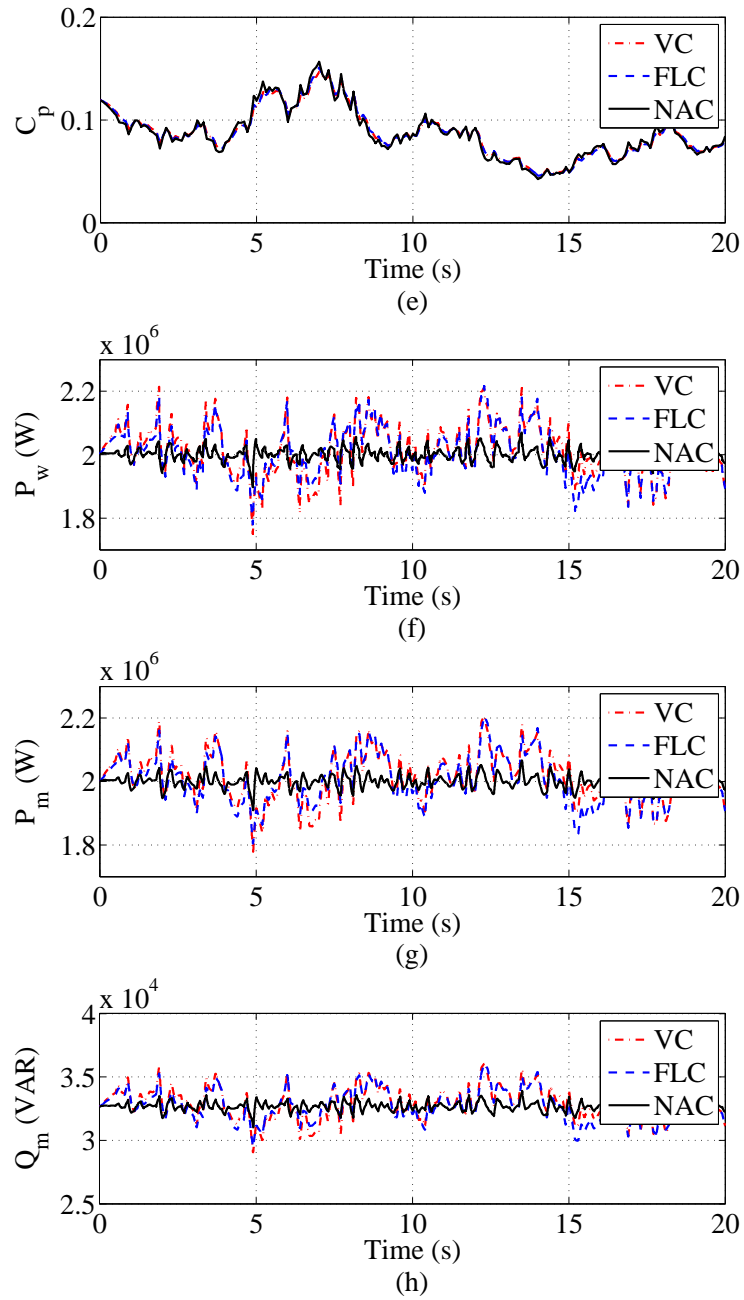
Figure 3.8: Responses of the PMSG-WT to random wind. (e) Power coefficient C_p. (f) Mechanical power P_w. (g) Active generating power P_m. (h) Reactive generating power Q_m.
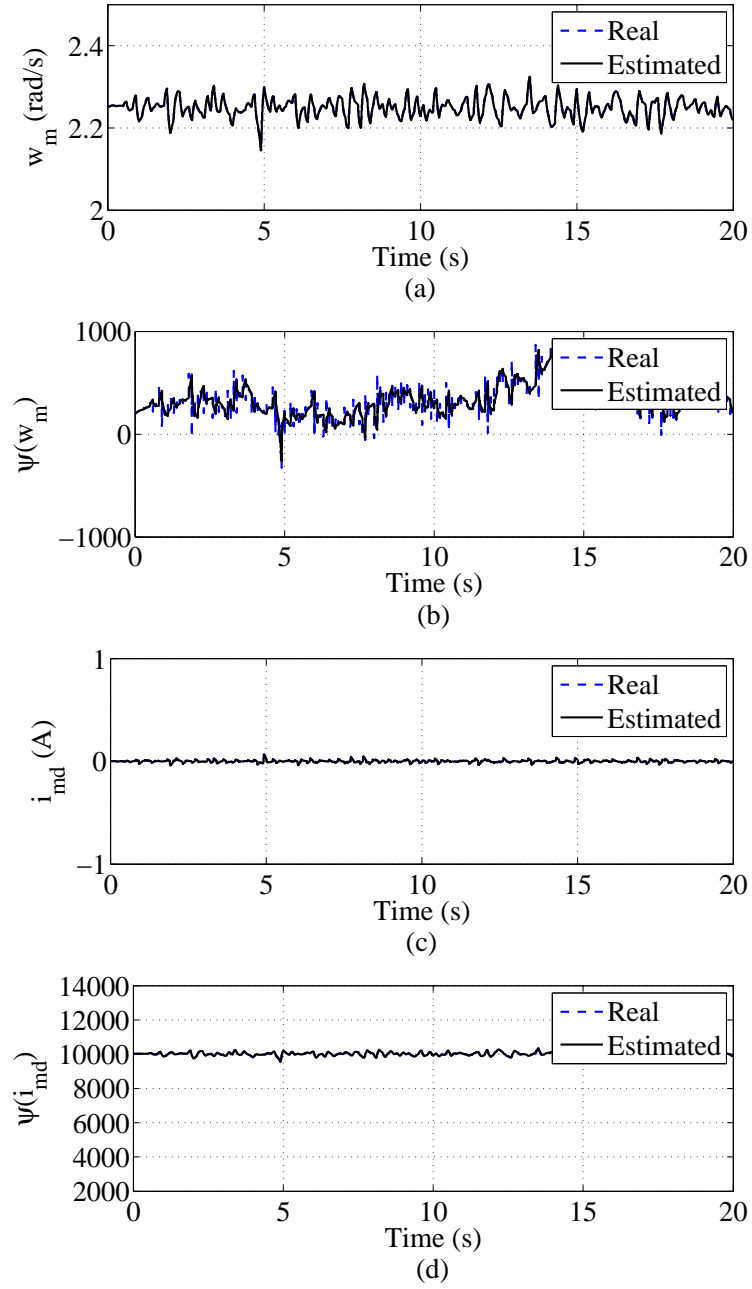
Figure 3.9: Estimates of states and perturbations
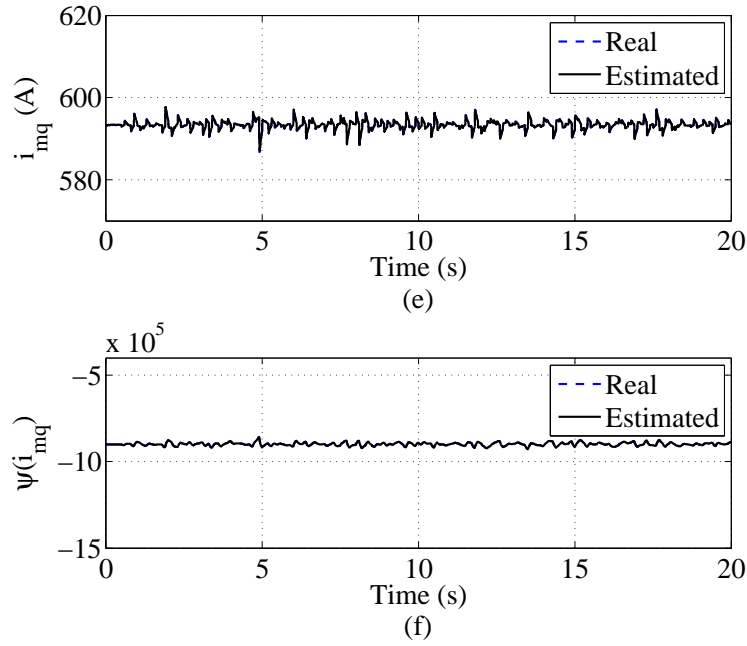
Figure 3.10: Estimates of states and perturbations

varying wind speed. Note that the FLC uses the full state feedback except $\frac{dV}{dt}$ and extract parameters of the system, but the NAC is without requiring the details of the system information and extract parameters.

The estimates of the states and perturbations are shown in Fig. 3.5 and 3.6. It can be seen from Fig. 3.5 and 3.6 that, both the states and perturbations can be well estimated by the observers. The estimated perturbations including nonlinearities, uncertainties and disturbance are used for compensation of the real perturbation.

3.4.2 Random Wind

The responses of the WT to random wind is shown in Fig. 3.7 and 3.8. Wind speed is shown in Fig. 3.7 (a). When wind speed is time-varying, both the VC and FLC cannot provide satisfactory tracking performances of the mechanical rotation speed w_m shown in Fig. 3.7 (b). The NAC keeps w_m around rated mechanical rotation speed. Fig. 3.8 (f) shows that the NAC almost maintain the extracted wind power at rated value, that the VC and FLC cannot achieve. During the whole oper-

ating period, the NAC can always keep consistent responses of P_m and Q_m shown in Fig. 3.8 (g) and (h). The performances of the VC and FLC are affected by the varying wind speed. The estimates of the states and perturbations are shown in Fig. 3.9 and 3.10. It can be seen from Fig. 3.9 and 3.10 that, both the states and perturbations can be well estimated by the observers.

3.5   Conclusions

This chapter has proposed a nonlinear adaptive pitch controller for PMSG-WT to limit the extracted power from time-varying wind in Region 3. The proposed NAC has overcome the drawback of the VC designed based one operating point and the shortcoming of the FLC relying on the full system states and detailed nonlinear system model. The simulation results have shown that the proposed NAC can limit the extracted wind power in Region 3, and realize a satisfactory dynamic performance without requiring accurate PMSG-WT model, parameters and full-state measurements, and considering all system nonlinearities and interactions.

Chapter 4

Enhancing Fault Ride-Through Capability of a Full-Rated Converter Based Wind-Turbine

4.1   Introduction

To enable the reliable integration of large capacity of wind power, most of the current power grid codes require that a wind power generation system (WECS) must have fault ride-through capability (FRTC) or low-voltage ride-through capability (LVRTC) [20–24]. When many wind turbines disconnect with the power grid under grid voltage dips, it may result in more serious fault, or even cause the grid to collapse. The FRTC enables WECSs to remain connected with the power grid during and after grid faults, or undergoing voltage dips due to load disturbances, and to provide active/reactive power control to the power grid [25]. In addition, the wind turbine and generator can still operate normally to extract wind power and generate active/reactive power, respectively, under grid voltage dips if no new control strategy has been applied in controlling wind turbine or generator. The Irish grid code, as shown in Fig. 4.1, is adopted as an example to demonstrate a typical FRTC requirement [35]. Permanent magnet synchronous generator based wind turbine (PMSG-WT) connects the grid via a back-to-back voltage-source converter
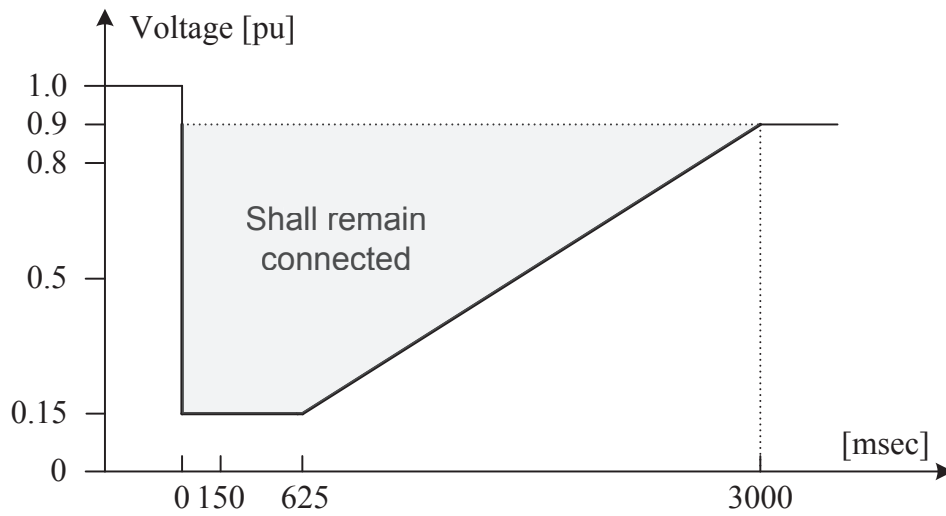
Figure 4.1: Fault ride-through requirements of wind farms adopted by the Irish grid code

(VSC) and a step-up transformer, as shown in Fig. 1.2. It has been widely used, especially for offshore wind farms due to merits such as no gearbox, self excitation, high efficiency and low noise. As the VSC decouples dynamics of the generator and the grid, the FRTC of the PMSG-WT mainly depends on the control and operation of the grid-side converter (GSC) [29, 30].

The FRTC of WPGSs can be enhanced by installing additional protection devices, such as a rectifier-boost damping resistor for protection of the DC-link voltage [26], active crowbars installed to protect the machine-side converter of the PMSG [27] and the rotor-side converter of the doubly fed induction generator (D-FIG) [28]. Using the extra device increases the cost of the whole system. Another effective alternative to enhance the FRTC of WPGSs is to redesign or improve the control algorithms applied on the VSCs, which can avoid installation of additional e-quipment and allow reduction of the power rating of the protection devices [29–35]. In addition, modification converter topology, such as neutral point clamped converters controlled by symmetrical components based vector current controller, have been presented [25, 90]. When the grid-voltage sags happen during the operation of PMSG, a conventional vector controller (VC) with proportional-integral (PI) loops

cannot limit the inrush grid-side current and the DC-link voltage within their safe boundaries and thus will damage converters or other power electronic devices [91]. This is partly because the conventional VCs are derived from the steady-state operating conditions of the WECS and the PI loops are tuned specially based on one operation point, both of which make them incapable of dealing with faulty conditions which are far away from the designed point and have strong transient nature. Thus it is a challenging task to tune the parameters of VC to provide a consistent performance over a wide range of operating conditions [92].

Feedback linearising control (FLC) has been applied to improve the FRTC of a full-rated converter based wind turbine by controlling the GSC [35]. By designing a state transformation and a nonlinear feedback control law, a nonlinear system is transformed into a fully or partially decoupled linear one, then powerful linear techniques are used to complete the control design [77]. The FLC can provide a global optimal controller covering the whole operation region and greatly improve the FRTC, as it takes into account the system nonlinearities. However, the FLC requires the accurate system model and will result in a complex control law and a weak robustness to parameter uncertainties and external disturbances [73, 76, 93, 94]. On the other hand, most FLC controllers require full states feedback and many measured variables to calculate the nonlinear controller [29, 30]. To improve the robustness of the FLC, several methodologies have been proposed, such as sliding mode controller [29, 95, 96] and a FLC based on revised control output [91]. All these work assumed that the generator output can be reduced simultaneously and proportionally to the drop of the grid voltage. Moreover, most of them have not considered the machine-side dynamics during the test of different voltage dips.

This chapter is closely related with the FLC reported in [35]. The designed NAC improves the robustness and reduces the controller complexity of the FLC by removing the requirement of a detailed model and full state feedback, and provides adaptivity for time-varying parameter uncertainties and external disturbances. The NAC proposed will be compared with the FLC and the VC in simulation studies under different situations. The NAC methodology is based on the author's previous work which has been proposed to improve the robustness of the FLC against

parameter uncertainties and external disturbances and remove the dependance of the detailed model of the FLC. The FLC has been applied successfully in power systems [65, 97, 98]. The NAC defines a lumped perturbation term to include coupling nonlinear dynamics, model uncertainties and other unknown disturbances. It then designs a perturbation observer to estimate the perturbation which is used to compensate the real perturbation and realize an adaptive linearizing of the original nonlinear system, without requiring the accurate system model and full-state measurements, and still considering all system nonlinearities and unknown time-varying dynamics, such as grid faults and intermittent wind power inputs.

The remaining parts of this chapter are organized as follows. Section II presents system model and problem formulation. In Section III, the nonlinear adaptive control based on perturbation estimation is recalled. The design of NAC, based on an FLC, is presented in Section IV. Section V carries out simulation studies to verify the performance of the proposed NAC, compared with the VC and the FLC. Section VI presents the conclusions of this work.

4.2 Problem Formulation

Fig. 1.2 shows the detailed scheme of a PMSG-WT connecting to the grid via a back-to-back VSC. The output power of the generator is controlled by the machine-side VSC, while the grid-side VSC is responsible for delivering active power to the grid via the DC-link and maintaining the DC-link voltage. Two VSCs are controlled separately and the dynamic of the PMSG-WT and the power grid is decoupled via the DC-link. As the FRTC of the WECS mainly relies on the control of the grid-side VSC and the DC-link, the detailed model of the machine-side VSC, the generator and the WT has not presented in this chapter. Moreover, the machine-side dynamic is simplified as a controlled current source, assuming that the DC-link voltage is maintained as a constant. The time-varying active power output of the generator due to the change of wind power input is simulated by varying the machine-side DC current i_{dc2}. Note that to fully investigate the impact of the machine-side dynamic against to the FRTC, the detailed model and dynamic of the machine-side should be

considered together with that of the grid-side VSC.

When there are voltage dips caused by grid faults or load disturbances, the DC-link voltage and the grid-side current of the GSC will increase sharply and may exceed their safe boundaries. Another disturbance is the variable active power generated from the wind turbine due to the variable wind power inputs. The objective of this chapter is to design an NAC controller for the GSC to improve the LVRTC of the WECS, i.e., reducing the magnitude and variation of the grid-side current and DC-link voltage and limiting them within their safe boundaries, under grid-side voltage dips and the variable wind power inputs.

Under symmetrical operation voltage and synchronously rotating d-q reference frame, state-space model of the grid-side VSC and the DC-link capacitor of the WECS can be obtained as [35]

$$\dot{x} = f(x) + g_1(x)u_1 + g_2(x)u_2 \tag{4.2.1}$$

where

$$f(x) = \begin{bmatrix} \frac{1}{L_g}E_{gd} - \frac{R_g}{L_g}i_{gd} + wi_{gq} \\ \frac{1}{L_g}E_{gq} - \frac{R_g}{L_g}i_{gq} - wi_{gd} \\ \frac{3E_{gd}i_{gd}}{2CV_{dc}} - \frac{i_{dc2}}{C} \end{bmatrix},$$

$$g_1(x) = [-\frac{1}{L_g} \quad 0 \quad 0]^{\mathrm{T}},$$

$$g_2(x) = [0 \quad -\frac{1}{L_g} \quad 0]^{\mathrm{T}},$$

$$x = [i_{gd} \quad i_{gq} \quad V_{dc}]^{\mathrm{T}},$$

$$u = [u_1, u_2]^T = [V_{gd}, V_{gq}]^T,$$

$$y = [y_1, y_2]^T = [h_1(x), h_2(x)]^T = [i_{gq}, V_{dc}]^T$$

where $x \in R^3$, $u \in R^2$ and $y \in R^2$ are state vector, input vector and output vector, respectively; $f(x)$, $g(x)$ and $h(x)$ are smooth vector fields. (E_{gd}, E_{gq}), (V_{gd}, V_{gq}) and (i_{gd}, i_{gq}) are d-axis and q-axis components of three-phase grid voltage (E_a, E_b, E_c), three-phase GSC voltage (V_a, V_b, V_c) and three-phase grid current (i_a, i_b, i_c) respectively, R_g and L_g are equivalent resistance and inductance between GSC and the high voltage terminals of the grid-connected transformer, C is DC-link capacitor and w is angular speed of grid voltage, i_{dc1} is the grid-side DC-link current, i_{dc2} is the machine-side DC-link current, i_{dc} is the capacitor current, and V_{dc} is DC-link capacitor voltage. Note that the d-axis of the synchronous rotating frame
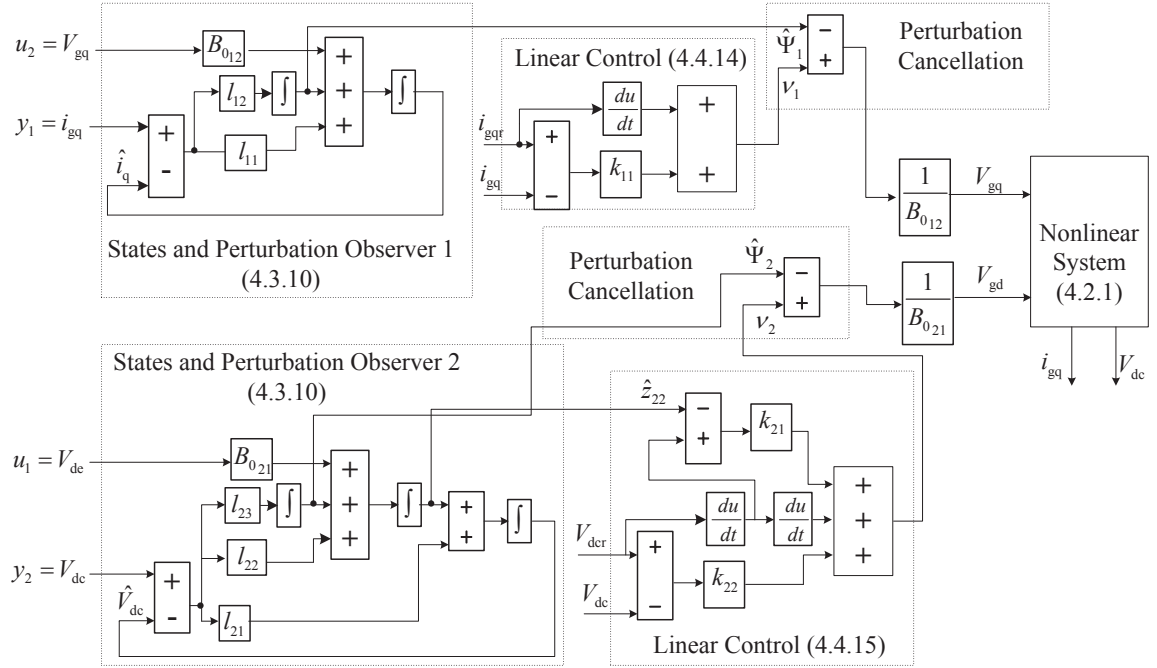
Figure 4.2: Block diagram of nonlinear adaptive controller

is aligned with the grid voltage vector, which result in $E_{\mathrm{gq}} = 0$ and $E_{\mathrm{gd}} = E$ (peak value of the grid voltage).

4.3 NAC Based Controllers Design

This section will present the design of NAC for the grid-side VSC. Following the procedure described in Section 2.3, input/output linearisation of the system (4.2.1) can be obtained as

$$\begin{pmatrix} \dot{y}_1 \\ \ddot{y}_2 \end{pmatrix} = \begin{pmatrix} F_1(x) \\ F_2(x) \end{pmatrix} + B(x) \begin{pmatrix} u_1 \\ u_2 \end{pmatrix} \tag{4.3.1}$$

where

$$F_1(x) = \frac{1}{L_{\text{g}}} E_{\text{gq}} - \frac{R_{\text{g}}}{L_{\text{g}}} i_{\text{gq}} - w i_{\text{gd}} \tag{4.3.2}$$

$$F_2(x) = \frac{3 E_{\text{gd}}}{2 C V_{\text{dc}}} \left(\frac{1}{L_{\text{g}}} E_{\text{gd}} - \frac{R_{\text{g}}}{L_{\text{g}}} i_{\text{gd}} + w i_{\text{gq}} \right)$$
$$- \frac{3 i_{\text{gd}} E_{\text{gd}}}{2 C V_{\text{dc}}^2} \left(\frac{3 E_{\text{gd}} i_{\text{gd}}}{2 C V_{\text{dc}}} - \frac{1}{C} i_{\text{dc2}} \right) \tag{4.3.3}$$
$$- \frac{1}{C} \dot{i}_{\text{dc2}}$$

$$B(x) = \left(\begin{array}{c} B_1(x) \\ B_2(x) \end{array} \right) = \left(\begin{array}{cc} 0 & -\frac{1}{L_{\text{g}}} \\ -\frac{3 E_{\text{gd}}}{2 C L_{\text{g}} V_{\text{dc}}} & 0 \end{array} \right) \tag{4.3.4}$$

$$B(x)^{-1} = \left(\begin{array}{cc} 0 & -\frac{2 C L_{\text{g}} V_{\text{dc}}}{3 E_{\text{gd}}} \\ -L & 0 \end{array} \right) \tag{4.3.5}$$

As $det[B(x)] = \frac{3 E_{\text{gd}}}{2 C V_{\text{dc}} L_{\text{g}}^2} \neq 0$ when $E_{\text{gd}} \neq 0$, that is, $B(x)$ is nonsingular for all operation points. Thus, the FLC controller is obtained as

$$\left(\begin{array}{c} u_1 \\ u_2 \end{array} \right) = B(x)^{-1} \left(\left(\begin{array}{c} -F_1(x) \\ -F_2(x) \end{array} \right) + \left(\begin{array}{c} v_1 \\ v_2 \end{array} \right) \right) \tag{4.3.6}$$

Note FLC controller (4.3.6) is the one proposed in [35], which inlcudes dynamics of E_{de}, i_{dc2} and $\dot{i}_{\text{dc2}}$.

The original system is linearized as

$$\left(\begin{array}{c} \dot{y}_1 \\ \ddot{y}_2 \end{array} \right) = \left(\begin{array}{c} v_1 \\ v_2 \end{array} \right) \tag{4.3.7}$$

$$v_1 = \dot{y}_{1\text{r}} + k_{11} e_1 \tag{4.3.8}$$

$$v_2 = \ddot{y}_{2\text{r}} + k_{21} \dot{e}_2 + k_{22} e_2 \tag{4.3.9}$$

where v_1 and v_2 are inputs of linear systems, k_{11}, k_{21} and k_{22} are gains of linear controller, $y_{1\text{r}}$ and $y_{2\text{r}}$ are the desired output references, and $e_1 = y_{1\text{r}} - y_1$ and $e_2 = y_{2\text{r}} - y_2$ as track errors, the error dynamics are

$$\dot{e}_1 + k_{11} e_1 = 0 \tag{4.3.10}$$

$$\ddot{e}_2 + k_{21}\dot{e}_2 + k_{22}e_2 = 0 \tag{4.3.11}$$

Based on equation (6.3.5) and (4.3.1), perturbation terms $\Psi_1(x)$ and $\Psi_2(x)$ are defined as:

$$q_1 : \begin{cases} \Psi_1(x) &= F_1(x) + (B_1(x) - B_{0_1}) \begin{bmatrix} u_1 \\ u_2 \end{bmatrix}, \\ B_{0_1} &= \begin{bmatrix} 0 & -\frac{1}{L_{g0}} \end{bmatrix} \end{cases}$$

$$\tag{4.3.12}$$

$$q_2 : \begin{cases} \Psi_2(x) &= F_2(x) + (B_2(x) - B_{0_2}) \begin{bmatrix} u_1 \\ u_2 \end{bmatrix} \\ B_{0_2} &= \begin{bmatrix} -\frac{3E_{de}}{2C_0 L_{g0} V_{dc}} & 0 \end{bmatrix} \end{cases}$$

where C_{g0} and L_{g0} are nominal values of C and L respectively, and B_{0_1} and B_{0_2} are nominal control gains. Here we assume E_{gd} is measurable.

Defining the state variables as $z_{11} = y_1$, $z_{12} = \Psi_1$; $z_{21} = y_2$, $z_{22} = y_2^{(1)}$, $z_{23} = \Psi_2$, two subsystems q_1 and q_2 are given as

$$q_1 : \begin{cases} \dot{z}_{11} &= \Psi_1(x) + B_{0_1} \begin{bmatrix} u_1 \\ u_2 \end{bmatrix}, \\ z_{11} &= y_1 \end{cases}$$

$$\tag{4.3.13}$$

$$q_2 : \begin{cases} \dot{z}_{21} &= z_{22} \\ \dot{z}_{22} &= \Psi_2(x) + B_{0_2} \begin{bmatrix} u_1 \\ u_2 \end{bmatrix} . \\ z_{21} &= y_2 \end{cases}$$

For sub-systems q_1 and q_2, one second-order SPO and one third-order SPO like (6.3.12) are designed to estimate the perturbations $\hat{z}_{12} = \hat{\Psi}_1$, $\hat{z}_{23} = \hat{\Psi}_2$, and states $\hat{z}_{11}, \hat{z}_{21}$ and $\hat{z}_{22}$. By using the estimated perturbations to compensate the real perturbations, output feedback control laws for sub-systems q_1 and q_2 can be obtained as following:

$$q_1 : \begin{cases} u_2 &= \frac{1}{B_{0_{12}}}(-\hat{z}_{12} + v_1) \\ v_1 &= k_{11}(z_{11r} - z_{11}) + \dot{z}_{11r} \end{cases} \tag{4.3.14}$$

$$q_2 : \begin{cases} u_1 & = & \frac{1}{B_{0_{21}}} \left(-\hat{z}_{23} + v_2 \right) \\ v_2 & = & \ddot{z}_{21\mathrm{r}} + k_{22}(z_{21\mathrm{r}} - z_{21}) \\ & & + k_{21}(\dot{z}_{21r} - \hat{z}_{22}) \end{cases} \tag{4.3.15}$$

The final control law represented by physical variables, such as voltages, currents, resistances, inductances and capacitances, are given as following:

$$\begin{cases} u_1 = \frac{2C_0 L_{\mathrm{g}0} V_{\mathrm{dc}}}{3E_{\mathrm{gd}}} [-\hat{\Psi}_2 + k_{22}(V_{\mathrm{dcr}} - V_{\mathrm{dc}}) \\ \qquad + k_{21}(\dot{V}_{\mathrm{dcr}} - \hat{z}_{22}) + \ddot{V}_{\mathrm{dcr}}] \\ u_2 = -L_{\mathrm{g}0}[-\hat{\Psi}_1 + k_{11}(i_{\mathrm{gqr}} - i_{\mathrm{gq}}) + \dot{i}_{\mathrm{gqr}}] \end{cases} \tag{4.3.16}$$

Note that the NAC proposed only requires the nominal value of parameters of $L_{\mathrm{g}0}$ and C_0, measurements of two output variables i_{gq} and V_{dc}, and the grid voltage E_{gd}. It is worth noting that performance is only degraded slightly when the measurement of the grid voltage E_{gd} is replaced by its nominal value E_{gd}, which can be demonstrated in the simulation studies. This further reduces the requirement of measurements of the NAC.

To clearly illustrate the principle of the proposed NAC, a block diagram is shown in Fig. 4.2.

4.4 Simulation Results

Simulation studies are carried out to test the improvement of FRTC provided by the proposed NAC, comparing with the VC and FLC. A 1-MW variable-speed WT connected with a transformer rated at 1.2 MVA given in [35] is used, which is conceived to step-up voltage of 690 V to the grid voltage of 110 KV. The transformer is represented as an ideal transformer with a series resistor $R_{\mathrm{g}} = 1.98 \times 10^{-3}$ Ω and inductor $L_{\mathrm{g}} = 6.31 \times 10^{-5}$ H at the low voltage side of the transformer. The dc-link capacitor value is $C = 0.1340$ F. Some grid codes, such as in Irish and UK, require that the WECS should export the active power to the grid in proportion to the retained grid voltage level, to prevent the grid-side VSC from damaging by the large inrush current caused by the voltage sags [23], [24]. Thus the machine-side DC-link current $i_{\mathrm{dc}2}$ is assumed to be reduced at the same time when the grid

voltage is reduced [35]. Based on the power balance equation (4.2.1) and assuming $i_{\text{dc1}} = i_{\text{dc2}}$ at the steady state, for a given $E_{\text{de}}(t)$, i_{dc2} is obtained as:

$$i_{\text{dc2}_{\text{step}}} = \frac{3i_{\text{gd}}(0)}{2V_{\text{dc}}(0)} E_{\text{gd}}(t) \tag{4.4.1}$$

The rated operating condition of the WECS is: $V_{\text{dc}(0)} = 1050$ V, $E_{\text{gd}(0)} = 690$ V, $i_{\text{gd}}(0) = -966.18$ A and $i_{\text{gq}}(0) = 0$. Based on this rating condition, the maximum step of i_{dc2} corresponding to the maximum expected change in the machine-side DC-link current for this drive rating is -1000 A. To limit the rate of the disturbance, the step change of the i_{dc2} is smoothed via a low-pass filter during the simulation study.

Parameters of NACs for subsystem q_1 and q_2 are designed based on pole-placement and listed as following:

q_1 : observer: $\alpha_{11} = 1.6 \times 10^4$, $\alpha_{12} = 6.4 \times 10^7$, $\epsilon_1 = 1 \times 10^{-2}$; controller: $k_{11} = 1.6 \times 10^3$.

q_2 : observer: $\alpha_{21} = 6 \times 10^3$, $\alpha_{22} = 1.2 \times 10^7$, $\alpha_{23} = 8 \times 10^9$, $\epsilon_2 = 1 \times 10^{-2}$; controller: $k_{21} = 8.5 \times 10^2$, $k_{22} = 3 \times 10^5$.

Note that FLC uses same controller parameters as the NAC, and both VC and FLC use same parameters as reported in [35].

4.4.1   Fault Ride-Through Capability

FRTC of the WECS with NAC is tested at different reduced grid voltage levels and corresponding step disturbances i_{dc2}. In each case, the grid voltage is set at different levels and kept at that level for the whole test period, then a step disturbance i_{dc2} is calculated via equation (4.4.1) and applied at $t = 20$ ms.

Responses of different controllers to 15% of nominal grid voltage and a -150 A step disturbance i_{dc2} are shown in Fig. 4.3. From Fig. 4.3, FLC and NAC can reach their steady states within 10 ms and VC cannot damp the oscillations even after 120 ms, while their control efforts are almost same, as shown in Fig. 4.3. Response of perturbation estimation is shown in Fig. 4.4.
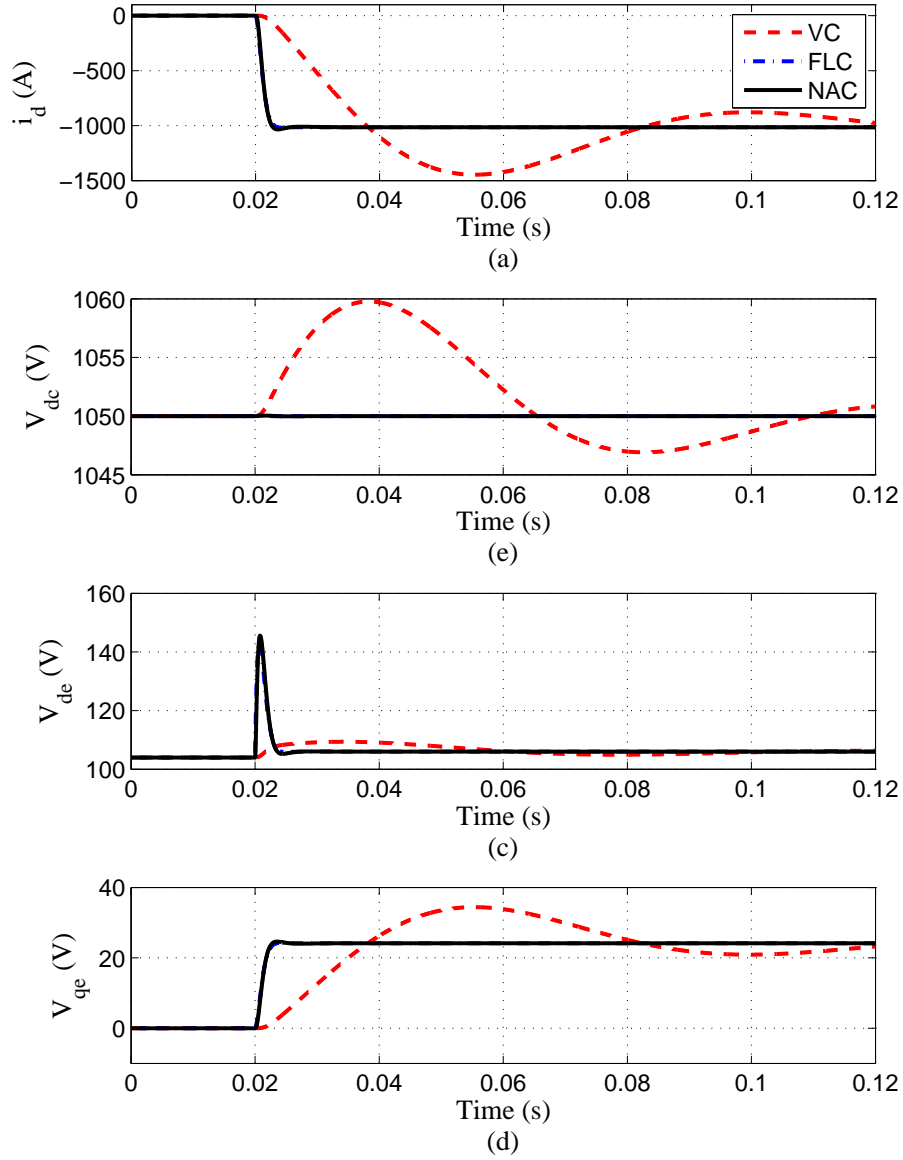
Figure 4.3: Responses to 15% nominal grid voltage and -150 A step perturbation in the DC-link current i_{dc2}
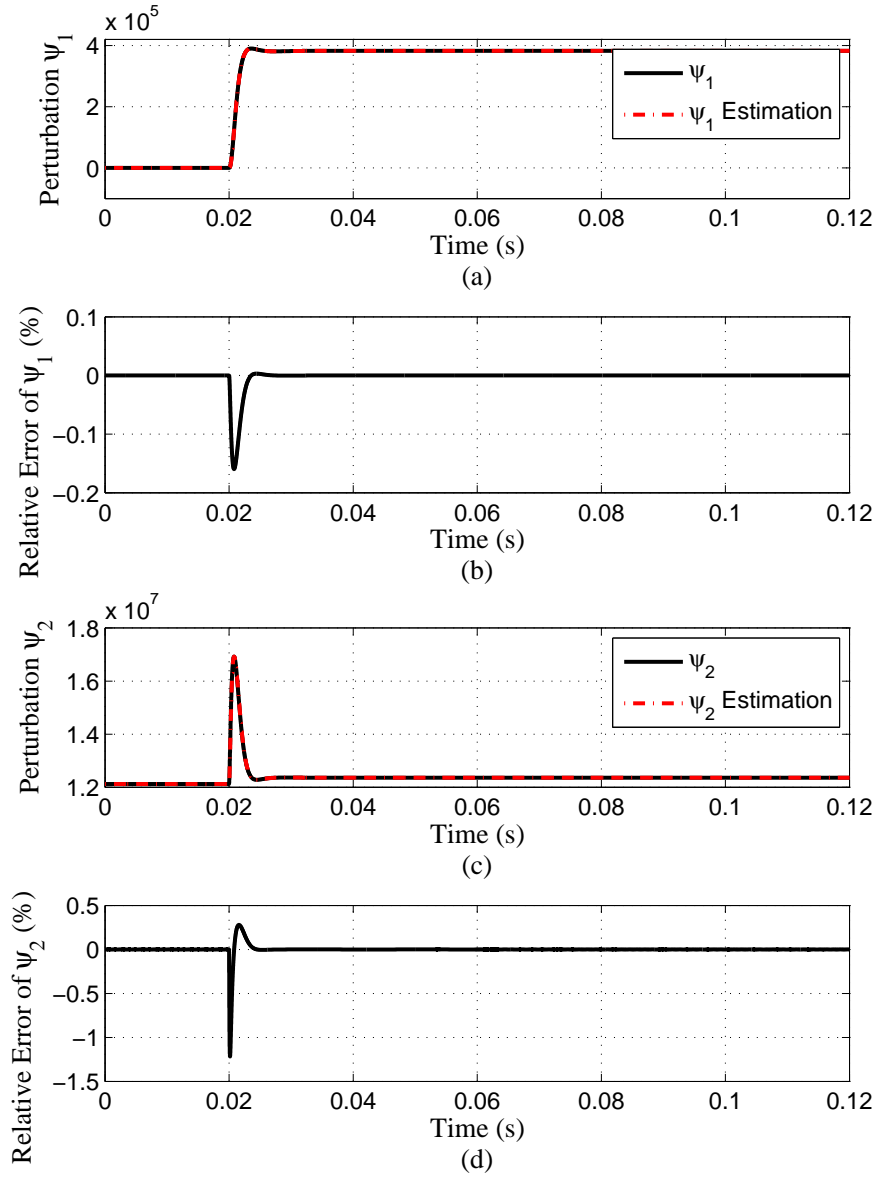
Figure 4.4: Estimate of perturbation $\Psi_{1,2}(x)$ at 15% nominal grid voltage level and -150 A step perturbation in the DC-link current i_{dc2}
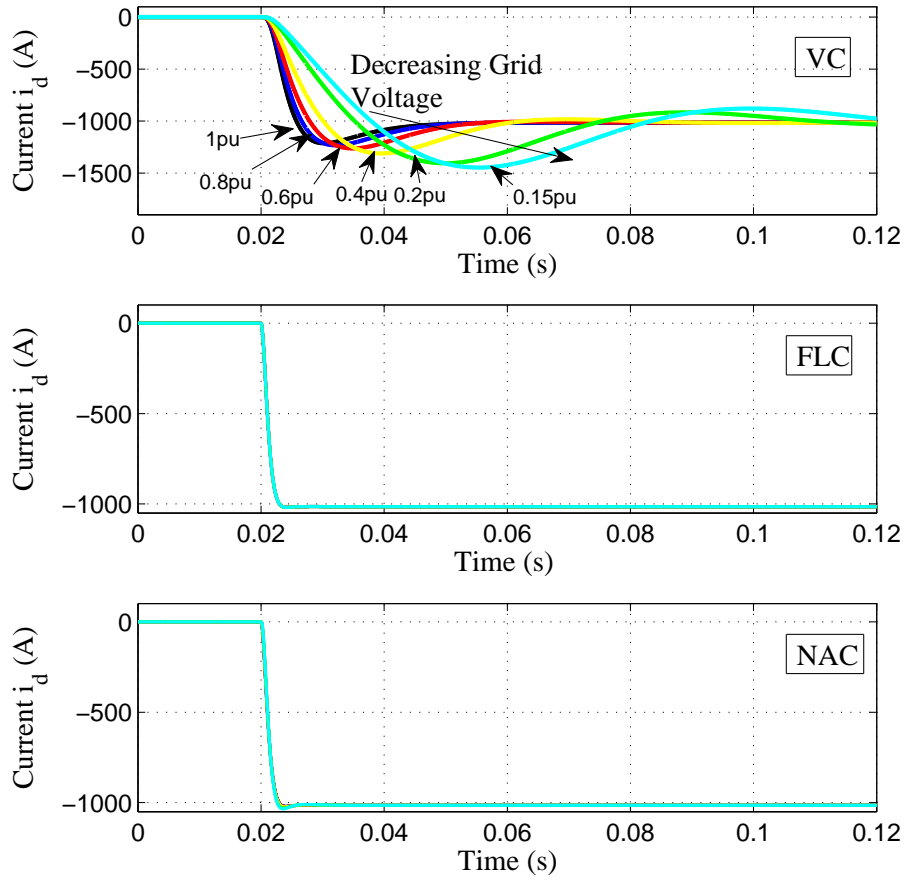
Figure 4.5: Response of grid current i_{gd} to different grid voltage levels and corresponding step disturbances of machine side DC-link current i_{dc2}
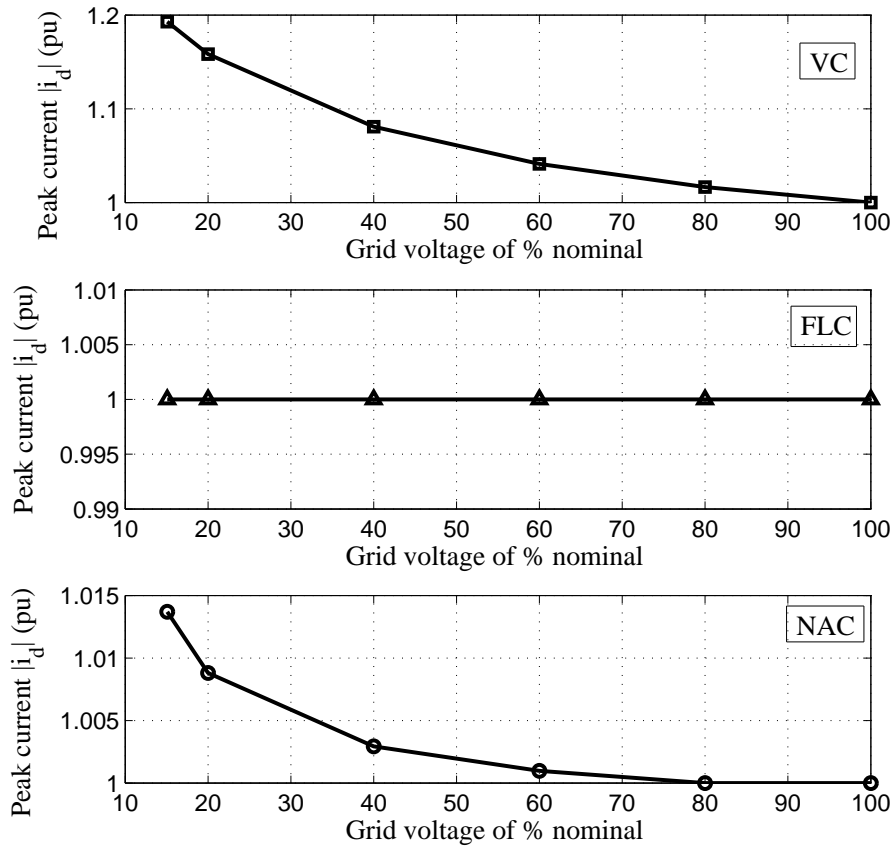
Figure 4.6: Peak magnitude i_{gd} (in pu) to different grid voltage levels and corresponding step disturbances of machine side DC-link current i_{dc2}
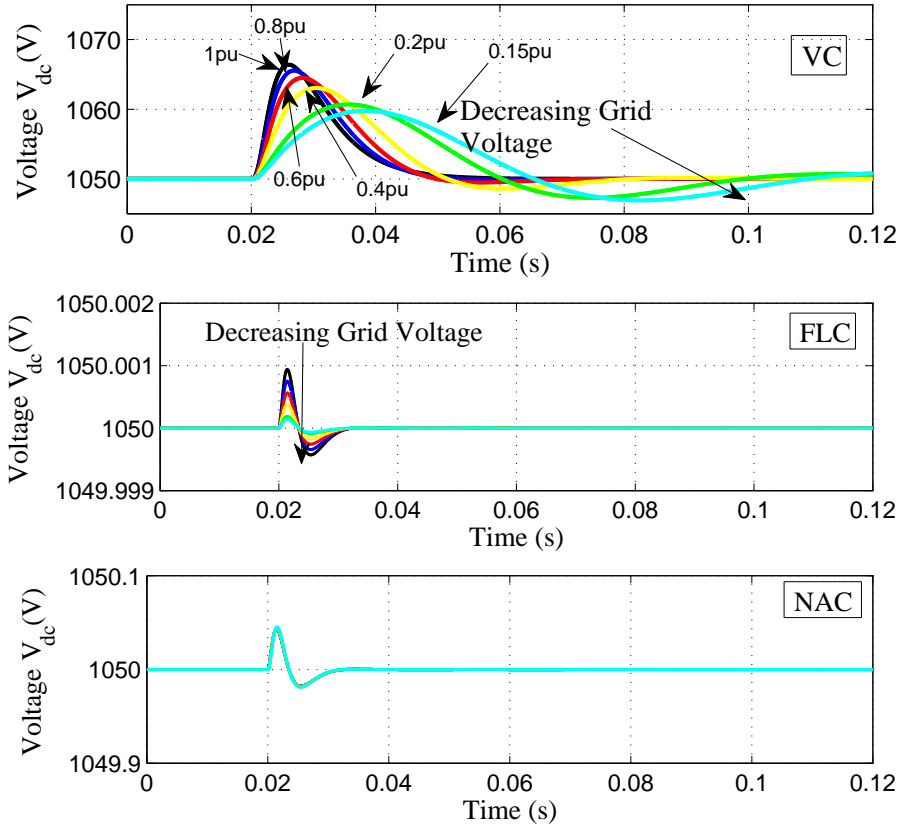
Figure 4.7: Response of DC-link Voltage V_{dc} to different grid voltage levels and corresponding step disturbances of machine side DC-link current i_{dc2}

Responses to different grid voltage levels reducing from 100% to 15% of its nominal, including grid current i_{gd} and its peak magnitude, and DC-link voltage V_{dc}, are shown in Fig. 4.5, 4.6 and 4.7, respectively. Note that the nominal peak magnitudes of i_{d} of three controllers are different.

As shown in Fig. 4.5, the response of i_{gd} provided by VC degrades significantly when the grid voltage level is reduced from 100% to 15% of the nominal, with an increase of peak value of $|i_{\mathrm{gd}}|$ from 1200 A to 1400 A. Both FLC and NAC can provide a consistent transient response of i_{gd} for varying grid voltage levels, and smaller overshoot and faster transient response comparing with the VC. As shown in Fig. 4.6, the peak value of $|i_{\mathrm{gd}}|$ is increased by approximately 20% under the VC, while FLC and NAC can almost have the peak value of $|i_{\mathrm{gd}}|$ unchanged. Fig. 4.7 shows that the dynamic of DC-link voltage V_{dc} by VC has bigger deviation and longer transient period than FLC and NAC which result in almost consistent transient dynamic.

This is because the VC is designed based on one operation point and not capable of providing optimal performance for varying operation points [35]. Both the FLC and the NAC can achieve satisfactory performance at different grid voltage levels as the nonlinear dynamics caused by variation of operation points and external disturbances have been compensated. The FLC can almost keep the peak value of $|i_{\mathrm{gd}}|$ unchanged, and the decrease is less than 0.5%. The peak value of $|i_{\mathrm{gd}}|$ is little affected by the varying grid voltage levels under the NAC. The peak of $|i_{\mathrm{gd}}|$ decreases by approximately 2%. The FLC behaves a little better than the NAC because the NAC relies on state and perturbation observer which has estimation error. However, the FLC is based on full state feedback and accurate system model, the NAC only employs the output feedback and does not require the detailed system model.

4.4.2 Robustness Against Parameter Uncertainties

When there is a fault in the transmission or distribution grid, the resistance R_{g} and inductance L_{g} values of the grid may change significantly [35]. Several simulations are performed for plant-model mismatches of R and L with $\pm20\%$ uncertainties. All tests are under 15% of nominal grid voltage and a corresponding -150 A
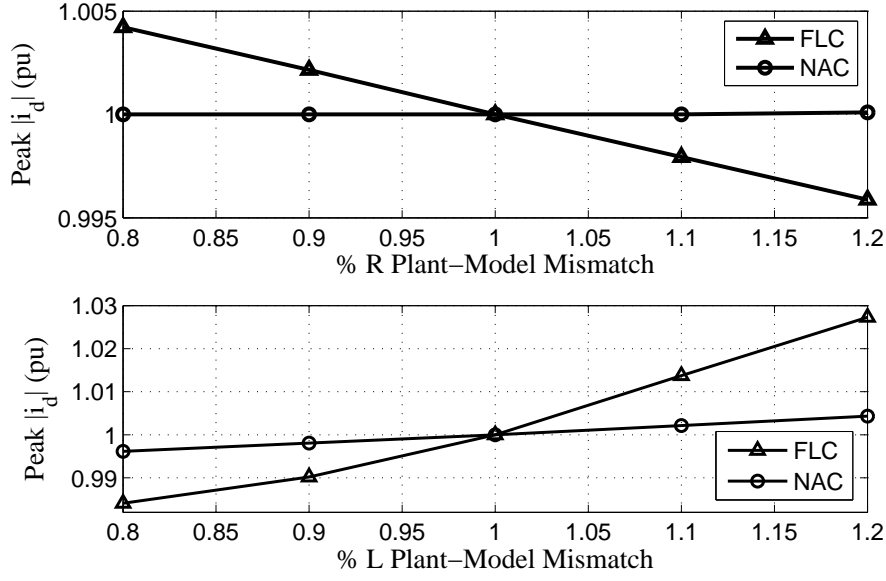
Figure 4.8: The peak current i_{gd} (in pu) to a -150 A step change in the DC-link current i_{dc2} and a 15% nominal grid voltage for plant-model mismatches in the range of $\pm 20\%$ (one parameter changes and others keep constant)

step disturbance i_{dc2} at 0.02 s.

As shown in Fig. 4.8, the peak grid current $|i_{\text{gd}}|$ (in pu) controlled by NAC is almost not affected, while FLC results in small range of variation, i.e., less than 0.5% to R and 2% to L, respectively. Responses to mismatch of L and R changing at the same time are shown in Fig. 4.9. The magnitude of $|i_{\text{gd}}|$ changes around 3% under the FLC and almost does not change under the NAC. This is because the proposed NAC estimates all uncertainties and does not need the accurate system model and thus has better robustness than FLC which requires an accurate system model.

4.4.3 Robustness Against Measurements Noises

The proposed NAC is an output feedback controller and only needs three measurements, the DC-link voltage V_{dc}, grid-voltage E_{gd} and q-axis grid current i_{q}. However, FLC requires all state variables and other measurements to calculate the system nonlinearities. To test the robustness against the measurement noise, white
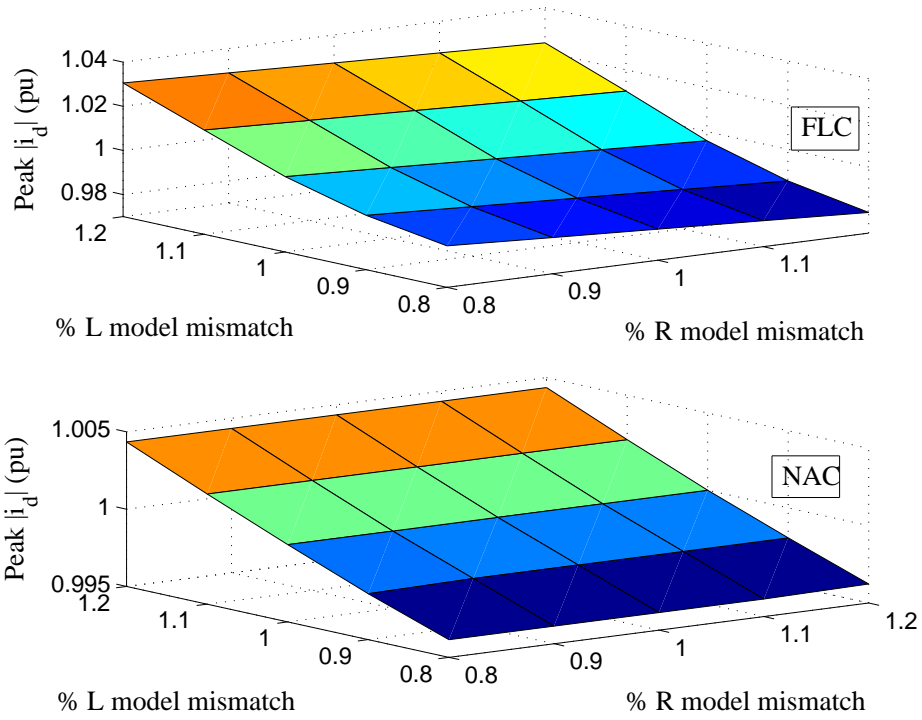
Figure 4.9: The peak current i_{gd} (in pu) to a -150.7 A in the DC-link current i_{dc2} at 15% nominal grid voltage for plant-model mismatches in the range of $\pm 20\%$ (different parameters may change at the same time)
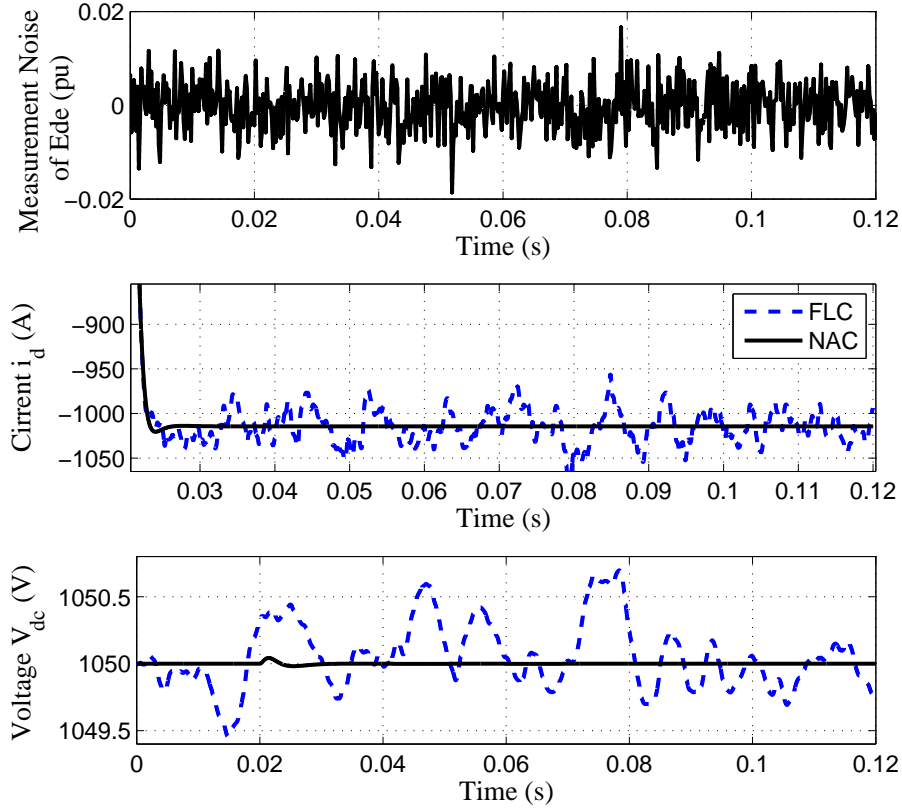
Figure 4.10: Response to -1000 A maximum step change of the DC-link current i_{dc2} at nominal grid voltage E_{gd} and E_{gd} with $\pm 2\%$ white noise of nominal grid voltage

noise of $\pm 2\%$ of nominal grid voltage has been injected into E_{gd} and E_{gq}, respectively. As shown in Fig. 4.10 and Fig. 4.11, the performance of the NAC is not affected by the noise in the measurement of grid voltage, but the performance of the FLC has been degraded greatly. It is worth noting that the grid voltage only contributes to the control gain of the NAC, the measurement of the grid voltage E_{gd} could be further replaced by its nominal value, which can further reduce one measurement. Similar results can be obtained by injecting noise into i_{dc2}.

4.4.4   Robustness Against Machine-Side Disturbances

Above simulation studies are carried out to test the start-up process of the wind turbine, i.e., the WECS is operated under different grid voltage levels with zero
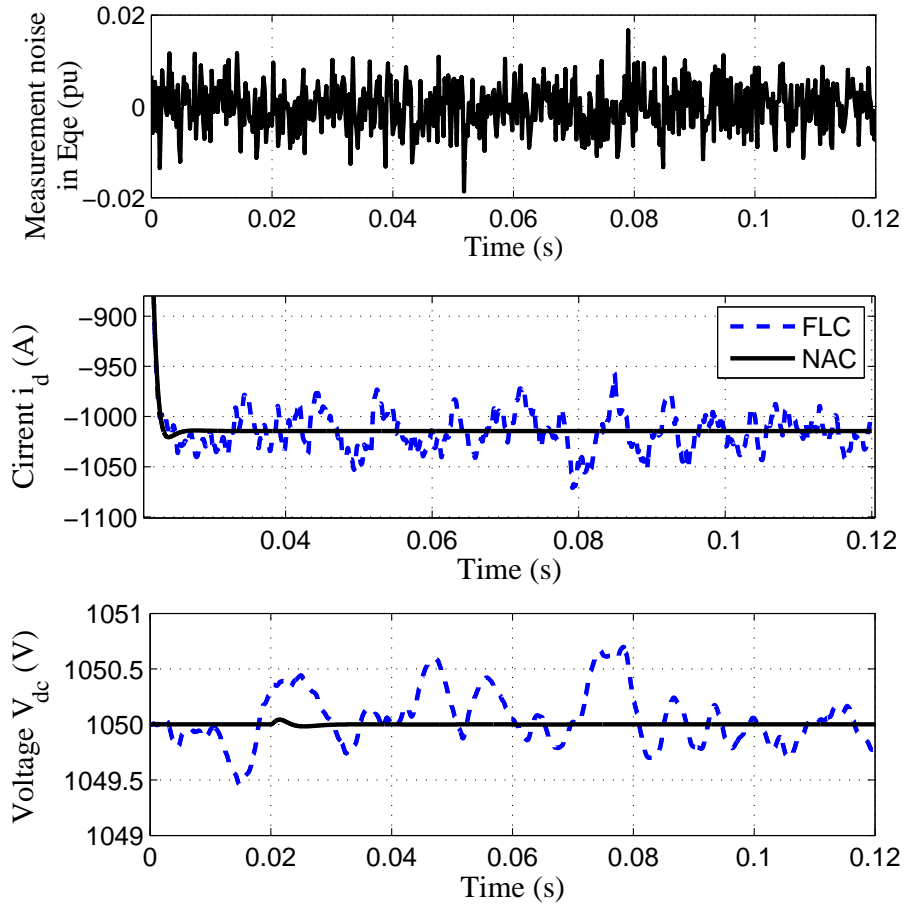
Figure 4.11: Response to -1000 A maximum step change of the DC-link current i_{dc2} at nominal grid voltage E_{gd} and E_{gq} with $\pm 2\%$ white noise of nominal grid voltage

output power and then the maximum expected power injection from the WECS is applied according to reduced grid voltage level, as used in [29,35]. However, during the normal operating condition, the grid voltage dips can occur at any time and the machine-side output power (i_{dc2}) cannot be reduced simultaneously due to the slow behavior of wind turbine in change of its generation output. Several measures, including change of the operation mode or installation of additional hardware devices, can be used to improve the FRTC via consuming the energy and thus accelerating the reduction of the active power output of the WECS during the voltage dips, such as dissipating via braking chopper, or storing in the inertia of the WECS and additional energy storage devices [25], [99], [100].

To test performance of the proposed NAC considering the impact of the slow dynamic of the wind turbine output, the following six test cases are designed: 1) i_{dc2} is reduced after 15 ms; 2) i_{dc2} will not be reduced; 3) i_{dc2} will be reduced based on a real GE wind turbine with ramp rate 0.45 p.u./sec [101]; 4) i_{dc2} is set as $-600 + 50sin(20t)$ A; 5) i_{dc2} will be increased at the same time; 6) i_{dc2} will be changed after 15 ms and based on a real GE wind turbine with ramp rate 0.45p.u./sec.

The first test case is set as: the grid voltage E_{gd} dips from 690 V to 414 V at 0.02 s and the DC-link current i_{dc2} increases from -1000 A to -600 A after 15 ms delay. This 15 ms time delay is introduced to simulate the response time of the WECS after detecting the grid fault and taking actions, assuming additional measures such as braking chopper or energy storage [25], [99], [100]. Fig. 4.12 shows that larger overshoots and longer recovery time of current and voltage are obtained by the VC comparing with the FLC or NAC, and that the NAC obtains the best performance.

In the second case, it is assumed that the output of the WECS will not be reduced during the period of voltage dips. The test case is set as: the grid voltage dips from 690 V to 103.5 V (0.15pu) at 0.02 s and the dc-link current i_{dc2} keeps at -1000 A. From Fig. 4.13, it can be seen that the NAC can obtain smaller current and voltage overshoots and shorter recovery time than the FLC, while the VC cannot maintain a stable current and voltage response.

The third case simulates a real GE wind turbine with power ramp rate 0.45 p.u./sec [101] and is set as follows. The grid voltage E_{gd} reduces from 690 V to

Figure 4.12: Transient response to the grid voltage E_{gd} dipping from 690 V to 414 V at 0.02 s and the DC-link current i_{dc2} increases from -1000 A to -600 A after 15 ms delay
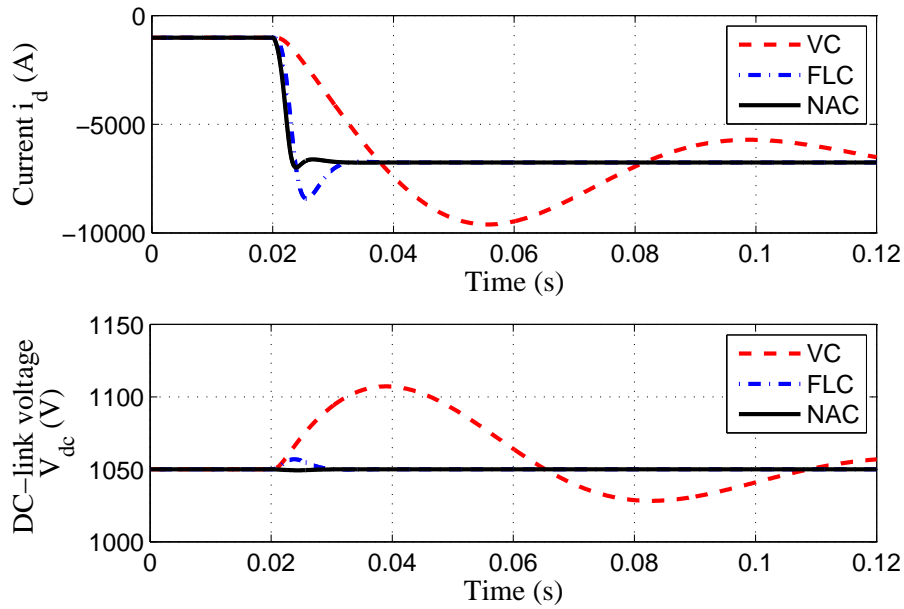
Figure 4.13: Transient response to the grid voltage dips from 690 V to 103.5 V at the 0.02 s and the dc-link current i_{dc2} keeps at -1000 A

552 V (0.8pu) at 0.02 s and stay at 552 V for 600ms, and then recovers from 552 V to 690 V at 0.62 s. The DC-link current i_{dc2} is changed based on the ramp rate limit 0.45 p.u./sec: increasing from -1000 A at 0.02 s to -800A at 0.465 s, then decreasing from -800 A at 0.62 to -1000 A at 1.065 s. It can be seen from Fig. 4.14 that the NAC has the lowest current and voltage overshoots and shortest recovery time comparing the VC and the FLC.

The fourth case is to test the fluctuation of the input wind power by injecting i_{dc2} as $-600 + 50sin(20t)$ A and reducing E_{gd} from 690 V to 414 V at 0.02 s. Note that no control action is assumed to be taken at the machine side to reduce the active power output during the grid voltage dips. From Fig. 4.15(a), it can be seen that both the FLC and the NAC have smaller current and voltage overshoots comparing with the VC. A constant DC-link voltage V_{dc} is critical for both grid-side and machine-side converters, but the V_{dc} cannot be kept constant and without oscillation during the whole period of test under the VC.

The worst case is that the machine-side power injection may rise at the instant of grid voltage dips, due to the intermittent wind power. In the case five, the grid voltage E_{gd} dips from 690 V to 414 V at 0.02 s, but the DC-link current i_{dc2} increases from -600 A to -700 A at the same time. This case is to simulate a sudden increment of the wind speed at the same instant of the grid voltage dips. The simulation results are shown in Fig. 4.16, it can be seen that both the FLC and NAC achieve a satisfactory performance. Compared with the FLC and NAC, larger current and voltage overshoots and slower transient responses are obtained by the VC.

To test the transient performance when grid voltage sags appears and disappears, the sixth test case is set as: the grid voltage E_{gd} dips from 690 V to 414 V at 0.02 s, lasts for 0.05s and then increases from 414 V to 690 V at 0.07 s, and the DC-link current i_{dc2} increases from -1000 A to -600 A at 0.035 s, then decreases from -600 A to -1000 A at 0.085 s. The 15 ms delay is introduced to simulate the response time of the WECS corresponding to the fault, assuming additional devices installed for dissipating or storing the energy of the WECS. Note that this case is similar to the third case in which a real power ramp rate is considered. Fig. 4.17 shows that larger overshoots and longer recovery time of current and voltage are obtained by the VC
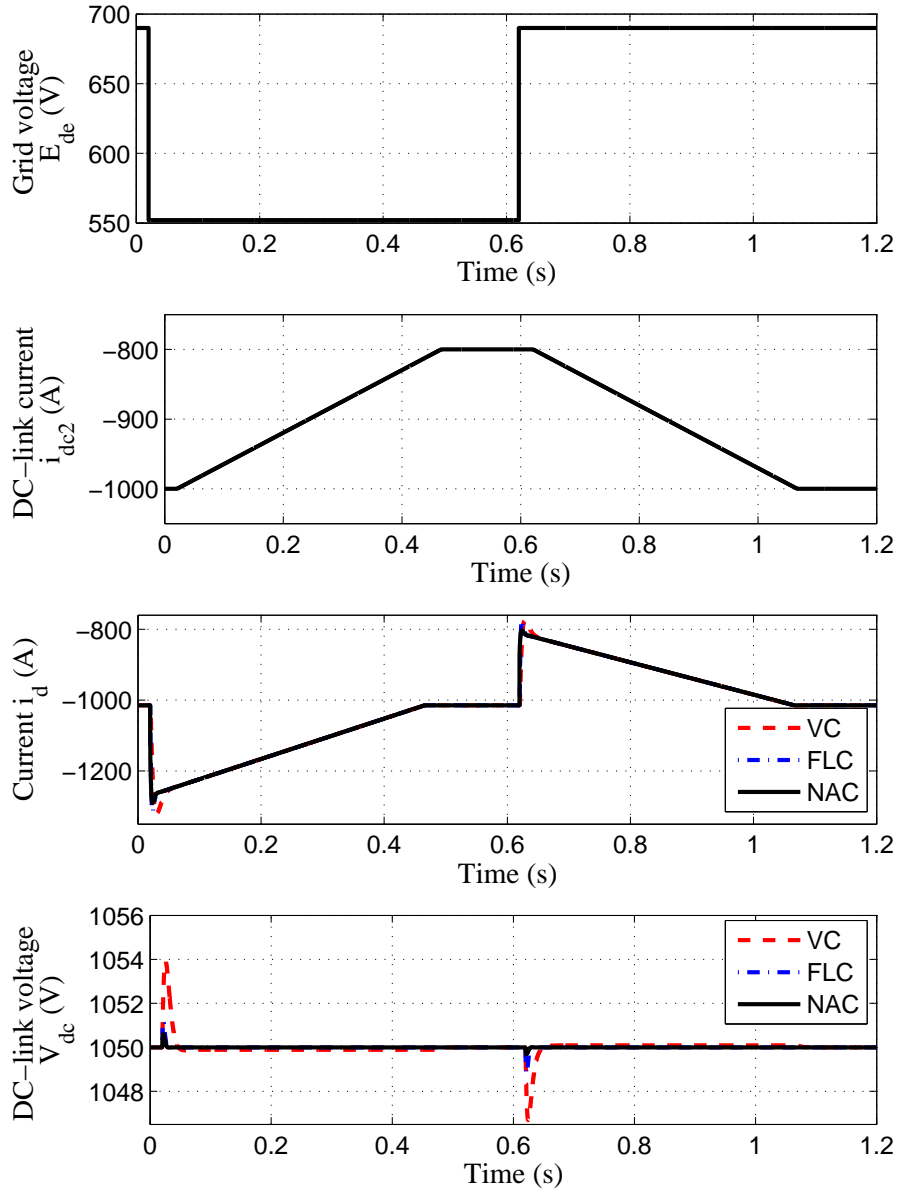
Figure 4.14: Transient response to the grid voltage E_{gd} dipping from 690 V to 552 V at 0.02 s, then increasing from 552 V to 690 V at 0.62 s, and the DC-link current i_{dc2} increases from -1000 A at 0.02 s to -800A at 0.465 s, then decreases from -800 A at 0.62 to -1000 A at 1.065 s
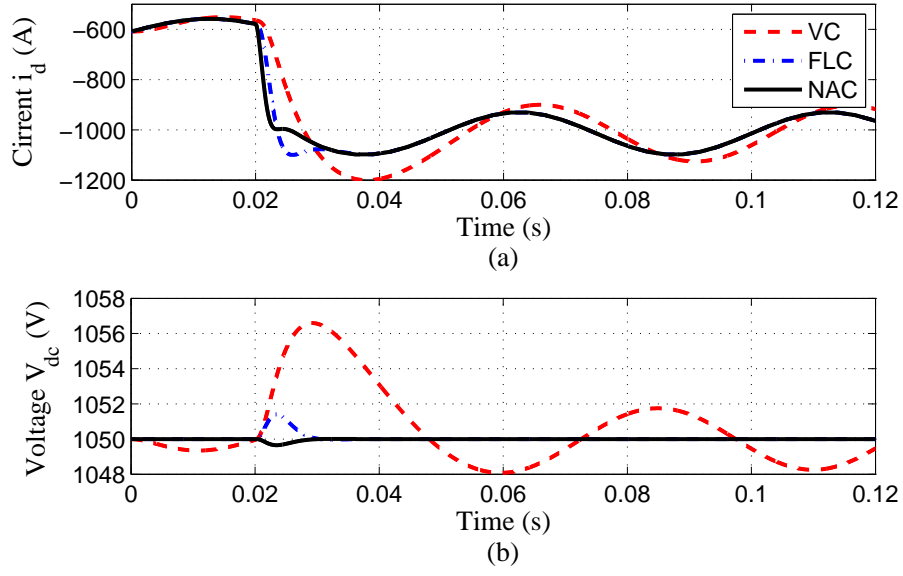
Figure 4.15: Transient response to a $-600 + 50sin(20t)$ A dc-link current i_{dc2} is $-600 + 50sin(20t)$ A and the grid voltage E_{gd} dipping from 690 V to 414 V at 0.02 s
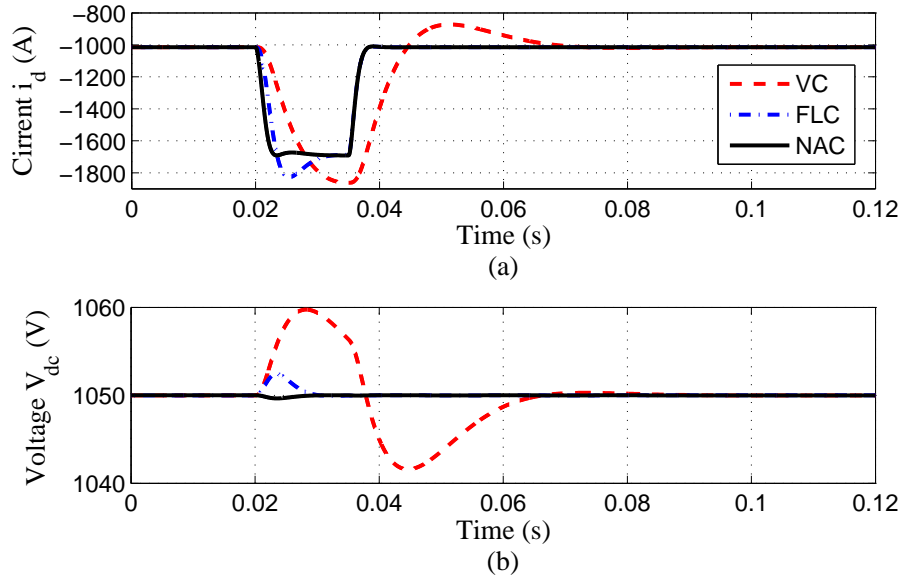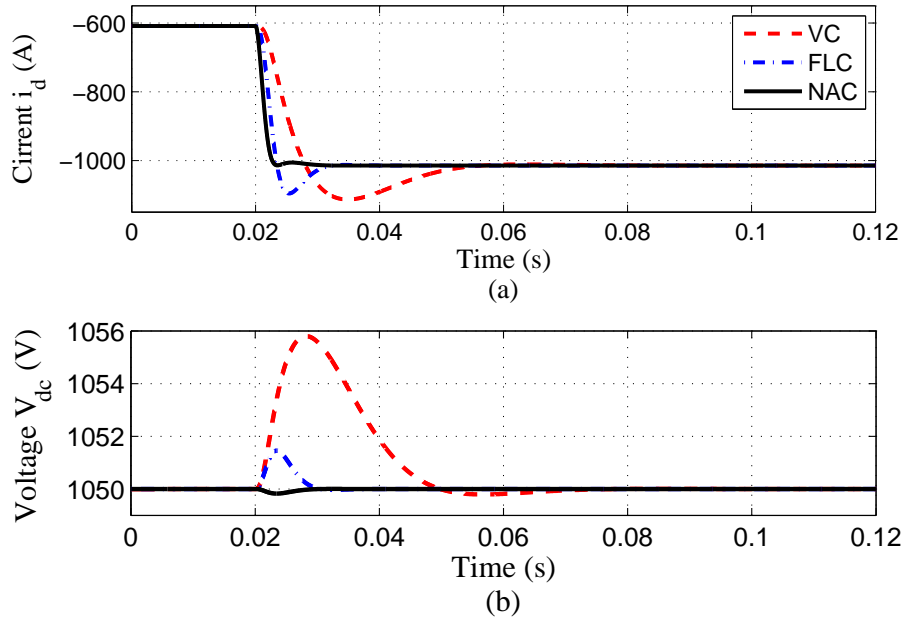

Figure 4.16: Transient response to the grid voltage E_{gd} dipping from 690 V to 414 V at 0.02 s, and the DC-link current i_{dc2} increasing from -600 A to -700 A at the same time.
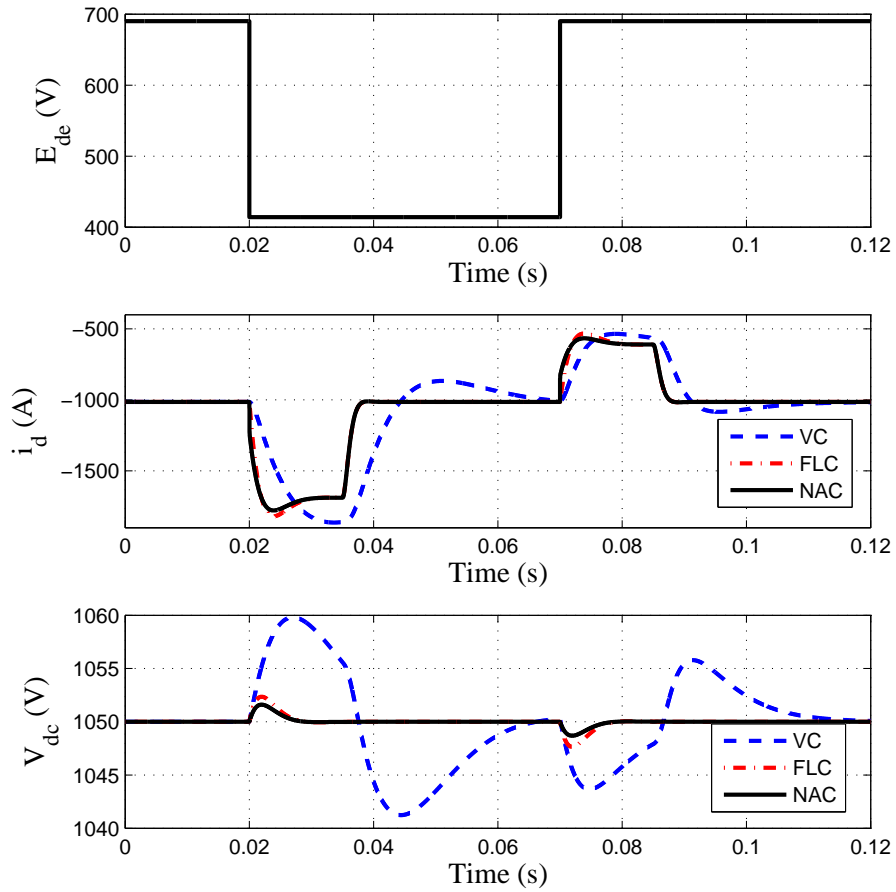
Figure 4.17: Transient response to the grid voltage E_{gd} dipping from 690 V to 414 V at 0.02 s, then increasing from 414 V to 690 V at 0.07 s, and the DC-link current i_{dc2} increases from -1000 A to -600A at 0.035 s, then decreases from -600 A to -1000 A at 0.085 s

comparing with the FLC or the NACand the NAC obtains the best performance.

4.5   Conclusions

This chapter has investigated a novel NAC for the grid-side converter to improve the FRTC of a full-rated converter based variable-speed wind turbine. The proposed NAC adopts a state and perturbation observer to obtain real-time estimates of system states and perturbations, which include all uncertainties and time-varying nonlinearities and external disturbances, especially the dynamics caused by grid voltage dips and the variable wind power inputs, and the original nonlinearities. The proposed controller outperforms the conventional VC by providing a global optimal performance across the whole operation region. It does not require the detailed system model and parameters and is an output feedback controller. Thus, it has a relatively simpler controller and much better robustness than the FLC when there are model uncertainties and unknown disturbances. Comparing with other nonlinear adaptive methods, the proposed NAC can deal with time-varying uncertain dynamics.

Performance enhancement has been tested by simulation studies at different voltage dip's levels, and various uncertainties, including model mismatch, measurement noises and time-varying wind power inputs. Simulation results have shown that the proposed NAC can provide satisfactory performances with smaller current and voltage overshoots during grid fault and better robustness against uncertainties, compared with the VC and the model-based FLC.

Finally, the proposed NAC can be easily extended to enhance the FRTC of other types of energy sources which are integrated with the grid with a full-rated back-to-back converter, such as solar photovoltaic and energy storage. Further studies will focus on carrying the experimental test of the proposed method on a hardware prototype and investigating its potentiality of dealing with asymmetrical voltage sags.

Chapter 5

Coordinated Nonlinear Adaptive Control of Machine-side and Grid-side Converter of PMSG-WT

5.1 Introduction

In the wind energy conversion system (WECS) shown in Fig. 1.2, it consists two voltage-source converters (VSCs), i.e., machine-side converter (MSC) and grid-side converter (GSC). The GSC is responsible to maintain the DC-link voltage and deliver active power to the grid, whereas the objective of the MSC is controlling output power of the generator. The control of the MSC and GSC can be decoupled when the DC-link voltage can be well regulated. In addition, for the machined side, as the electromagnetic torque has much faster response than the mechanical torque, thus the decoupled control between wind turbine (WT) and generator can be applied in Region 3.

For the control of the MSC, several literatures regarding maximum power point tracking (MPPT) have been published, such the use of wind turbine (WT) speed control or torque control in Region 2, e.g., [11, 68, 102]. Some previously published works proposed pitch control methods to limit the extracted wind power when wind speed is above the rated speed, e.g., [83, 103–105]. However, there are relatively

few works that suggest control strategies based on varying operating condition for WTs. In this chapter, the control strategy of the MSC includes mechanical rotation speed control at speeds lower than rated rotor speed and pitch control at rated power area.

Numerous designed controllers have been studied for the control of the GSC, i.e., conventional vector control (VC) with proportional-integral (PI) loops, feedback linearisation control (FLC), sliding mode control and nonlinear adaptive control (NAC) [29, 35, 63, 91]. Although these advanced control methods have provided satisfactory performances of the GSC and enhanced the fault ride-through capability (FRTC) of the permanent magnet synchronous generator based WT (PMSG-WT), all these work assumed that the generator output can be looked as a current source which can be reduced simultaneously and proportionally to the drop of the grid voltage. In addition, the dynamics of the machine-side during the tests of different voltage dips have not been considered in [29, 35, 91] or have been simply simulated by varying current in [63]. However, a real WT cannot be simply replaced by a current source. To investigate the performances of the PMSG-WT under normal and fault operation conditions, it requires the coordinated control for the GSC and MSC of the PMSG-WT.

This chapter presents a coordinated nonlinear adaptive control (CNAC) of the MSC and GSC of the PMSG-based WECS. This chapter integrates the author's work reported in Chapter 2-4. Under normal operation condition, for MSC control, the MPPT operation is realized by mechanical rotation speed control and stator current control in Region 2. The proposed MPPT control method in Chapter 2 is employed in this chapter. It requires mechanical rotation speed to track its optimal value. In Region 3, the power is limited by mechanical rotation speed control and stator current control. The mechanical rotation speed and electromagnetic torque are required to track their rated values, respectively. For GSC control, in Region 2 and 3, the active and reactive power injected into grid is regulated using DC-link voltage control and grid current control loop designed in Chapter 4. Under the grid voltage dips, the GSC control strategy is the same as it in normal operation. For the MSC control strategy, only pitch control is applied. The pitch control is employed to help

enhance the FRTC of the WECS. The extracted wind power can be reduced through increasing pitch angle. The proposed control strategy realises the control objectives without requiring the accurate system model and full state measurements in different operating regions, provides high robustness against parameter uncertainties, and enhances the FRTC of the WECS.

5.2 Coordinated Control System

The proposed control block diagram for the WECS is shown in Fig. 5.1.

In normal operation, for the MSC, the MPPT algorithm presented in Chapter 2 is applied to extract the maximum wind power when the WECS operates in Region 2. In Region 2, the mechanical rotation speed w_{m} is required to track its optimal reference w_{mopt}, while the d-axis stator current reference i_{mdr} is 0. When the WECS operates in Region 3, the pitch control developed in Chapter 3 is employed to limit the captured power from wind. In this region, the extracted wind power should be maintained at rated value. It in turn requires both the mechanical rotation speed w_{m} and mechanical torque T_{m} to keep at their rated values, respectively. For the GSC, the active power P_{m} generated by the PMSG is first transferred to DC-link, then from DC-link to grid. Two VSCs are controlled separately and the dynamic of the PMSG-WT and the power grid is decoupled via the DC-link when dc-Link voltage V_{dc} is always maintained at its reference V_{dcr}. In order to regulated the dc-link voltage V_{dc}, a novel dc-link voltage V_{dc} control strategy has been developed in Chapter 4. In addition, q-axis GSC current reference i_{gqr} is 0, d-axis grid voltage E_{gd} is rated voltage, and q-axis grid voltage E_{gq} is 0. The injected grid reactive power Q_{g} should be around 0 when GSC controller can realize its control objectives.

Under the grid voltage dips, the GSC controller is the same as it in normal operation. Both the active and reactive current references for the grid-side converter given by the FRTC requirement has not been applied in GSC controller. Hence, the dc-link voltage V_{dc} should be kept constant. It will not absorb excess active power. For the MSC, the generating active power is still delivering to the grid during the grid voltage E_{gd} dips. The generated active power P_{m} is the same as the injected
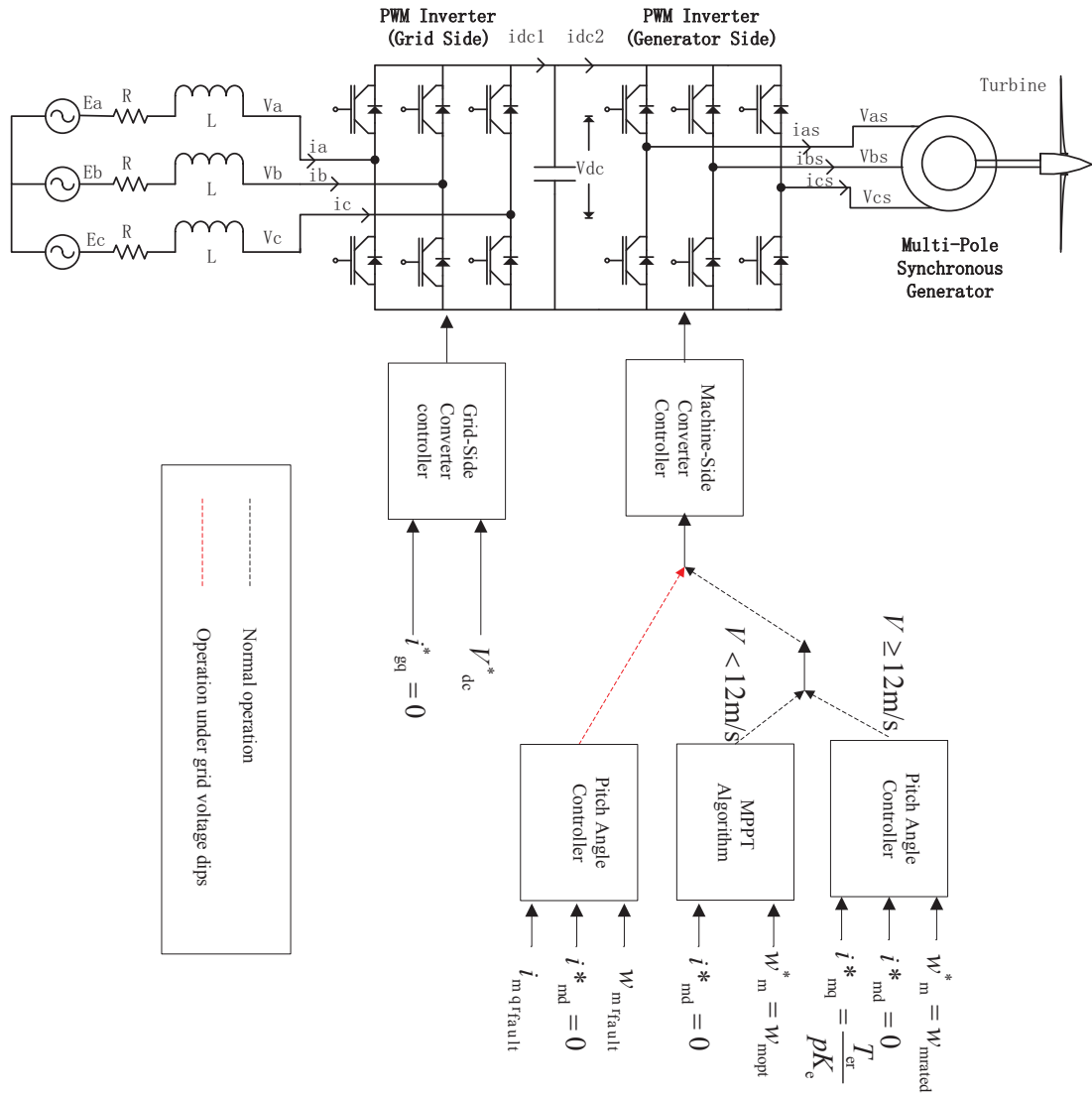
Figure 5.1: Control block diagram under normal operation and grid voltage dips

grid active power P_{g} when MSC controller does not take any control action. The GSC current i_{gd} will increase rapidly when the dc-link voltage V_{dc} is well regulated and the grid voltage dips. This may damage converters or other power electronic devices. Hence, the WECS should export the active power to the grid in proportion to the retained grid voltage level, to prevent the grid-side VSC from damaging by the large inrush current caused by the voltage sags [23], [24]. The generated active power P_{m} should reduce at the same time when the grid voltage is reduced. For this reason, pitch control is applied to assist in reducing generated active power P_{m} in this chapter, thus enhancing FRTC or low voltage rid-through capability (LVRTC). When the pitch control is applied in MSC under the grid voltage dips, the mechanical rotation speed reference $w_{\text{mr}_{\text{fault}}}$ is the same as before. However, the electromagnetic torque reference $T_{\text{er}_{\text{fault}}}$ is in proportion to the retained grid voltage level shown in (5.2.1).

$$T_{\text{er}_{\text{fault}}} = \frac{E_{\text{gd}}(t)}{E_{\text{gd}}(0)} T_{\text{er}_{\text{normal}}} \tag{5.2.1}$$

where $T_{\text{er}_{\text{fault}}}$ is the electromagnetic torque reference applied in pitch control after the grid voltage dips; $E_{\text{gd}}(t)$ is the value of the grid voltage after the grid voltage dips; $E_{\text{gd}}(0)$ is the rated grid voltage; and $T_{\text{er}_{\text{normal}}}$ is the electromagnetic torque in normal condition.

According to (3.2.2), the q-axis stator current reference $i_{\text{mqr}_{\text{fault}}}$ applied in pitch control is $\frac{T_{\text{er}_{\text{fault}}}}{pK_e}$.

5.3   Simulation Results

To verify the effectiveness of the proposed NAC, a series of simulations studies are carried out and the VC and FLC are employed for comparison. A 2-MW WECS is investigated. The parameters of the PMSG-WT system are R=39 m, ρ=1.205 kg/m^3, rated wind speed V_{r}=12 m/s, J_{tot}=10000 kg·m^2, K_e=136.25 V.s/rad, p=11, $L_{\text{md}} = 5.5 \times 10^{-3}$ H, $L_{\text{mq}} = 3.75 \times 10^{-3}$ H, and R_{s}=50 $\mu\Omega$; the parameters of the grid are $L_{\text{g}} = 6.31 \times 10^{-5}$ H, $C = 0.06$ F, and $R_{\text{g}} = 1.98 \times 10^{-3}$ Ω.

Parameters of NACs for WECS are the same as listed in Chapter 2-4. Note that

FLC uses same controller parameters as the NAC, moreover the FLC uses the full state feedback and the exact parameters.

5.3.1   Time-Varying Wind

Ramp-Change Wind

The responses of the WT to ramp-change wind is shown in Fig. 5.2 and 5.3. Wind speed is shown in Fig. 5.2 (a). In the Region 3, the VC achieves the worst tracking performance of the mechanical rotation speed w_{m} with the longest recovery time and biggest overshoots among the three controllers. The maximum tracking error ($\frac{w_{\mathrm{m}}-w_{\mathrm{mr}}}{w_{\mathrm{mr}}} \times 100\%$) is more than 15% under the VC. The tracking error of the w_{m} still exists under the FLC. The best tracking performance is provided by the NAC. In Region 2, both the FLC and NAC provide satisfactory tracking performances of the w_{m}. However, the VC still has tracking error of the w_{m}. It can be explained that the VC designed based one operation point and cannot provide optimal performance in the whole operation region. The FLC exists tracking error in Region 3, because the $\frac{dV}{dt}$ is not known in the FLC design. In Region 2, the FLC know the full state measurements and accurate system parameters. Hence, the FLC can achieve high performance.

In Region 3, the pitch angle β_{ref} changes with the varying wind speed to limit the extracted wind power. In Region 2, the β_{ref} will keep constant. The response of the β_{ref} is shown in Fig. 5.2 (d). In Region 3, the VC requires more time to reach the expected β_{ref} comparing with the FLC or NAC.

Fig. 5.3 (e)-(h) show the responses of the power coefficient C_p, T_{m} and T_{e} to ramp-change wind. The expected wind power can be achieved by the NAC even when wind speed varies, that both the VC and FLC cannot provide, as shown in Fig. 5.3 (h).

The responses of the PMSG to ramp-change wind is shown in Fig. 5.4 and 5.5. Fig. 5.4 (a) and (b) show that larger overshoots and longer recovery time of the stator voltages V_{mdq} are obtained by the VC comparing with the FLC or NAC, moreover the NAC obtain the best performance. The stator current i_{md} can be well tracked by

Figure 5.2: Responses of the WT to ramp-change wind. (a) Wind speed V. (b) Mechanical rotation speed w_m. (c) Relative error of mechanical rotation speed w_m. (d) Pitch angle reference β_r.

Figure 5.3: Responses of the WT to ramp-change wind. (e) Power coefficient C_p. (f) Mechanical rotation torque T_m. (g) Electromagnetic torque T_e. (h) Mechanical power P_w.
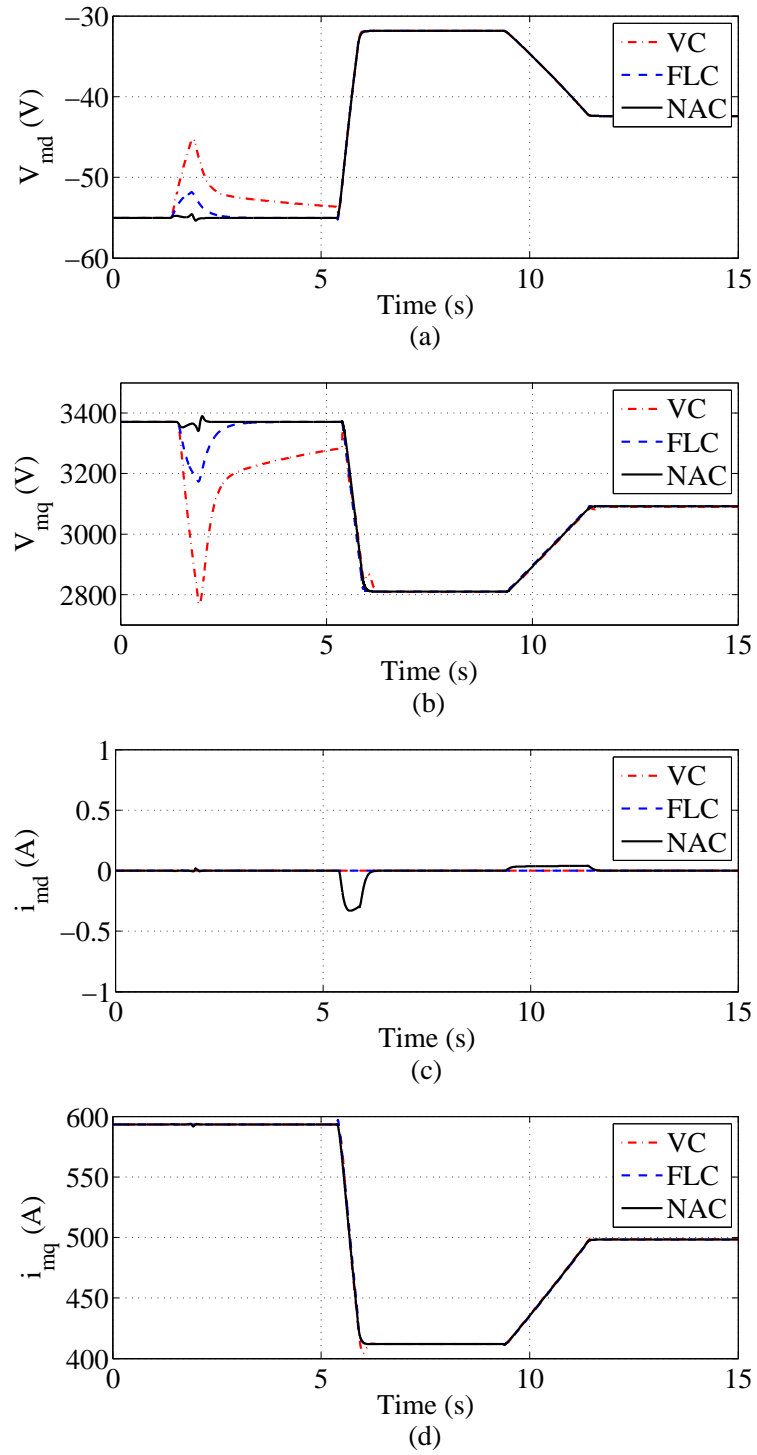
Figure 5.4: Responses of the PMSG to ramp-change wind. (a) d-axis voltage V_{md}. (b) q-axis voltage V_{mq}. (c) d-axis current i_{md}. (d) d-axis current i_{mq}.
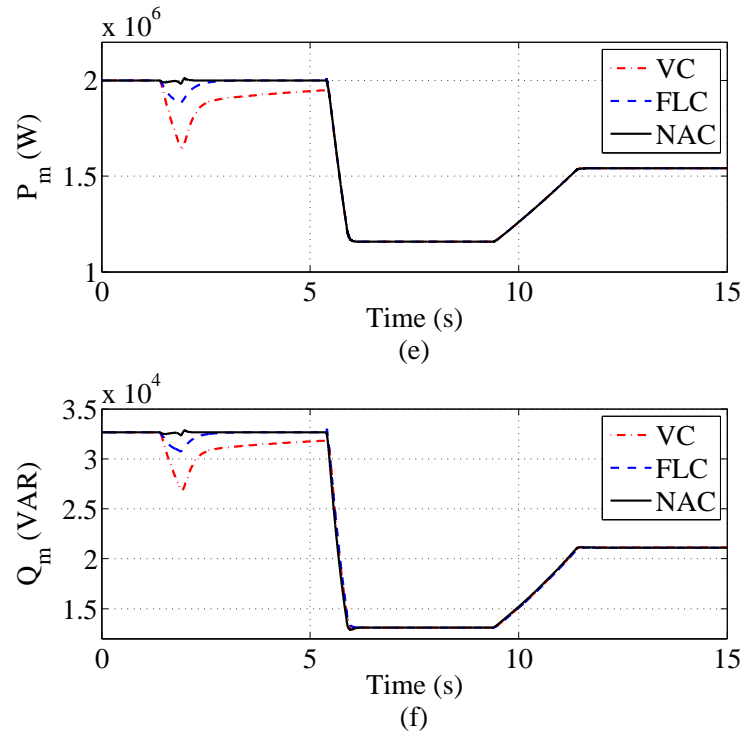
Figure 5.5: Responses of the PMSG to ramp-change wind. (e) Active generating power P_m. (f) Reactive generating power Q_m.
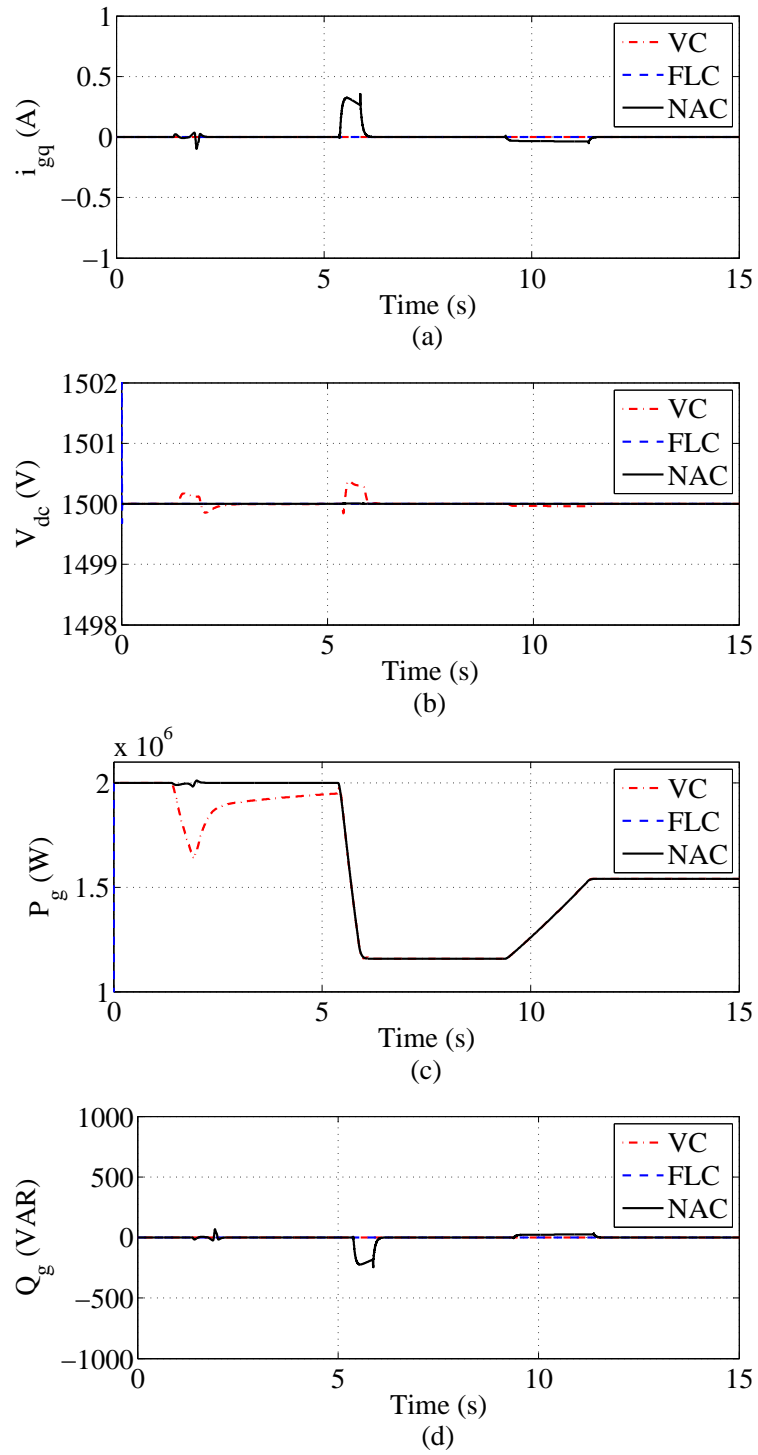
Figure 5.6: Responses of the grid to ramp-change wind. (a) q-axis current i_{gq}. (b) DC-link Voltage V_{dc}. (c) Active grid power P_g. (d) Reactive grid power Q_g.
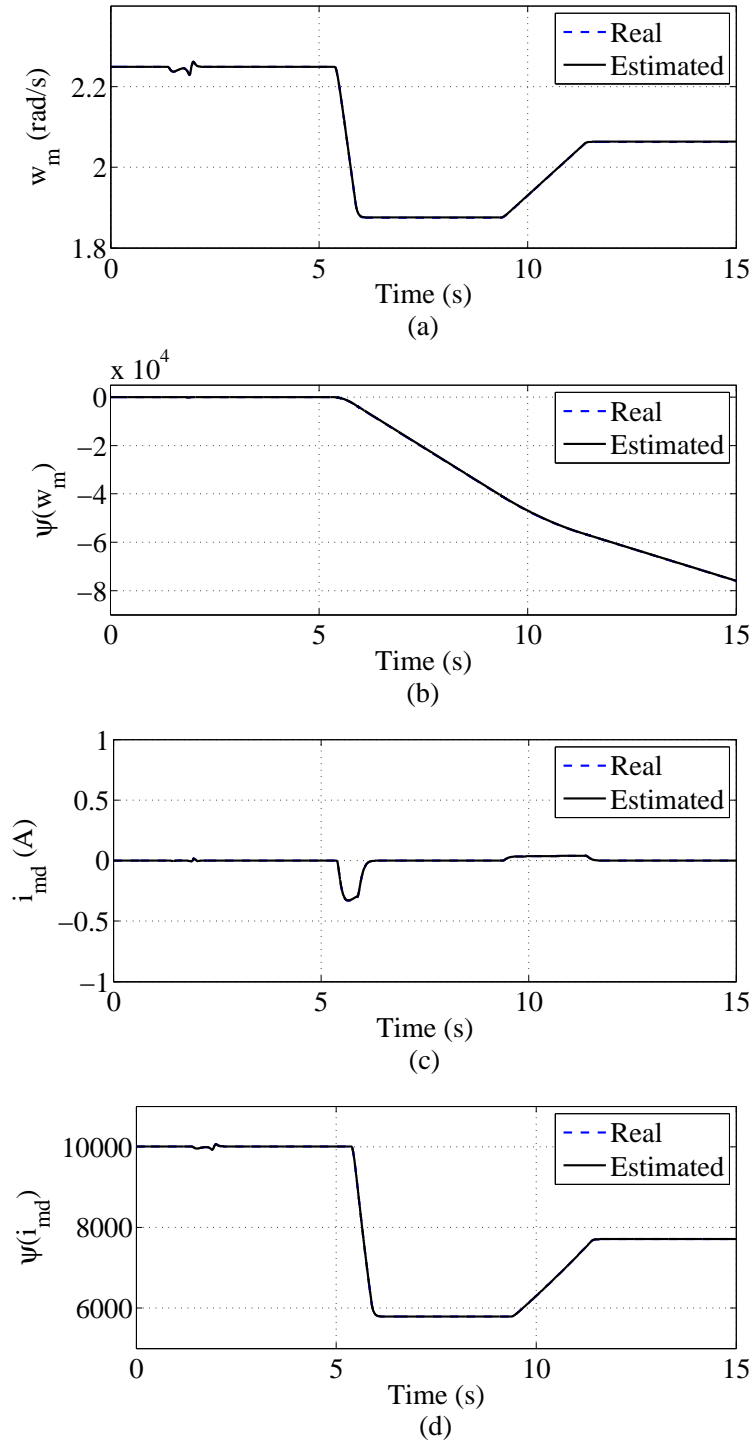
Figure 5.7: Estimates of states and perturbations to ramp-change wind
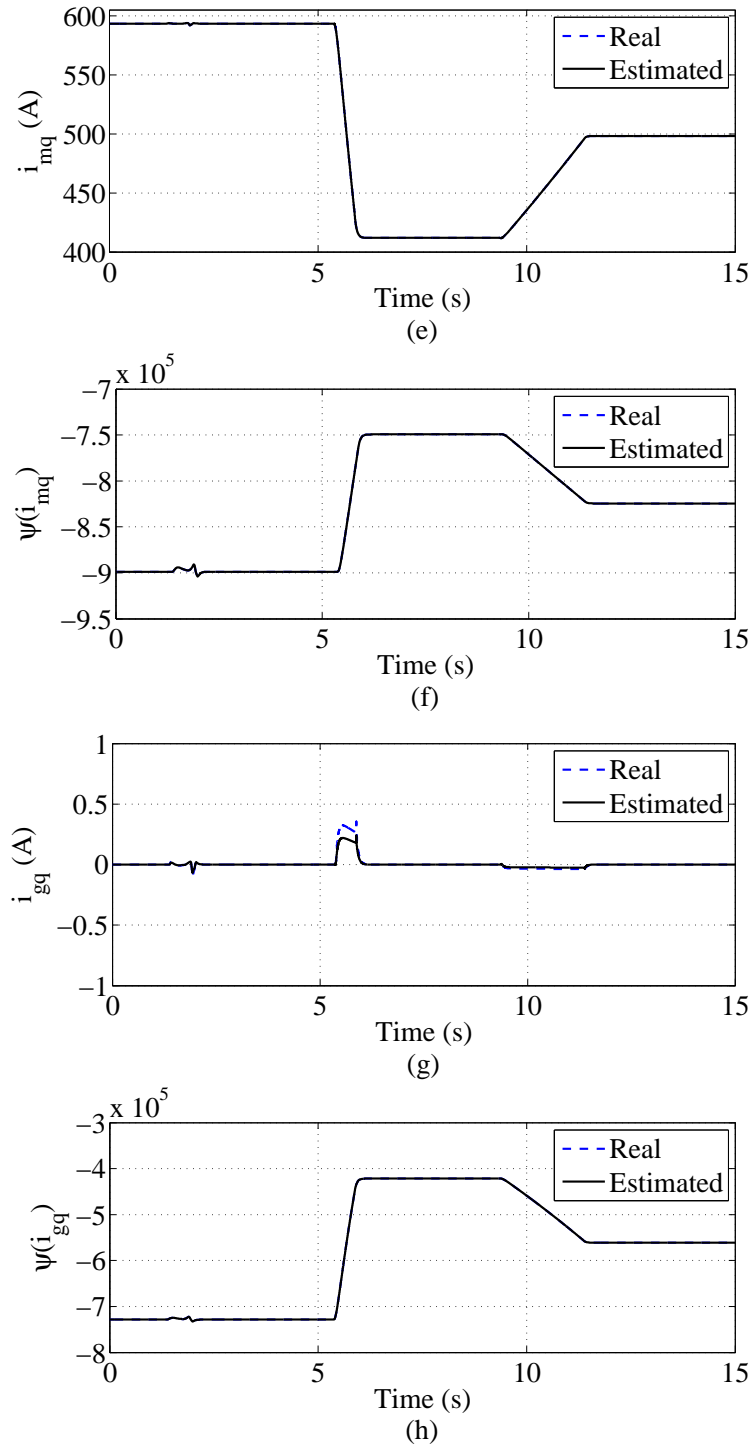
Figure 5.8: Estimates of states and perturbations to ramp-change wind
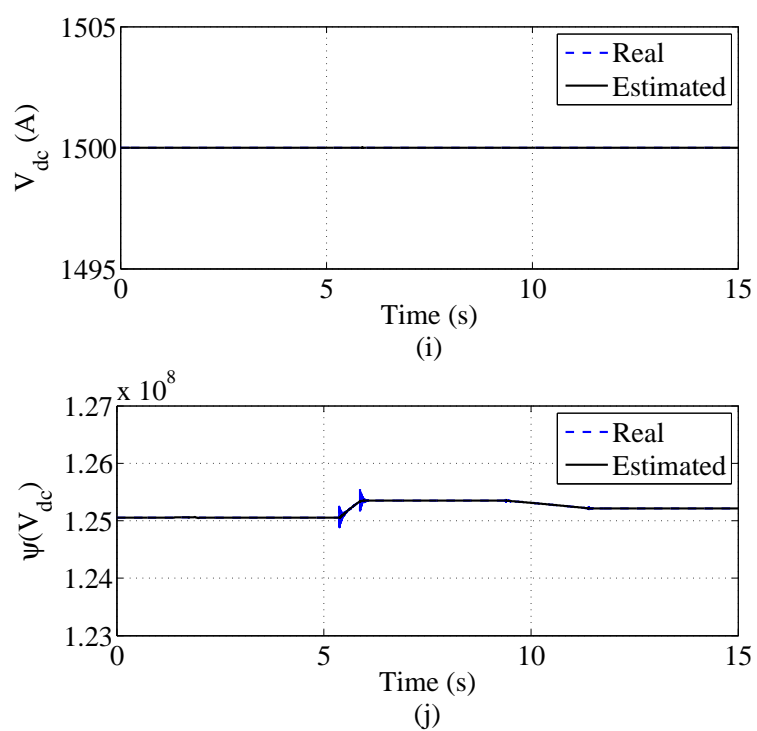
Figure 5.9: Estimates of states and perturbations to ramp-change wind

all controllers shown in Fig. 5.4 (c). Fig. 5.4 (d) shows the response of i_{mq}. The active power P_{m} and reactive power Q_{m} of the PMSG are shown in Fig. 5.5 (e) and (f), respectively.

The responses of the grid to ramp-change wind is shown in Fig. 5.6. Fig. 5.6 (a) show that the q-axis current i_{gq} can be almost maintained at 0 by all controllers. The VC has larger overshoots and longer recovery time of the DC-link voltage V_{dc}. The injected active power P_{g} and reactive power Q_{g} of the grid are shown in Fig. 5.6 (c)-(d), respectively.

During the whole operating period, the NAC can always keep consistent responses of P_{m}, Q_{m}, P_{g} and Q_{g}. The performances of the VC and FLC are affected by the varying wind speed. Note that the FLC uses the full state feedback except $\frac{dV}{dt}$ in Region 3 and extract parameters of the system, but the NAC is without requiring the details of the system information and extract parameters.

The estimates of the states and perturbations are shown in Fig. 5.7-5.9. It can be seen from Fig. 5.7-5.9 that, both the states and perturbations can be well estimated by the observers. The estimated perturbations including nonlinearities, uncertainties and disturbance are used for compensation for the real perturbation.

Random Wind

The responses of the WT to random wind is shown in Fig. 5.10 and 5.11. Wind speed is shown in Fig. 5.10 (a). When wind speed is time-varying, both the VC and FLC cannot provide satisfactory tracking performances of the mechanical rotation speed w_{m} shown in Fig. 5.10 (b). The NAC keeps w_{m} around reference mechanical rotation speed. The maximum tracking errors ($\frac{w_{\text{m}} - w_{\text{mr}}}{w_{\text{mr}}} \times 100\%$) are approximately 13% and 5% under the VC and FLC, respectively. Fig. 5.11 (f)-(h) show the responses of mechanical torque T_{m}, electromagnetic torque T_{e}, and mechanical power P_{w}, respectively. The responses of the PMSG to random wind is shown in Fig. 5.12 and 5.13. During the whole operating period, the NAC can always keep consistent responses of P_{m} and Q_{m}. The performances of the VC and FLC are affected by the time-varying wind speed. It can be seen from Fig. 5.15-5.17 that, the observers can well estimate the states and perturbations to compensate the real perturbations.
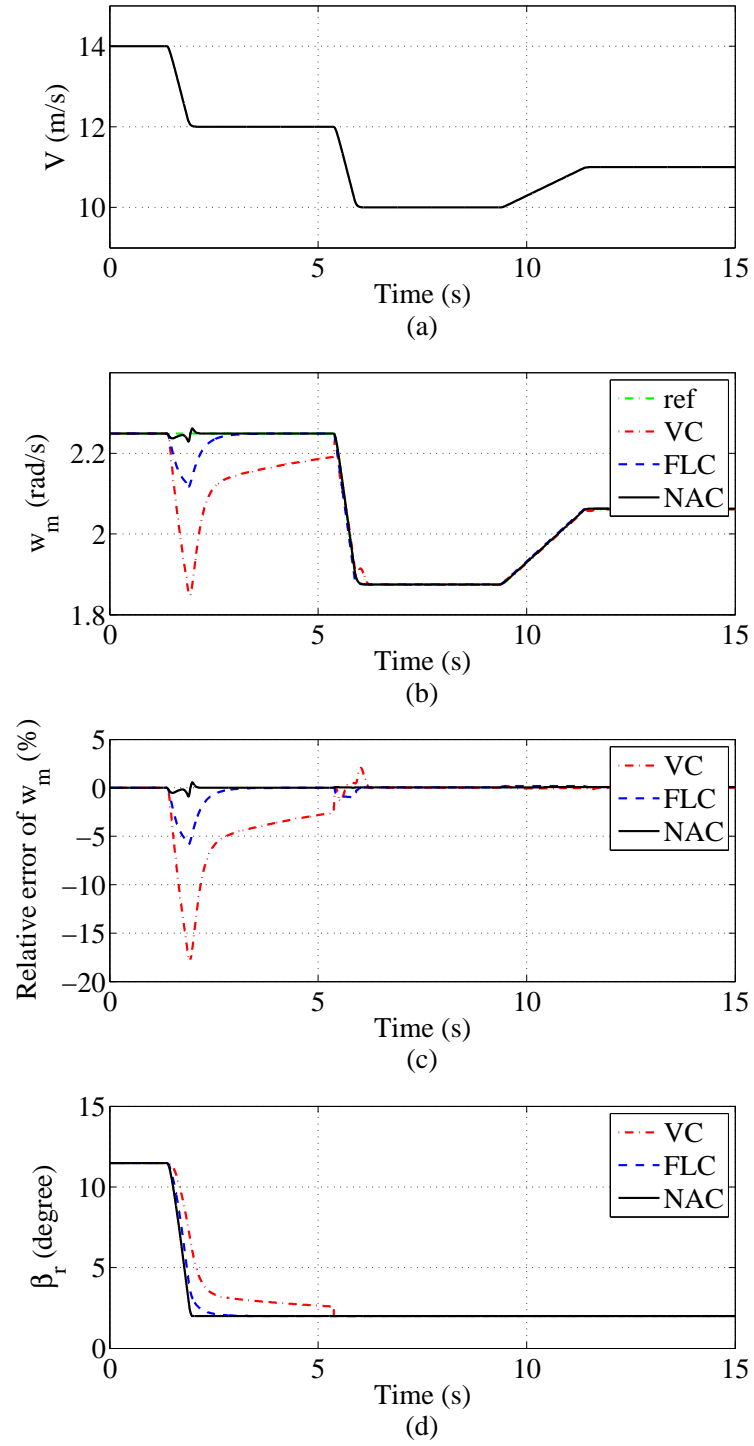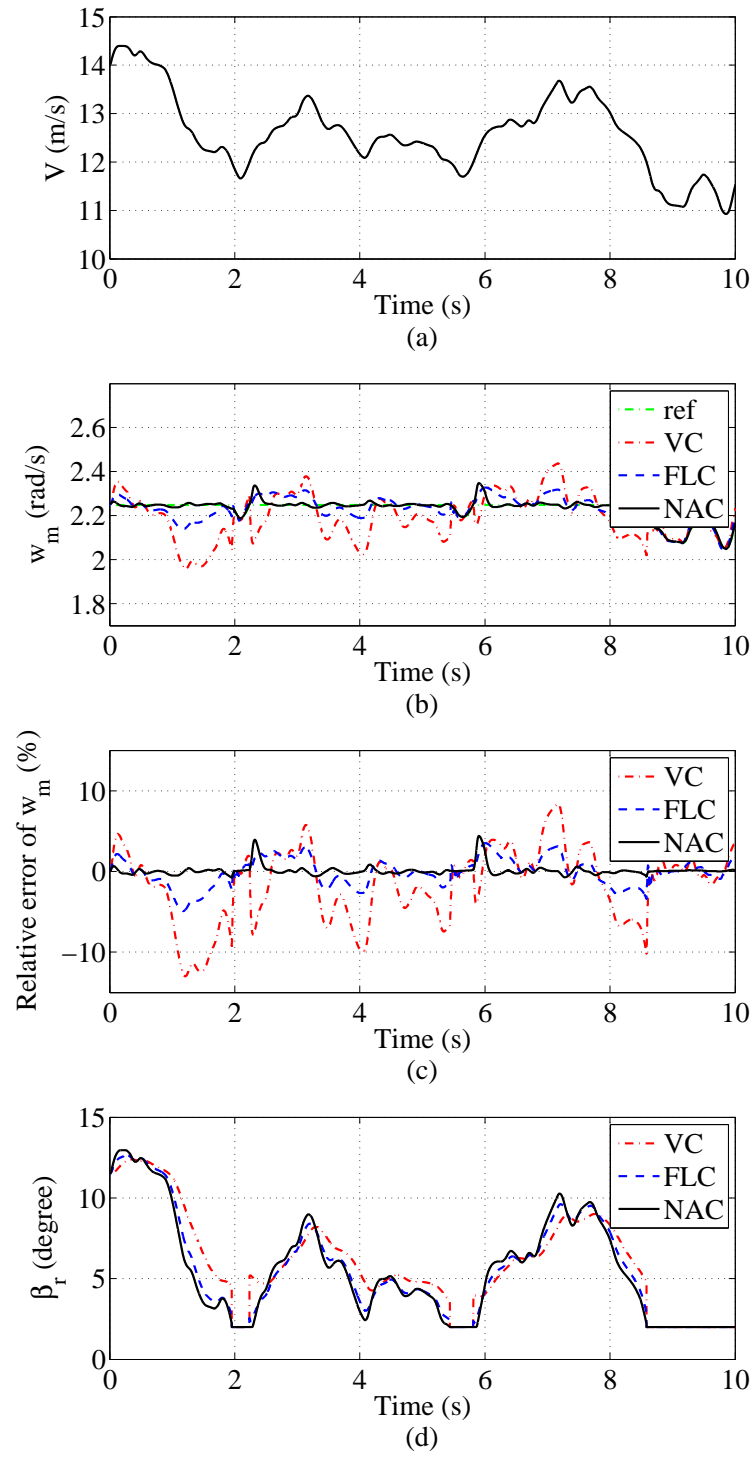
Figure 5.10: Responses of the WT to random wind. (a) Wind speed V. (b) Mechanical rotation speed w_m. (c) Relative error of mechanical rotation speed w_m. (d) Pitch angle reference β_r.
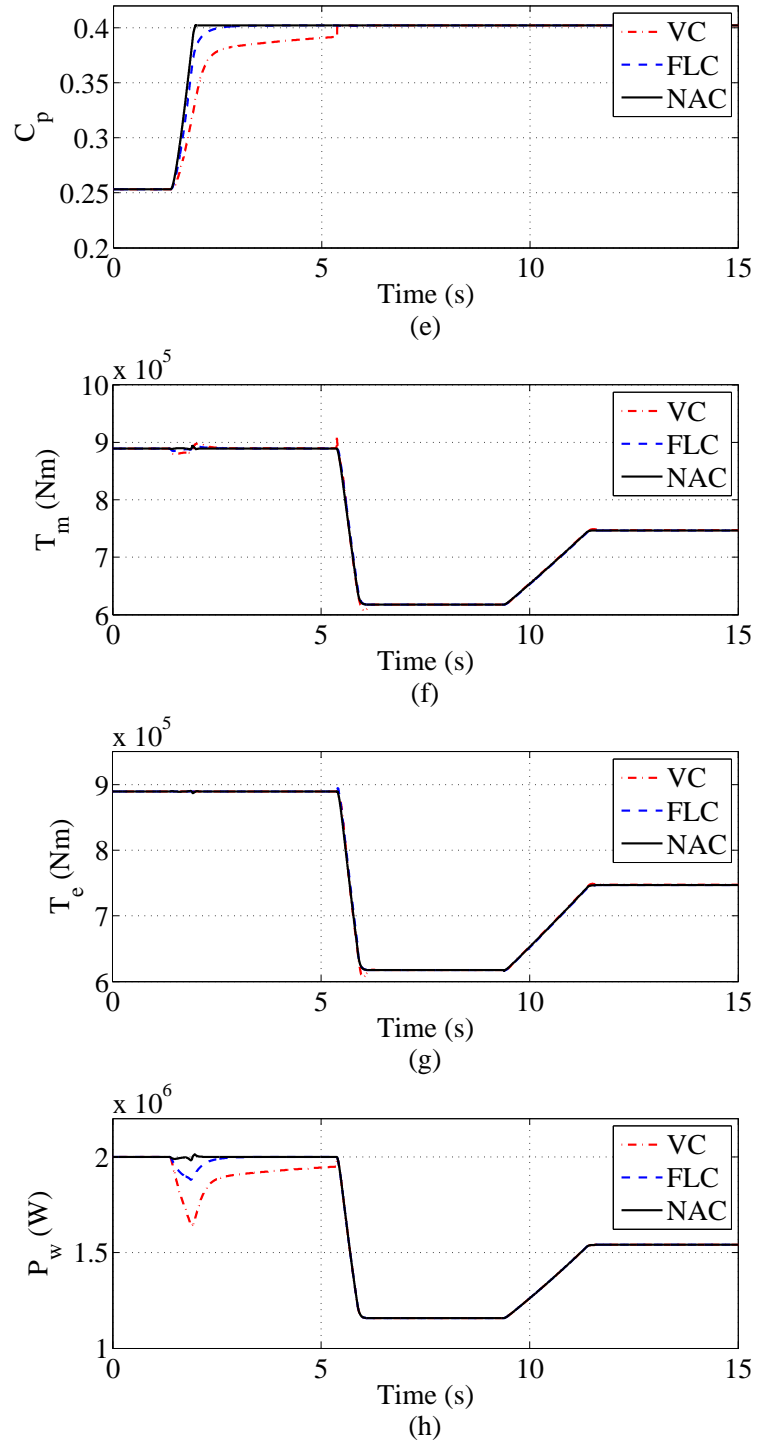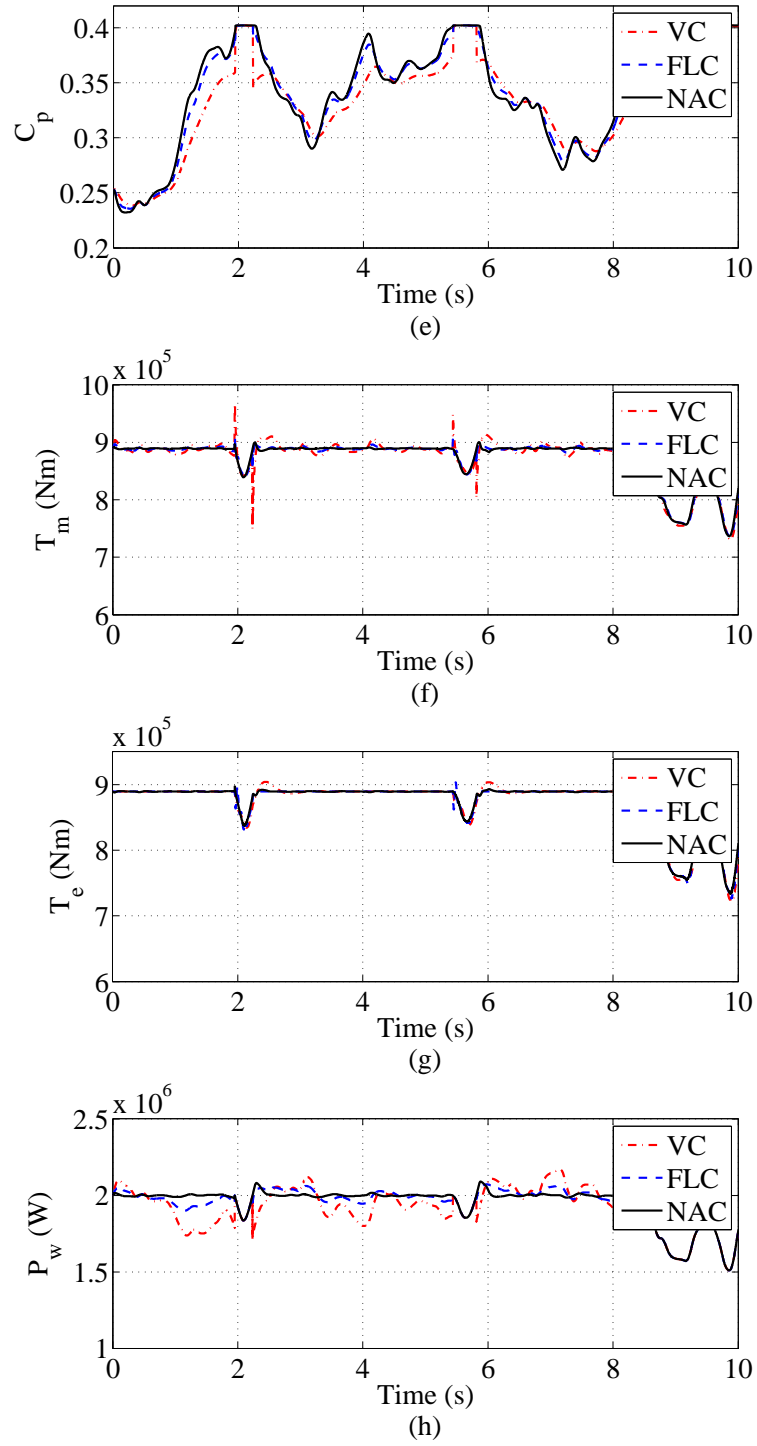
Figure 5.11: Responses of the WT to random wind. (e) Power coefficient C_p. (f) Mechanical rotation torque T_m. (g) Electromagnetic torque T_e. (h) Mechanical power P_w.
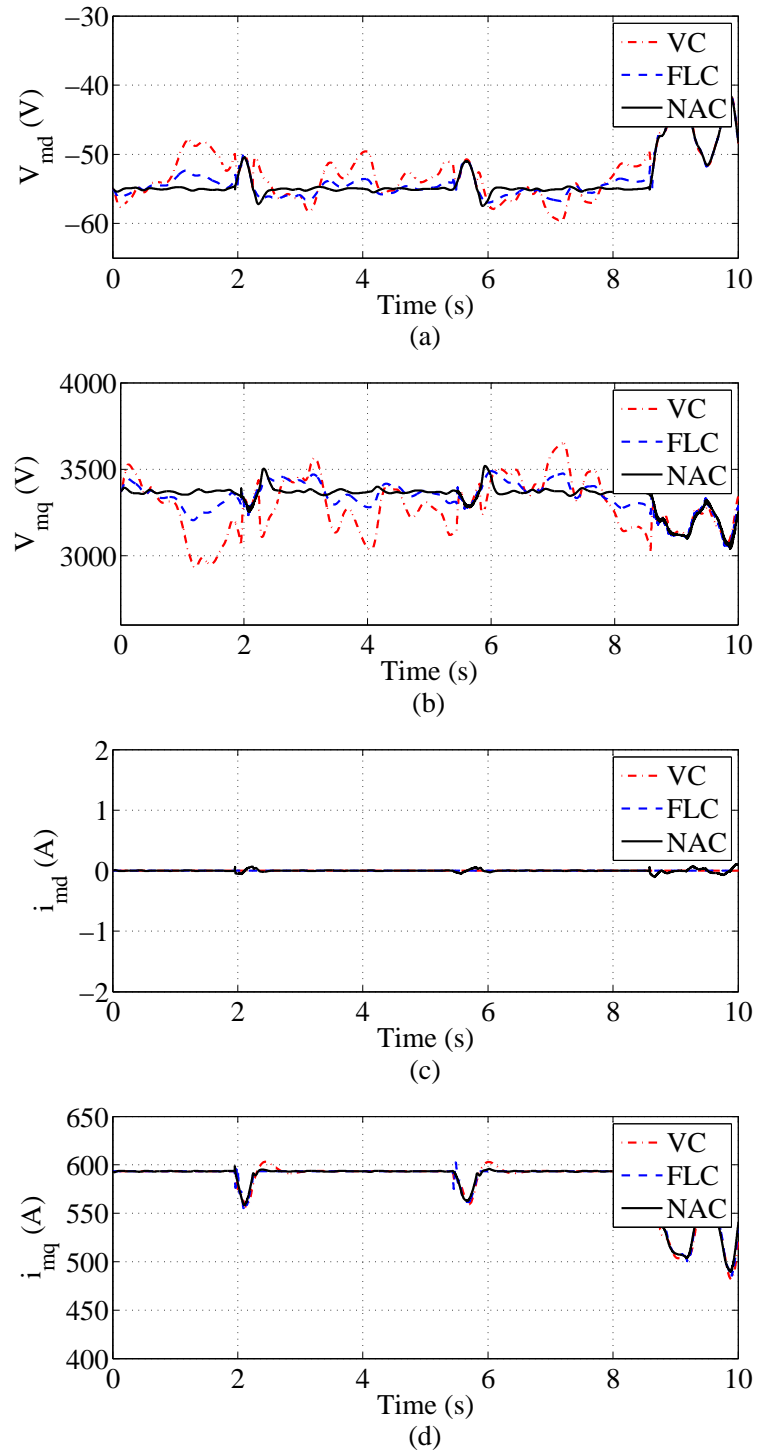
Figure 5.12: Responses of the PMSG to random wind. (a) d-axis voltage V_{md}. (b) q-axis voltage V_{mq}. (c) d-axis current i_{md}. (d) q-axis current i_{mq}.
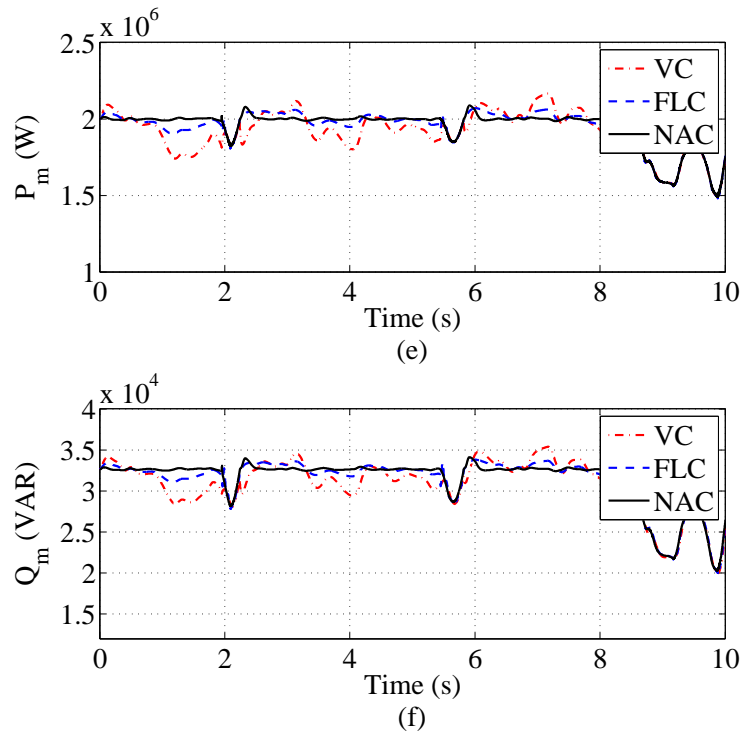
Figure 5.13: Responses of the PMSG to random wind. (e) Active generating power P_m. (f) Reactive generating power Q_m.
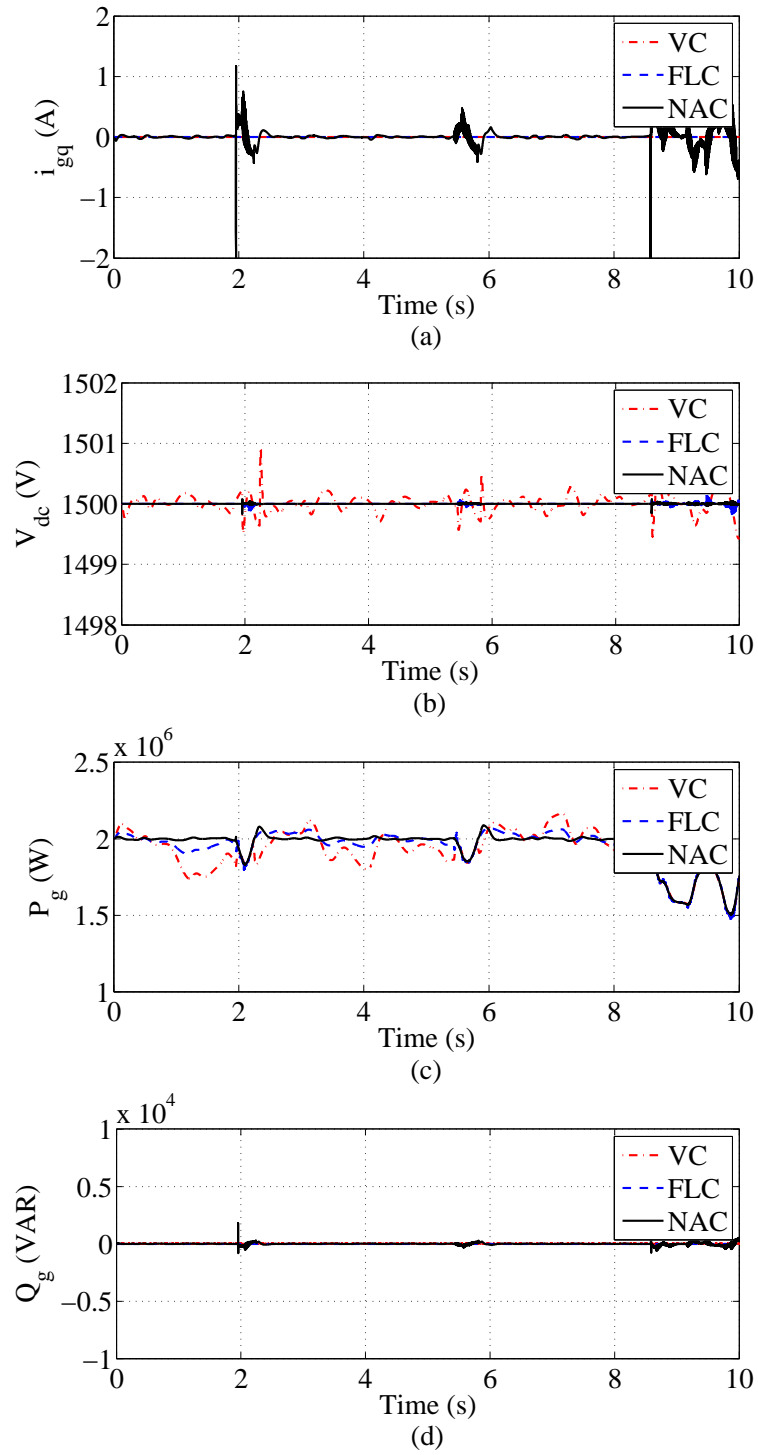
Figure 5.14: Responses of the grid to random wind. (a) q-axis current i_{gq}. (b) DC-link Voltage V_{dc}. (c) Active grid power P_g. (d) Reactive grid power Q_g.
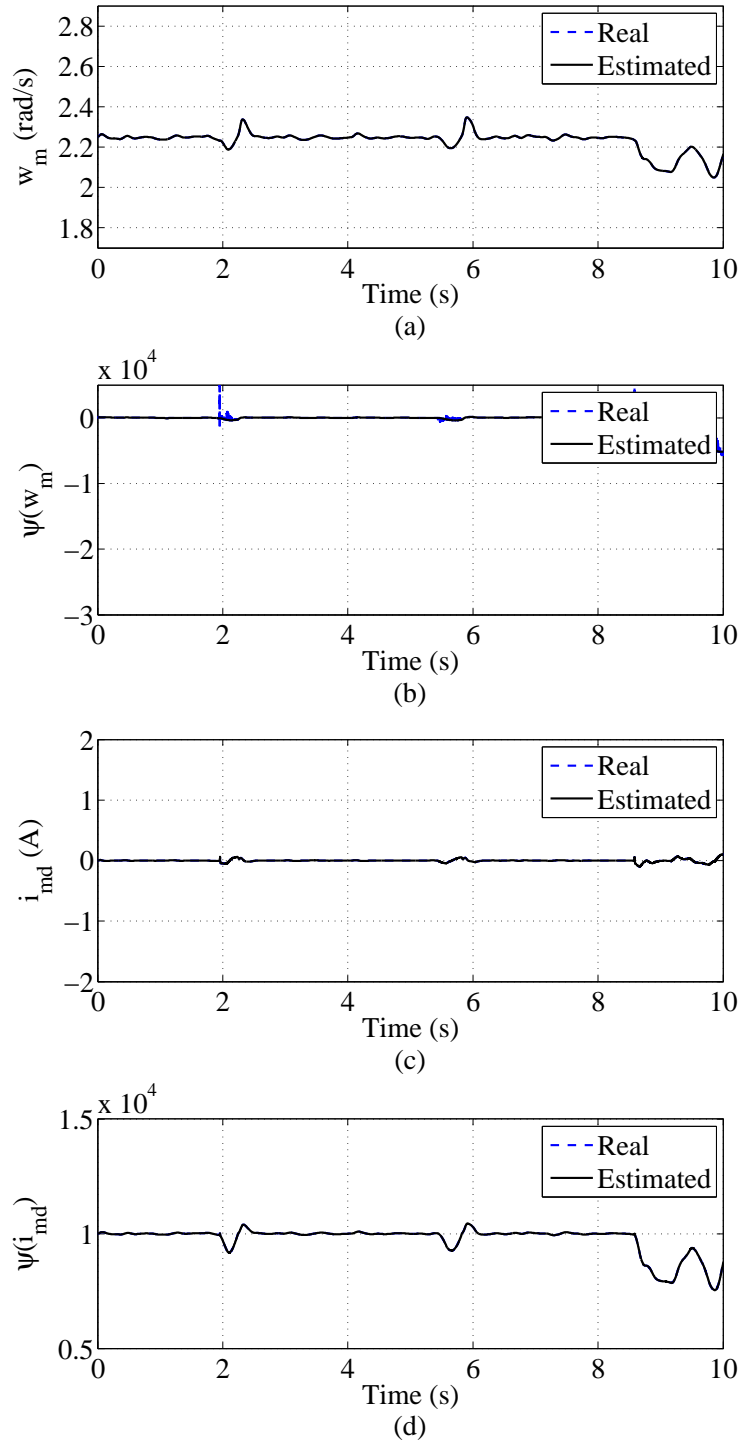
Figure 5.15: Estimates of states and perturbations to random wind
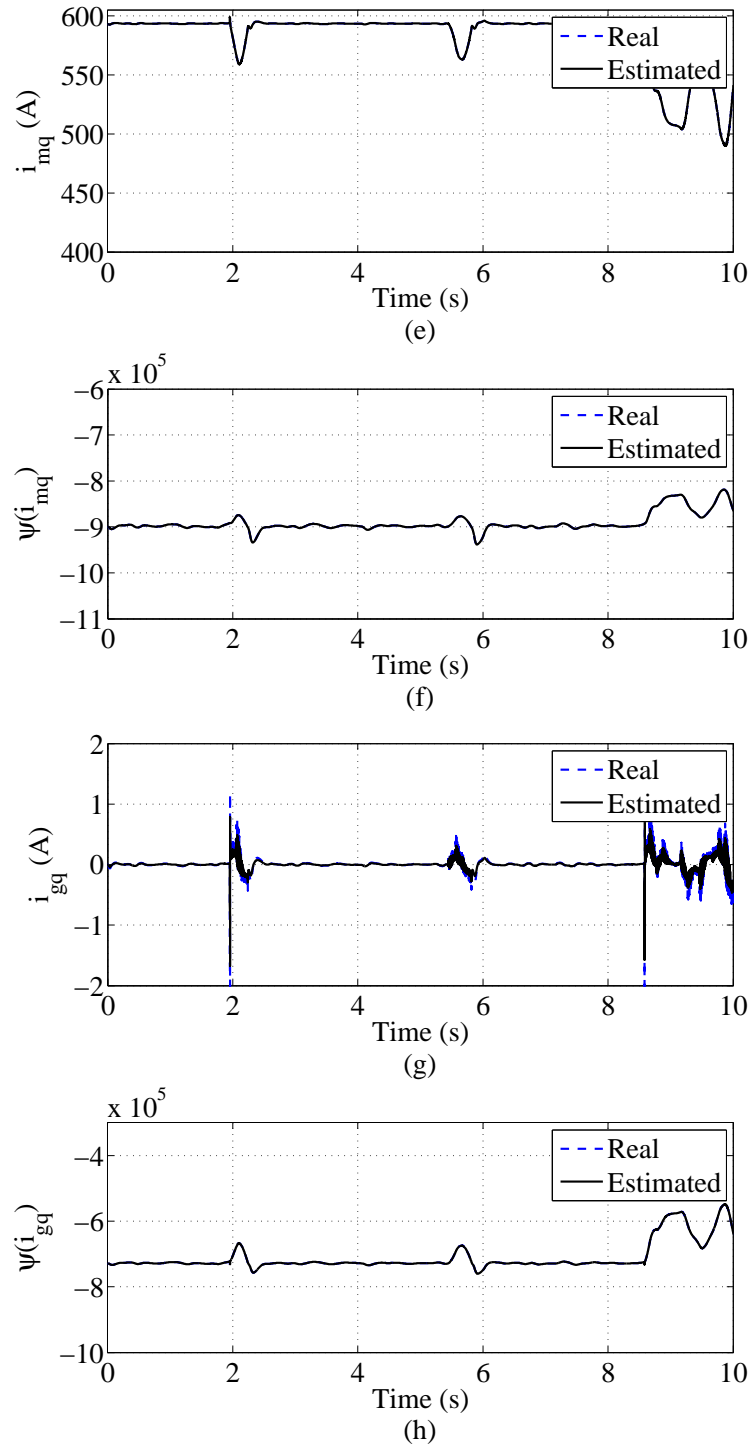
Figure 5.16: Estimates of states and perturbations to random wind
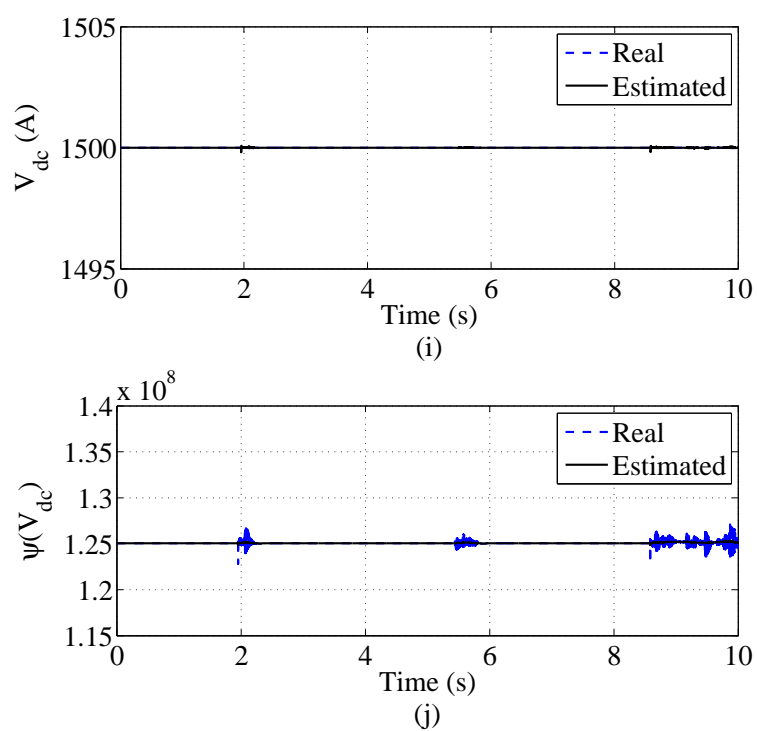
Figure 5.17: Estimates of states and perturbations to random wind

5.3.2   Grid Voltage Dips

In the following test cases, wind speed keeps at 10 m/s and the grid voltage dips from 690 V at 0.58s and recovers at 0.68s.

Grid Voltage Dips Without Protection

Figs. 5.18-5.21 show the responses of the WT and PMSG to constant wind speed under grid voltage dips, respectively. From Fig. 5.22 (c), it can be seen that the d-axis grid current i_{gd} increases to approximately 1400A during voltage dips. The dc-link voltage V_{dc} can be well controlled around 1500V by these three controllers. The responses of the injected grid active is shown in Fig. 5.23 (f).

LVRT Compliance With the Pitch Control

During grid voltage dips, if the extracted wind power does not change, the grid current i_{gd} increases under well controlled DC-link voltage V_{dc}. The fast increasing grid current i_d may damage the devices. If the captured wind power is reduced, the increasing grid current i_{gd} can be reduced. In order to reduce the captured wind power, the power coefficient is decreased by using pitch control. This control strategy can be applied to assist the WECS in protecting the devices and improving the FRTC of the WECS.

From Fig. 5.18-5.23, satisfactory performances can be obtained by all three controllers under rated grid voltage. When the grid voltage dips are detected, the pitch control is applied to reduce the captured wind power. When pitch control strategy is applied, the mechanical rotational speed w_m should keep constant, and the mechanical torque T_m is reduced to the required value. However, the mechanical rotational speed w_m increases when pitch control, as shown Fig. 5.27 (c). It is because that the pitch angle rate is limited in the range ± 20 degree/s under the emergency condition. From 5.27 (d), it can be seen that the pitch angle reference β_r rate is much higher than ± 20 degree/s under the FLC and NAC. Hence, the real pitch angle β applied to the WT cannot be same as the β_r due to pitch angle rate limit. It in turn results in the increment of the w_m. Fig. 5.28 (e) shows the power
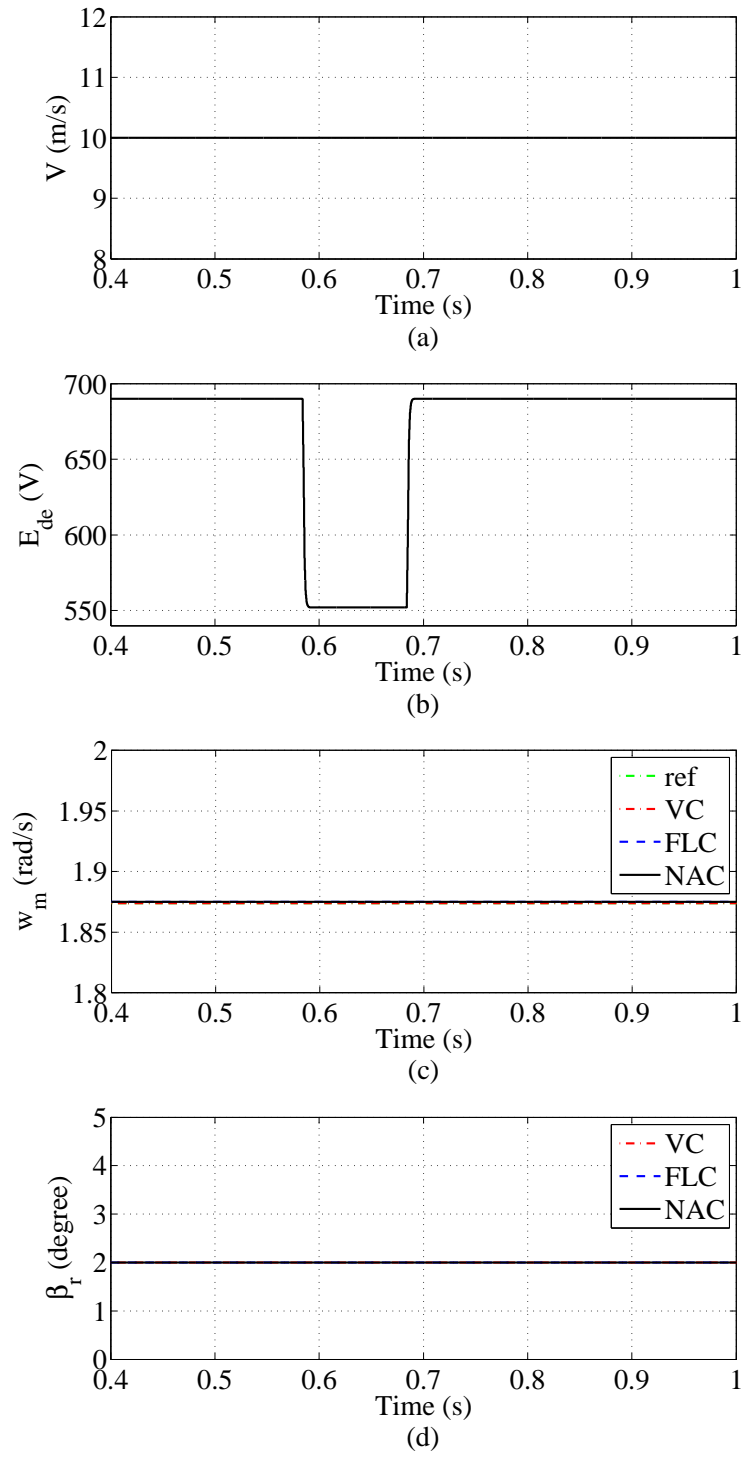
Figure 5.18: Responses of the WT to constant wind speed under grid voltage dips. (a) Wind speed V. (b) Grid Voltage E_{gd}. (c) Mechanical rotation speed w_{m}. (d) Pitch angle reference β_{r}.
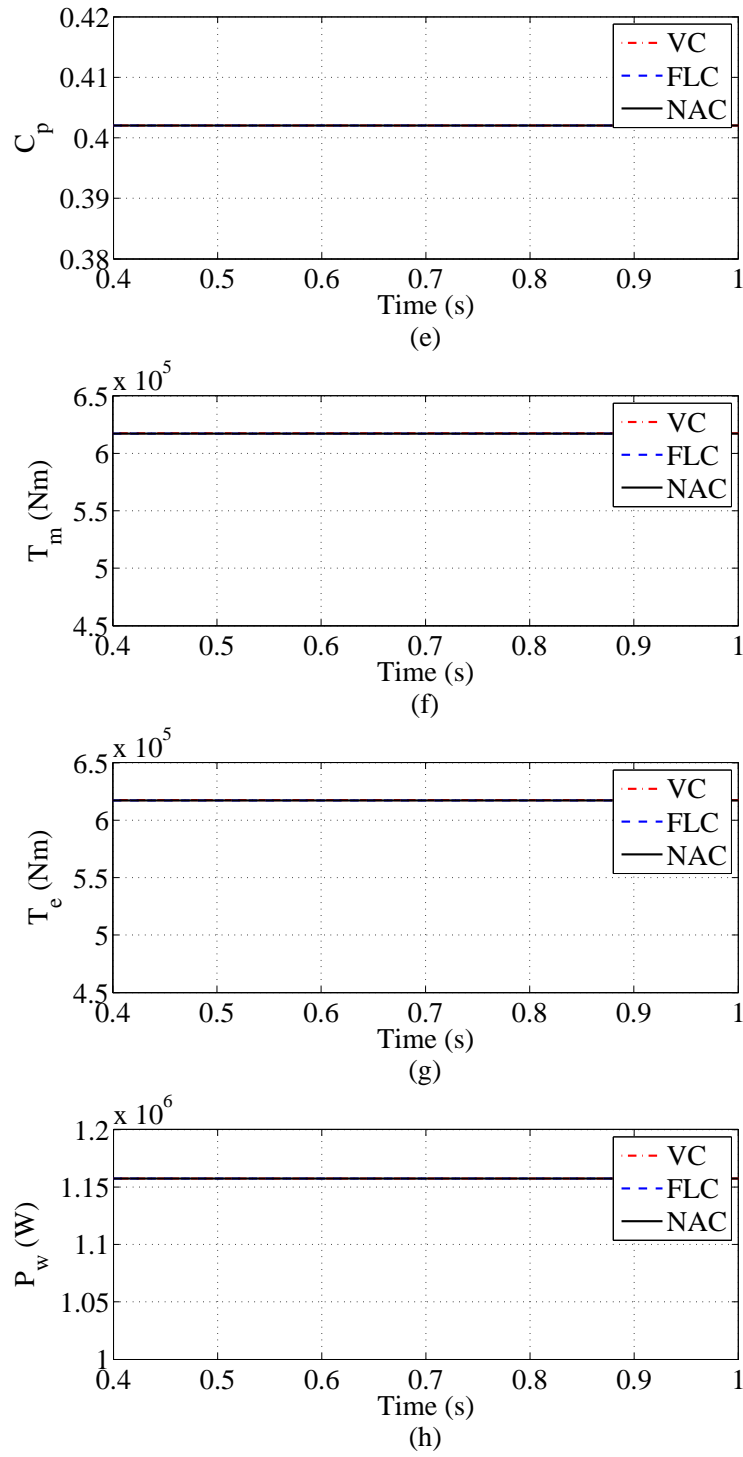
Figure 5.19: Responses of the WT to constant wind speed under grid voltage dips. (e) Power coefficient C_p. (f) Mechanical rotation torque T_{m}. (g) Electromagnetic torque T_{e}. (h) Mechanical power P_{w}.
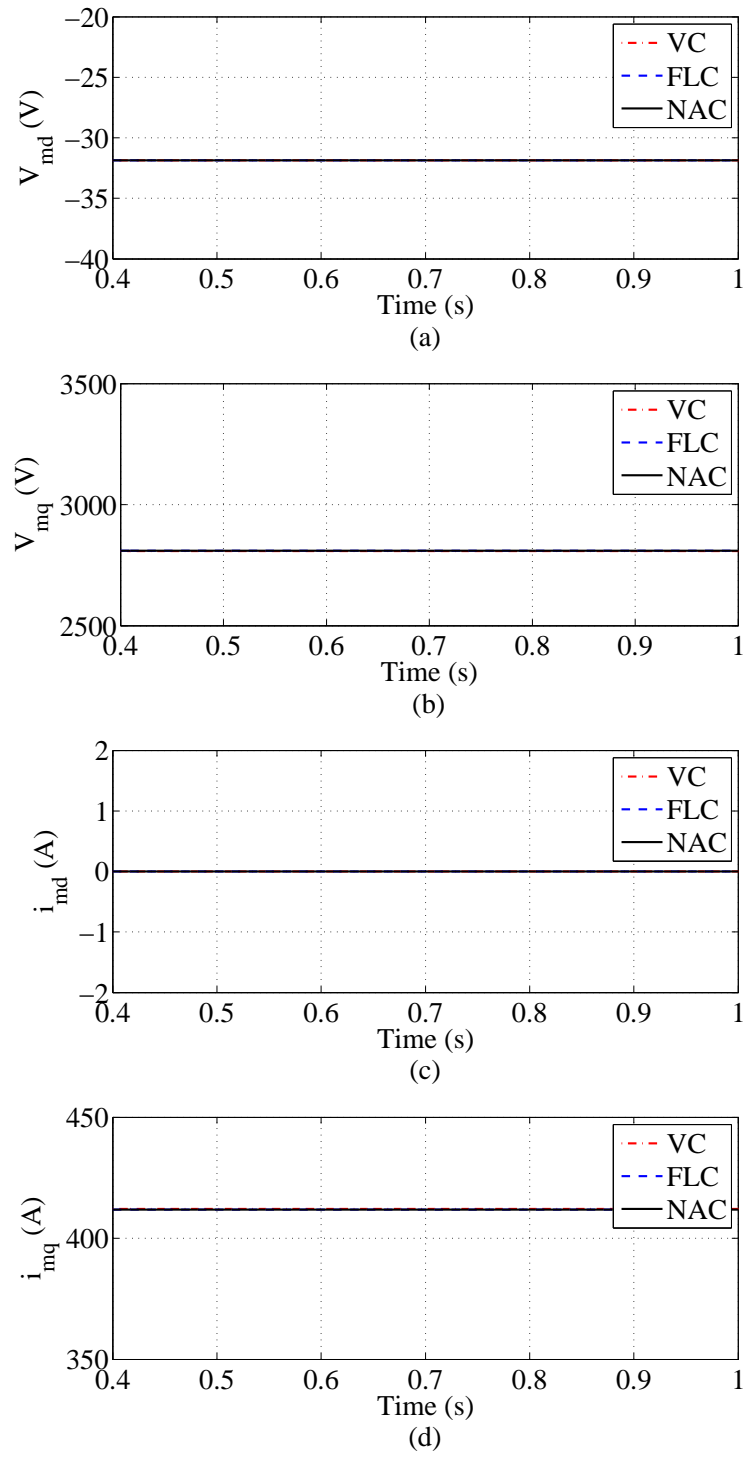
Figure 5.20: Responses of the PMSG to constant wind speed under grid voltage dips. (a) d-axis voltage V_{md}. (b) q-axis voltage V_{mq}. (c) d-axis current i_{md}. (d) q-axis current i_{mq}.
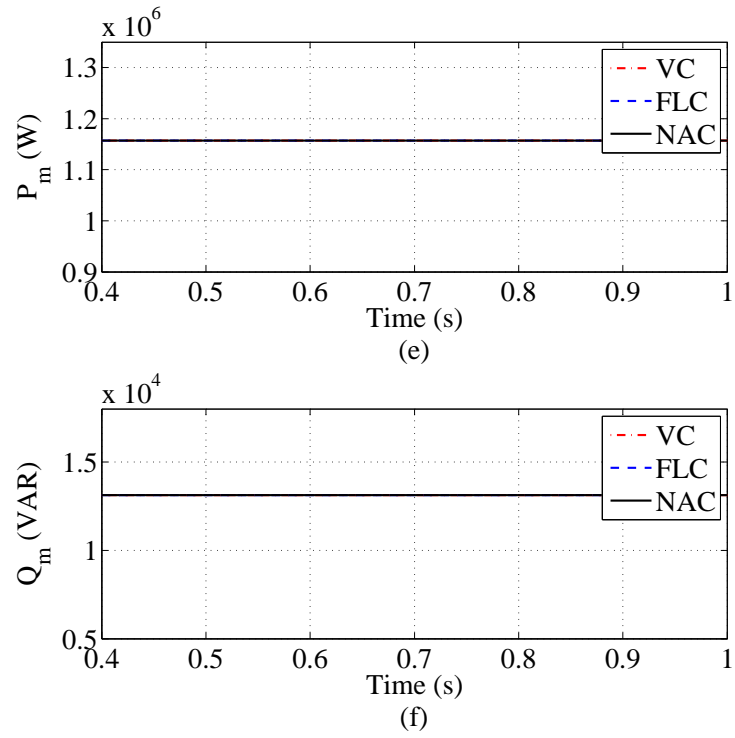
Figure 5.21: Responses of the PMSG to constant wind speed under grid voltage dips. (e) Active generating power P_{m}. (f) Reactive generating power Q_{m}.
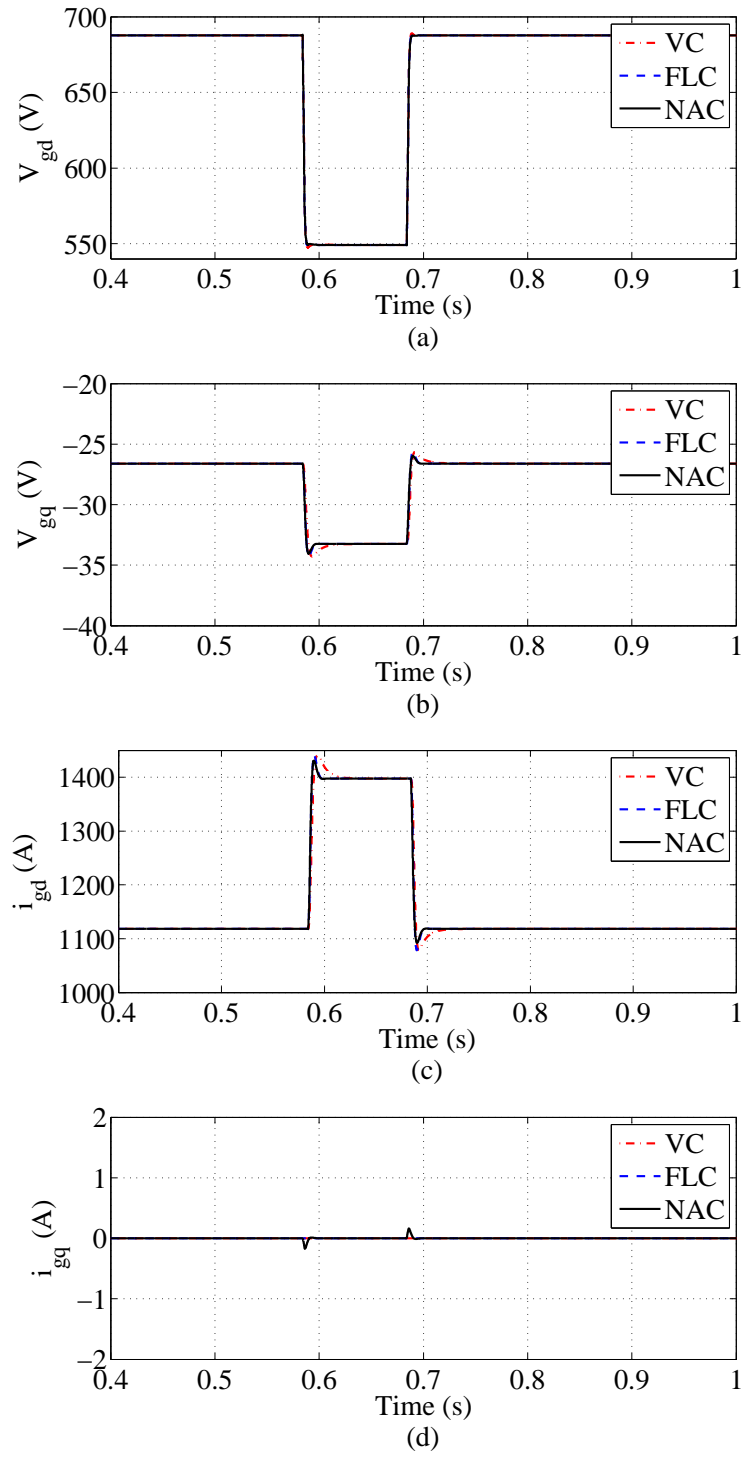
Figure 5.22: Responses of the grid to constant wind speed under grid voltage dips. (a) d-axis voltage V_{gd}. (b) q-axis voltage V_{gq}. (c) d-axis current i_{gd}. (d) q-axis current i_{gq}.
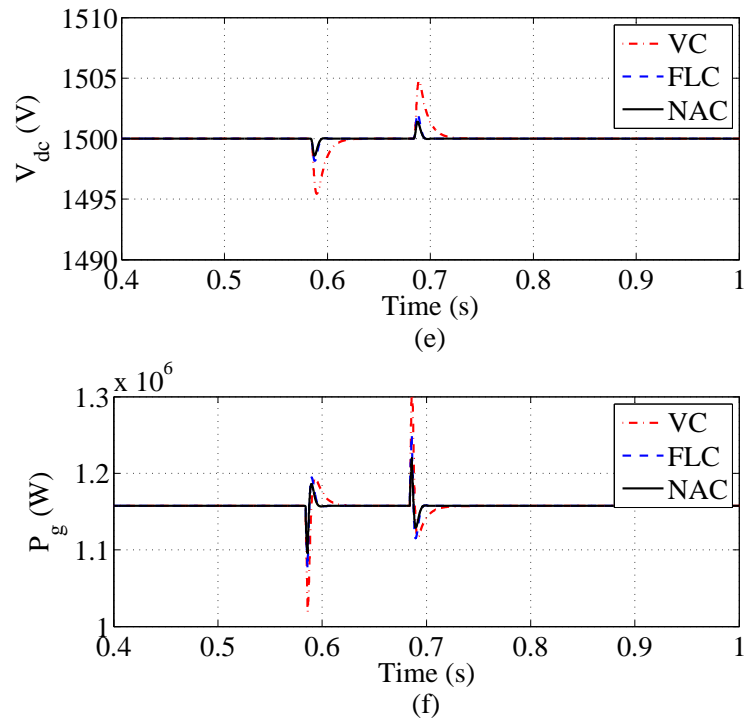
Figure 5.23: Responses of the grid to constant wind speed under grid voltage dips. (a) d-axis voltage V_{gd}. (b) q-axis voltage V_{gq}. (c) d-axis current i_{gd}. (d) q-axis current i_{gq}. (e) DC-link Voltage V_{dc}. (f) Active grid power P_g.
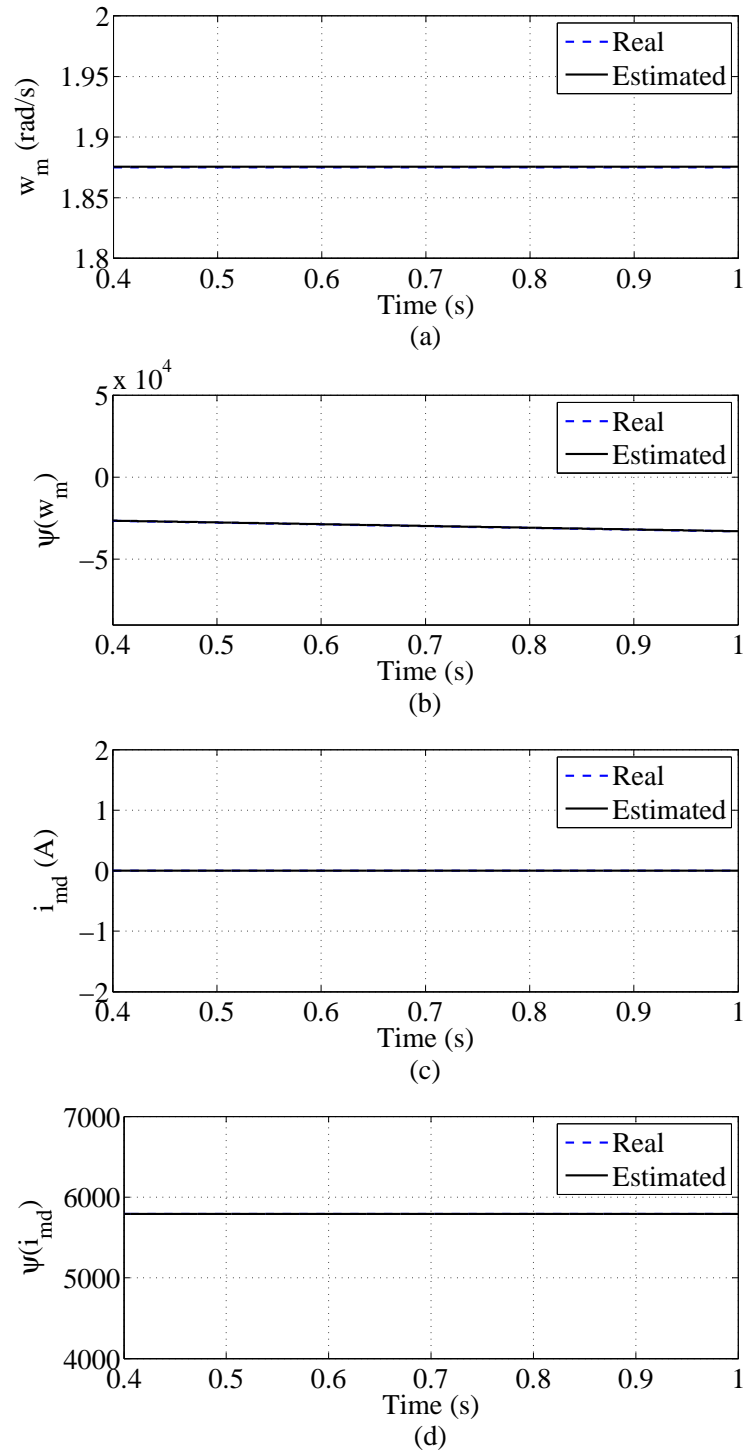
Figure 5.24: Estimates of states and perturbations to constant wind speed under grid voltage dips
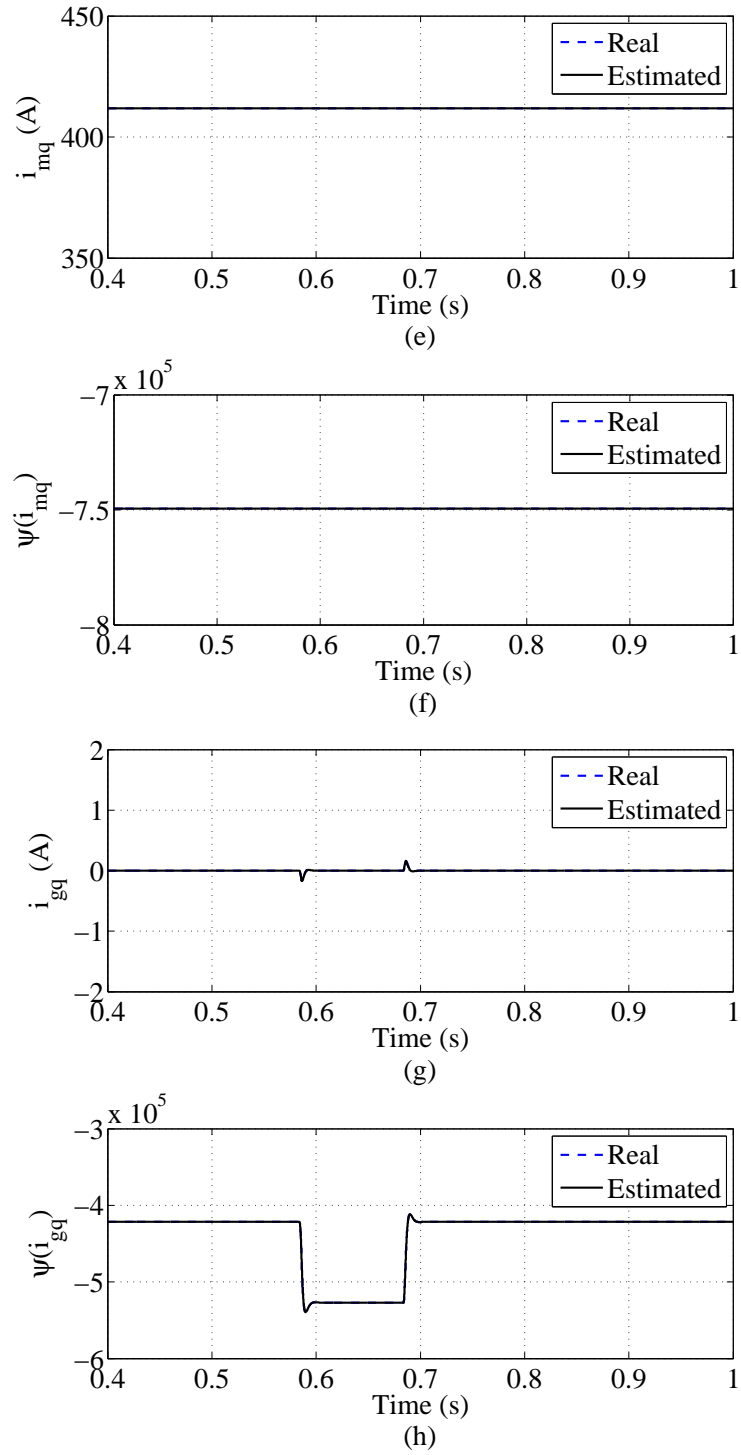
Figure 5.25: Estimates of states and perturbations to constant wind speed under grid voltage dips
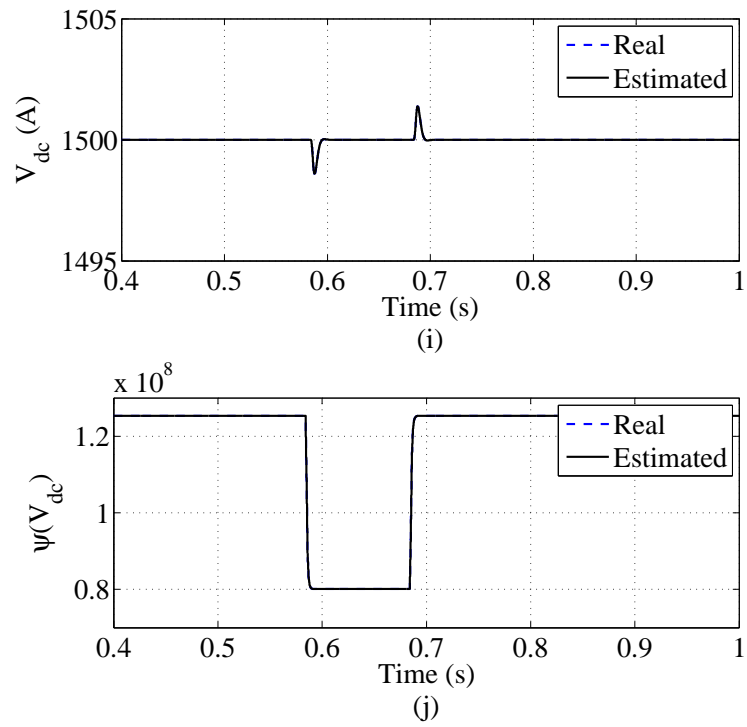
Figure 5.26: Estimates of states and perturbations to constant wind speed under grid voltage dips
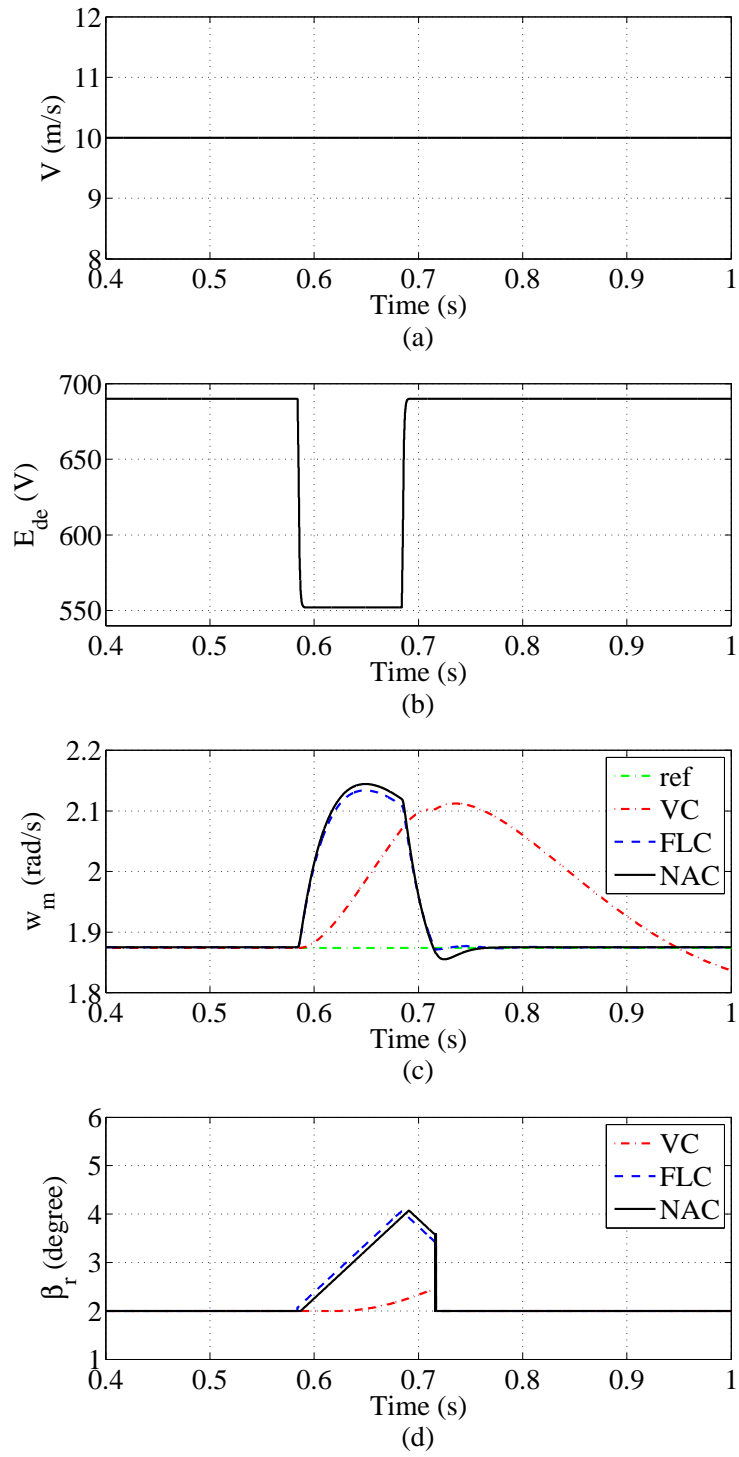
Figure 5.27: Responses of the WT to constant wind speed with protection under grid voltage dips. (a) Wind speed V. (b) Grid Voltage E_{gd}. (c) Mechanical rotation speed w_{m}. (d) Pitch angle reference β_{r}.
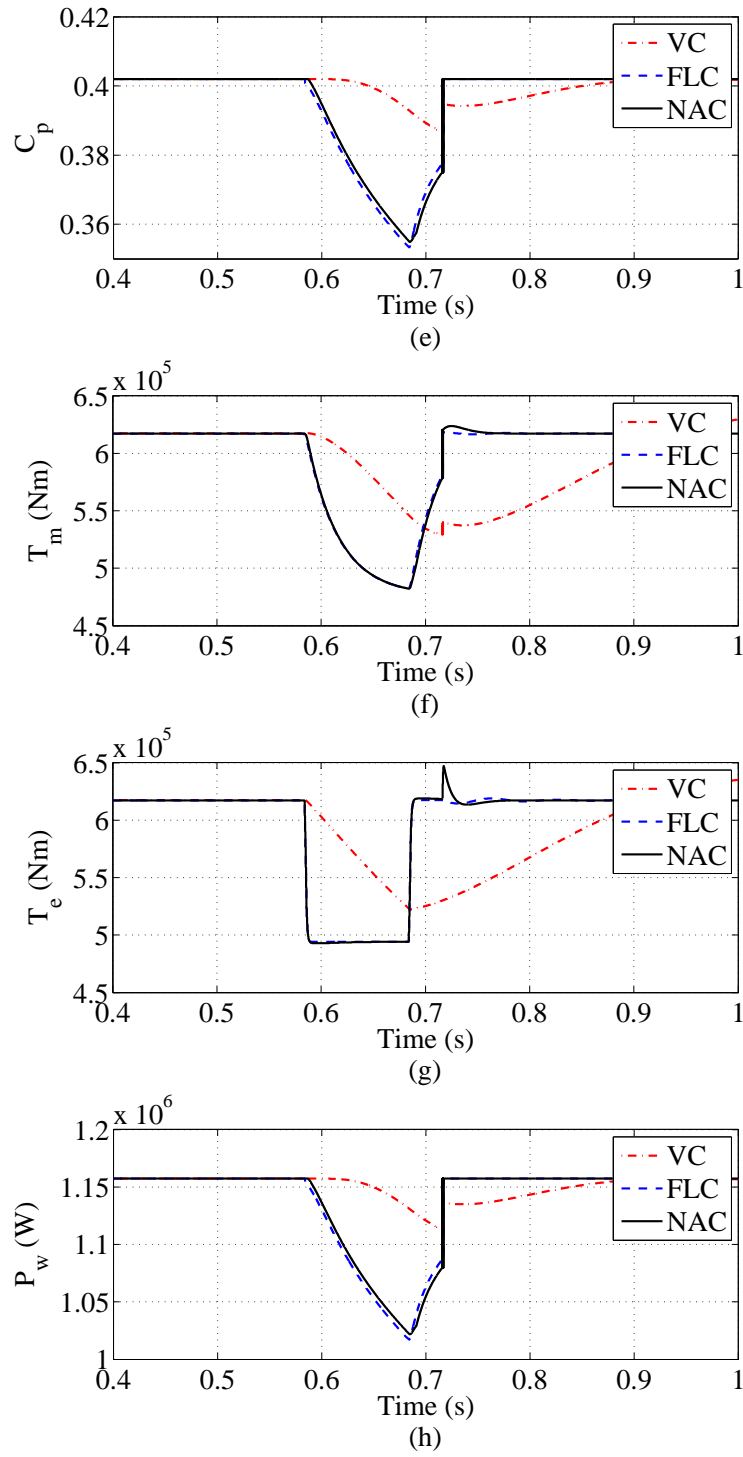
Figure 5.28: Responses of the WT to constant wind speed with protection under grid voltage dips. (e) Power coefficient C_p. (f) Mechanical rotation torque T_m. (g) Electromagnetic torque T_e. (h) Mechanical power P_w.
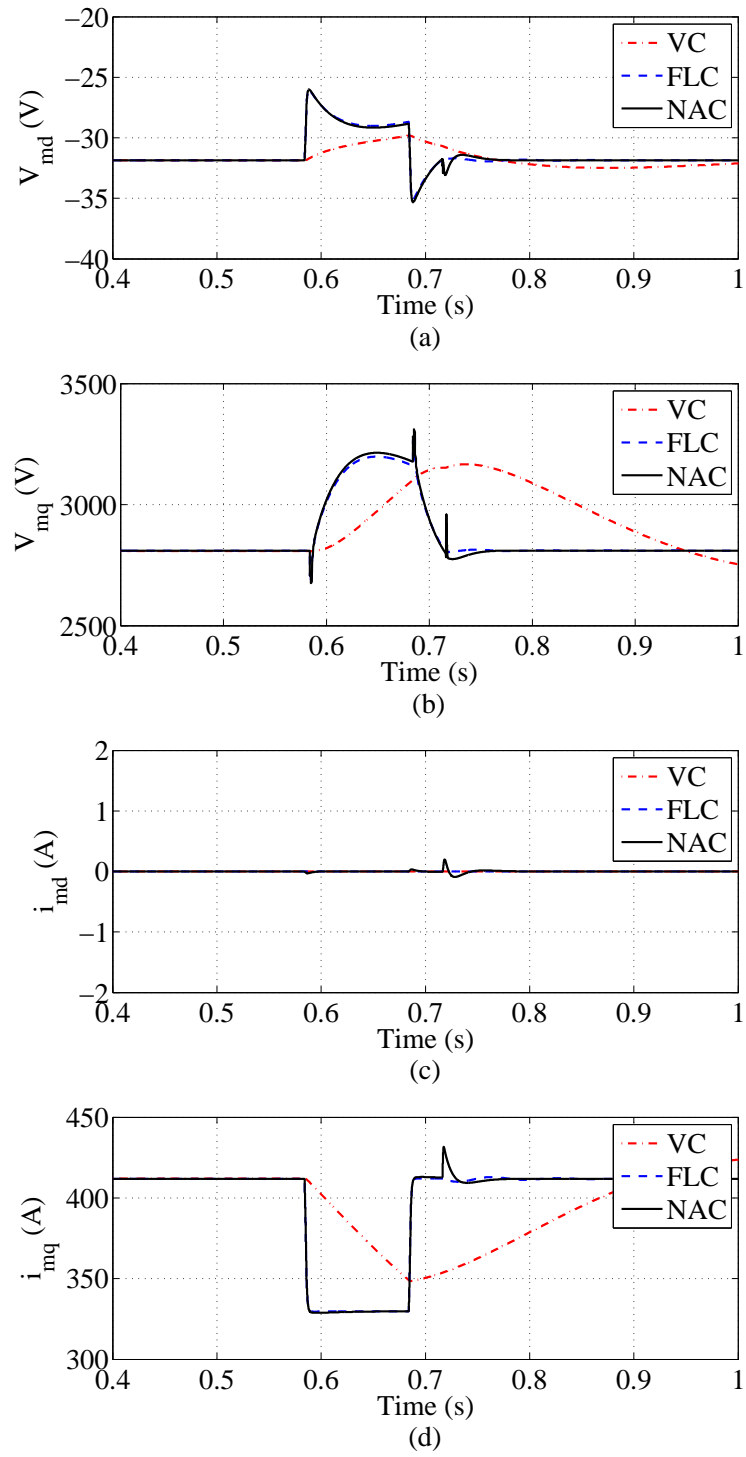
Figure 5.29: Responses of the PMSG to constant wind speed with protection under grid voltage dips. (a) d-axis voltage V_{md}. (b) q-axis voltage V_{mq}. (c) d-axis current i_{md}. (d) q-axis current i_{mq}.
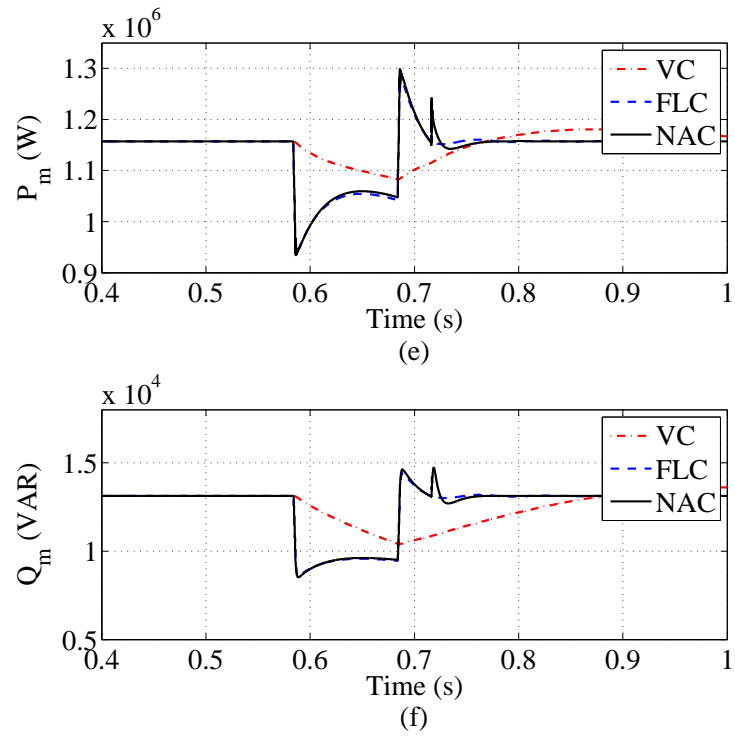
Figure 5.30: Responses of the PMSG to constant wind speed with protection under grid voltage dips. (e) Active generating power P_m. (f) Reactive generating power Q_m.
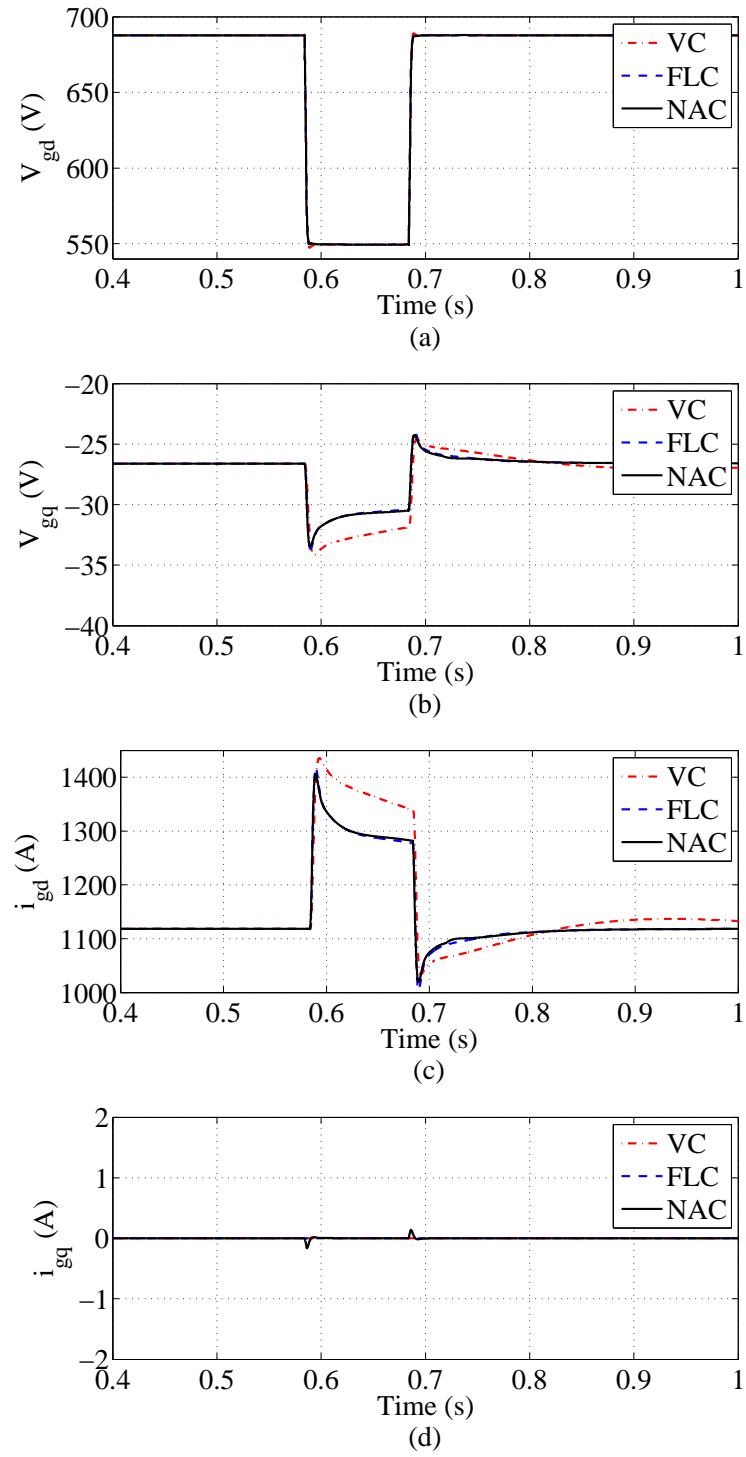
Figure 5.31: Responses of the grid to constant wind speed with protection under grid voltage dips. (a) d-axis voltage V_{gd}. (b) q-axis voltage V_{gq}. (c) d-axis current i_{gd}. (d) q-axis current i_{gq}.
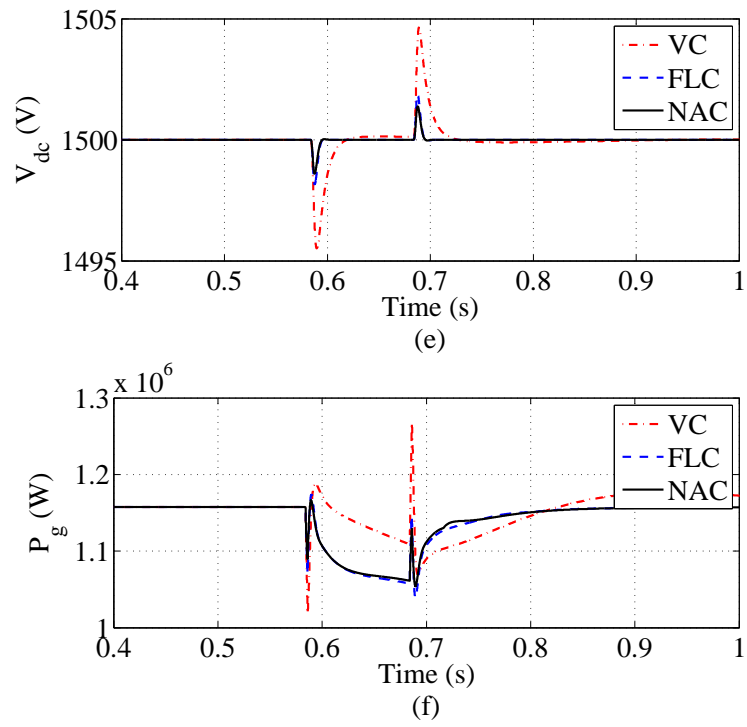
Figure 5.32: Responses of the grid to constant wind speed with protection under grid voltage dips. (e) DC-link Voltage V_{dc}. (f) Active grid power P_g.
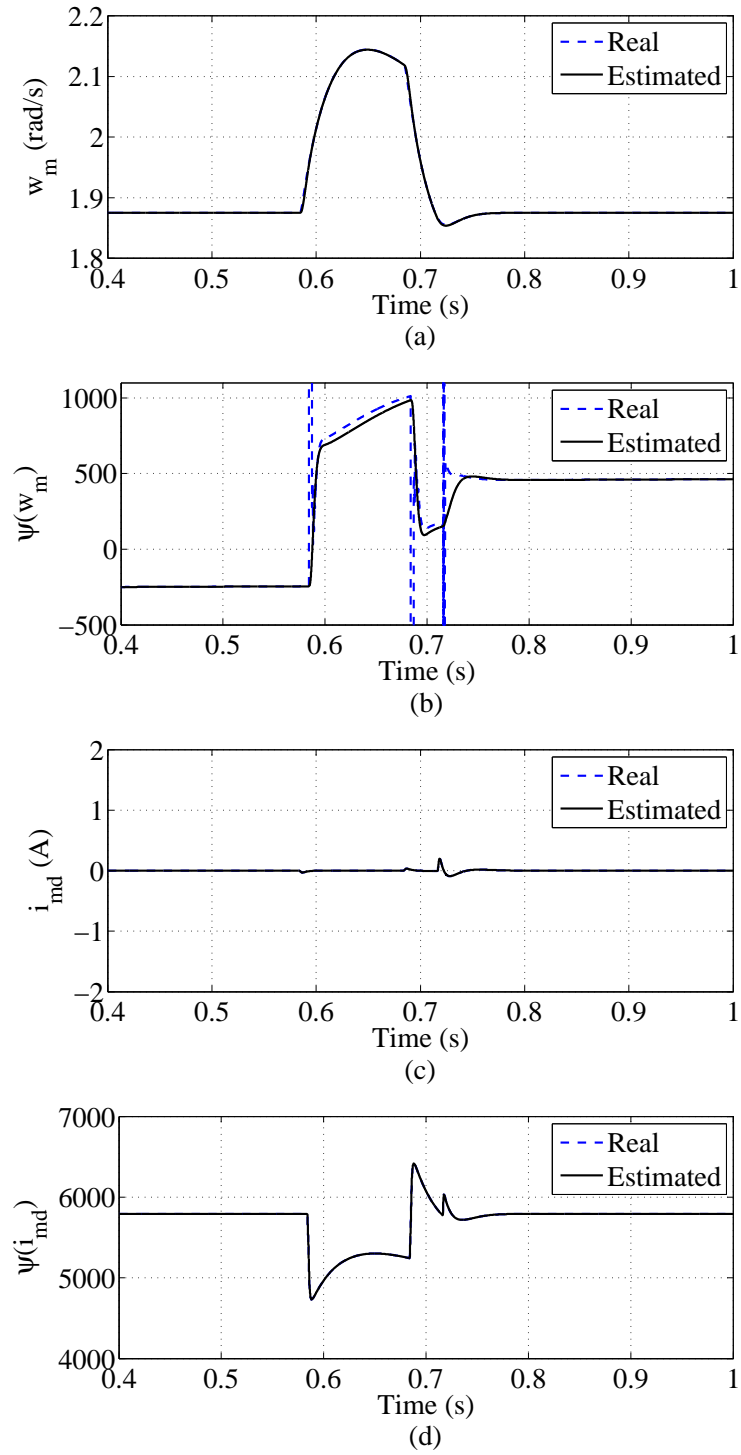
Figure 5.33: Estimates of states and perturbations to constant wind speed with protection under grid voltage dips
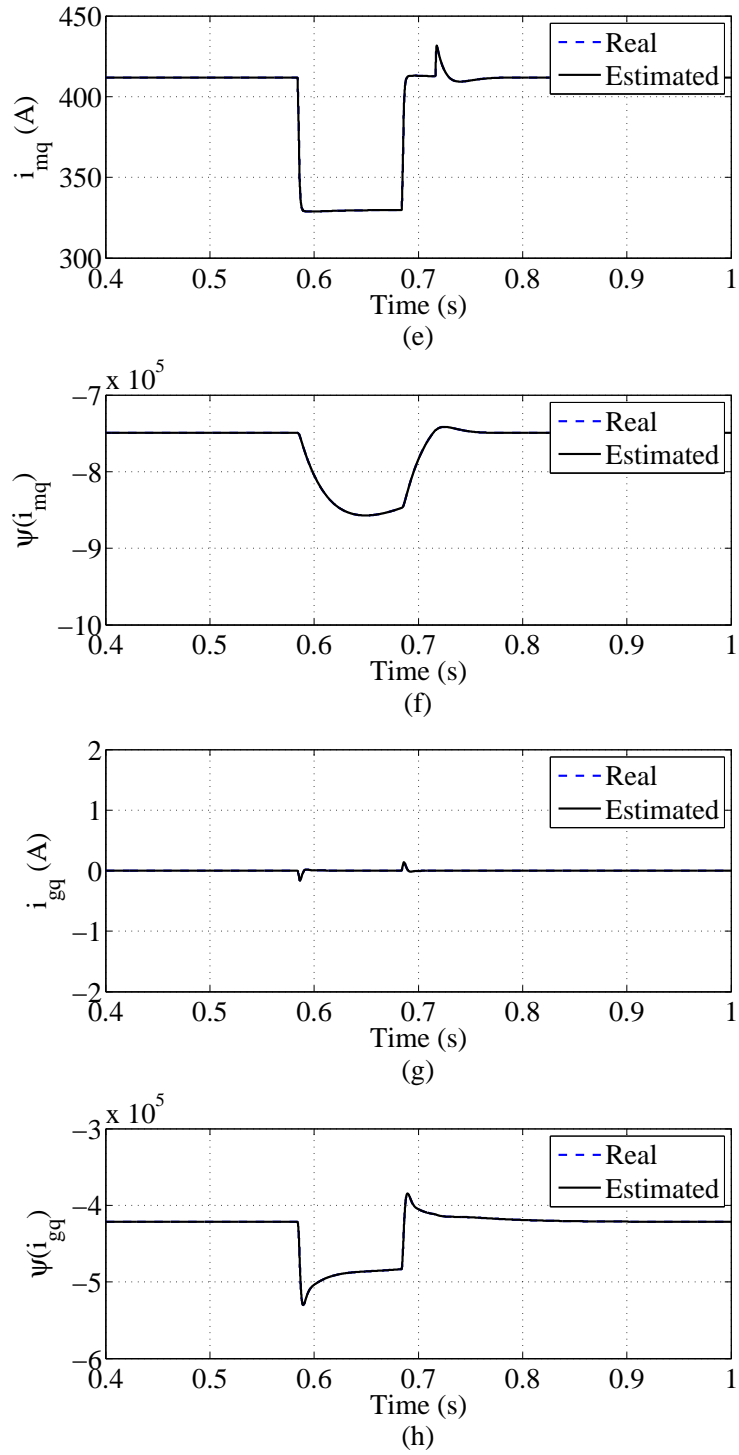
Figure 5.34: Estimates of states and perturbations to constant wind speed with protection under grid voltage dips
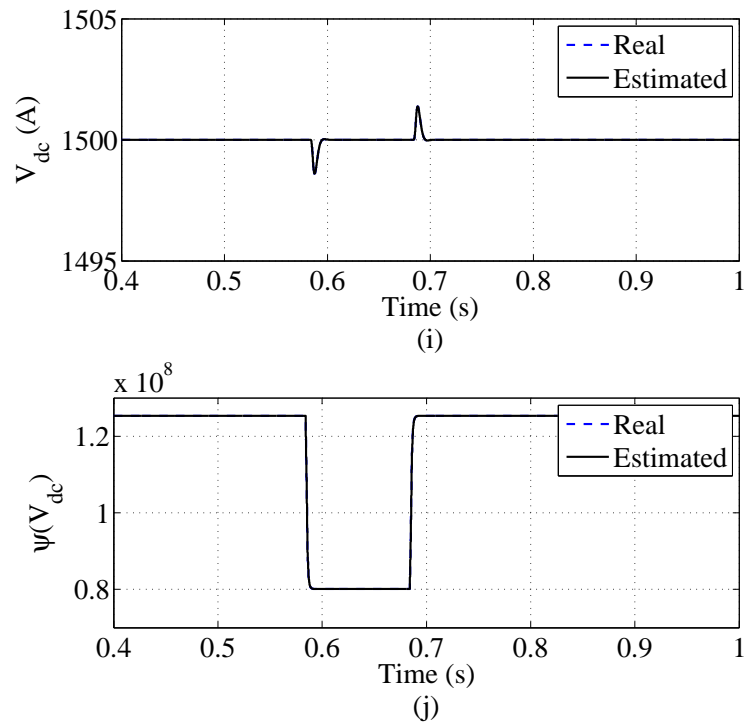
Figure 5.35: Estimates of states and perturbations to constant wind speed with protection under grid voltage dips

coefficient C_p can be reduced by varying pitch angle. The decrement of the C_p is much larger under the FLC and NAC than the VC. It can be explained that the VC has much slower response of the β compared to the FLC or NAC. If the β cannot decrease quickly, the C_p cannot has fast reduction. Both the T_m and T_e reduced quickly under the FLC and NAC, as shown 5.28 (f) and (g). However, the VC has smaller reduction and longer recovery time. Fig. 5.28 (h) shows both the NAC and LFC has larger reduction of captured wind power P_w than the VC when the grid voltage dips.

The responses of the PMSG to constant wind speed with protection under grid voltage dips is shown in Fig. 5.29 and 5.30. When the grid voltage dips, the electromagnetic torque reference T_{er} is reduced proportionally to the grid voltage dips to keep balance between the generating power P_m and injected grid power P_g. It in turn limits the increasing grid current i_{gd} to protect the devices. If the stator current i_{md} is well controlled, the T_e is proportional to the i_{mq}. However, it can be seen from Fig. 5.29 (d) that, the i_{mq} cannot track its reference under the VC. Both the FLC and NAC provide satisfactory tracking performance of i_{mq}. Fig. 5.30 (e) shows the active generating power P_m has bigger reduction with shorter recovery time under the FLC and NAC than the VC.

Fig. 5.31 and 5.32 shows the responses of the grid under grid voltage dips. It can be seen from Fig. 5.31 and 5.32 that, the grid current i_{gd} achieve smaller current under the FLC and NAC than VC when voltage dips happen. When pitch control strategy is not applied under grid voltage dips, the i_{gd} reaches approximately 1400A shown in Fig. 5.22 (c). The i_{gd} can be reduced to approximately 1300A under the FLC and NAC When pitch control strategy is used, as shown in Fig. 5.31. However, the VC does not limit the i_{gd} significantly as FLC or NAC. The dc-link voltage V_{dc} has smaller overshoots and shorter recovery time under the FLC and NAC than the VC. When pitch control strategy is applied, the injected active grid power P_g has bigger reduction under the FLC and NAC compared to the VC. The FRTC of the WECS can be enhanced by using the FLC or NAC. Note that the FLC requires full state feedback and accurate system model and parameters.

5.4   Conclusions

This chapter has proposed a CNAC for the GSC and MSC of the WECS based PMSG. The objectives of different operating regions can be achieved by using the NAC. It provides better performances of the WECS than the VC designed based on optimal operating point and FLC requiring accurate system model and detailed system model in different operating regions. In addition, the nonlinear adaptive pitch control has been used to assist in reducing the extracted wind power to enhance the FRTC of the WECS. In the future work, the active crowbars can be applied in enhancing the FRTC of WECSs to protect the WECS.

Chapter 6

Speed Control of a Permanent Magnet Synchronous Motor With Time-Varying Unknown Load Torque

6.1 Introduction

Permanent magnet synchronous motors (PMSMs) has become attractive and competitive in AC drive applications with merits such as self-excitation, high efficiency, low inertia, low noise, high torque to current ratio and fast dynamic response [106, 107]. The vector control (VC) with proportional-integral (PI) loops is already widely applied in the PMSM system due to its relative simple implementation and decoupled power regulation. It aims to achieve similar torque control performance to a separately excited dc motor where torque and flux can be decoupled controlled. However, a practical PMSM system is a nonlinear system and faced with unavoidable uncertainties and load disturbance, such as parameter variations, friction force, and unknown load disturbances. As a result, linear control schemes like linear quadratic regulator control algorithm may not provide high dynamic performance for a PMSM over a time-varying operation conditions [108–111].Some nonlinear control strategies have been proposed, such as predictive functional control [110], robust control [111], feedback linearisation control (FLC) [112, 113], s-

liding mode control [108, 109, 114], fuzzy control [115], adaptive control [116–119] and backstepping control [46, 120, 121].

The drive robustness against disturbances like load torque variation and system parameter variations is an important requirement of high-performance drives. This leads to the necessity of a compensation for the torque disturbance. Unfortunately, the load torque disturbances are not easily measured directly or predicted. In view of the robustness against a certain disturbance, the observer-based controller has been proposed as a successful scheme in industrial applications to suppress load torque disturbance [78, 116, 122–127]. However, since the exactly known system parameters are required for observers, parameter variations still seriously affect the performance of such schemes. In [124], a model-based method using a nonlinear reduced-order observer was introduced for speed and rotor position estimation of PMSM. It can provide a satisfactory performance under load torque disturbance, but it lacks of experimental verifications. A sensorless nonlinear control scheme for driving an unknown load torque is proposed [125]. An extended nonlinear observer (ENO) is applied to estimate the states of the motor and disturbance torque. The proposed control scheme presents a very satisfactory performance in the whole speed range, under slowing varying load torque and uncertainties in the mechanical parameters. However, the observer performance is sensitive to electrical parameter variations that may lead to dynamics of the scheme unstable. In [126], a nonlinear speed control for a PMSM using disturbance estimation approach is developed to achieve satisfactory performance under the presence of the parameter variation and the external disturbances caused by the inertia of the drive train and load torque variations. However, the resistance and inductance should be exactly known, and the estimated parameters need to be unknown constant or slowly varying. In [116], an adaptive speed controller for the PMSM speed-regulation system combining the extended state observer (ESO) with the inertia identification technique together is developed to provide robustness against the variations of inertia. However, this adaptive controller requires full system states and the updated inertia information by using inertia identification techniques, and the cases of load torque disturbance and other parameter variations have not been considered in detail. In [127], a composite

control frame based on the extend state observer (ESO) is developed to achieve a satisfactory position response in the presence of inertia load variation or load disturbance. However, this research treats only the position control, the speed control and performance robustness of the position control to other parameter variations are desired to be extended. In [78], a robust current-control scheme for a PMSM with a linear discrete disturbance observer is developed to provide robustness against electrical parameters variations and an efficient solution for torque-ripple minimization in PMSM drives. However, the load torque disturbance has not been considered.

In this chapter, nonlinear adaptive controller (NAC) is developed for PMSM to track mechanical rotation speed and provide high robustness against system parameter uncertainties and unknown time-varying load disturbances. In addition, a nonlinear controller with an extended nonlinear observer (NCENO) based on the control method proposed in [125] is used for speed control of the PMSM in d-q model. In the NCENO design, the mechanical rotation speed, rotor position and stator current are required to be measured, only the unknown load torque and its derivative are estimated by the ENO. The designed NAC improves the NCENO adaptivity to parameter uncertainties. The NAC proposed will be compared with the NCENO and VC in simulation and experiment studies under different situations.

The remaining parts of this chapter is organized as follows. In Section II, the PMSM is reviewed. The design of the NAC, based on a FLC, is presented in Section III. Section IV carries out simulation and experimental results to verify the performance of the proposed NAC, compared with the VC and NCENO. Finally, conclusions of this chapter are presented in Section V.

6.2   Permanent Magnet Synchronous Motor Model

The state-space model of the PMSM is given as [112]:

$$\dot{x} = f(x) + g_1(x)u_1 + g_2(x)u_2 \qquad (6.2.1)$$

where

$$f(x) = \begin{bmatrix} -\frac{R_s}{L_{md}}i_{md} + \frac{w_e L_{mq}}{L_{md}}i_{mq} \\ -\frac{R_s}{L_{mq}}i_{mq} - \frac{1}{L_{mq}}w_e(L_{md}i_{md} + K_e) \\ \frac{1}{J_{tot}}(T_e - T_m - T_f - Bw_m) \end{bmatrix},$$

$$g_1(x) = [\frac{1}{L_{md}} \quad 0 \quad 0]^T,$$

$$g_2(x) = [0 \quad \frac{1}{L_{mq}} \quad 0]^T,$$

$$x = [i_{md} \quad i_{mq} \quad w_m]^T,$$

$$u = [u_1, u_2]^T = [V_{md}, V_{mq}]^T,$$

$$y = [y_1, y_2]^T = [h_1(x), h_2(x)]^T = [i_{md}, w_m]^T$$

where $x \in R^3$, $u \in R^2$ and $y \in R^2$ are state vector, input vector and output vector, respectively; $f(x)$, $g(x)$ and $h(x)$ are smooth vector fields. V_{md} and V_{mq} are the stator voltages in the d-q axis, i_{md} and i_{mq} are the stator currents in the d-q axis, R_s is the stator resistance, L_{md} and L_{mq} are d-q axis inductances, K_e is the permanent magnetic flux given by the magnets, p is the number of pole pairs, J_{tot} is the total inertia of the drive train that is equal to the summation of WT inertia constant and generator inertia constant, B is the friction coefficient of the motor, $w_e(= pw_m)$ is the electrical generator rotation speed, and T_m, T_e, T_f and $T_d = T_m + T_f$ are the load torque, electromagnetic torque, static friction torque and disturbance torque, respectively.

The electromagnetic torque is expressed as:

$$T_e = p[(L_{md} - L_{mq})i_{md}i_{mq} + i_{mq}K_e] \tag{6.2.2}$$

6.3 Design of Nonlinear Adaptive Controller

6.3.1 Input-output Linearisation

For system (6.2.1), choose the output of the first subsystem as $y_1 = h_1(x) = i_{md}$ and output of the second subsystem as $y_2 = h_2(x) = w_m$, we have

$$\begin{bmatrix} y_1^{(1)} \\ y_2^{(2)} \end{bmatrix} = \begin{bmatrix} F_1(x) \\ F_2(x) \end{bmatrix} + B(x) \begin{bmatrix} u_1 \\ u_2 \end{bmatrix} \tag{6.3.1}$$

where

$$F_1(x) = \frac{1}{L_{\mathrm{md}}}(-i_{\mathrm{md}}R_{\mathrm{s}} + w_{\mathrm{e}}L_{\mathrm{mq}}i_{\mathrm{mq}}) \tag{6.3.2}$$

$$F_2(x) = -\frac{p}{J_{\mathrm{tot}}L_{\mathrm{mq}}}[K_e + (L_{\mathrm{md}} - L_{\mathrm{mq}})i_{\mathrm{md}}](L_{\mathrm{md}}w_{\mathrm{e}}i_{\mathrm{md}}$$

$$+ R_{\mathrm{s}}i_{\mathrm{mq}} + w_{\mathrm{e}}K_e) + \frac{pi_{\mathrm{mq}}(L_{\mathrm{md}} - L_{\mathrm{mq}})}{J_{\mathrm{tot}}L_{\mathrm{md}}}(-R_{\mathrm{s}}i_{\mathrm{md}}$$

$$+ L_{\mathrm{mq}}w_{\mathrm{e}}i_{\mathrm{mq}}) - \frac{1}{J_{\mathrm{tot}}}(\frac{dT_{\mathrm{m}}}{dt} + \frac{dT_{\mathrm{f}}}{dt})$$

$$- \frac{B}{J_{\mathrm{tot}}^2}[p(L_{\mathrm{md}} - L_{\mathrm{mq}})i_{\mathrm{md}}i_{\mathrm{mq}} + pi_{\mathrm{mq}}K_e - T_{\mathrm{m}}$$

$$- T_{\mathrm{f}} - Bw_{\mathrm{m}}) \tag{6.3.3}$$

$$B(x) = \left[\begin{array}{c} B_1(x) \\ B_2(x) \end{array} \right] = \left[\begin{array}{cc} \frac{1}{L_{\mathrm{md}}} & 0 \\ \frac{pi_{\mathrm{mq}}(L_{\mathrm{md}} - L_{\mathrm{mq}})}{J_{\mathrm{tot}}L_{\mathrm{md}}} & \frac{p[K_e + (L_{\mathrm{md}} - L_{\mathrm{mq}})i_{\mathrm{md}}]}{J_{\mathrm{tot}}L_{\mathrm{mq}}} \end{array} \right] \tag{6.3.4}$$

As $det[B(x)] = \frac{p[K_e + (L_{\mathrm{md}} - L_{\mathrm{mq}})i_{\mathrm{md}}]}{J_{\mathrm{tot}}L_{\mathrm{md}}L_{\mathrm{mq}}} \neq 0$ when $K_e \neq 0$, that is, $B(x)$ is non-singular for all nominal operation points. The system (6.2.1) has relative degree $r_i = \begin{bmatrix} 1 & 2 \end{bmatrix}$.

6.3.2 Perturbation and Fictitious State

Assume all nonlinearities of system (6.3.1) are unknown, and define perturbation terms as

$$\left[\begin{array}{c} \Psi_1 \\ \Psi_2 \end{array} \right] = \left[\begin{array}{c} F_1(x) \\ F_2(x) \end{array} \right] + (B(x) - B_0)\left[\begin{array}{c} u_1 \\ u_2 \end{array} \right] \tag{6.3.5}$$

where Ψ_i is the perturbation term, $B_0 = B(x)|_{x=x(0)}$ is the nominal control gain. Then system (6.3.1) can be rewritten as

$$\left[\begin{array}{c} y_1^{(1)} \\ \\ y_2^{(2)} \end{array} \right] = \left[\begin{array}{c} \Psi_1(x) \\ \Psi_2(x) \end{array} \right] + B_0\left[\begin{array}{c} u_1 \\ u_2 \end{array} \right] \tag{6.3.6}$$

For the first subsystem, defining state variables as $z_{11} = y_1$, and a fictitious state to represent the perturbation $z_{12} = \Psi_1$, the first subsystem can be represented as

$$\begin{cases} z_{11} & = & y_1 \\ \dot{z}_{11} & = & z_{12} + B_{0_1}u \\ \dot{z}_{12} & = & \dot{\Psi}_1 \end{cases} \tag{6.3.7}$$

where B_{0_1} is the first row of the B_0, $B_{0_{ij}}$ is the ith row j^{th} column element of the B_0.

For the second subsystem, defining state variables as $z_{21} = y_2$ and $z_{22} = y_2^{(1)}$, and a fictitious state to represent the perturbation $z_{23} = \Psi_2$, the first subsystem can be represented as

$$\begin{cases} z_{21} & = & y_2 \\ \dot{z}_{21} & = & z_{22} \\ \dot{z}_{22} & = & z_{23} + B_{0_2}u \\ \dot{z}_{23} & = & \dot{\Psi}_2 \end{cases} \tag{6.3.8}$$

where B_{0_2} is the second row of the B_0.

For subsystems (6.3.7) and (6.3.8), several types of perturbation observers, such as sliding mode observer, high gain observer and linear Luenberger observer, have been proposed [65]. This chapter uses high gain observer, while other types observers can be designed similarly.

6.3.3 States and Perturbation Observer

When all states are available, the perturbation of the first subsystem is estimated by a second-order perturbation observer (PO) which uses the last state z_{11} as measurement as follows

$$\begin{cases} \dot{\hat{z}}_{11} & = & \hat{z}_{11} + l_{11}(z_{11} - \hat{z}_{11}) + B_{0_1}u_i \\ \dot{\hat{z}}_{12} & = & l_{12}(z_{12} - \hat{z}_{12}), \end{cases} \tag{6.3.9}$$

where $\hat{z}_{ij}$ is the estimations of z_{ij}, and l_{1j}, $j = 1,2$ are gains of the high gain observer. By choosing

$$l_{1j} = \frac{\alpha_{1j}}{\epsilon_1^j}, j = 1,2 \tag{6.3.10}$$

where ϵ_1^j, $0 < \epsilon_1 < 1$ is a positive constant to be specified and the positive constants α_{1j}, j=1,2, are chosen such that the roots of

$$s^2 + \alpha_{11}s + \alpha_{12} = 0 \tag{6.3.11}$$

are in the open left-half complex plan.

When the second subsystem output $y_2 = z_{21}$ is available, a third-order states and perturbation observer (SPO) can be designed to estimate the system states and perturbation as

$$\begin{cases} \dot{\hat{z}}_{21} &= \hat{z}_{22} + l_{21}(z_{21} - \hat{z}_{21}) \\ \dot{\hat{z}}_{22} &= \hat{z}_{23} + l_{22}(z_{21} - \hat{z}_{21}) + B_{0_2}u \\ \dot{\hat{z}}_{23} &= l_{23}(z_{21} - \hat{z}_{21}), \end{cases} \tag{6.3.12}$$

where $\hat{z}_{ij}$ is the estimations of z_{ij}, $l_{1j} = \frac{\alpha_{1j}}{\epsilon_2^j}$, $j = 1, 2, 3, 4$ are gains of the high gain observer, ϵ_2, $0 < \epsilon_2 < 1$ is a small positive parameter to be specified to represent times of the time-dynamics between the observer and the real system. The parameters α_{2j}, $j = 1, 2, 3, 4$, are chosen such that the roots of

$$s^3 + \alpha_{21}s^2 + \alpha_{22}s + \alpha_{23} = 0 \tag{6.3.13}$$

are in the open left-half complex plan.

6.3.4 Nonlinear Adaptive Controller

For sub-system q_1, a second-order PO like (6.3.9) is designed to estimate the perturbation $\hat{z}_{12} = \hat{\Psi}_1$; and for sub-system q_2, a third-order SPO like (6.3.12) is designed to estimate the $\hat{z}_{22}$ and perturbation $\hat{z}_{23} = \hat{\Psi}_2$. By using the estimated perturbation to compensate the real perturbation, control laws for sub-systems q_1 and q_2 can be obtained as following:

$$\begin{bmatrix} u_1 \\ u_2 \end{bmatrix} = B_0^{-1} \left[\begin{bmatrix} -\hat{z}_{12} \\ -\hat{z}_{23} \end{bmatrix} + \begin{bmatrix} v_1 \\ v_2 \end{bmatrix} \right] \tag{6.3.14}$$

where $v_{1,2}$ is defined as
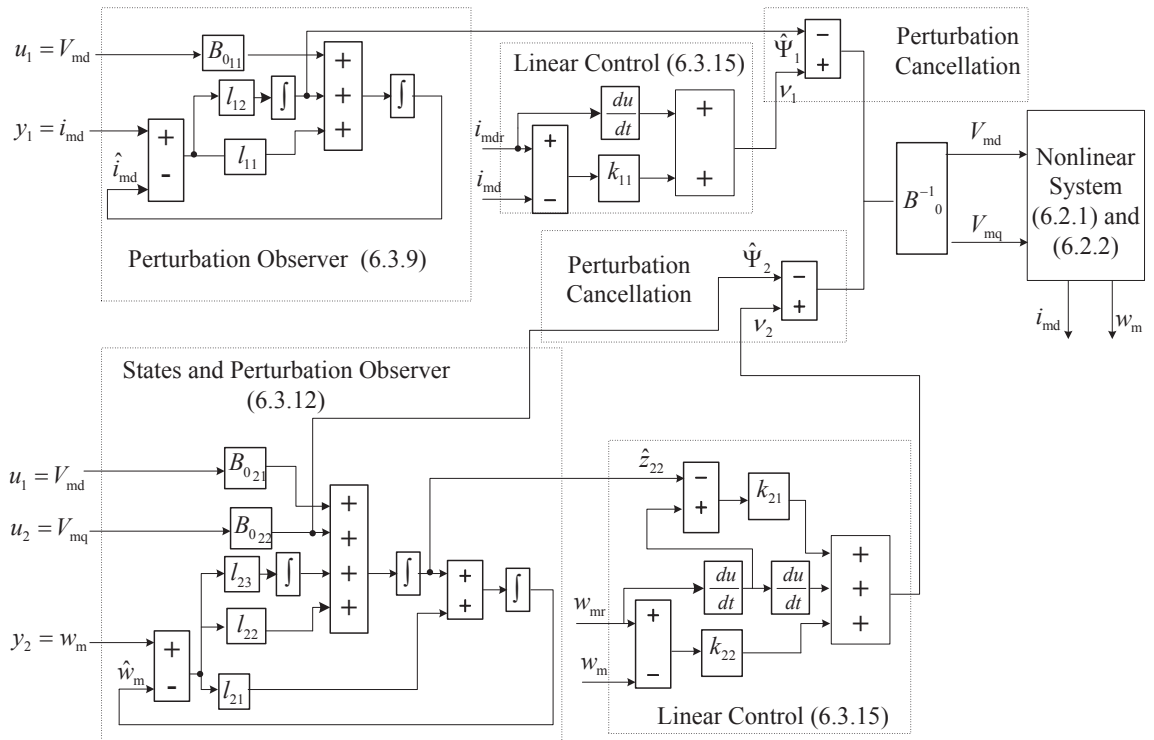
Figure 6.1: Block diagram of nonlinear adaptive controller

$$\begin{cases} v_1 &= k_{11}(z_{11r} - z_{11}) + \dot{z}_{11r} \\ v_2 &= \ddot{z}_{21r} + k_{22}(z_{21r} - z_{21}) \\ &\quad + k_{21}(\dot{z}_{21r} - \hat{z}_{22}) \end{cases} \qquad (6.3.15)$$

The final control law represented by physical variables, such as current, inductance, total inertia, field flux and mechanical rotation speed, are given as following:

$$\begin{cases} u_1 = L_{md0}[k_{11}(i_{mdr} - i_{md}) + \dot{i}_{mdr} - \hat{\Psi}_1] \\ u_2 = -\frac{i_{mq}L_{mq0}(L_{md0} - L_{mq0})}{K_{e0} + (L_{md0} - L_{mq0})i_{md}}[k_{11}(i_{mdr} - i_{md}) + \dot{i}_{mdr} - \hat{\Psi}_1] \\ \quad + \frac{J_{tot0}L_{mq0}}{p[K_{e0} + (L_{md0} - L_{mq0})i_{md}]}[k_{22}(w_{mr} - w_m) \\ \quad + k_{21}(\dot{w}_{mr} - \hat{z}_{22}) + \ddot{w}_{mr} - \hat{\Psi}_2] \end{cases} \qquad (6.3.16)$$

Note that in the controller design, the NAC proposed only requires the nominal value of parameters of L_{md0}, L_{mq0}, K_{e0} and J_{tot0}, measurements of two output variables i_{md} and w_m, and i_q=5 A is chosen.

The following parameters are used in the VC employed in the speed and current control loops. Speed control loop: $k_p = 2$; $k_i = 4$. Current control loops: $k_p = 2$; $k_i = 6$.

Parameters of NACs for subsystem q_1 and q_2 are designed based on pole-placement and listed as following:

q_1 : observer: $\alpha_{11} = 3.2 \times 10^2$, $\alpha_{12} = 2.56 \times 10^4$, $\epsilon_1 = 1 \times 10^{-2}$; controller: $k_{11} = 4 \times 10^1$.

q_2 : observer: $\alpha_{21} = 2.1 \times 10^2$, $\alpha_{22} = 1.47 \times 10^4$, $\alpha_{23} = 3.43 \times 10^5$, $\epsilon_2 = 2 \times 10^{-2}$; controller: $k_{21} = 2.2 \times 10^1$, $k_{22} = 4.84 \times 10^2$.

To clearly illustrate its principle, block diagram of the NAC proposed is shown in Fig. 6.1.

6.4 Simulation and Experimental Results

To validate the effectiveness of the proposed NAC, simulation and experimental results are presented. For simulation and experiment, the specifications of the

PMSM are given as follows: rated power $P_{\text{reted}} = 250$ W; rated current (RMS) $I_{\text{rated}} = 5.7$ A; rated voltage $V_{\text{rated}} = 42$ V; rated speed $w_{\text{rated}} = 4000$ RPM, $p = 5$; $R = 0.19\,\Omega$; $L_{\text{d}} = L_{\text{q}} = 0.49$ mH; $K_e = 0.0151$ V.s/rad; $B = 2.6 \times 10^{-3}$ N.m.s/rad; $J = 1.23 \times 10^{-3}$ Kg.m^2; and static friction torque $T_{\text{f}} = 0.121$ N.m.

Note that the simulation and experiment use the same set of controller parameters.

6.4.1   Simulation Results

Case 1: Constant Mechanical Rotation Speed

The reference mechanical rotation speed w_{m} and a unknown step-change load torque T_{m} are shown in Fig. 6.2 (a) and (b), respectively. It can be seen from Fig. 6.2 (c) and (d) that, the NAC can achieve the best tracking performance of the mechanical rotation speed w when the unknown step-change load torque is applied. The maximum relative error ($\frac{w_{\text{m}} - w_{\text{mref}}}{w_{\text{mref}}} \times 100\%$) is approximately 4% and 3% under the VC and NCENO, respectively. Although the performance of the NAC is little impacted by the unknown load torque variation, the maximum relative error ($\frac{w_{\text{m}} - w_{\text{mref}}}{w_{\text{mref}}} \times 100\%$) is less than 1%. The voltage and current responses are shown in Fig. 6.3. From Fig. 6.3, it can be seen that both the VC, NCENO and NAC can keep the i_{d} around 0.

The estimates of the states and perturbations are shown in Fig. 6.4-6.7. It can be seen from Fig. 6.4-6.7 that, both the states and perturbations can be well estimated by the observers. The estimated perturbations including nonlinearities, uncertainties and disturbance are used for compensation.

Case 2: Time-Varying Mechanical Rotation Speed

Both the mechanical rotation speed w_{m} and load torque T_{m} vary, which are shown in Fig. 6.8 (a) and (b), respectively. The NAC achieves satisfactory tracking performances of both the w_{m} and i_{md}, and provides high robustness for the load torque disturbance shown in Fig. 6.8 and Fig. 6.9. When both the w_{m} and T_{m} vary, the tracking performance of the w_{m} is not satisfactory and with approximately 2.5% and 2.3% maximum relative error ($\frac{w_{\text{m}} - w_{\text{mref}}}{w_{\text{mref}}} \times 100\%$) under the VC and NCENO, respectively.
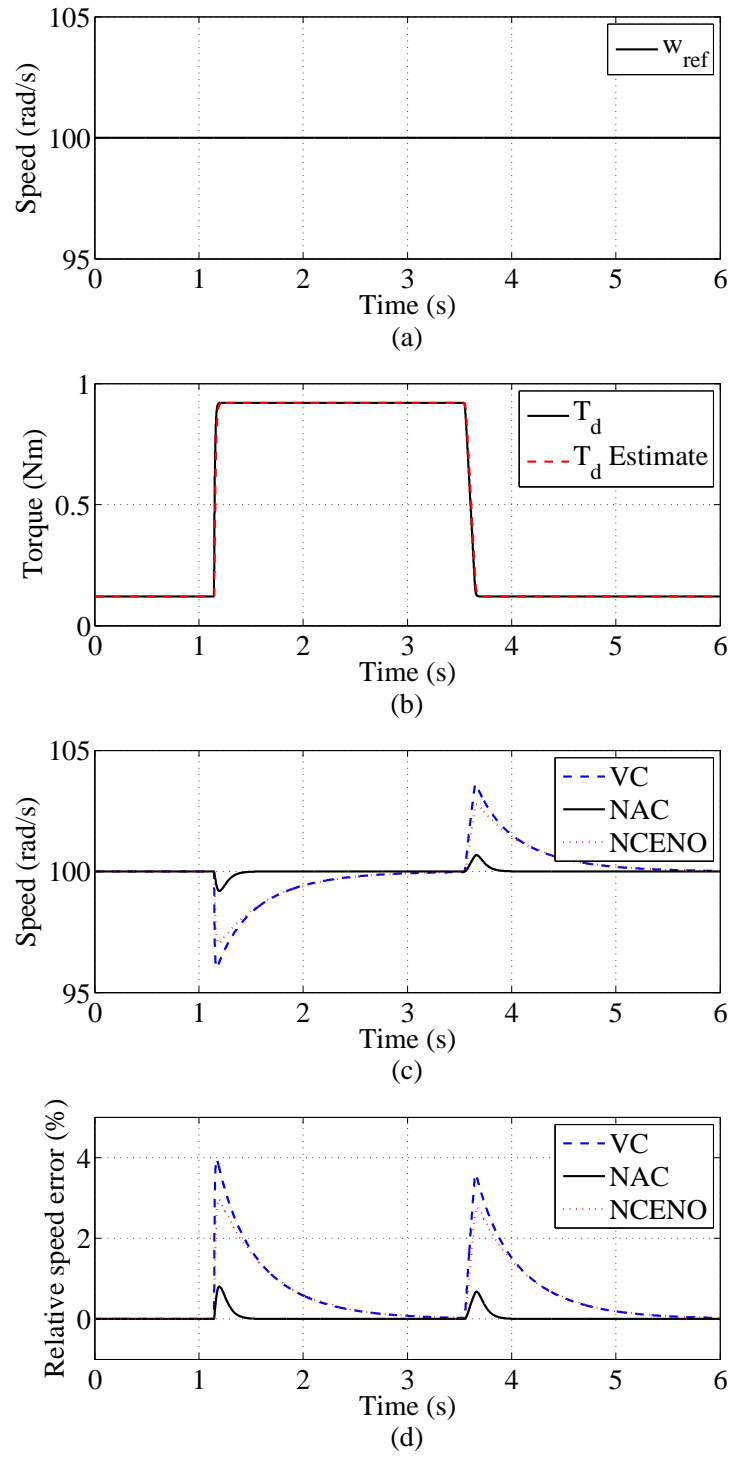
Figure 6.2: Responses of constant mechanical rotation speed under unknown step-change load torque disturbance. (a) Reference mechanical rotation speed w_{ref}; (b) Load torque T_m; (c) Mechanical rotation speed w_m; (d) Relative error of the w_m.

Figure 6.3: Responses of time-varying mechanical rotation speed under unknown time-varying load. (a) d-axis voltage V_{md}; (b) q-axis voltage V_{mq}; (c) d-axis current i_{md}; (d) q-axis current i_{mq}.

Figure 6.4: Estimations of system states and perturbations. (a) z_{11}; (b) Estimate error z_{11}; (c) z_{12}; (d) Estimate error z_{12}.

Figure 6.5: Estimations of system states and perturbations. (e) z_{21}; (f) Estimate error z_{21}; (g) z_{22}; (h) Estimate error z_{22}.
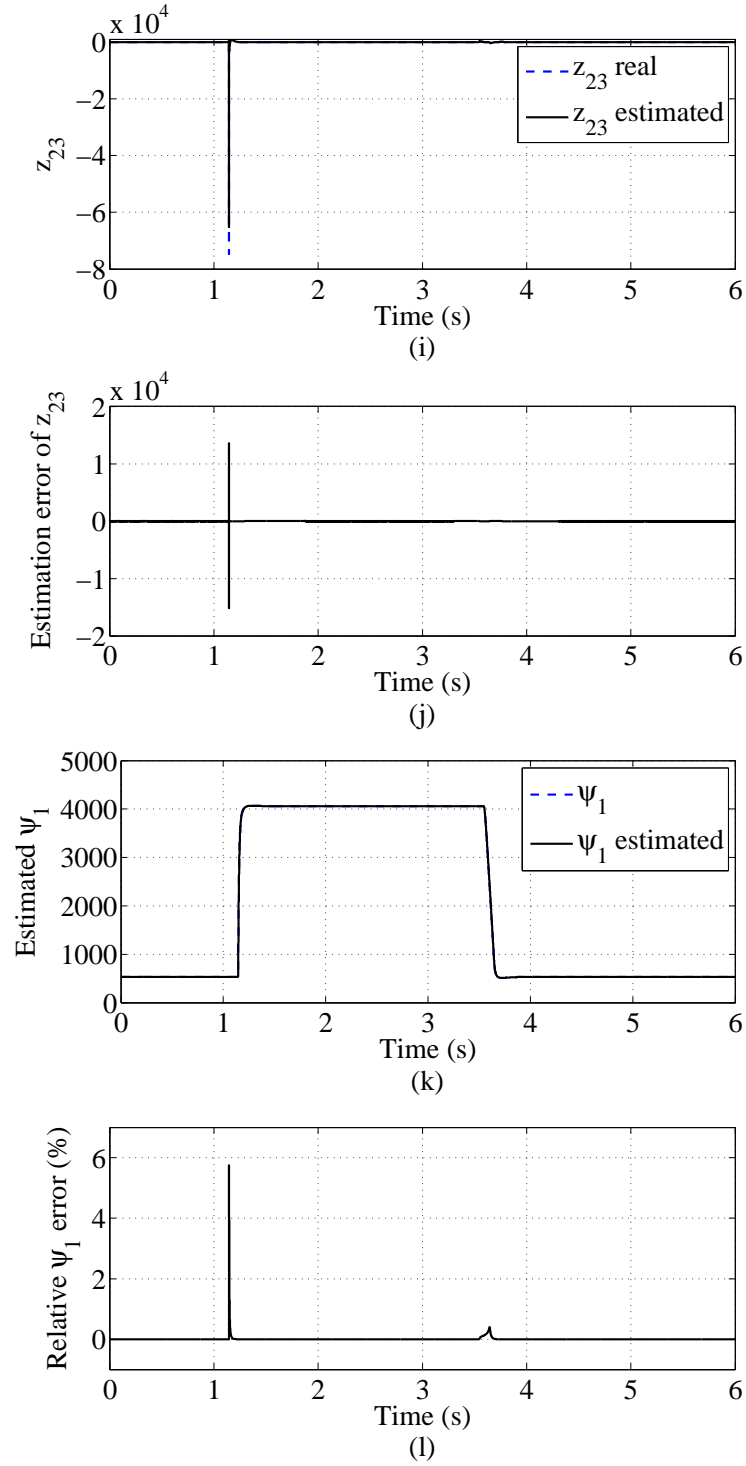
Figure 6.6: Estimations of system states and perturbations. (i) z_{23}; (j) Estimate error z_{23}; (k) Perturbation Ψ_1; (l) Relative error of perturbation Ψ_1.
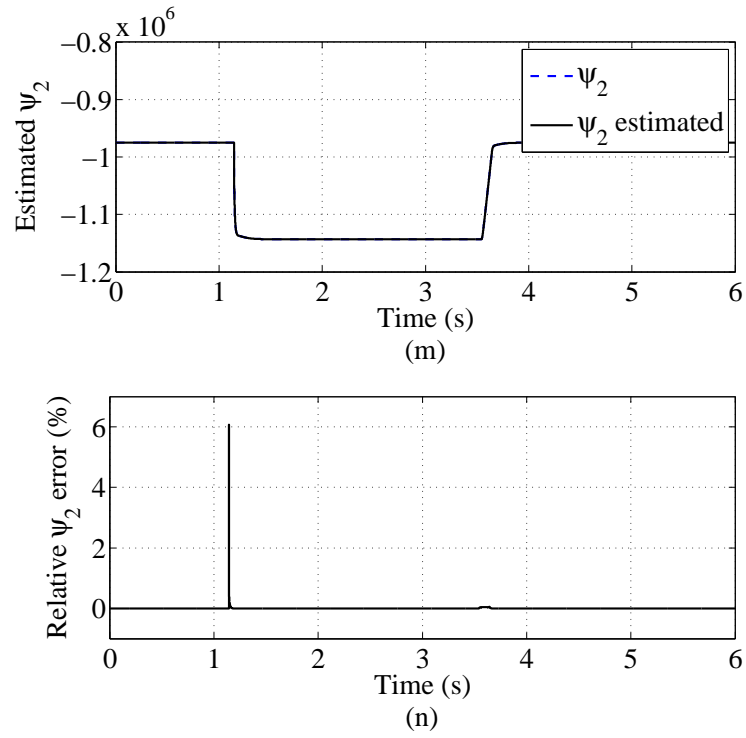
Figure 6.7: Estimations of system states and perturbations. (m) Perturbation Ψ_2; (n) Relative error of perturbation Ψ_2.
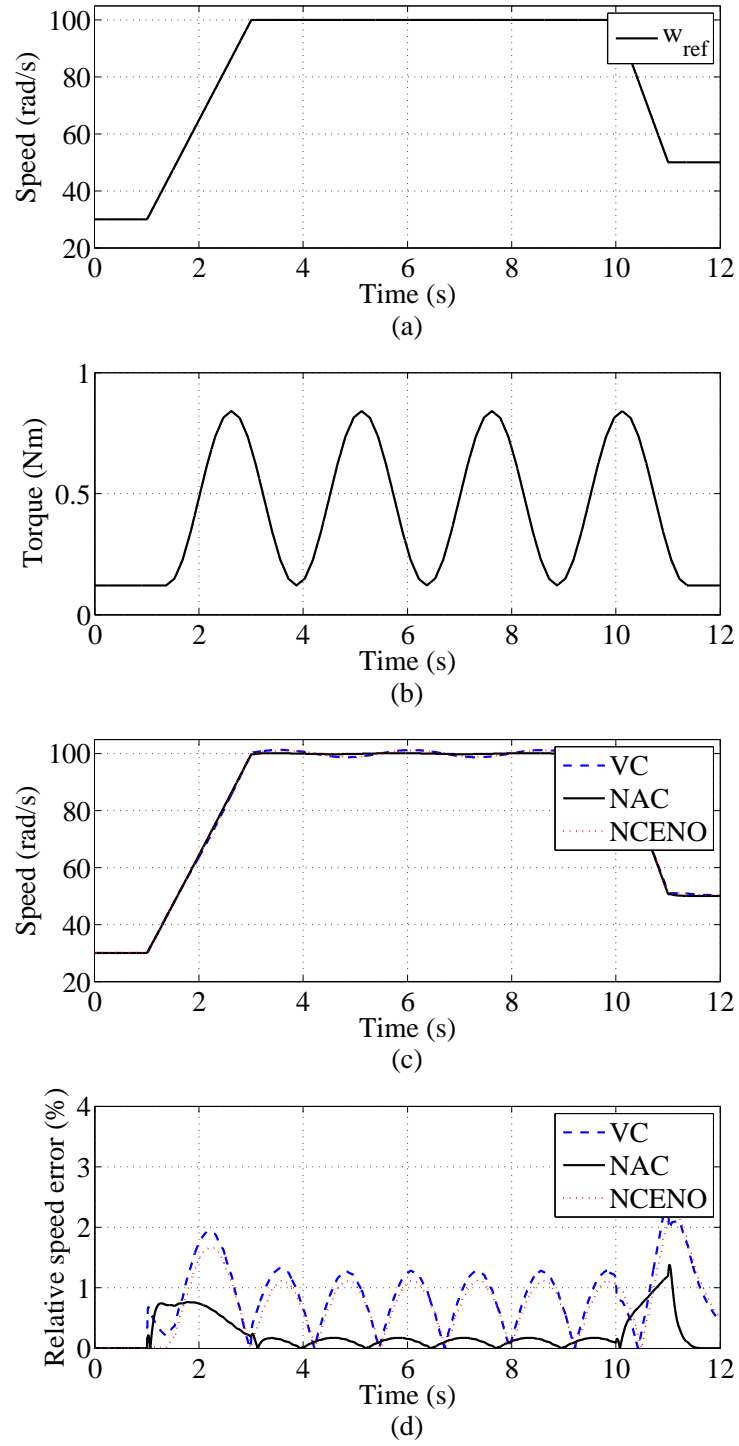
Figure 6.8: Responses of time-varying mechanical rotation speed under unknown time-varying load. (a) Load torque T_{m}; (b) Mechanical rotation speed w_{m}; (c) Relative error of the w_{m}.
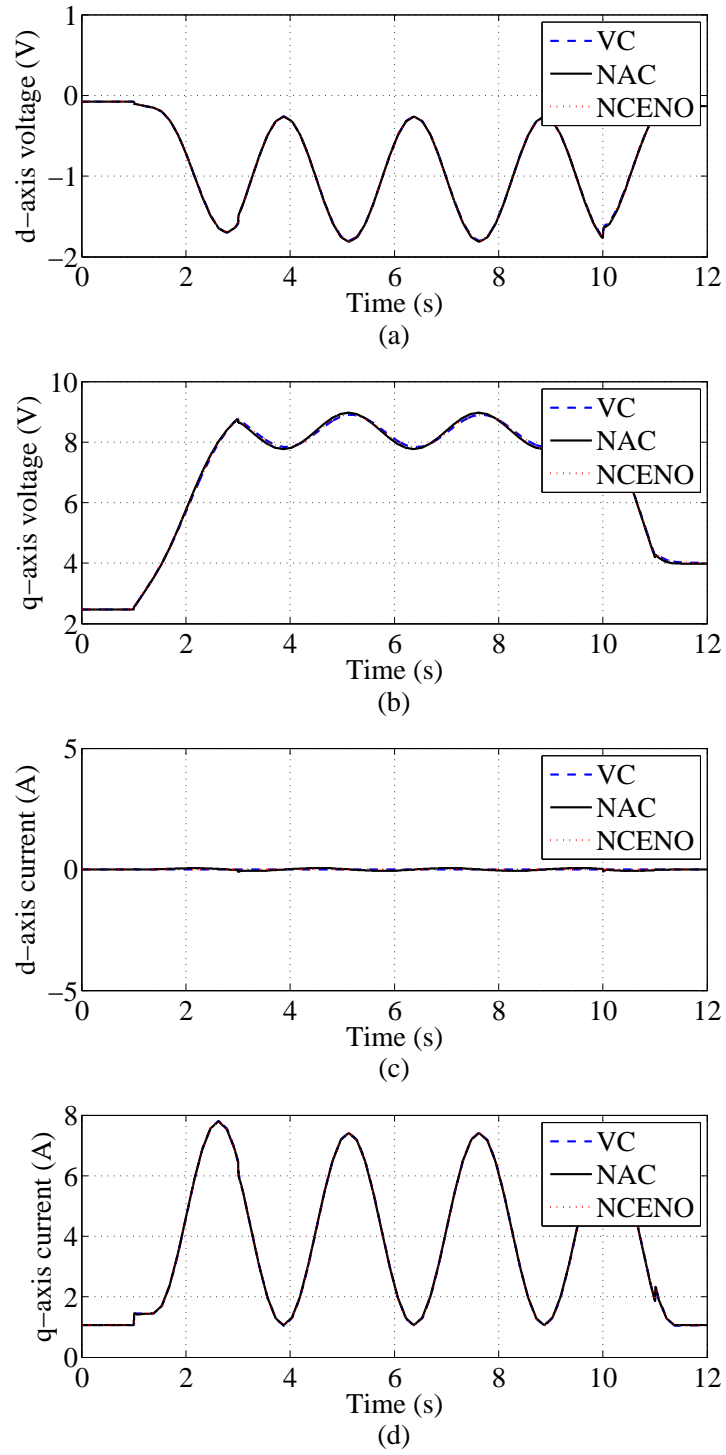
Figure 6.9: Responses of time-varying mechanical rotation speed under unknown time-varying load. (a) d-axis voltage V_{md}; (b) q-axis voltage V_{mq}; (c) d-axis current i_{md}; (d) q-axis current i_{mq}.
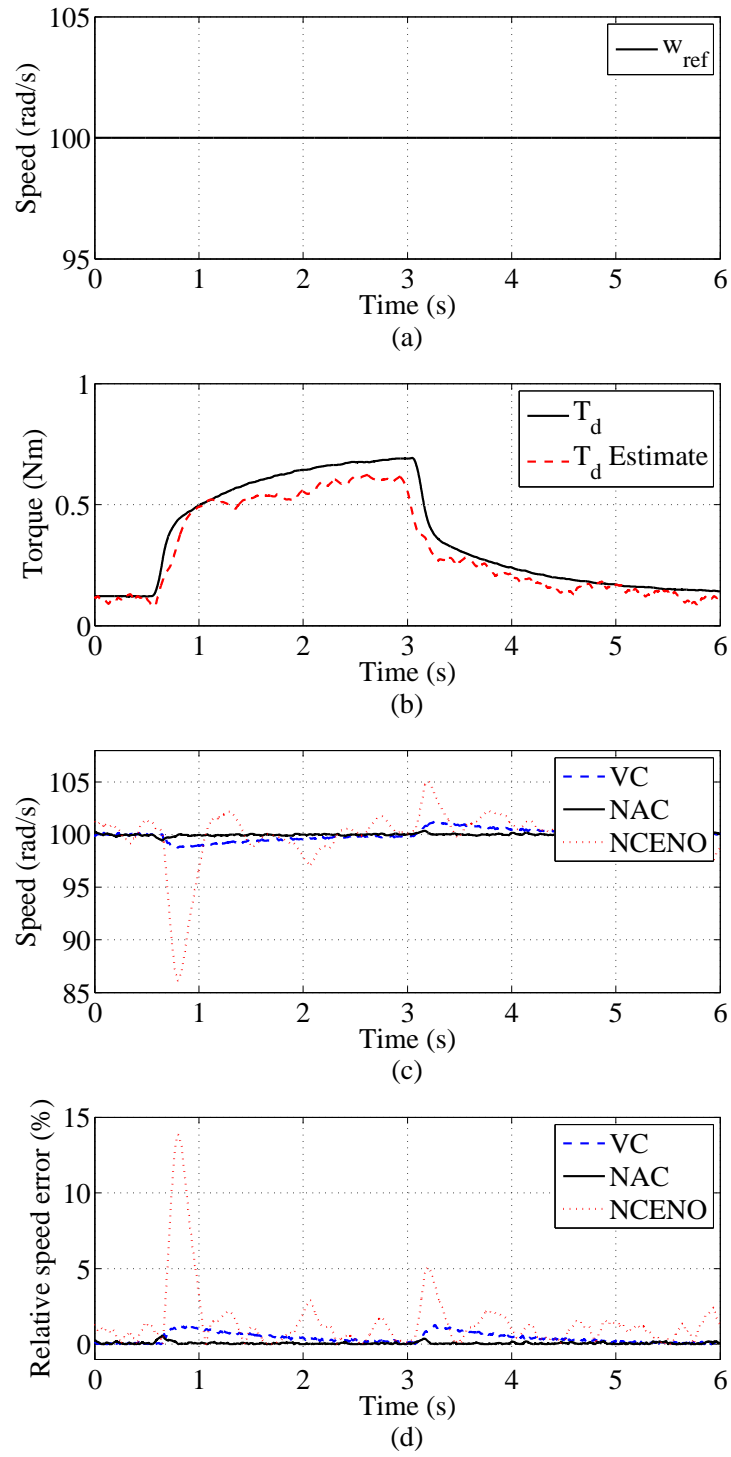
Figure 6.10: Responses of constant mechanical rotation speed under unknown step-change load torque disturbance. (a) Reference mechanical rotation speed w_{ref}; (b) Load torque T_{m}; (c) Mechanical rotation speed w_{m}; (d) Relative error of the w_{m}.
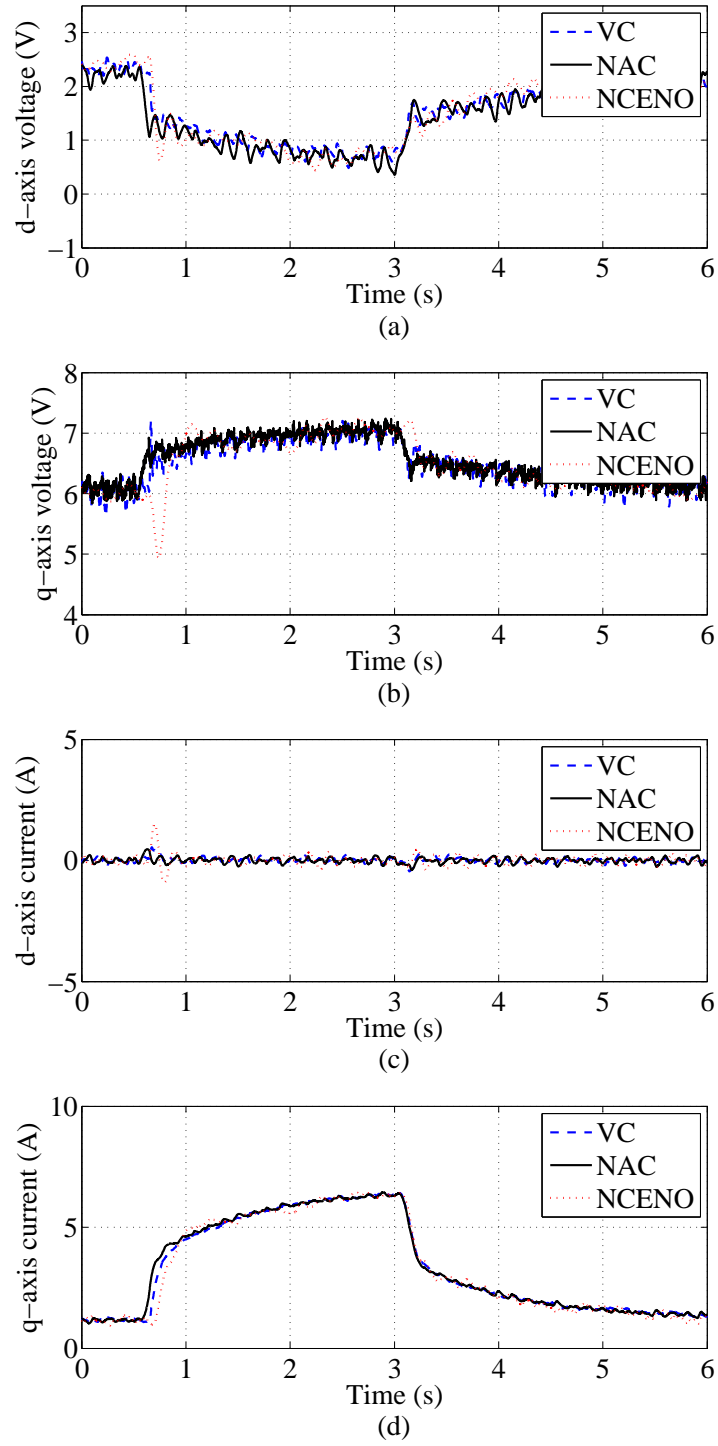
Figure 6.11: Responses of time-varying mechanical rotation speed under unknown time-varying load. (a) d-axis voltage V_{md}; (b) q-axis voltage V_{mq}; (c) d-axis current i_{md}; (d) q-axis current i_{mq}.
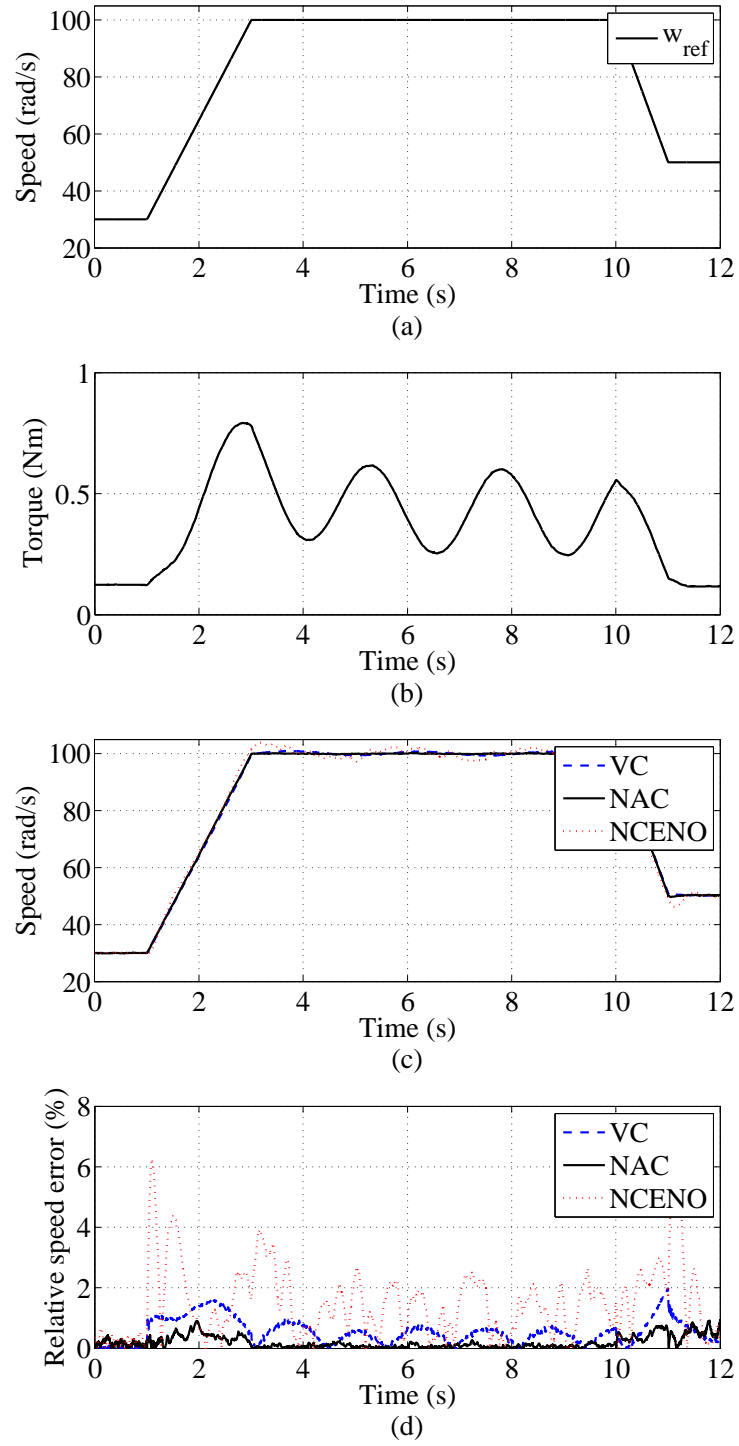
Figure 6.12: Responses of time-varying mechanical rotation speed under unknown time-varying load. (a) Load torque T_{m}; (b) Mechanical rotation speed w_{m}; (c) Relative error of the w_{m}.
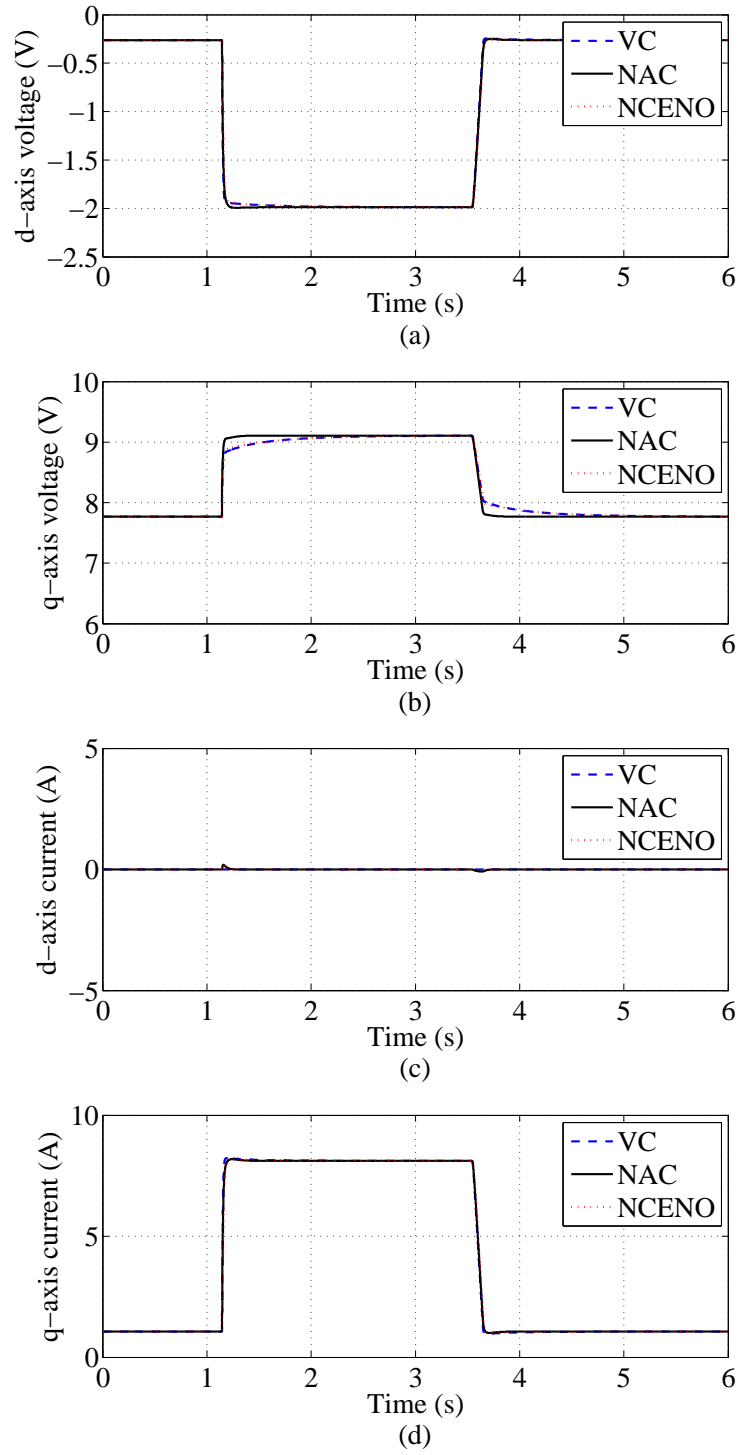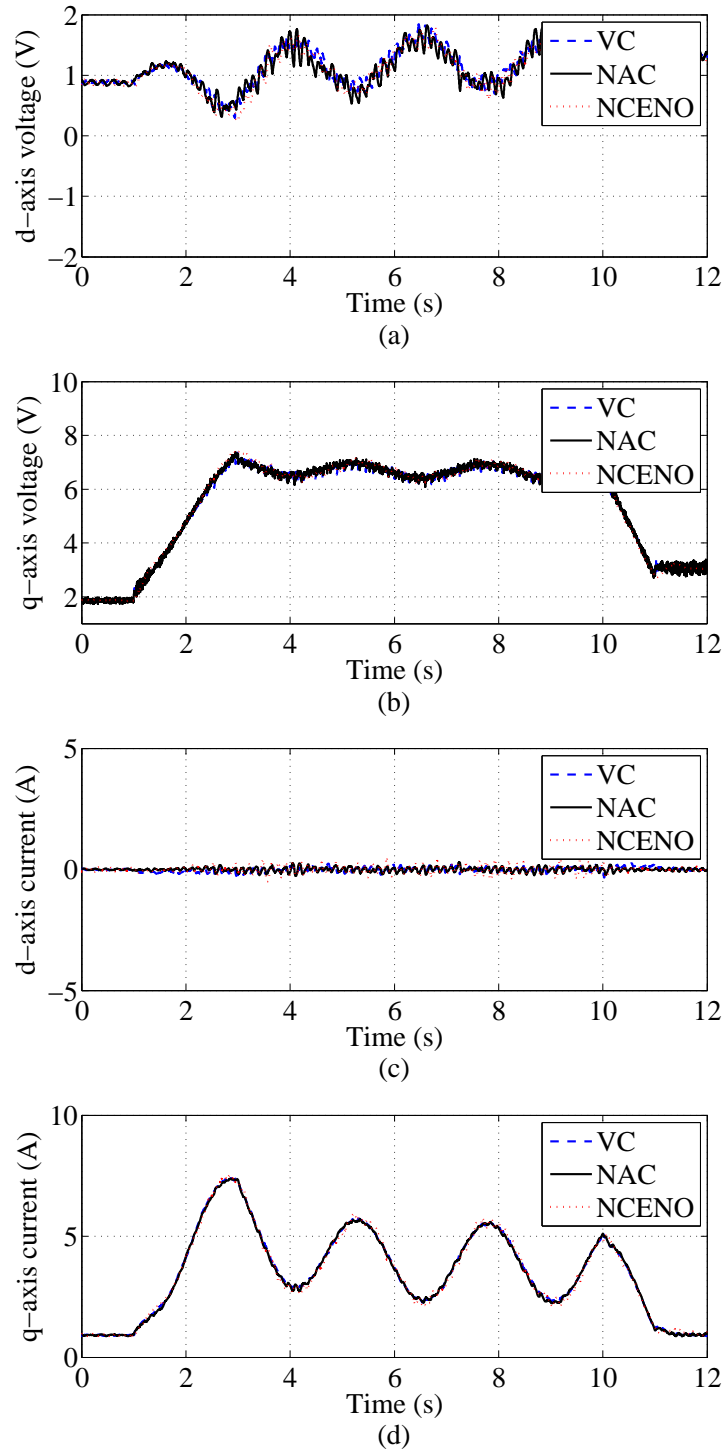
Figure 6.13: Responses of time-varying mechanical rotation speed under unknown time-varying load. (a) d-axis voltage V_{md}; (b) q-axis voltage V_{mq}; (c) d-axis current i_{md}; (d) q-axis current i_{mq}.
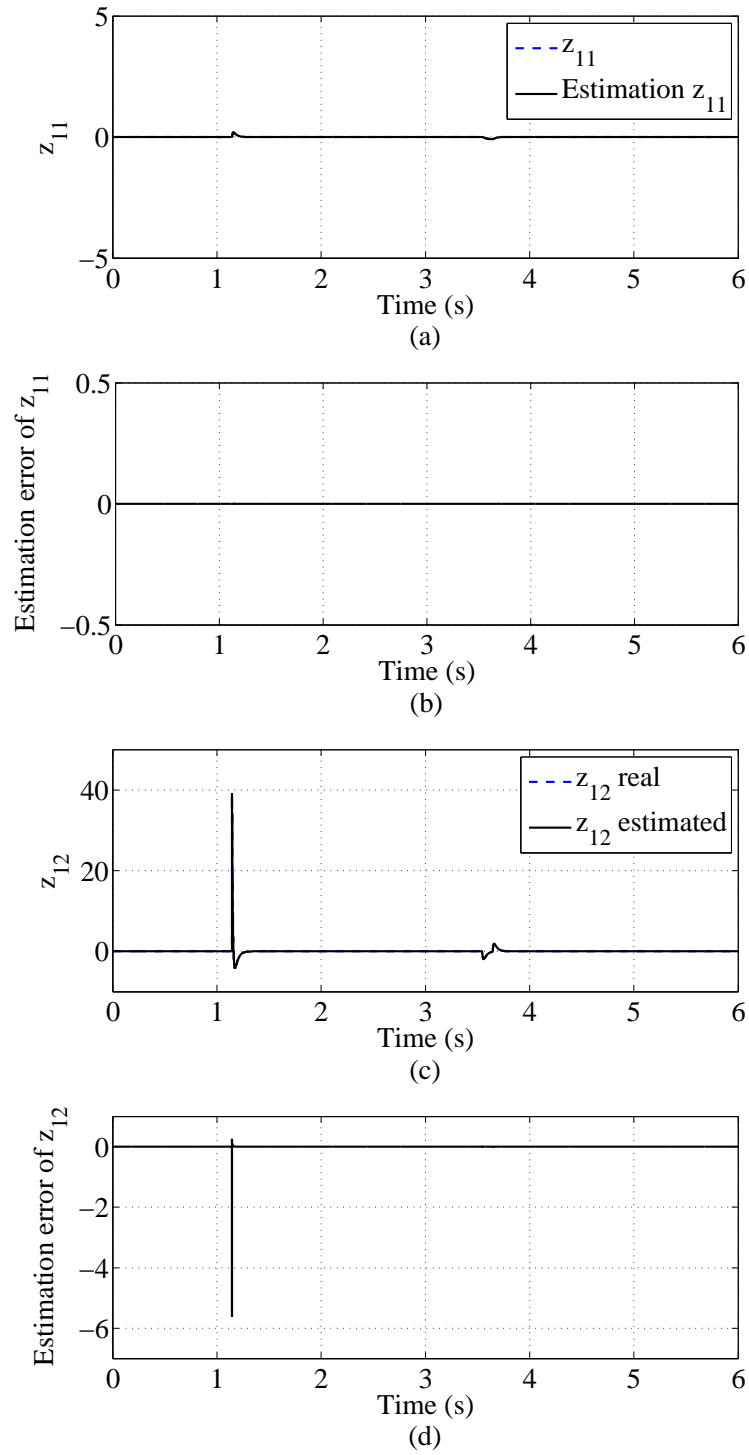
6.4.2 Experimental Results

The experiment tests have been done to verify the effectiveness of the proposed NAC. The experiment setup is the same as that in Section 2.5. The PMSM is coupled with a DC motor which is used to produce load torque to PMSM.

Case 1: Constant Mechanical Rotation Speed

Figs. 6.10 and 6.11 show the experiment results. In this test, the unknown load torque T_m is provide by the DC motor, which is different with the load torque in simulation test shown in Fig. 6.2 (b). Fig. 6.10 (a) and (b) shows the reference mechanical rotation speed w_{ref} and unknown time-varying load torque T_m, respectively. The mechanical rotation speed w_m and relative error ($\frac{w_m - w_{mref}}{w_{mref}} \times 100\%$) are shown in Fig. 6.10 (c) and (d), respectively. Fig. 6.11 shows the d-axis, q-axis stator voltages (V_{md}, V_{mq}), d-axis, and q-axis stator currents (i_{md}, i_{mq}) respectively. From Fig. 6.10 and 6.11, it can be seen that the proposed NAC achieves a better dynamic performance than the VC and NCENO.

Case 2: Time-Varying Mechanical Rotation Speed

In this experiment test case, the applied time-varying load torque T_m is shown in Fig. 6.12 (b). It can be seen form Fig. 6.12 and 6.13 that, the applied unknown load torque affects the system performances under the VC and NCENO. The NAC can provide high robustness against unknown load torque disturbance even when the mechanical rotation speed w_m varies.

## 6.5 Conclusions

This chapter has proposed a perturbation estimation based NAC for PMSM. In the proposed NAC, the observers are designed to estimate the system states and perturbation which includes all unknown and time-varying dynamics of the PMSM, i.e., system parameter uncertainties, nonlinearities and unknown load torque disturbance . The estimates of perturbations are employed to achieve adaptive feedback linearisation. The proposed NAC does not require the detailed knowledge of the nonlinearities, parameters of the PMSM and full state measurements, and considers all system nonlinearities and external disturbances. Both simulation and experi-

Jian Chen

mental results have shown that the proposed NAC can achieve satisfactory dynamic performances in the presence of parameter variations and unknown time-varying load torque disturbance, compared with the structured VC.

Chapter 7

Conclusions, Future Work and Limitation

This chapter has summarised the obtained results of this thesis and contributions. At the end of this chapter, suggestions for future investigations are also listed.

7.1 Conclusions

At the beginning of the thesis, the background, control methodologies, motivations, objectives, and the contributions of this research work have been presented. In order to improve the dynamic performance of the permanent magnet synchronous generator based wind turbine (PMSG-WT), this thesis has focused on the development of advanced control algorithms for the PMSG-WT. Hence, the nonlinear adaptive control (NAC) has been firstly used to control the PMSG-WT and PMSM. In addition, it has improved the performance of the VC and FLC.

For the maximum power point tracking (MPPT) in Region 2, Chapter 2 has proposed a nonlinear adaptive controller for PMSG-WT to extract maximum power from time-varying wind. Both the VC and FLC are applied for MPPT control under time-varying wind. The simulation and experiment results have shown that the proposed NAC extracts the maximum power from wind, realizes a satisfactory dynamic performance and has a high robustness against parameter uncertainties and

measurement noises. It has overcome the drawback of the VC designed based one operating point and the shortcoming of the FLC relying on the full system states and detailed nonlinear system model.

Chapter 3 has proposed a nonlinear adaptive pitch controller for PMSG-WT to limit the extracted power from time-varying wind in Region 3. The simulation results have shown that the proposed NAC can maintain the extracted wind power at rated power in Region 3, and realise a satisfactory dynamic performance without requiring accurate PMSG-WT model, parameters and full state measurements, and considering all system nonlinearities and interaction.

In Chapter 4, a novel NAC for the grid-side converter has been investigated to improve the FRTC of a full-rated converter based variable-speed wind turbine. The proposed controller outperforms the conventional VC by providing a global optimal performance across the whole operation region. It does not require the detailed system model and parameters and is an output feedback controller. Thus, it has a relatively simpler controller and much better robustness than the FLC when there are model uncertainties and unknown disturbances. Comparing with other nonlinear adaptive methods, the proposed NAC can deal with time-varying uncertain dynamics. Performance enhancement has been tested by simulation studies at different voltage dip's levels, and various uncertainties, including model mismatch, measurement noises and time-varying wind power inputs. Simulation results have shown that the proposed NAC can provide satisfactory performances with smaller current and voltage overshoots during grid fault and better robustness against uncertainties, compared with the VC and the model-based FLC. Finally, the proposed NAC can be easily extended to enhance the FRTC of other types of energy sources which are integrated with the grid with a full-rated back-to-back converter, such as solar photovoltaic and energy storage. Further studies will focus on carrying the experimental test of the proposed method on a hardware prototype and investigating its potentiality of dealing with asymmetrical voltage sags.

Chapter 5 has proposed a coordinated nonlinear adaptive control (CNAC) for the GSC and MSC of the WECS based PMSG. The objectives of different operating regions can be achieved by using the NAC. It provides better performances of the

WECS than the VC designed based on optimal operating point and FLC requiring accurate system model and detailed system model in different operating regions. In addition, the nonlinear adaptive pitch control has been used to assist in reducing the extracted wind power to enhance the FRTC of the WECS.

In Chapter 6, a NAC of the PMSM is developed to track mechanical rotation speed. In addition, the conventional VC and NCENO based on the control method proposed in [125] have been used for speed control of the PMSM. Both simulation and experimental results have shown that the proposed NAC achieves satisfactory dynamic performances in the presence of parameter variations and unknown time-varying load torque disturbance.

7.2   Future Work

The possible future work is listed based on the following ideas.

- In Chapter 2, the effectiveness of the NAC in extracting the maximum wind power has been verified by simulation and experiment tests. However, the experiment test is based on a small scale prototype WT emulated by a DC motor. The experiment verification of the NAC based on a real WT is more persuasive.

- In Chapter 3, the simulation studies have been carried out to demonstrate the performance of the proposed nonlinear adaptive control (NAC), based on MATLAB/SIMULINK. In the future work, a NAC of two-mass wind turbine model will be studied and an aeroelastic simulator, FAST, will be used to validate the proposed NAC.

- In Chapter 4, the simulation studies have demonstrated the effectiveness of the proposed nonlinear adaptive control (NAC) in enhancing the fault ride-through capability (FRTC) of a full-rated converter based variable-speed wind turbine. In the future work, the verification of the proposed control strategy can be realised via experiment test.

- In Chapter 5, the proposed control strategy can provide satisfactory dynamic performance and enhance the FRTC of the WECS. It can assist the WECS in reducing the large inrush current when grid voltage dips. However, this control strategy cannot fully limit the increasing current when severe grid voltage dips occur. In the future work, the active crowbars can be used to enhance the FRTC of WECSs to protect the WECS.

- The NAC also can be used for speed control of the induction motor (IM). We have successfully applied the NAC in IM, and the experiment tests have done based dSPACE. It is not included in this thesis. In the future work, a observer will be designed to estimate the rotor flux based on the stator voltage and current.

7.3   Limitations of the NAC

Although the NAC provides satisfactory system performances and high robustness against uncertainties and disturbances, but it still has two major limitations. Firstly, it cannot provide high system performances when the inputs occur step changes. It is because that the observer cannot estimate the perturbation so fast to completely compensate the real perturbation. Secondly, in the real experiment tests, the values of the parameters of the observer cannot be chosen too large, it will expand the system noise influence that may affect the system performances.

References

[1] Y. Zhao, C. Wei, Z. Zhang, and W. Qiao, "A review on position/speed sensorless control for permanent-magnet synchronous machine-based wind energy Conversion systems," *IEEE J. Emerging Sel. Top. Power Electron.*, vol. 1, no. 4, pp. 203-216, Dec. 2013.

[2] J. Yang, "Fault analysis and protection for wind power generation systems," *Ph.D. Thesis*, University of Glasgow, Mar. 2011.

[3] British Wind Energy Association. Offshore Wind. Available: http://www.bwea.com/offshore/index.html, 2010.

[4] H. Li and Z. Chen, "Overview of different wind generator systems and their compaisons," *IET Renew. Power Gener.*, vol. 2, no. 2, pp. 123-138, Jun. 2008.

[5] M. E. Haque, Y. C. Saw, and M. M. Chowdhury, "Advanced control scheme for an IPM synchronous generator-based gearless variable speed wind turbine," *IEEE Trans. Sustainable Energy*, vol. 5, no. 2, pp. 354-362, Apr. 2014.

[6] Y. S. Kim, I. Y. Chung, and S. I. Moon, "An analysis of variable-speed wind turbine power-control methods with fluctuating wind speed," *Energies*, vol. 6, no. 7, pp. 3323-3338, Jul. 2013.

[7] R. Pena, J.C. Clare and G.M. Asher, "Doubly fed induction generator using back-to-back PWM converters and its application to variable speed wind-energy generation," *IET Electr. Power Appl.*, vol. 143, no. 3, pp. 231-241, May 1996.

[8] M. Chinchilla, S. Arnaltes, and J. C. Burgos, "Control of permanent-magnet generators applied to variable-speed wind-energy systems connected to the grid," *IEEE Trans. Energy Convers.*, vol. 21, no. 1, pp. 130-135, Mar. 2006.

[9] M. E. Haque, M. Negnevitsky, and K. M. Muttaqi, "A novel control strategy for a variable-speed wind turbine with a permanent-magnet synchronous generator," *IEEE Trans. Ind. Appl.*, vol. 46, no. 1, pp. 331-339, Jan./Feb. 2010.

[10] J. RIbrant and L. M. Bertling, "Survey of failures in wind power systems with focus on Swedish wind power plants during 19972005," *IEEE Trans. Energy Convers.*, vol. 22, no. 1, pp. 167-173, Mar. 2007.

[11] C. M. Hong, C. H. Chen, and C. S. Tu, "Maximum power point tracking-based control algorithm for PMSG wind generation system without mechanical sensors," *Energy Convers. Manage.*, vol. 69, pp. 58-67, May 2013.

[12] S. M. Muyeen, A. Al-Durra, and J. Tamura, "Variable speed wind turbine generator system with current controlled voltage source inverter," *Energy Convers. Manage.*, vol. 52, no. 7, pp. 2688-2694, Jul. 2011.

[13] M. Seixas, R. Relício, and V. M. F. Mendes, "Fifth harmonic and sag impact on PMSG wind turbines with a balancing new strategy for capacitor voltages," *Energy Convers. Manage.*, vol. 79, no. 7, pp. 721-730, Mar. 2014.

[14] M. L. Corradini, G. Ippoliti, and G. Orlando, "Robust control of variable-speed wind turbines based on an aerodynamic torque observer," *IEEE Trans. Control Syst. Technol.*, vol. 21, no. 4, pp. 1199-1206, Jun. 2013.

[15] A. D. Hansen and G. Michalke, "Multi-pole permanent magnet synchronous generator wind turbines' grid support capability in uninterrupted operation during grid faults," *IET Renew. Power Gener.*, vol. 3, no. 3, pp. 333-348, Sep. 2009.

[16] J. A. Baroudi, V. Dinavahi, and A. M. Knight, "A review of power converter topologies for wind generators," *Renewable Energy*, vol. 32, no. 14, pp. 2369-2385, Nov. 2007.

[17] S. H. Li, T. A. Haskew, R. P. Swatloski, and W. Gathings, "Optimal and direct-current vector control of direct-driven PMSG wind turbines," *IEEE Trans. Power Electron.*, vol. 27, no. 5, pp. 2325-2337, May. 2012.

[18] W. E. Leithead and B. Connor, "Control of variable speed wind turbines: dynamic models," *Int. J. Control*, vol. 73, no. 13, pp. 1173-1188, Sep. 2000.

[19] W. E. Leithead and B. Connor, "Control of variable speed wind turbines: design task," *Int. J. Control*, vol. 73, no. 13, pp. 1189-1212, Sep. 2000.

[20] C. T. Lee, C. W. Hsu, and P. T. Cheng, "A low-voltage ride-through technique of grid-connected converters of distributed energy resources," *IEEE Trans. Ind. Appl.*, vol. 47, no. 4, pp. 1821-1832, Jul./Aug. 2011.

[21] K. H. Kim, Y. C. Jeung, D. C. Lee, and H. G. Kim, "LVRT scheme of PMSG wind power systems based on feedback linearization," *IEEE Trans. Power Electron.*, vol. 27, no. 5, pp. 2376-2384, May 2012.

[22] M. Popat, B. Wu, and N. R. Zargari, "Fault ride-through capability of cascaded current-source converter-based offshore wind farm," *IEEE Trans. Sustainable Energy*, vol. 4, no. 2, pp. 314-323, Apr. 2013.

[23] F. Iov, A. Hansen, P. Sorensen, and N. Cutululis, "Mapping of grid faults and grid codes," *Risoe Natl. Lab., Tech. Univ. Denmark, Copenhagen, Tech. Rep.*, 2007

[24] M. Tsili and S. Papathanassiou, "A review of grid code technical requirements for wind farms," *IET Renew. Power Gener.*, vol. 3, no. 3, pp. 308-332, Sep. 2009.

[25] S. Alepuz, A. Calle, S. Busquets-Monge, S. Kouro, and B. Wu, "Use of stored energy in PMSG rotor inertia for low-voltage ride-through in back-to-back NPC converter-based wind power systems," *IEEE Trans. Ind. Electron.*, vol. 60, no. 5, pp. 1787-1796, May 2013.

[26] J. Yang, Y. J. Gao, and J. O'Reilly, "Permanent magnet synchronous generator converter protection analysis during DC wind farm open-circuit fault condition," in *Proc. IEEE EPEC*, pp. 1-6, 2009.

[27] M. Rizo, A. Rodriguez, E. Bueno, F. J. Rodriguez, and C. Giron, "Low voltage ride-through of wind turbine based on interior permanent magnet synchronous generators sensorless vector controlled," in *Proc. IEEE ECCE*, pp. 2507-2515, 2010.

[28] S. Seman, J. Niiranen, and A. Arkkio, "Ride-through analysis of doubly fed induction wind-power generator under unsymmetrical network disturbance," *IEEE Trans. Power Syst.*, vol. 21, no. 4, pp. 1782-1789, Nov. 2006.

[29] J. Matas, M. Castilla, J. M. Guerrero, L. Garcia de Vicuna, and J. Miret, "Feedback linearization of direct-drive synchronous wind turbines via a sliding mode approach," *IEEE Trans. Power Electron.*, vol. 23, no. 3, pp. 1093-1103, May 2008.

[30] J. Y. Dai, D. W. Xu, B. Wu, and N. R. Zargari, "Unified DC-link current control for low-voltage ride-through in current-source-converter-based wind energy conversion systems," *IEEE Trans. Power Electron.*, vol. 26, no. 1, pp. 288-297, Jan. 2011.

[31] J. Q. Liang, W. Qiao, and R. G. Harley, "Direct transient control of wind turbine driven DFIG for low voltage ride-through," in *Proc. IEEE PEMWA*, pp. 1-7, 2009.

[32] A. P. Grilo, A. S. A. Mota, L. T. M. Mota, and W. Freitas, "An analytical method for analysis of large-disturbance stability of induction generators," *IEEE Trans. Power Syst.*, vol. 22, no. 4, pp. 1861-1869, Nov. 2007.

[33] T. Vrionis, X. Koutiva, N. Vovos, and G. Giannakopulos, "Control of an HVDC link connecting a wind farm to the grid for fault ride-through enhancement," *IEEE Trans. Power Syst.*, vol. 22, no. 4, pp. 2039-2047, Nov. 2007.

[34] W. H. Hu, Z. Chen, Y. Wang, and Z. A. Wang, "Low voltage ride-through of variable speed wind turbines with permanent magnet synchronous generator," in *Proc. Ecologic Vehicles and Renewable Energies*, 2009.

[35] A. Mullane, G. Lightbody, and R. Yacamini, "Wind turbine fault ride through enhancement," *IEEE Trans. Power Syst.*, vol. 20, no. 4, pp. 1929-1937, Nov. 2005.

[36] W. Lin, C. Hong, T. Ou, and T. Chiu, "Hybrid intelligent control of PMSG wind generation system using pitch control with RBFN," *Energy Convers. Manage.*, vol. 52, no. 2, pp. 1244-1251, Feb. 2011.

[37] S. H. Li, T. A. Haskew, and L. Xu, "Conventional and novel control designs for direct driven PMSG wind turbines," *Electr. Power Syst. Res.*, vol. 80, no. 3, pp. 328-338, Mar. 2010.

[38] S. Morimoto, H. Nakayama, M. Sanada, and Y. Takeda, "Sensorless output maximization control for variable-speed wind generation system using IPMSG," *IEEE Trans. Ind. Appl.*, vol. 41, no. 1, pp. 60-67, Jan./Feb. 2005.

[39] W. Qiao, L. Y. Qu, and R. G. Harley, "Control of IPM synchronous generator for maximum wind power generation considering magnetic saturation," *IEEE Trans. Ind. Appl.*, vol. 45, no. 3, pp. 1095-1105, May/Jun. 2009.

[40] A. Uehara, A. Pratap, T. Goya, T. Senjyu, A. Yona, N. Urasaki, and T. Funabashi, "A coordinated control method to Smooth wind power fluctuations of a PMSG-based WECS," *IEEE Trans. Energy Convers.*, vol. 26, no. 2, pp. 550-558, Jun. 2011.

[41] A. Isidori, "Nonlinear control systems," *Springer-Verlag*, Berlin, Germany, 1995.

[42] A. Isidori, "Nonlinear control systems II," *Springer-Verlag*, London, 1999.

[43] J. J. E. Slotine and W. P. Li, "Applied nonlinear control," *Prentice-Hall Inc.*, London, 1991.

[44] H. K. Khalil, "Nonlinear systems," *Prentice-Hall Inc.*, London, 1996.

[45] J. Jung and S. Lim, "A feedback linearizing control scheme for a PWM converter-inverter having a very small dc-link capacitor," *IEEE Trans. Ind. Appl.*, vol. 35, no. 5, pp. 1124-1131, Sep. 1999.

[46] M. A. Rahman, D. M. Vilathgamuwa, M. N. Uddin, and K. J. Tseng, "Nonlinear control of interior permanent-magnet synchronous motor," *IEEE Trans. Ind. Appl.*, vol. 39, no. 2, pp. 408-416, Mar./Apr. 2003.

[47] O. Akhrif, F. A. Okou, L. A. Dessaint, and R. Champagne, "Application of a multivariable feedback linearization scheme for rotor angle stability and voltage regulation of power systems," *IEEE Trans. Power Syst.*, vol. 14, no. 2, pp. 620-628, May 1999.

[48] M. Krstic, I. Kanellakopoulos, and P. V. Kokotovic, "Nonlinear and adaptive control design," *John Wiley Inc.*, New York, 1995.

[49] S. S. Sastry and A. Isidori, "Adaptive control of linearizable systems," *IEEE Trans. Autom. Control*, vol. 34, no. 11, pp. 1123-1131, Nov. 1989.

[50] J. B. Pomet and L. Praly, "Adaptive nonlinear regulation: estimation from the Lyapunov equation," *IEEE Trans. Autom. Control*, vol. 37, no. 6, pp. 729-740, Jun. 1992.

[51] R. Marino and P. Tomei, "Global adaptive output-feedback control of nonlinear systems. I. Linear parameterization," *IEEE Trans. Autom. Control*, vol. 38, no. 1, pp. 17-32, Jan. 1993.

[52] R. Marino and P. Tomei, "Global adaptive output-feedback control of nonlinear systems. II. Linear parameterization," *IEEE Trans. Autom. Control*, vol. 38, no. 1, pp. 33-48, Jan. 1993.

[53] I. Kanellakopoulos, P. V. Kokotovic, and A. S. Morse, "Adaptive nonlinear control with incomplete state information," *Int. J. Adapt Control Signal Process.*, vol. 6, pp. 367-394, Jul. 1992.

[54] A. R. Teel, "Adaptive tracking with robust stability," in *Proceedings of the 32th IEEE conference on Decision and Control*, San Antonio, TX, pp. 570-575, 1993.

[55] H. Khalil, "High gain observers in nonlinear feedback control," *Springer*, London, 1999.

[56] F. Esfandiari and H. K. Khalil, "Output feedback stabilization of fully linearizable systems," *Int. J. Control*, vol. 56, no. 5, pp. 1007-1037, 1992.

[57] F. Esfandiari and H. K. Khalil, "Semiglobal stabilization f a class of nonlinear systems using output feedback," *IEEE Trans. Autom. Control*, vol. 38, no. 9, pp. 1412-1415, Sep. 1993.

[58] H. K. Khalil, "Robust servomechanism output feedback controllers for a class of feedback linearizable systems," *Automatica*, vol. 30, no. 10, pp. 1587-1599, Oct. 1994.

[59] H. K. Khalil, "Adaptive output-feedback control of nonlinear systems represented by input-output models," *IEEE Trans. Autom. Control*, vol. 41, no. 2, pp. 177-188, Feb. 1996.

[60] S. Oh and H. K. Khalil, "Nonlinear output-feedback tracking using high-gain observer and variable structure control," *Automatica*, vol. 33, no. 10, pp. 1845-1856, 1997.

[61] H. K. Khalil and E. G. Strangas, "Robust speed control of induction motors using position and current measurements," *IEEE Trans. Autom. Control*, vol. 41, no. 8, pp. 1216-1220, Aug. 1996.

[62] L. Jiang "Nonlinear adaptive control and applications in power systems," *Ph.D. Thesis*, University of Liverpool, Mar. 2001.

[63] J. Chen, L. Jiang, Wei Yao, and Q. H. Wu, "Perturbation estimation based nonlinear adaptive control of a full-rated converter wind-turbine for fault ride-through capability enhancement," *IEEE Trans. Power Syst.*, vol. PP, no. 99, pp. 1-11, Apr. 2014.

[64] L. Jiang and Q. H. Wu, "Nonlinear adaptive control via sliding-mode state and perturbation observer," *IET Control Theory Appl.*, vol. 149, no. 4, pp. 269-277, Jul. 2002.

[65] L. Jiang, Q. H. Wu, and J. Y. Wen, "Decentralized nonlinear adaptive control for multimachine power systems via high-gain perturbation observer," *IEEE Trans. Circuits Syst. Regul. Pap.*, vol. 51, pp. 2052-2059, Oct. 2004.

[66] L. Jiang, Q. H. Wu, G. P. Liu, and D. Rees, "Robust adaptive control of induction motor based on perturbation Estimation," *Proc. IEEE IEMDC*, pp. 101-106, 2007

[67] M. A. Abdullah, A. H. M. Yatim, C. W. Tan, and R. Saidur, "A review of maximum power point tracking algorithms for wind energy systems," *Renewable Sustainable Energy Rev.*, vol. 16, no. 5, pp. 3220-3227, Jun. 2012.

[68] Y. Xia, K. H. Ahmed, and B. W. Williams, "A review of maximum power point tracking algorithms for wind energy systems," *IEEE Trans. Power Electron.*, vol. 26, no. 12, pp. 3609-3620, Dec. 2011.

[69] I. Munteanu, N. A. Cutululis, A. I. Bratcu, and E. Ceanga, "Optimization of variable speed wind power systems based on LQG approach," *IEEE Trans. Power Electron.*, vol. 13, no. 7, pp. 903-912, Jul. 2005.

[70] B. Boukhezzar and H. Siguerdidjane, "Comparison between linear and non-linear control strategies for variable speed wind turbines," *Control Eng. Pract.*, vol. 18, no. 12, pp. 1357-136, Dec. 2010.

[71] S. Z. Chen, N. C. Cheung, K. C. Wong, and J. Wu, "Integral sliding-mode direct torque control of doubly-fed induction generators under unbalanced grid voltage," *IEEE Trans. Energy Convers.*, vol. 25, no. 2, pp. 356-368, Jun. 2010.

[72] F. Delfino, F. Pampararo, R. Procopio, and M. Rossi, "A feedback linearization control scheme for the integration of wind energy conversion systems into distribution grids," *IEEE Syst. J.*, vol. 6, no. 1, pp. 85-93, Mar. 2012.

[73] I. C. Baik, K. H. Kim, and M. J. Youn, "Robust nonlinear speed control of PM synchronous motor using boundary layer integral sliding mode control technique," *IEEE Trans. Control Syst. Technol.*, vol. 8, no. 1, pp. 47-54, Jan. 2000.

[74] R. Krishnan and P. Vijayraghavan, "Fast estimation and compensation of rotor flux linkage in permanent magnet synchronous machines," in Proc. *IEEE-ISIE*, vol. 2, pp. 661-666, 1999.

[75] A. Yoo and S. K. Sul, "Design of flux observer robust to interior permanent-magnet synchronous motor flux variation," *IEEE Trans. Ind. Appl.*, vol. 45, no. 5, pp. 1670-1677, Sep./Oct. 2009.

[76] J. M. Mauricio, A. E. Leon, A. Gomez-Exposito, and J. A. Solsona, "An adaptive nonlinear controller for DFIM-based wind energy conversion systems," *IEEE Trans. Energy Convers.*, vol. 23, no. 4, pp. 1025-1035, Dec. 2008.

[77] C. L. Xia, Q. Geng, X. Gu, T. N. Shi, and Z. F. Song, "Input-output feedback linearization and speed control of a surface permanent-magnet synchronous wind generator with the boost-chopper converter," *IEEE Trans. Ind. Electron.*, vol. 59, no. 9, pp. 3489-3500, Sep. 2012.

[78] Y. A. R. I. Mohamed, "Design and implementation of a robust current-control scheme for a PMSM vector drive with a simple adaptive disturbance observer," *IEEE Trans. Ind. Electron.*, vol. 54, no. 4, pp. 1981-1988, Aug. 2007.

[79] F. Valenciaga and P. F. Puleston, "High-order sliding control for a wind energy conversion system based on a permanent magnet synchronous generator," *IEEE Trans. Energy Convers.*, vol. 23, no. 3, pp. 860-867, Sep. 2008.

[80] D. S. L. Dolan and P. W. Lehn, "Simulation model of wind turbine 3p torque oscillations due to wind shear and tower shadow," *IEEE Trans. Energy Convers.*, vol. 21, no. 3, pp. 717-724, Sep. 2006.

[81] F. M. Hughes, O. Anaya-Lara. G. Ramtharan, N. Jenkins, and G. Strbac, "Influence of tower shadow and wind turbulence on the performance of power

system stabilizers for DFIG-based wind farms," *IEEE Trans. Energy Convers.*, vol. 23, no. 2, pp. 519-528, Jul. 2008.

[82] R. Fadaeinedjad, G. Moschopoulos and M. Moallem, "The impact of tower shadow, yaw error, and wind shears on power quality in a wind-diesel system," *IEEE Trans. Energy Convers.*, vol. 24, no. 1, pp. 102-111, Mar. 2009.

[83] A. Kumar and K. Stol, "Simulating feedback linearization control of wind turbines using high-order models," *Wind Energy*, vol. 13, no. 5, pp. 419-432, Jul. 2010.

[84] E. A. Bossanyi, "The design of closed loop controllers for wind turbines," *Wind Energy*, vol. 3, no. 3, pp. 149-163, Jul./Sep. 2000.

[85] V. Akhmatov, H. Knudsen, A. H. Nielsen, J. K. Pedersen, and N. J. Poulsen, "Modelling and transient stability of large wind farms," *Int. J. Electr. Power Energy Syst.*, vol. 25, no. 2, pp. 123-144, Feb. 2003.

[86] B. Connor, W. E. Leithead, and M. Grimble, "LQG control of a constant speed horizontal axis wind turbine," in *Proc. IEEE CCA*, pp. 251-252, Aug. 1994.

[87] R. Sakamoto, T. Senjyu, T. Kaneko, N. Urasaki, T. Takagi, S. Sugimoto, and H. Sekine, "Output power leveling of wind turbine generator by pitch angle control using $H\infty$ control ," in *Proc. IEEE PES*, pp. 2044-2049, 2006.

[88] M. J. Grimble, "Horizontal axis wind turbine control : comparison of classical , LQG and $H\infty$ designs," *Dyn. Control*, vol. 6, no. 2, pp. 143161, Apr. 1996.

[89] J. Y. Seol and I. J. Ha, "Feedback-linearizing control of IPM motors considering magnetic saturation effect," *IEEE Trans. Power Electron.*, vol. 20, no. 2, pp. 416-424, Mar. 2005.

[90] S. Alepuz, S. Busquets-Monge, J. Bordonau, J. A. Martinez-Velasco, C. A. Silva, J. Pontt, and J. Rodriguez, "Control strategies based on symmetrical

components for grid-connected converters under voltage dips," *IEEE Trans. Ind. Electron.*, vol. 56, no. 6, pp. 2162-2173, Jun. 2009.

[91] J. Matas, P. Rodriguez, J. M. Guerrero, and J. C. Vasquez, "Ride through improvement of wind-turbines via feedback linearization," in *Proc. IEEE ISIE*, pp. 2377-2382, 2008.

[92] J. B. Hu, H. Nian, B. Hu, Y. K. He, and Z. Q. Zhu, "Direct active and reactive power regulation of DFIG using sliding-mode control approach," *IEEE Trans. Energy Convers.*, vol. 25, no. 4, pp. 1028-1039, Dec. 2010.

[93] J. G. Zhou and Y. Y. Wang, "Real-time nonlinear adaptive backstepping speed control for a PM synchronous motor," *Control Eng. Pract.*, vol. 13, no. 10, pp. 1259-1269, Oct. 2005.

[94] A. Kaddouri, O. Akhrif, and H. Le-Huy, "Adaptive nonlinear control for speed regulation of a permanent-magnet synchronous motor," in *Proc. IEEE IECON*, vol. 3, pp. 1079-1084, 1999.

[95] Y. J. Huang, T. C. Kuo, and S. H. Chang, "Adaptive sliding-mode control for nonlinear systems with uncertain parameters," *IEEE Trans. Syst. Man Cybern. Part B Cybern.*, vol. 38, no. 2, pp. 534-539, Apr. 2008.

[96] C. M. Lin and Y. J. Mon, "Decoupling control by hierarchical fuzzy sliding-mode controller," *IEEE Trans. Control Syst. Technol.*, vol. 13, no. 4, pp. 593-598, Jul. 2005.

[97] L. Jiang, Q. H. Wu, J. Wang , C. Zhang, and X. X. Zhou, "Robust observer-based nonlinear control of multimachine power systems," *IEE Proc.-Gener. Transm. Distrib.*, vol. 148, no. 6, pp. 623 -631, Nov. 2001.

[98] Q. H. Wu, L. Jiang, and J.Y. Wen, "Decentralised adaptive control of interconnected non-linear systems using high gain observer," *Int. J. Control*, vol. 77, no. 8, pp. 703-712, May 2004.

[99] J. F. Conroy and R.Watson, "Low-voltage ride-through of a full converter wind turbine with permanent magnet generator," *IET Renew. Power Gener.*, vol. 1, no. 3, pp. 182 -189, Sep. 2007.

[100] T. H. Nguyen and D.-C. Lee, "Advanced fault ride-through technique for PMSG wind turbine systems using line-side converter as STATCOM," *IEEE Trans. Ind. Electron.*, vol. 60, no. 7, pp. 2842-2850, Jul. 2013.

[101] K. Clark, N. Miller, and J. Sanchez-Gasca, "Modeling of GE wind turbine-generators for grid studies," *Version 4.2, GE Energy*, 2008.

[102] H. Li, K. L. Shi, and P. G. McLaren, "Neural-network-based sensorless maximum wind energy capture with compensated power coefficient," *IEEE Trans. Ind. Appl.*, vol. 41, no. 6, pp. 1548-1556, Nov./Dec. 2005.

[103] M. Simoes, B. Bose, and R. Spiegel, "Design and performance evaluation of a fuzzy-logic-based variable-speed wind generation system," *IEEE Trans. Ind. Appl.*, vol. 33, no. 4, pp. 956-965, Jul./Aug. 1997.

[104] D. Leith and W. Leithead, "Implementation of wind turbine controllers," *Int. J. Control*, vol. 66, no. 3, pp. 349-380, 1997.

[105] H. Camblong, "Digital robust control of a variable speed pitch regulated wind turbine for above rated wind speeds," *Control Eng. Pract.*, vol. 16, no. 8, pp. 946-958, Aug. 2008.

[106] R. Krishnan, *Electric Motor Drives: Modeling, Analysis, and Control.*, Upper Saddle River, NJ, Unite States: Prentice-Hall, 2001.

[107] H. Nakai, H. Ohtani, E. Satoh, and Y. Inaguma, "Development and testing of the torque control for the permanent-magnet synchronous motor," *IEEE Trans. Ind. Electron.*, vol. 52, no. 3, pp. 800-806, Jun. 2005.

[108] V. Q. Leu, H. H. Choi, and J. W. Jung, "Fuzzy sliding mode speed controller for PM synchronous motors with a load torque observer," *IEEE Trans. Power Electron.*, vol. 27, no. 3, pp. 1530-1539, Mar. 2012.

[109] X. G. Zhang, L. Z. Sun, K. Zhao, and L. Sun, "Nonlinear speed control for PMSM system using sliding-mode control and disturbance compensation techniques," *IEEE Trans. Power Electron.*, vol. 28, no. 3, pp. 1358-1365, Mar. 2013.

[110] H. X. Liu and S. H. Li, "Speed control for PMSM servo system using predictive functional control and extended state observer," *IEEE Trans. Ind. Electron.*, vol. 59, no. 2, pp. 1171-1183, Feb. 2012.

[111] N. T. -T. Vu, H. H. Choi, R. -Y. Kim, and J. -W. Jung, "Robust speed control method for permanent magnet synchronous motor," *IET Electr. Power Appl.*, vol. 6, no. 7, pp. 399-411, Aug. 2012.

[112] C. -K. Lin , T. -H. Liu, and S. -H. Yang, "Nonlinear Position Controller Design With Input-Output Linearisation Technique For An Interior Permanent Magnet Synchronous Motor Control System," *IET Electr. Power Appl.*, vol. 1, no. 9, pp. 14-26, Mar. 2008.

[113] B. Grcar, P. Cafuta, M. Znidaric, and F. Gausch, "Nonlinear control of synchronous servo drive," *IEEE Trans. Control Syst. Technol.*, vol. 4, no. 2, pp. 177-184, Mar. 1996.

[114] H. Kim, J. Son, and J. Lee, "A high-speed sliding-mode observer for the sensorless speed control of a PMSM," *IEEE Trans. Ind. Electron.*, vol. 58, no. 9, pp. 4069-4077, Sep. 2011.

[115] J. -W. Jung, T. H. Kim, and H. H. Choi, "Speed control of a permanent magnet synchronous motor with a torque observer: a fuzzy approach," *IET Control Theory Appl.*, vol. 4, no. 12, pp. 2971-2981, Dec. 2010.

[116] S. H. Li and Z. G. Liu, "Adaptive speed control for permanent-magnet synchronous motor system with variations of load inertia," *IEEE Trans. Ind. Electron.*, vol. 56, no. 8, pp. 3050-3059, Aug. 2009.

[117] H. H. Choi, N. T. -T. Vu, and J. -W. Jung, " Digital implementation of an adaptive speed regulator for a PMSM," *IET Electr. Power Electron.*, vol. 26, no. 1, pp. 3-8, Feb. 2011.

[118] S. J. Underwood and I. Hussain,"Online parameter estimation and adaptive control of permanent-magnet synchronous machines," *IEEE Trans. Ind. Electron.*, vol. 57, no. 7, pp. 24352443, Jul. 2010.

[119] K. -H. Kim, "Model reference adaptive control-based adaptive current control scheme of a PM synchronous motor with an improved servo performance," *IET Electr. Power Appl.*, vol. 3, no. 1, pp. 8-18, Jan. 2009.

[120] M. Morawiec, "The adaptive backstepping control of permanent magnet synchronous motor supplied by current source inverter," *IEEE Trans. Ind. Inf.*, vol. 9, no. 2, pp. 1047 -1055, May 2013.

[121] T.-H. Liu , H.-T. Pu and C.-K. Lin, " Implementation of an adaptive position control system of a permanent-magnet synchronous motor and its application," *IET Electr. Power Appl.*, vol. 4, no. 9, pp. 121-130, Feb. 2010.

[122] J. A. Solsona and M. I. Valla, "Disturbance and Nonlinear luenberger observers for estimating mechanical variables in permanent magnet synchronous motors under mechanical parameters uncertainties," *IEEE Trans. Ind. Electron.*, vol. 50, no. 4, pp. 717 -725, Aug. 2003.

[123] G. C. Zhu, L. A. Dessaint, Q. Akhrif, and A. Kaddouri, "Speed tracking control of a permanent-magnet synchronous motor with state and load torque observer," *IEEE Trans. Ind. Electron.*, vol. 47, no. 2, pp. 346 -355, Apr. 2000.

[124] J. Solsona, M. I. Valla, and C. Muravchik, "A nonlinear reduced order observer for permanent magnet synchronous motors," *IEEE Trans. Ind. Electron.*, vol. 43, no. 4, pp. 492-497, Aug. 1996.

[125] J. Solsona, M. I. Valla, and C. Muravchik, "Nonlinear control of a permanent magnet synchronous motor with disturbance torque estimation," *IEEE Trans. Energy Convers.*, vol. 15, no. 2, pp. 163-168, Jun. 2000.

[126] K. -H. Kim and M. -J. Youn, "A nonlinear speed control for a PM synchronous motor using a simple disturbance estimation technique," *IEEE Trans. Ind. Electron.*, vol. 49, no. 3, pp. 524-535, Jun. 2002.

[127] Y. X. Su, C. H. Zheng, and B. Y. Duan, "Automatic disturbances rejection controller for precise motion control of permanent-magnet synchronous motors," *IEEE Trans. Ind. Electron.*, vol. 52, no. 3, pp. 814-823, Jun. 2005.